Winners and losers in a melting Arctic *p. 572*

Molecular mechanisms of neurodegeneration *p. 601*

Hints of Weyl fermions found in solids *pp. 613 & 622*

Science

$10
7 AUGUST 2015
sciencemag.org

AAAS

Concrete connection

High-strength rock explains caldera uplift and Roman concrete *p. 617*

CONTENTS

590 & 647
More optogenetics tools

7 AUGUST 2015 • VOLUME 349 • ISSUE 6248

578

NEWS

IN BRIEF

IN DEPTH

FEATURES

INSIGHTS

PERSPECTIVES

BOOKS *ET AL.*

LETTERS

Published by AAAS

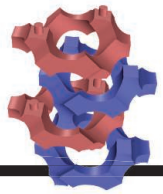

613 & 622

Weyl points in a double gyroid

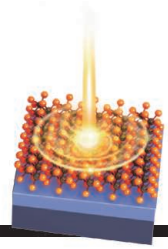

625

Enhancing transistor contacts

RESEARCH

IN BRIEF

REVIEW

RESEARCH ARTICLES

REPORTS

DEPARTMENTS

ON THE COVER

Ruins of the Serapeo market in Pozzuoli, Italy. The hard caprock of Italy's Campi Flegrei geothermal system is made up of a fiber-reinforced rock formed by the mixture of lime with regional volcanic ash known as pozzolana. The caprock shares many physical properties with Roman concrete, helping to explain the rock strains and strengths in the region. See page 617.
Photo: © Roger Ressmeyer/Corbis

PHOTO: (TOP) JONATHAN WILKER

SCIENCE (ISSN 0036-8075) is published weekly on Friday, except the last week in December, by the American Association for the Advancement of Science, 1200 New York Avenue, NW, Washington, DC 20005. Periodicals mail postage (publication No. 484460) paid at Washington, DC, and additional mailing offices. Domestic individual membership and subscription (51 issues): $153 ($74 allocated to subscription). Domestic institutional subscription (51 issues): $1282; Foreign postage extra: Mexico, Caribbean (surface mail) $55; other countries (air assist delivery) $85. First class, airmail, student, and emeritus rates on request. Canadian rates with GST available upon request, GST #1254 88122. Publications Mail Agreement Number 1069624. **Printed in the U.S.A.**
Change of address: Allow 4 weeks, giving old and new addresses and 8-digit account number. **Postmaster:** Send change of address to AAAS, P.O. Box 96178, Washington, DC 20090–6178. **Single-copy sales:** $10.00 current issue, $15.00 back issue prepaid includes surface postage; bulk rates on request. *Science* is indexed in the *Reader's Guide to Periodical Literature* and in several specialized indexes.

Published by AAAS

Science
AAAS
1200 New York Avenue, NW, Washington, DC 20005
Bateman House, 82-88 Hills Road, Cambridge, UK CB2 1LQ

SUBSCRIPTION SERVICES For change of address, missing issues, new orders and renewals, and payment questions: 866-434-AAAS (2227) or 202-326-6417, FAX 202-842-1065. Mailing addresses: AAAS, P.O. Box 96178, Washington, DC 20090-6178 or AAAS Member Services, 1200 New York Avenue, NW, Washington, DC 20005

INSTITUTIONAL SITE LICENSES 202-326-6755 **REPRINTS:** Author Inquiries 800-635-7181 **COMMERCIAL INQUIRIES** 803-359-4578 **PERMISSIONS** 202-326-6765, permissions@aaas.org **AAAS Member Services** 202-326-6417 or http://membercentral.aaas.org/discounts

Science serves as a forum for discussion of important issues related to the advancement of science by publishing material on which a consensus has been reached as well as including the presentation of minority of conflicting points of view. Accordingly, all articles published in *Science*—including editorials, news and comment, and books reviews—are signed and reflect the individual views of the authors and not official points of view adopted by AAAS or the institutions with which the authors are affiliated.

INFORMATION FOR AUTHORS See pages 678 and 679 of the 6 February 2015 issue or access www.sciencemag.org/about/authors

Published by AAAS

EDITORIAL

The next century of ecology

The science of ecology is about relationships—among organisms and habitats, on all scales—and how they provide information that helps us better understand our world. In the past 100 years, the field has moved from observations to experiments to forecasting. Next week, the Ecological Society of America (ESA), the world's largest ecological society, celebrates its centennial in Baltimore, an opportunity to reflect on the field's past and future. The gathering of international scientists, policy-makers, and students will not only explore the knowledge in hand, but consider what else is needed to chart a course over the next century in which humanity sustains and even improves the relationships that underpin life on Earth.

Characterized by a focus on interactions, from genes to global scales, and between living and nonliving components of ecosystems, basic ecological research has spawned important paradigm changes over the past 100 years. For example, we have learned that a simple graphical model of biogeography can explain species distribution patterns at many spatial scales. Another major change has been the development of our understanding of succession after disturbances, from major forest fires to the effects of antibiotics on intestinal microbial communities. As ecological science becomes more interdisciplinary, shifts in thinking and unexpected impacts will continue. Early ecologists who thought about principles governing plant and animal communities never imagined that their ideas would provide the foundation for understanding the human microbiome, affecting our nutrition, immune system, and even psychological state. The new field of synthetic ecology, in which ecologists and medical professionals design beneficial microbial communities, has its origins in century-old ecological field studies. These examples foretell how the roles of ecologists and the applications of ecological principles are likely to change in the next century, and why medical students and practitioners need to understand ecology.

"We enter a time when society is armed with the scientific knowledge and ability to make responsible decisions."

The good news is that ecology's role in society has grown dramatically over the past century. Basic research on organism and environment interactions has had far-reaching impacts on legislation. In the United States, this knowledge has contributed the scientific basis for the landmark Endangered Species Act (1973) and Clean Water Act (1972). In this vein, in the 1990s, the ESA's Sustainable Biosphere Initiative encouraged the world's ecologists to identify major environmental challenges. Today, its Earth Stewardship Initiative frames a commitment by ecologists to make their science relevant to society through activities ranging from practical demonstrations to communication campaigns directed at other communities, including communities of faith. ESA's meeting in Baltimore will highlight ongoing studies of the city's urban ecology as a model to create more livable and sustainable cities, linking environmental stewardship to design and planning.

The international community also is placing more emphasis on ecology, as demonstrated by the new Intergovernmental Platform on Biodiversity and Ecosystem Services. Its first assessment, focused on pollinators, and reports will provide actionable science-based recommendations that should catalyze better incorporation of ecological science into management and legislation. The new U.S. National Ecological Observatory Network should elucidate the importance of the biosphere in Earth system dynamics and its governing role in climate, a resource for all countries. With newly developed tools, analytical methods, and models to forecast the future of the world's environment, ecologists can inform policy-makers and political leaders about how to prevent, mitigate, or adapt to environmental change.

From the microbes inhabiting the earth beneath our feet to environments of the universe unknown to us now, the next 100 years of ecological discoveries will influence our lives. We enter a time when society is armed with the scientific knowledge and ability to make responsible decisions.

– David W. Inouye

David W. Inouye is president of the Ecological Society of America; professor emeritus at the University of Maryland, College Park, MD; and a principal investigator at the Rocky Mountain Biological Laboratory, Crested Butte, CO. E-mail: inouye@umd.edu

10.1126/science.aab1685

PHOTOS: (TOP RIGHT) MARTHA INOUYE; (INSET) © TANG YAU HOONG/IKON IMAGES/CORBIS

NEWS

> “You have to have something in writing saying you will be using it for research purposes.”

A technical support specialist for a company selling performance-enhancing compound FG-4592, to *The New York Times* on 29 July. Online chemical supply companies sell the drug—found in tests of two cyclists—but only to researchers.

IN BRIEF

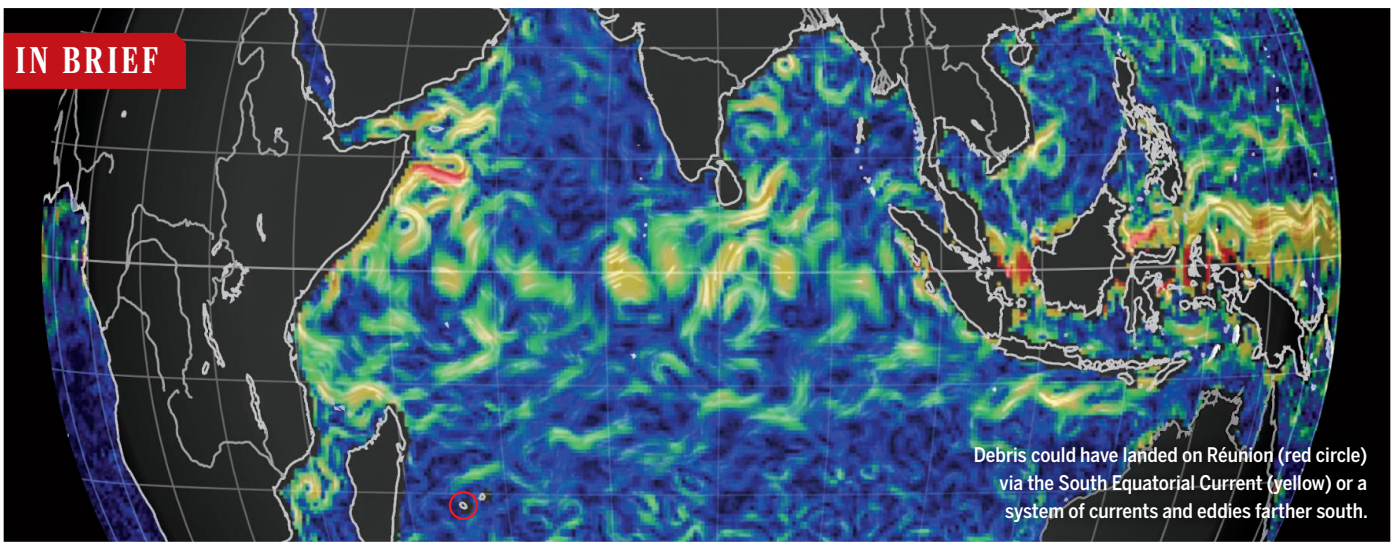

Debris could have landed on Réunion (red circle) via the South Equatorial Current (yellow) or a system of currents and eddies farther south.

IMAGES: (TOP TO BOTTOM) CAMERON BECCARIO/EARTH.NULLSCHOOL.NET/DATA FROM ESR; OSCAR THIRD DEGREE RESOLUTION OCEAN SURFACE CURRENTS; OAK RIDGE NATIONAL LABORATORY/FLICKR

New evidence in the hunt for MH370

A piece of an airplane wing, recovered last week from the island of Réunion in the Indian Ocean, may hold new clues to the fate of Malaysia Airlines flight 370 (MH370), which disappeared in March 2014 (*Science*, 30 May 2014, p. 963). Experts began analyzing the wing component this week to determine whether it belonged to the missing plane; among other pieces of evidence, the part's encrusting of goose barnacles may provide information about the temperature and chemical composition of the water through which it traveled. Meanwhile, oceanographers at the National Oceanography Centre in Southampton, U.K., analyzed decades of Indian Ocean currents to recreate two possible scenarios by which debris from a crash in the southern Indian Ocean could have ended up far to the west, on an island off the coast of Madagascar. The analysis revealed two possible scenarios, they reported on 31 July: A swirl of currents called a subtropical gyre may have pushed the debris north toward the powerful South Equatorial Current, which would then shunt it to the west. A global ocean simulation called the NEMO model suggests an alternate route: The debris may have been carried along by a complex pattern of swirling currents and eddies traveling slowly westward.

AROUND THE WORLD

Boost for exascale computing

WASHINGTON, D.C. | The United States is officially in the exascale hunt, an effort to make a supercomputer some 30 times more powerful than today's top machine. Last week President Barack Obama signed an executive order creating a national strategic computing initiative, which aims to coordinate high-performance computing research and development between federal agencies. Past U.S. supercomputing efforts have largely been pursued independently by different federal agencies. But the top machines are now so complex and expensive that agencies must pool their R&D budgets. The order should make it easier for agencies to justify increasing their budget requests to Congress for supercomputing R&D. “This is an extremely important step for high performance computing in the U.S.,” says Horst Simon, deputy director of the Lawrence Berkeley National Laboratory in California.
http://scim.ag/Obamaexascale

Titan at Oak Ridge National Laboratory is the world's second fastest supercomputer.

U.S. plan to cut emissions

WASHINGTON, D.C. | President Barack Obama on 3 August formally released a long-awaited plan to regulate greenhouse gas emissions from U.S. power plants. The Clean Power Plan aims to cut emissions by 2030 to 32% below 2005 levels, mostly by creating disincentives to burn coal to generate electricity. It would also boost incentives to build lower carbon power sources, capture carbon emissions from power plants, and conserve energy. Analysts say the plan could cut the share of U.S. electricity produced by coal combustion to about 27%, down from about 50% today, while expanding generation from renewables by one-third. White House officials call the plan, which is expected to cost $8.4 billion annually, "fair and flexible." But opponents in Congress and industry vow to mount legislative and legal challenges, which could take years to resolve. http://scim.ag/plantemissions

South Korea not 'MERS-free' yet

SEOUL | South Korea has almost conquered the explosive Middle East respiratory syndrome (MERS) epidemic that began in May—but not quite. The virus resulted in 186 laboratory-confirmed infections and 36 deaths. On 28 July, Korean Prime Minister Hwang Kyo-ahn declared a "de facto end" to the outbreak; but to officially call the country MERS-free, South Korea has to wait 28 days—twice the virus's incubation period—after the last patient has died or cleared the virus, says a spokesperson for the Korea Centers for Disease Control and Prevention (KCDC). However, one patient, lingering in hospital isolation, continues to test positive for the virus; the 28-day countdown begins when that patient either dies or tests negative. KCDC hopes to get those negative results "soon" the KCDC spokesman says, in which case the outbreak could be formally declared over by early to mid-September. http://scim.ag/SKoreaMERS

Golden rice retraction proceeds

BETHESDA, MARYLAND | A controversial 2012 study that showed genetically engineered golden rice could alleviate vitamin A deficiency in children was retracted by the *American Journal of Clinical Nutrition* on 29 July, nearly 2 years after investigations found problems with how the study had been conducted. In 2008, Guangwen Tang of Tufts University led a trial that gave golden rice, spinach, or a supplement to 68 children aged 6 to 8 in China's

PHOTO: VINCE O'SULLIVAN/FLICKR

Three Q's

Last week, the death of Cecil the lion, allegedly shot by an American trophy hunter after it was lured outside Zimbabwe's Hwange National Park, sparked international outrage. Cecil (pictured) was part of a study led by **David Macdonald** of the University of Oxford's Wildlife Research Conservation Unit in the United Kingdom. The lion's death has had one positive outcome: Donations to Macdonald's program poured in after TV host Jimmy Kimmel made a plea for lion conservation on 28 July. They have been tracking the movements of more than 200 lions with satellites to better understand the animals' behavior.

Q: What was your reaction when you heard of Cecil's death?
A: It is my day-to-day work to find animals that I'm working on suffering gruesome deaths. I seek to make the best of it by using the information to build a stronger scientific case. On the other hand, I'm a conservation biologist because I care about wildlife. And as I have studied [Cecil] for years … I was saddened at the thought of its death. And because it appears in this case that at least some of the actors in this were behaving illegally, one is not only saddened but enraged.

Q: How did you feel when Kimmel asked viewers to support your research?
A: He has catalyzed a wonderful action. Our project relies entirely on philanthropic gifts. To run this project … is going to cost us between £150,000 and £200,000 ($234,000 and $312,000) next year. We had no idea how we were going to pay for that.

Q: Has the appeal raised enough money?
A: At the moment it is close to half a million dollars. Hopefully it means we will be able to expand the project from Zimbabwe into adjoining areas in Botswana and Zambia. It would be a fitting memorial, you might say, to the sad and reprehensible loss of this lion.

Hunan province; the findings showed the beta-carotene in golden rice was just as effective at alleviating the deficiency. But Greenpeace claimed the children were used as "guinea pigs," sparking media outrage in China. External and internal panels at Tufts found multiple irregularities in the trial in September 2013, but also found that the study was safe and its conclusions valid. Last year, Tang asked the Massachusetts Superior Court to stop the journal from retracting the article, but the petition was denied last month.
http://scim.ag/goldriceretract

Misconduct probe suit dismissed

BOSTON | A case brought by two cardiac stem cell researchers against their institution for allegedly mishandling an ongoing misconduct investigation was dismissed last week in federal district court. The plaintiffs, Piero Anversa and Annarosa Leri, sued Harvard Medical School and its affiliate, Brigham and Women's Hospital (BWH), claiming that the inquiry into their lab at BWH wrongfully damaged their reputations. The complaint, filed in December, acknowledged that some papers from the lab contained fictitious data points and altered figures, but blamed a former senior researcher on their team. They accused the investigatory panel of factual errors, missed deadlines, conflicts of interest, and disclosure of confidential information. The judge decided that, before bringing the case back to court, Anversa and Leri must wait for the investigation to conclude and air their grievances with the U.S. Office of Research Integrity in an administrative hearing.
http://scim.ag/BWHsuit

The hexacopter observed humpback whales engaging in "bubble-net feeding."

Giving whales a breathalyzer test—from the air

Whales, like many cetaceans, are prone to respiratory tract infections, which can increase death rates for already endangered populations. Assessing whales' health, however, isn't an easy proposition: Scientists hoping to measure bacteria and fungi in a whale's "breath"—the moist air it shoots from its blowhole—need to get close enough to take a sample. Enter the whalecopter, a small, remote-controlled drone developed by researchers at the Woods Hole Oceanographic Institution in Massachusetts and the National Oceanic and Atmospheric Administration. The drone—a six-propeller hexacopter (left)—can collect breath samples and take detailed photos of the whales' spouts from the air. In a test at the Stellwagen Bank National Marine Sanctuary last month, the whalecopter took full-body photographs (above) of 36 animals and collected breath samples from another 16, which the team will analyze for microorganism assemblages. The researchers plan to go out again next March to the relatively pristine Antarctic Peninsula to collect breath samples from the same species.

NEWSMAKERS

Neuroscience booster indicted

One of the leading advocates for neuroscience research in the U.S. Congress was indicted last week for alleged misuse of $600,000 in connection with a failed 2007 campaign to become mayor of Philadelphia. The U.S. Justice Department has accused **Representative Chaka Fattah (D–PA)** and four associates of carrying out "a wide-ranging conspiracy involving bribery, concealment of unlawful campaign contributions, and theft of charitable and federal funds to advance their own personal interests." Elected in 1994, Fattah, 58, is credited with helping to lay the groundwork for the Obama administration's new BRAIN Initiative. He says he will fight the charges and plans to seek reelection next year. http://scim.ag/Fattah

BY THE NUMBERS

20

Rain deficit, in inches, in California from 2012 to 2015—equivalent to a year's worth of rain for the state. The culprit: a dearth of "atmospheric rivers," water vapor–rich air currents from the Pacific Ocean (*Journal of Geophysical Research: Atmospheres*).

24°C

Update to the office "thermoneutral zone"—not too hot or cold for most men and women. Previous models, used since the 1960s, suggested 21°C based on men wearing suits (*Nature Climate Change*).

13%

Increase in purchases of "social identity" items, such as gold earrings or cologne, when classical music is playing in a store (*Journal of Retail*).

PHOTOS: ACQUIRED UNDER NATIONAL MARINE FISHERIES SERVICE PERMIT 17355-01 AND NOAA CLASS G FLIGHT AUTHORIZATION 2015-ESA-4-NOAA/PHOTO BY JOHN DURBAN, SOUTHWEST FISHERIES SCIENCE CENTER, NMFS, NOAA AND MICHAEL MOORE, WOODS HOLE OCEANOGRAPHIC INSTITUTION (2)

The clinical trial analysis included data on 4394 Guineans who received the Ebola vaccine, produced by Merck.

PHOTO: SEAN HAWKEY

INFECTIOUS DISEASES

Unusual Ebola vaccine study pays off in Guinea

A vaccination trial targeting contacts of cases produces landmark results

By **Martin Enserink**

Ana Maria Henao-Restrepo, a Colombian epidemiologist working for the World Health Organization (WHO), faced the challenge of a lifetime this year in Guinea: coordinating a vaccine trial with an untested design, during an Ebola epidemic in one of the world's poorest countries, where the health system is dilapidated and the population mistrusts both its own government and foreign assistance. "I need every one of my 20 years of experience in public health here," Henao-Restrepo said when *Science* visited her in Conakry, Guinea's capital, in late April.

Rattling on her cellphone in French, she was overseeing the work of nine teams of Guinean health workers. Every day, they fanned out over the Basse Guinée region, bringing a refrigerated experimental vaccine to communities with a newly diagnosed case of Ebola. A whiteboard kept track of the teams' mobile numbers and schedules—they often traveled 4 or 5 hours away from the capital. "It can be very frustrating," Henao-Restrepo says. "Sometimes I go to bed at night wondering if this is going to happen."

It did. On 31 July, *The Lancet* published an interim analysis of the trial, with Henao-Restrepo as the first author. It shows that the vaccine, produced by Merck, appears to be remarkably effective at preventing Ebola. The paper—the first from a slew of drug and vaccine trials set up during the epidemic—was hailed as a landmark by scientists and public health experts. "It's a wonderful result," says Adrian Hill, a vaccine researcher at the University of Oxford in the United Kingdom. "We will teach about this in public health schools," adds Michael Osterholm, an epidemiologist at the University of Minnesota, Twin Cities. WHO officials are now hopeful that the Merck vaccine can help end Guinea's epidemic; it may also be deployed in Sierra Leone, where the outbreak continues as well.

The outcome was particularly gratifying for Guinea, because it almost missed the chance to contribute to Ebola vaccine research, says Guinean epidemiologist Mandy Kader Konde, one of the study's three principal investigators. Last fall, when scientists began planning tests of the Merck vaccine and another produced by GlaxoSmithKline (GSK), the U.S. National Institutes of Health partnered with the Liberian government, and the U.S. Centers for Disease Control and Prevention teamed with Sierra Leone. "There was nothing for Guinea," Kader Konde says.

In November, WHO took the unusual initiative of organizing a Guinea trial itself, in a coalition with the Norwegian Institute of Public Health, Doctors Without Borders, and a dozen other institutes in Africa, Europe, and the United States. It opted to test the Merck product, called rVSV-ZEBOV. Developed at the Public Health Agency of Canada, the vaccine consists of a livestock pathogen, vesicular stomatitis virus, equipped with the glycoprotein on the Ebola virus's surface.

But by then, with the number of Ebola cases dwindling, it was becoming clear that traditional study designs could yield results only if researchers vaccinated massive numbers of people. A phase III study in Liberia testing both the GSK and the Merck vaccines, which aimed to enroll 27,000 people, was put on hold after the epidemic there ended. The Sierra Leone study, using only Merck's vaccine, is ongoing but unlikely to provide efficacy data.

Consequently, the Guinea consortium opted for an unprecedented ring vaccination design, in which only the people most at risk—those who came into contact with an Ebola infected person and the contacts' contacts—were enrolled. The rings of contacts, or clusters, were randomly assigned to two arms: Half got the shot right away, whereas the other half had to wait for 3 weeks.

The study team kept a low profile and initially avoided bringing non-African foreigners to study sites so as not to fuel distrust or "turn it into a safari park," Henao-Restrepo says. She agreed to let *Science* visit a vaccination team working in Matam, a Conakry neighborhood, however. An Ebola case had occurred in Matam 3 weeks earlier, and the community had landed in the trial's delayed vaccination arm. On a shaded terrace off the main street, the eight-member team, dressed in scrubs and seated behind tables, asked people for their consent and then gave them a single shot in the upper arm. The mood was calm. The cluster's index case, a woman, had recovered and returned home from Conakry's Ebola treatment center, a few kilometers away; she dropped by to see what was happening.

The interim analysis published in *The Lancet* covers the first 90 clusters, with 4394 vaccinees. Because it's unclear exactly how long it takes for the vaccine to trigger protection—and to exclude people already infected preimmunization but not yet sick—the team counted only Ebola cases that occurred at least 10 days after a cluster entered the study. No such cases appeared in the clusters that received the shots as soon as possible; 16 cases occurred in the delayed arm (in seven different clusters). That translates to 100% efficacy in the trial; statistically speaking, there is a 95% chance that the vaccine's efficacy is between 74.7% and 100%, says biostatistician and co-author Ira Longini of the University of Florida in Gainesville. "I'm extremely confident this vaccine is highly effective."

Study coordinator Ana Maria Henao-Restrepo faced huge obstacles.

There was other evidence of that as well. Some of those immunized—in both arms of the trial—did get Ebola, but they all got sick within 6 days of vaccination. That indicates they were infected before they were vaccinated, Longini says. (A study published online by *Science* this week shows that the vaccine protects macaques after about a week; it also showed that Merck's vaccine, based on an Ebola strain from the Democratic Republic of the Congo, protects the animals just as well against the West African strain.)

The ring strategy helped eradicate smallpox in the 1970s, using a vaccine known to be effective, but no one had ever tested a new vaccine this way. "It was absolutely very creative," Osterholm says. "Had this been a standard trial, we would never have had this answer." The rapid, targeted deployment of the vaccine also represents the way the developers had envisioned it might be used, says virologist Heinz Feldmann of the National Institute of Allergy and Infectious Diseases in Hamilton, Montana, who has worked on the vaccine for almost 15 years and co-authored the new macaque study in *Science*. "We never thought it would be used to vaccinate the entire population." The idea is to build a stockpile that can be deployed rapidly to nip new outbreaks in the bud, says Marie-Paule Kieny, an assistant director-general at WHO.

Kieny also hopes the vaccine can help finally end the current epidemic. The interim analysis was so convincing that on 26 July the study team began offering the vaccine immediately to every new cluster. (The team will keep collecting data, however.) Already, the end appears tantalizingly close: According to WHO's latest report, there were just seven Ebola cases in the week ending on 26 July. Sierra Leone and Liberia are discussing whether to use the vaccine as well, says Mark Feinberg, vice president at Merck Vaccines. It is unlicensed, however, so the regulatory framework needs to be figured out. (In Guinea, the lack of a license is not a problem because vaccination continues as part of the established clinical trial.)

Osterholm says the challenge now is to gather similar data for the GSK vaccine, comprised of a chimp adenovirus carrying the Ebola glycoprotein gene. Some data suggest this vaccine may cause fewer side effects, and when given in a so-called prime-boost regimen, it might offer longer lasting protection, Osterholm says. "We shouldn't assume that there is only one answer here." The plan was to set up a separate ring vaccination study for the GSK vaccine, but that seems impossible now, Kieny says; the Guinean government wants to stick with the proven vaccine, until Ebola is gone.

Henao-Restrepo was set to return to Conakry this week after spending 3 weeks in WHO's Geneva headquarters, analyzing the data and finishing the *Lancet* paper. "There is a lot that we will still learn," she says. "This is really an example of what we can achieve if the international community works together." ■

CONSERVATION BIOLOGY

Monarchs pose a puzzle

Mexico's sharp winter declines not apparent in summer surveys elsewhere

By **Emily DeMarco**

Each summer, female monarch butterflies flutter around their breeding grounds in northern North America in search of nectar, a mate, and a milkweed plant on which to lay eggs. And they have an audience. Thousands of volunteers periodically survey the charismatic black and orange insects, helping scientists track population trends. Others count monarchs as they migrate south each fall to warmer climes. Now, one of the most systematic analyses of these tallies and other data has raised questions about how well researchers understand why monarchs have seen a dramatic decline on their major wintering grounds in Mexico.

The confusing picture emerges from seven monarch studies published this week in the *Annals of the Entomological Society of America*. One paper suggests that, even as wintering populations of monarchs have plummeted over the past 2 decades, there's been no similarly steep decline in a key summer breeding area that stretches across the midwestern United States and southern Canada. Others find that some fall migration counts also show no major downward trend. At the same time, the butterflies may be laying fewer eggs overall, concludes one study.

Such findings "present a puzzle," says ecologist Leslie Ries, now of Georgetown University in Washington, D.C., and an author of one of the studies. They "make me wonder if we really have the strongest evidence to be able to say we know what's causing the decline that we see in Mexico." The uncertainty could pose problems for conservationists trying to protect the butterflies.

The ambiguity is fueled, in part, by the monarch's complex population structure and life cycle, which includes a lengthy migration completed, relay-style, by several generations of insects (see graphic, p. 571). Each spring, many monarchs head north from Mexico to the southeastern United States, where they produce the first of up to three generations that can swell the total population. The offspring then spend the

PHOTO: SEAN HAWKEY

summer feeding and breeding on milkweed throughout the northern United States and southern Canada. In the fall, a final generation makes the trek back to Mexico. (Other regional monarch populations have different migration and breeding patterns.)

The cycle can make it hard to get a handle on summer and fall monarch numbers, but researchers agree on one thing: Over the past 20 years, the number of monarchs returning to the largest known wintering ground in central Mexico's highland forests has plunged by more than 90% (*Science*, 7 February 2014, p. 583). Many have blamed the decline primarily on the expansion of herbicide-resistant crops in the summer breeding grounds, which has led to the wide use of chemicals that kill milkweed. But few studies have systematically examined monarch population trends in these areas.

The new papers help fill that gap. One draws on 18 years of monarch sightings collected by citizen scientists. Between 1997 and 2014, at least some monarchs were spotted in all of the butterfly's historical eastern breeding range (some breed in the far west), suggesting the summer population is hanging on. And a second study, relying on hourly monarch counts made by volunteers at hundreds of summer breeding sites between 1993 and 2014, found no statistically significant population trend, up or down.

There's "a disconnect" between those results and the wintering data, Ries says. That's because if milkweed loss is driving the winter decline, then summer populations seemingly should be shrinking, too.

One possible answer, Ries and others say, is that the volunteers may have undersampled agricultural areas hit hard by herbicides, instead favoring sites popular with butterfly-watchers, such as parks and protected areas. Another view is that the last 7 or 8 years of the summer numbers do contain evidence—albeit statistically weak—of the monarch's decline. "If they had 9 or 10 years [of data], it probably would be [statistically] significant," contends entomologist Lincoln Brower of Sweet Briar College in Virginia, who was not involved with the studies.

Other researchers say the egg-laying study suggests summer monarchs are struggling. It found that monarch egg densities on milkweed plants have declined since 2006. "It's pretty scary," says biologist and co-author Karen Oberhauser of the University of Minnesota, Twin Cities. "It probably means there aren't enough monarchs out there to find the remaining patches" of breeding habitat.

The results have also put a spotlight on the need to better understand what is happening to monarchs during their fall migration south, researchers say. Two of the studies examine counts of migrating monarchs made from the mid-1990s to 2014 at stations in northern Michigan and Ontario, Canada. The Ontario tallies show a moderate decline, whereas the Michigan numbers show no clear trend. That suggests monarch deaths occurring farther south during the migration could be responsible for the sharp winter decline, says ecologist Andrew Davis of the University of Georgia, Athens, a co-author of two of the papers. Migrating monarchs run "a gauntlet of dangers," including predators, parasites, and even speeding cars, he says. "There is a tremendous amount of mortality, and we don't know how much."

The biggest knowledge gap is for Texas, Brower says, which is in the middle of both the main fall and spring flyways. Researchers "desperately" need monitoring data from that throughway, he says.

Such studies could help ensure that government agencies and environmental groups focus their time and money on the right solutions. Currently, the U.S. Fish and Wildlife Service and others have focused on conserving or restoring milkweed breeding habitat. "But if the problem is that the monarchs are dying during the migration," Davis says, "I'm not sure just trying to produce more at the start of the [fall] migration is the answer." Other steps, such as protecting migratory pathways, may also be needed. The concerns over migration are real, says ecologist Ernest Williams of Hamilton College in Clinton, New York, but "they should be added to—but not replace—the other issues we know to be affecting monarchs." ■

A relay for life

Monarch butterflies have a multigenerational migration cycle that traverses a continent. Although there are several populations, one of the largest and best-known is the eastern North American population that winters in central Mexico.

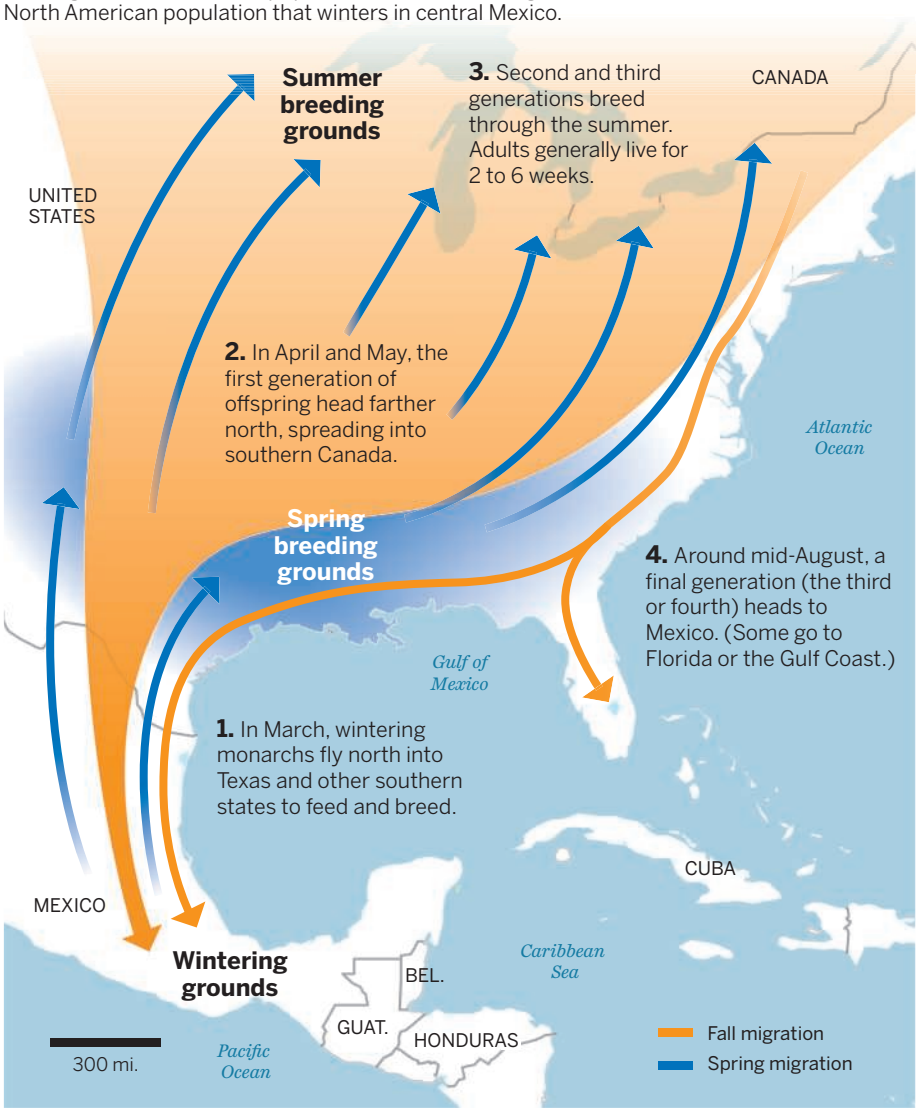

GRAPHIC: A. CUADRA/*SCIENCE*

ASTROPHYSICS

Catching cosmic rays where they live

The International Space Station gears up to study high-energy particles in space

By **Emily Conover**

The International Space Station (ISS), which has sometimes struggled to find its scientific purpose, is broadening its role as a cosmic ray observatory. Within a year, two new instruments are slated to join a massive detector, the Alpha Magnetic Spectrometer (AMS), which the station has hosted since 2011. The ISS's perch above Earth's atmosphere is ideal for detecting high-energy particles from space, says astrophysicist Eun-Suk Seo of the University of Maryland, College Park, principal investigator of the Cosmic Ray Energetics and Mass for the International Space Station (ISS-CREAM) experiment. What's more, she notes, launch vehicles already go there regularly. "Why not utilize it?"

The AMS was a gargantuan effort costing $1.5 billion and requiring more than a decade of planning (*Science*, 22 April 2011, p. 408). The two smaller experiments—the CALorimetric Electron Telescope (CALET), and ISS-CREAM—will measure cosmic rays at energies many times higher than the AMS can reach, at a much lower price tag.

High-energy cosmic rays are scientists' best chance to glimpse what goes on inside exotic objects thought to accelerate them—such as exploding stars called supernovae. Ground-based detectors spot cosmic rays indirectly, by observing the showers of other particles they give off on striking the atmosphere. Astrophysicists hope direct measurements in space will give them a more straightforward handle on the energies and types of cosmic ray particles reaching Earth.

Whereas the AMS is a general-purpose detector, measuring electrons, protons, nuclei, and antimatter at a range of energies, the new experiments have more focused agendas. The $33 million CALET—an international project scheduled for launch from the Japan Aerospace Exploration Agency's Tanegashima Space Center on 16 August—sets its sights on high-energy electrons. These quickly lose energy as they travel through space, so any that are detected must come from less than a few thousand light-years away.

"CALET has the possibility of identifying nearby sources that can accelerate electrons," says Thomas Gaisser, an astrophysicist at University of Delaware, Newark, who is not involved with the project. Those sources could include supernova remnants, the highly magnetized, spinning neutron stars called pulsars, or even clumps of dark matter, the mysterious substance that makes up 85% of the matter in the universe.

ISS-CREAM (pronounced "ice cream"), slated for launch by SpaceX in June 2016, will focus on high-energy atomic nuclei, from hydrogen up through iron. Their composition could help reveal the unknown inner workings of supernovae. "We cannot even agree why stars explode," says Peter Biermann, a theoretical astrophysicist at the Max Planck Institute for Radio Astronomy in Bonn, Germany, who is not involved with the detector. "The cosmic rays are the best signature of whatever happens there."

The new experiments could also shed light on the nature of dark matter. Some models predict that dark matter particles colliding in space should annihilate one another, giving off electrons and antielectrons, or positrons. The AMS has already confirmed sightings of unexpectedly high numbers of positrons that could be signs of such reactions; CALET can't tell positrons from electrons, so it will look for a surplus in the total number of both particles at high energies. Detecting dark matter in this way would help scientists pin down some of its properties well enough to weed out incorrect theo-

Cosmic ray detectors on the ISS

New experiments, perched outside Earth's atmosphere, promise to turn the International Space Station into a well-rounded platform for unlocking the secrets of supernovae and even dark matter.

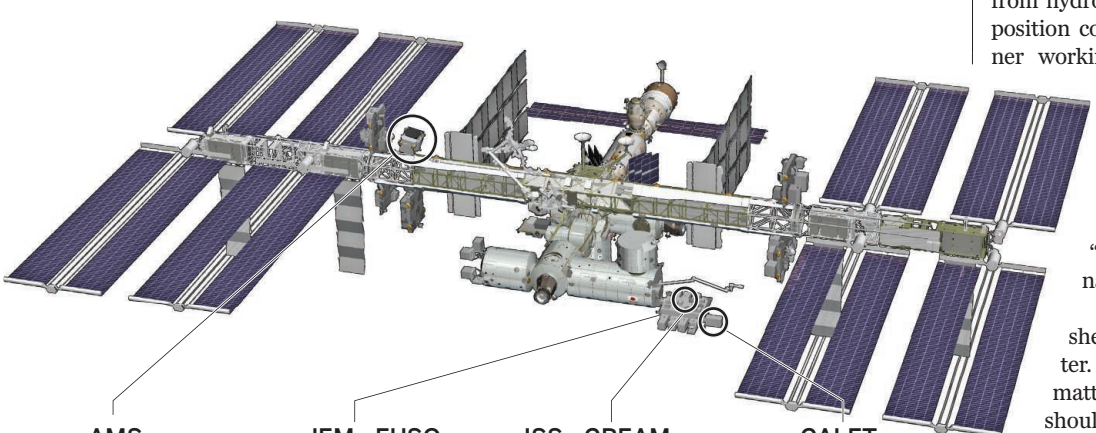

Alpha Magnetic Spectrometer
Installed in 2011

Extreme Universe Space Obsevatory
Proposed ~2021

Cosmic Ray Energetics and Mass
To be launched in 2016

CALorimetric Electron Telescope
Launching August 2015

CREDITS: (GRAPHIC) A. CUADRA/*SCIENCE*; (PHOTO) NASA, ESA, AND THE HUBBLE HERITAGE (STSCI/AURA)-ESA/HUBBLE COLLABORATION. ACKNOWLEDGMENT: J. HESTER (ARIZONA STATE UNIVERSITY)

Cosmic rays from supernova remnants such as the Veil Nebula may help explain the stellar blasts.

ries and come closer to identifying it. Still, many scientists argue that it will be hard to connect the positrons indisputably to dark matter, because other sources such as pulsars could also produce them.

Another cosmic question mark is a mysterious feature of cosmic rays known as the "knee." Low-energy cosmic rays are much more common than high-energy ones; as they increase in energy, their numbers steadily decline and then plunge in a way that, when graphed, resembles the bend in a human leg.

Scientists suspect the knee marks the energy at which supernovae begin to run out of steam. Because the oomph a supernova imparts depends on the particle's electric charge, nuclei with more protons should reach higher energies; ISS-CREAM will check whether this pattern holds. If results confirm that supernovae peter out around the knee, then more energetic cosmic rays must come from more powerful accelerators—possibly active galaxies powered by supermassive black holes.

The AMS, CALET, and ISS-CREAM may one day have more company in orbit. Another ISS detector, the Extreme Universe Space Observatory at the Japanese Experiment Module (JEM-EUSO)—now being considered for launch in 2021—would look down on Earth with a wide-angle camera, watching for ultraviolet light produced by the showers of particles that ultrahigh-energy cosmic rays spawn when they hit the atmosphere. Scientists hope JEM-EUSO will help them determine how high in energy cosmic rays can go and perhaps even trace them back to their sources, finally settling the question of their origins.

The space station experiments make for a complementary suite of detectors, rounding out the ISS as a cosmic ray observatory, says Vernon Jones, senior scientist for suborbital research at NASA. Researchers are delighted, he says. "It's a very laudable observatory. They've never had anything like it." ■

PHOTO: BRAZILIAN NAVY

OCEAN SCIENCE

Brazil looks to project scientific power on the Atlantic

New world-class research vessel to do double duty in mineral prospecting

By **Herton Escobar**, *in São Paulo, Brazil*

With 8500 kilometers of coastline and hundreds of marine scientists, Brazil has everything a country needs to make a mark in ocean research—everything except a world-class research ship, that is. That's about to change. At a ceremony in Rio de Janeiro on 23 July, Brazil unveiled its largest and most advanced scientific platform built for the high seas—a $77.5 million research vessel that scientists here hope will take them farther and deeper into the Atlantic Ocean than they have ever ventured.

Brazil is finally ready to start doing "grown-up" ocean science, says Andrei Polejack of the Ministry of Science, Technology and Innovation in Brasília. "We are very anxious to put this ship to work and start filling some of the big data gaps that still exist in the South Atlantic Ocean." But some academics worry that prospecting for mineral resources will dominate research aboard the ship, which was two-thirds funded by Petrobras and Vale, Brazil's largest oil and mining companies.

Christened the *Vital de Oliveira* after a 19th century Brazilian Navy hydrographer, the 78-meter-long vessel, equipped with a remotely operated vehicle capable of diving to 4000 meters, can berth 40 scientists for up to a month at sea. That puts it in the same league as the most capable research vessels fielded by the United States and Europe.

A new Brazilian National Institute for Oceanographic and Hydrographic Research is expected to allocate ship time to scientists and put out calls for proposals once grant money is available. But with industry the majority stakeholder and no public funds designated for operating costs, "I fear our access to the ship might be rather limited," says Michel Mahiques, an oceanographer at the University of São Paulo Oceanographic Institute. Polejack plays down that concern, arguing that the scientific objectives of industry and academia will often be aligned. "Most of the data that we need for the South Atlantic is so basic that it suits everybody's interests," he says.

With few research vessels plying it, the South Atlantic Ocean is a black box, with scant data available on its circulation patterns, temperature, salinity, biomass, carbon flux, and other basic parameters. That has practical as well as research consequences. "We have the supercomputers and the mathematical models, but we still lack a lot of experimental data to make reliable predictions" of weather patterns and ocean conditions, says Segen Estefen, an expert on oceanic infrastructure at the Federal University of Rio de Janeiro, who is overseeing the establishment of the new oceanographic institute. "There's an enormous amount of unmet demand for ship time in the scientific community," Mahiques adds.

Brazil's new research ship, the *Vital de Oliveira*, will fill data gaps on the South Atlantic Ocean.

Built in a shipyard in Xinhui, China, the *Vital de Oliveira* arrived in Brazil's port of Arraial do Cabo on 14 July along with 18 scientists who collected data on ocean–atmosphere interactions during the maiden voyage. The measurements "will help improve our weather forecast models for the region, especially in relation to extreme events such as tropical cyclones," says Ronald Souza, an oceanographer at the Brazilian National Institute for Space Research (INPE) in São José dos Campos. Marcelo Santini, an oceanographer and meteorologist at INPE and the Federal University of Santa Maria who was aboard for the 19-day trip, came away "extremely impressed" with the ship's capabilities. "It's really a big step above anything we have available today." ■

NEON technicians train at a monitoring tower located on the plains of Colorado.

RESEARCH FACILITIES

The dimming of NEON

NSF shrinks major U.S. ecology project

By **Jeffrey Mervis**

The National Science Foundation (NSF) this week acknowledged that it bit off more than it could chew when the agency agreed in 2010 to build a unique network of dozens of ecological stations across the United States. Facing cost overruns and construction delays, NSF officials have decided to reduce the overall scope of the troubled National Ecological Observatories Network (NEON) and eliminate a major aquatic research component.

NSF recently discovered that the $433 million project, originally intended to be finished next year, was "projected to be approximately $80 million over budget if it stayed on its current trajectory," says James Olds, head of NSF's biology directorate. After consulting with NEON officials and outside scientists, Olds says NSF "identified a descope option that will keep the project scientifically transformational and should bring it in on time and on budget."

The move to shrink NEON follows years of complaints from ecologists that NSF and project managers have been inflexible and have shut them out of decisions affecting its scientific aims. At the same time, a February report to NEON management from a high-level scientific advisory body acknowledged that some missteps are unavoidable because "the ecological research community has no experience with a project of this scale."

NSF's 3 August announcement came as a blow to those who plan to use NEON. "It's terrible news," says ecologist Walter Dodds of Kansas State University, Manhattan, who championed STREON, NEON's now-canceled aquatic experimentation component. But NEON Inc., the Boulder-based nonprofit that manages the project, vowed that "the project will remain positioned to meet the goal of transforming continental scale ecology," adding that large NSF-funded projects "commonly require adjustments of scope and in this regard NEON is not exceptional."

First proposed 15 years ago by then-NSF Director Rita Colwell, NEON was seen as ecology's entry into the world of big data. In lieu of the traditional approach of having scientists use their own methods and instruments to monitor a tiny slice of the world, NEON would standardize the process—and collect data on a massive, continental scale. After several false starts, researchers and NSF coalesced around a plan to collect 30-plus years of information from towers and sensors at sites within 20 ecological domains, including tropical forests, wetlands, high desert prairies, and even urban ecosystems. Within each domain, data from "core" terrestrial and aquatic sites would be supplemented by information from two "relocatable" sites, using equipment that could be moved every decade or so. Three planes would fly over the domains periodically to record changing vegetation patterns. The data, accessible to all, would allow scientists to assemble a large-scale picture of climate change, land-use trends, and the movement of invasive species.

Construction began in 2011 and was supposed to be completed by the end of 2016. But the path has never been smooth. Self-inflicted problems included high staff turnover and conflicts created by giving scientists what they felt was insufficient authority. The permitting process for some sites has been a nightmare, Olds says, and there are also some technical challenges yet to be overcome.

NSF recently concluded that NEON was running a year behind schedule, a time frame Olds says "is not acceptable." To get back on track, Olds says NEON will keep core sites in all 20 domains but reduce the number of relocatable sites. The planned initial cohort of 60 sites could be reduced to 50, says one scientist familiar with the project.

The biggest change is dropping STREON. Unlike NEON's other components, which gather information, STREON was designed to intentionally alter stream ecosystems—by adding nutrients, simulating extreme weather conditions, and removing predators—and then document how they responded. But obtaining permits for such experiments proved difficult. "You're asking for permission to put chemicals into the water for a very long time," Olds notes, "and any single owner can veto it."

Olds says that NSF is still "very interested in seeing [STREON] go forward … in a context other than the construction of NEON." But aquatic scientists are skeptical. It will be difficult to run STREON independently, they say, because it relies on NEON sites as controls. They also see NSF's decision as part of a systemic neglect of NEON's aquatic components. In June, Dodds and 18 other researchers wrote to NEON and NSF, noting that construction of aquatic sites lagged far behind terrestrial sites; they urged the agency and project managers to close the gap by shifting resources. NEON officials rejected the idea, stating "we cannot make one component of the observatory a higher priority than others."

Without STREON, Dodds says NEON will focus disproportionately on terrestrial ecosystems. And he says the move runs counter to a 2003 report by the National Academies that noted the importance of supplementing NEON's observational data with experimental results. "That's what the community felt was important," Dodds says. "Now there won't be any experimental elements."

NEON officials still need to work out descoping details, Olds says, adding that this week's move is designed to "strengthen NSF's oversight" of NEON Inc. And NSF hasn't wavered in its support for the project, Olds says, including spending $65 million a year over NEON's lifetime to operate facilities and share data. "It's in our budget," he notes. ■

PHOTO: ABRAHAM KARAM/NEON

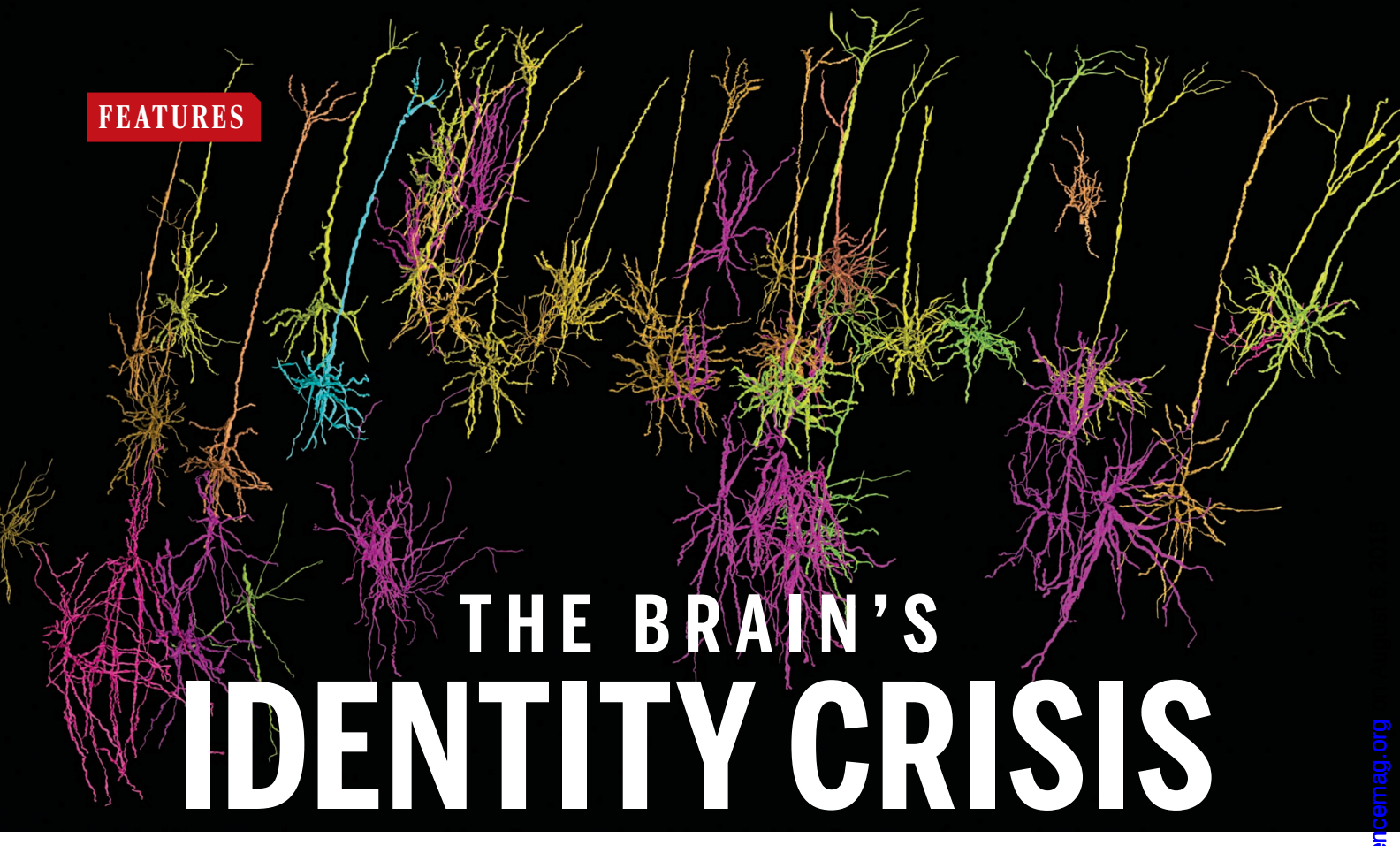

THE BRAIN'S IDENTITY CRISIS

Will new tools for classifying neurons put a 150-year-long debate to rest?

By **Emily Underwood**

The tiny Spanish town of Petilla de Aragón boasts no Marriott or Hyatt conference center. The medieval red tile-roofed village has about 30 year-round residents, and the nearest hotel that can accommodate a large group can only be reached via a winding, roughly hour-long drive along the southern slopes of the Pyrenees mountains.

Still, when Rafael Yuste, a veteran brain researcher at Columbia University, and Javier DeFelipe of the Cajal Institute in Madrid were searching for a place to gather some of the world's top neuroscientists in 2005, the town seemed an ideal location. They hoped that a pilgrimage to the birthplace of Santiago Ramón y Cajal—born in 1852 and considered by many to be the founding father of neuroscience—would inspire humility in attendees as they tackled a more than century-old debate: how to categorize a dizzyingly varied class of brain cells called interneurons. One of the building blocks of brain circuits, interneurons help keep brain activity in check and, when they malfunction, play a role in diseases such as epilepsy, schizophrenia, and autism.

Cajal was the first to identify what are now called interneurons—he called them "short-axon cells"—using a technique developed in 1872 by physician Camillo Golgi, which stains cells black by impregnating them with silver nitrate. So varied were the cells' structures in the human cortex—some look like stars, others like bird's nests, baskets, or spindles—that Cajal divided them into dozens of subtypes. He argued that the diversity of the cells, which he called the "butterflies of the soul," was the key to higher cognition.

Many researchers followed in Cajal's footsteps, identifying scores of new interneuron types based on features such as the shape of a cell's branches or the neurotransmitters it secretes. They rarely applied quantitative measurements or consistent criteria, however. As a result, by the time of the 2005 meeting in Spain, the literature on interneurons had grown so cluttered with overlapping and contradictory terminology that it was practically unintelligible, says Giorgio Ascoli, a neuroinformaticist at George Mason University in Virginia, who attended the conference. "It was like the Tower of Babel."

Does a neuron's shape determine its identity, or its behavior? Neurons in the mouse visual cortex, colored by firing speed: Magenta cells are slow-firing, yellow medium, blue fast.

Ascoli and many of the other neuroscientists who gathered in Cajal's hometown were confident that they could tidy up the problem by the end of the long weekend. "We thought, we are all rational people, we all believe in data, we will create labels and codes and agree to them, and make the Babel tower issue go away." But by lunchtime on the first day, he says, it was clear that the task with which they were charged was "simply put, impossible."

Neuronal classification—not just of interneurons, but of cells throughout the brain and the overall nervous system—is one of the oldest and most controversial problems in neuroscience. With the notable exception of the retina, in which roughly 60 neuronal types have been identified, and the 302 neurons of a worm called *Caenorhabditis elegans*, scientists don't agree on how to identify most neurons. "To the embarrassment of thousands of neuroscientists, we still lack the basic knowledge

PHOTO: ALLEN INSTITUTE FOR BRAIN SCIENCE

of how many types of neurons exist," says Peter Somogyi of the University of Oxford in the United Kingdom. That leaves them trying to make sense of the complex ecosystem of the central nervous system with only the most basic idea of the species making it up.

Lately, this problem has attracted a surge of attention from research efforts such as the U.S. Brain Research through Advancing Innovative Neurotechnologies (BRAIN) initiative, which, among other goals, aims to create a "census" of cells from brain tissue across different species. Without such a census, many researchers believe that BRAIN's primary goal of decoding complex cognitive processes by recording the activity of thousands to billions of neurons will be impossible, says Joshua Sanes, a molecular neurobiologist at Harvard University. "The recordings will be anonymous, and it will be a big mess," he says.

Scientists would also like to be able to pin down specific cell types that play a role in neurological disorders, or in the brain's responses to certain drugs. In a disease such as amyotrophic lateral sclerosis, for example, a subset of brain cells that helps control movement is obviously compromised. For other disorders, such as autism and schizophrenia, however, the neurons involved in producing symptoms are "utterly obscure," Sanes says.

He and many others now believe that a breakthrough in neuronal classification is imminent thanks to developments since the Spain meeting, such as new methods that rapidly sample gene activity from thousands of individual neurons, revealing patterns that distinguish cell types. Some see the quest to categorize as a fool's errand, however. "Evolution did not create cell types," but rather neurons whose gene activity adapts to their environment, argues Gordon Fishell, a neuroscientist at New York University (NYU) in New York City. But others say the dispute over whether neurons have well-defined identities is, as neuroscientist Amy Bernard of the Allen Institute for Brain Science in Seattle, Washington, puts it, "the kind of fight that happens when you don't have the right data."

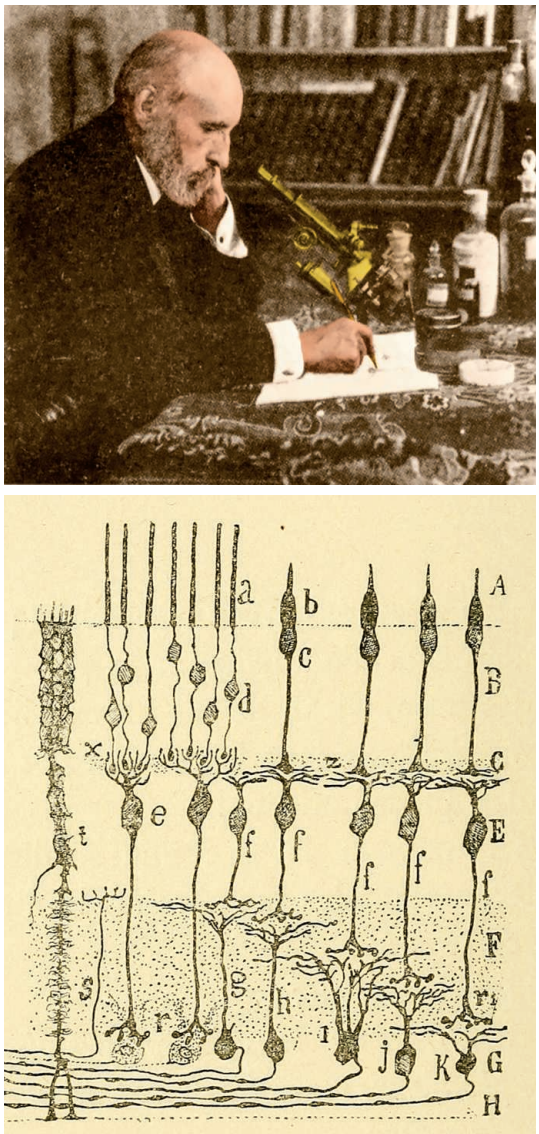

Santiago Ramón y Cajal (top) considered the retina the most beautiful structure in the nervous system, and illustrated dozens of cellular subtypes within its layers (bottom).

THIS CONFUSION WAS ON FULL DISPLAY at the Petilla de Aragón meeting. After giving up hope of agreeing on a classification system for interneurons, Yuste says, attendees instead came up with 500 terms to describe the cells' various qualities, such as the length and sinuosity of their dendritic branches. "It was a very dry list," says György Buzsáki, a neuroscientist at NYU.

The group did not attempt to address a deeper rift, dating back to Cajal, between "lumpers," who tend to focus on commonalities between neurons, and "splitters," who tend to divide cells into many subcategories based on subtle differences. The most extreme lumpers argue that there are only two types of brain cells, aside from blood vessels: neurons and glia. Extreme splitters say that there are as many cell types as there are cells in the brain.

Lumpers have long accused classical neuroanatomists of being "like stamp collectors," who simply "want to collect as many stamps as they can," says Christof Koch, scientific director of the Allen Institute. Lumpers consider Cajal "a pathological splitter," says Richard Masland, a neuroscientist at Harvard Medical School in Boston.

Cajal never knew to what extent the cells he examined were representative of the broader populations of neurons, because of the haphazard nature of the Golgi technique, which only stains a few random neurons in every slice of brain tissue. As a result, many scientists are skeptical of his big, beautiful catalogs of neuronal classes. Today, Masland adds, the best evidence that Cajal was "not hallucinating" his many subtypes comes from the retina—the poster child for neuronal diversity. Of all the brain's structures, Cajal considered the retina the most beautiful, and published an entire book illustrating the cells within its five distinct layers and identifying dozens of cell subtypes.

Yet the conventional wisdom about the retina in the 1970s was that the structure was "relatively simple," Masland says. Most scientists believed that it had only five types of neuronal cells: rods and cones, which respond to different wavelengths of light; ganglion cells, which receive input from the rods and cones; bipolar cells, which connect the rods and cones to the ganglion cells; and amacrine cells, the interneurons of the retina.

"A huge turning point," Masland says, occurred in the 1970s, when researchers recording cells' electrical activity found that these basic cell classes could be subdivided by function. Among ganglion cells, for instance, a dozen or so groups could be distinguished based on their sensitivity to stimuli such as the direction of motion and changes in light intensity. In the 1980s, Masland and others found further evidence of diversity by showing that subpopulations of neurons expressed different neurotransmitters, such as acetylcholine and serotonin. Today, most neuroscientists accept that there are not just five, but at least 60 different neuronal cell types in the retina. "And that's the lower limit," Masland says.

Having at least some well-defined neuronal classes in the retina makes it "a great place to start" when testing new methods for cellular classification, Sanes says. In recent years, his group and many other labs have turned to what some consider the most promising marker of cellular identity: gene activity. In May, Sanes and his colleagues published in *Cell* their first test run of a method that many in the field hope make it possible to automatically classify neurons en masse.

PHOTOS: (TOP TO BOTTOM) SCIENCE SOURCE; OPEN KNOWLEDGE COMMONS/HARVARD MEDICAL SCHOOL

Developed by geneticist Steven McCarroll and others at Harvard, the technique, called Drop-Seq, can quickly profile all the messenger RNA (mRNA), a reflection of which genes are being expressed, in thousands of individual brain cells. It starts by packaging each cell in a nano-sized oil droplet—a kind of nano test tube. After breaking open each cell and attaching a bead labeled with a unique barcode to all the RNA within, Drop-Seq sequences the genetic data in bulk.

The barcoded beads allow scientists to know from which cell each sequence came, Sanes notes. "Previously, if you wanted transcriptomic profiles for 10,000 cells, you'd have to use 10,000 test tubes." In the new study, Sanes and colleagues used the method to analyze the gene activity of more than 44,800 cells from a mouse retina. Using a machine-learning algorithm to sort through the cells' mRNA sequences, they identified 39 distinct subtypes within the 5 major classes of retinal cells. "It's not perfect yet—the computer tells you there are fewer cell types than we think are there—but it does get the main classes," Sanes says.

Other labs are performing similar analyses in lesser-known brain regions. This spring, neuroscientist Sten Linnarson of the Karolinska Institute in Sweden used a related but slower technique to analyze mRNA from more than 3000 individual cells within the mouse cortex, including interneurons and nonneuronal cells such as blood vessel and glia. After comparing the activity of 20,000 genes in each cell, he and his team identified 47 different subgroups (*Science*, 6 March, p. 1138). Single-cell RNA sequencing is "powerful and cheap enough to provide a definitive breakdown of the cell types that are in any given chunk of tissue all at once," says Linnarson, who expects the technique will be quickly adopted in "every little corner of the brain."

ALTHOUGH MASLAND CALLS RNA sequencing "probably the ultimate way to classify cells," he and others acknowledge that investigators don't know which genes are key to distinguishing neuronal type. One approach to identifying them is to trace a neuron's lineage from its birth onward, monitoring gene activity to see which ones turn on or off as the cell follows its developmental path.

At the Janelia Research Campus in Virginia, for example, neuroscientist Tzumin Lee is tracing the development of every neuron in the fly brain. Lee and his team label each of the larval fly's 100 neuroblasts, or neural stem cells, with a genetic marker that is transmitted to the next cell generation every time the cell divides. Then the team harvests RNA from developing flies at various points to track changes in gene activity as the insects' brains mature. Once the project is complete, the team will have a complete map of gene expression in the fly brain, including about 24,000 neurons. The approach "gets to the mechanism of how you create neuronal diversity," says neuroscientist Gerry Rubin, executive director of the Janelia Research Campus.

Masland, however, isn't persuaded that knowing the developmental trajectory of a cell will reveal how to classify it. "If you're trying to fix your car, you don't necessarily need to go back to the factory to understand its parts." And both RNA sequencing and analyses of cellular lineage miss what Somogyi calls the "most complex and beautiful issue" that defines a neuron's function: how its firing patterns change over time. Neuronal identity changes from moment to moment, Somogyi says, giving them "this incredible flexibility on the one hand, and reliability on the other."

Reliably classifying neurons will ultimately require multiple kinds of data—on cells' morphology, electrical behavior, and gene activity—says Andrea Beckel-Mitchener, director of the functional neurogenomics program at the National Institute of Mental Health in Bethesda, Maryland. The cell census-related grants the National Institutes of Health has begun funding on behalf of the BRAIN project aim for diversity: Just half of the 10 focus on RNA transcription, whereas the others explore variations in neuronal function. Similarly, the Allen Institute is collecting multiple kinds of data on retinal neurons—first electrophysiological and morphological measurements and ultimately single-cell genetic data. "The goal is to see whether every cell falls into one unambiguous class, like one of the 93 chemical elements," Koch says.

Ascoli and many other researchers also want to automate the process, using machine-learning algorithms to crunch through massive data sets without bias. Even if such algorithms can produce reliable cell classes, however, it's not clear what they'll ultimately tell us about how the brain works, Bernard says. Despite having a complete taxonomy of the neurons in *C. elegans*, scientists still don't have a full understanding of how the tiny worm's brain works, after all. That, Bernard notes, "doesn't lead me to believe this is an easy problem." But few would deny that knowing what makes up a brain is a good start. ■

Eying a way to ID neurons

The retina has five broad neuronal types—rods, cones, horizontal cells, bipolar cells, amacine cells, and ganglion cells (middle). Using a technique called Drop-Seq, researchers recorded gene activity in 44,800 individual cells from a mouse retina and, with the help of a machine-learning algorithm, sorted the cells into 39 distinct subtypes based on those data (right).

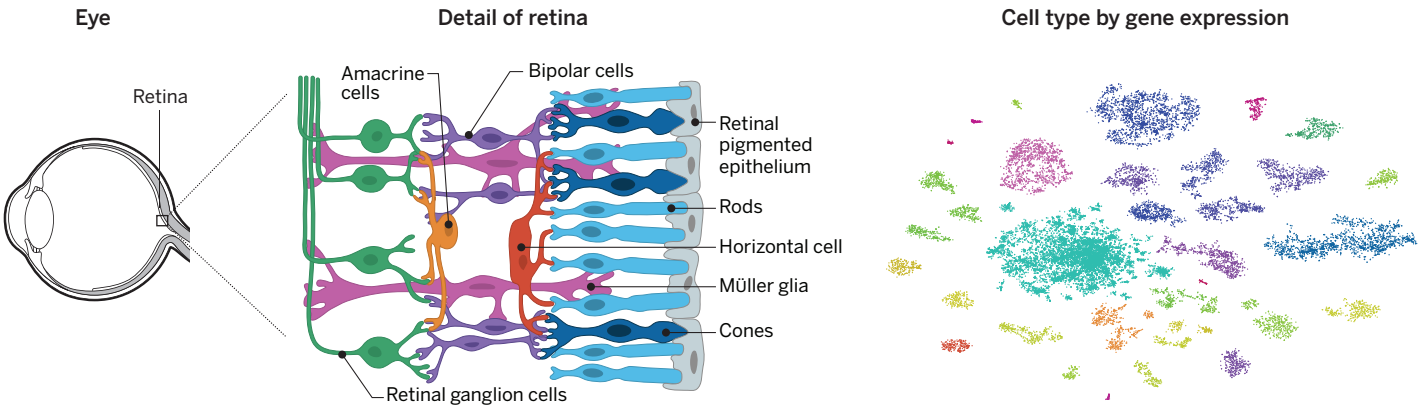

GRAPHICS: (EYE) V. ALTOUNIAN/*SCIENCE*; (RETINA/CELL TYPE) ADAPTED FROM E. Z. MACOSKO *ET AL.*, *CELL* **161** (21 MAY 2015) © 2015 ELSEVIER INC.

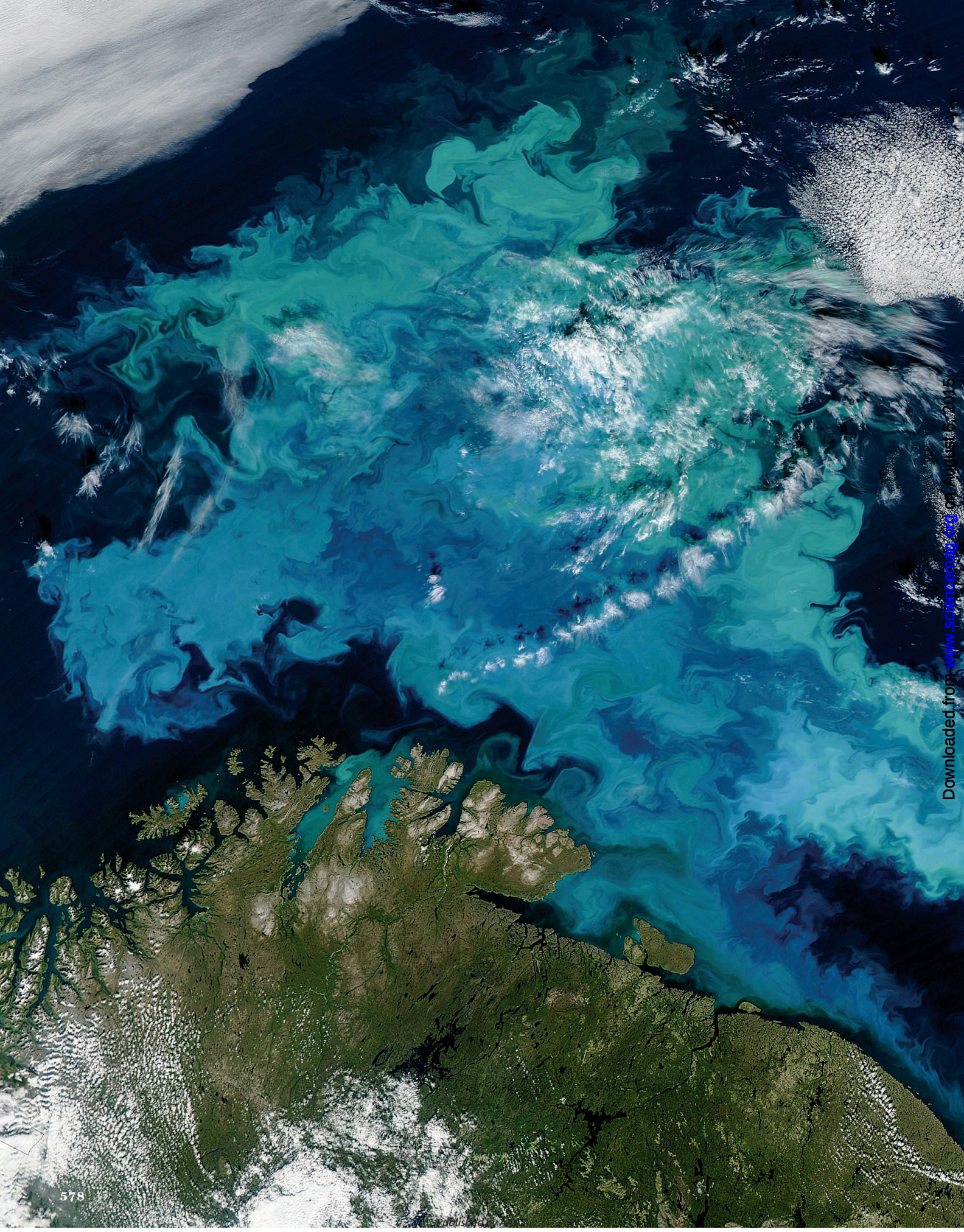

BOOM & BUST
IN THE GREAT WHITE NORTH

As the Arctic warms, retreating sea ice is revealing winners and losers in ecosystems under siege

By **Eli Kintisch** *in Ny-Ålesund, Norway*

Every day from June to September, biologist Markus Brand and a colleague climb into a small boat and putter into a fjord outside Ny-Ålesund, a research base 1000 kilometers north of the Arctic Circle. Meter-tall waves and driving snow are common here in the Svalbard archipelago, where the Atlantic and Arctic oceans meet, but that doesn't deter Brand, a graduate student from the Alfred Wegener Institute (AWI) in Helgoland, Germany. At several spots in the fjord, he hauls up heavy steel traps from the sea floor. Over 3 years Brand has caught 5000 fish, dissecting some and tagging and releasing others.

He is documenting a southern invasion. Varieties of Atlantic cod that normally ply waters well below the Arctic Circle are showing up in Svalbard—and thriving. This "atlantification" of the Arctic, as researchers call it, could open up whole new fisheries at the top of the world. But migrating fish are only one element in a cascade of biological changes driven by the rapid warming of the Arctic, where temperatures have risen more than twice as fast as they have farther south. The impacts can be seen "at all levels of the food chain," says marine scientist Marcel Babin of Laval University in Quebec City, Canada.

Diminishing sea ice is permitting more light to penetrate the water column, for instance, catalyzing massive phytoplankton blooms. That's good news for some fish, but animals that live atop the ice are in trouble as it recedes. Polar bears have retreated to land, where they've started to savage seabird colonies for sustenance (see sidebar, p. 581). Walruses, which normally rest on sea ice, are crowding instead onto Alaskan shores; last summer, scores of their young died in stampedes. The plight of apex predators has made the changing Arctic a cause célèbre for environmentalists. Activists in polar bear suits have shown up at presidential campaign rallies in New Hampshire, for example, and Bill McKibben, head of the climate action group 350.org in Brooklyn, New York, claims humankind has "broken the Arctic."

That may be an exaggeration, but scientists agree that profound shifts are underway. "It's the death of one ocean and the birth of another," says biologist Peter Thor of the Norwegian Polar Institute in Tromsø. "It's clear there's going to be winners and losers," says biologist Brenda Konar of the University of Alaska, Fairbanks. "Depending on who you want to win, you'll view the changes as good or bad."

Melt pools that let light penetrate ice are getting researchers' attention.

The convulsions up north will ripple south to temperate climes. Recent studies suggest the melting Arctic may be altering weather patterns across the Northern Hemisphere. And the biological changes will be felt farther south, too, as most of the fish and fowl that frequent the Arctic Ocean are migratory. As geoscientist Howard Epstein of the University of Virginia in Charlottesville puts it, "what happens in the Arctic doesn't stay in the Arctic."

PERCHED ON THE EASTERN EDGE of the Fram Strait just 1000 kilometers south of the North Pole (see map, p. 580), Norway's Svalbard Archipelago once was little more than a whaling outpost at the top of the world. In 1964, however, Norway converted one of Svalbard's mining settlements, Ny-Ålesund, into a research base. It was a prescient move, as the scientists from 10 nations who flock here now have a front-row seat to the monumental changes unfolding in the region.

Atmospheric readings taken every day above Ny-Ålesund by weather balloons underpin the finding that the Arctic has warmed by more than 2° since 1993. Research cruises around Svalbard have documented more fresh water flooding into the strait from rivers and melting glaciers, colliding with warmer water funneled northward by shifting ocean currents. "We see the Arctic here changing before our eyes," says AWI atmospheric scientist Roland Neuber.

The most profound change is loss of sea ice. Measured at its summer minimum, Arctic sea ice has lost an estimated 75% of its volume since 1979. That's a hammer blow for some bottom-dwellers in shallower waters around the fringes of the Arctic Ocean. Sea ice nourishes the sea floor: When algae clinging to the ice's rough underside die, their detritus sinks to feed benthic creatures like worms, snails, crustaceans, and shellfish. Existing benthic communities are already losing ground and retreating northward in the now largely ice-free Bering and Chukchi seas between Siberia and Alaska, says oceanographer Jacqueline Grebmeier of the University of Maryland's Chesapeake Biological Laboratory in Solomons. "Some call it the new normal," she says. But that change comes with a cost: Some clams, for example, are getting smaller, which makes them less nutritious for predators like the eider duck. "The duck's

Massive phytoplankton blooms, such as this one in the Barents Sea, are one result of rising temperatures.

PHOTOS: (LEFT TO RIGHT) NASA/GSFC/ESDIS/LANCE; © JENNY E. ROSS/CORBIS

prey base is half what it was 20 years ago in some areas of the Bering," Grebmeier says.

For other species, the new normal means boom times. Spied by satellite, widespread phytoplankton blooms appear in the open water as sea ice recedes. Another key factor is the thinning of the ice. Pocked by melt pools, it allows more light to filter through. During a July 2011 cruise on an icebreaker in the Chukchi Sea, researchers found, for the first time, massive phytoplankton blooms below the ice (*Science*, 15 June 2012, p. 1408).

"We were blown away. The blooms were as biologically productive as any ocean ecosystem on the planet," says oceanographer Kevin Arrigo of Stanford University in Palo Alto, California, who co-led the work. In a special issue on Arctic change last month in *Progress in Oceanography*, researchers estimated that primary production—a measure of marine photosynthesis—in the Arctic Ocean increased 30% between 1998 and 2012.

This burgeoning base for the food web, Arrigo says, will be "a huge change for many animals." Among the winners: zooplankton and fish in the middle of the water column, and open-ocean, or "pelagic," predators that don't depend on stable ice, unlike polar bears and walruses. For example, ringed seals in the Bering and Chuckchi region consumed, on average, 8% more fish a year from 2003 to 2012 than they did in 1975 to 1984, Justin Crawford of the Alaska Department of Fish and Game in Sand Point reported in the *Progress* volume. And bowhead whales, which filter plankton, are thriving. "It's a great time to be a bowhead. They're fat and having lots of calves," says marine biologist Sue Moore of the National Oceanic and Atmospheric Administration (NOAA) in Seattle, Washington. Humpbacks and fin whales are increasingly abundant north of the Bering Strait, too, she says, although researchers are unsure whether that's "a climate signal or just recovery from hunting."

A new Arctic Ocean

Animals that depend on sea ice to rest or hunt are struggling as the Arctic warms, whereas others thrive. Two snapshots 35 years apart show sea ice at its smallest annual extent.

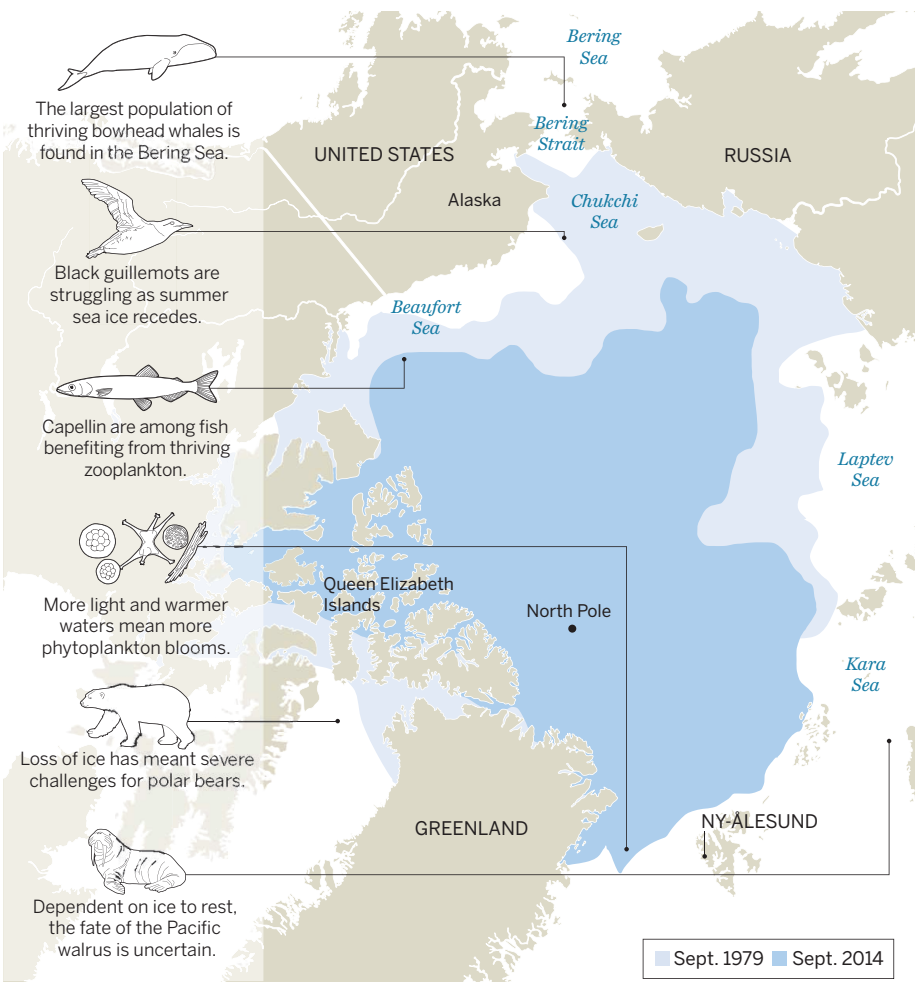

OUTSIDE NY-ÅLESUND'S glass-walled dining room, tawny arctic foxes scurry by, looking for bird eggs for a midday snack. Inside, several dozen researchers and staff dine on poached salmon, salted fish, and fresh oranges, courtesy of the monthly supply ship.

After lunch, plant physiologist Kai Bischof of the University of Bremen in Germany brings a pair of petri dishes to a laboratory. They contain fragments of kelp from the fjord; asking Ny-Åselund's divers to retrieve specific species is as convenient as "ordering pizza," Bischof says.

In the lab's cold rooms, racks brim with thousands of seaweed samples exposed to chemicals or other stimuli to simulate a range of possible future Arctic conditions. Bischof's latest samples will endure one such harsh world via ultraviolet (UV) light, which is increasing in the Arctic due to a depleted ozone layer. "We're going to shock them," he says mischievously. Work here has established that mature kelp should tolerate warmer waters, and the greater acidity produced by seawater's absorption of carbon dioxide from the atmosphere. The plant also shows signs of being able to cope with increasing UV light. Now, Bischof is studying whether spores and other early stages of the plants can withstand rapid environmental shifts.

Other species also show signs of resilience. CO_2 is more soluble in cold water, so researchers fear ocean acidification could hit northern populations of miniscule creatures especially hard, interfering with their ability to maintain their shells or properly regulate their metabolism. But in one hopeful sign, the Norwegian Institute's Thor and colleagues have found that young copepods, a key Arctic zooplankton, are more resilient to acidified water than their parents, perhaps a genetic adaptation.

A full tally of winners and losers would require regular monitoring cruises in the central Arctic Ocean, which nations now don't support, says Catherine Mecklenburg, a taxonomist with the California Academy of Sciences in San Francisco. Data are scarce, for instance, on the 235 species of fish known to frequent the Arctic. She estimates that more than half migrated there in the past from southern areas. "Against that backdrop," she says, "it's hard to identify which fish have moved into the Arctic recently."

Scientists have a better handle on seafood stocks in subarctic waters and are willing to wager which might expand northward. In a 2013 report in *Fisheries Oceanography*, 34 experts estimated that 12 of 17 key stocks in the Barents, Norwegian, and Bering seas had either a "potential" or "high potential" to expand to the high Arctic, including snow crab and Greenland halibut.

CREDITS: (DATA) SEA ICE INDEX; (ILLUSTRATIONS) A. CUADRA/*SCIENCE*

ADAPT OR PERISH appear to be the only options for Arctic denizens. Manfred Enstipp hopes to witness adaptation in action, in the penguinlike birds called little auks that are the most abundant fowl in the Arctic. The zoologist, who works for the Institut Pluridisciplinaire Hubert Curien in Strasbourg, France, spent days in Ny-Ålesund preparing a 5-meter-long plastic swimming pool, covered with plastic nets. He stocked it with a pair of auks and their favorite prey, copepods, captured in nearby waters; now, for 12 hours a day, he stares at computers that show the action in the pool. He hopes to observe the birds darting underwater to feed on copepods.

In the wild, little auks are voracious. Limited data suggest they catch as many as 60,000 of their 5-millimeter-long prey each day—an amazing six copepods per second. But in 2013, oceanographers off Ny-Ålesund reported that the bird's prey was changing. Copepods a tenth as big, usually found in more southern areas, began appearing around Svalbard. Enstipp wants to know whether the little auks can compensate for the smaller prey by catching more of them. "My hope is that they might switch foraging mode," from chomping larger prey to filter feeding on the smaller meals, Enstipp says.

Although the smaller newcomers might outcompete existing copepods, timing problems could affect their ability to persist in the Arctic. That's because the southern copepods require much longer seasonal growing cycles than the light-limited Arctic provides, researchers led by oceanographer Rubao Ji of the Woods Hole Oceanographic Institution in Massachusetts found. "Even a change of a few days [of growing season] can have a big negative effect on their ability to prepare for the winter," Ji says. That means the immigrant copepods may not be able to replace declining northern copepod populations, researchers say, potentially reducing overall zooplankton stocks.

The long-term prognosis for the Arctic is murky indeed. The phytoplankton bonanza may not last, warns University of Tromsø oceanographer Paul Wassmann. His caution is partly grounded in his computer model, which suggests that by 2100, melting of land and sea ice will deposit several meters of fresh water annually atop the salty, nutrient-rich waters in which phytoplankton bloom. Other modelers, however, argue that winds will mix the fresh water into deeper waters, keeping stratification from impeding the blooms.

Faced with such uncertain prospects for Arctic ecosystems, five nations this month agreed to bar fishing throughout the Arctic Ocean. "There's not enough science yet" to forecast how stocks might bear up under commercial fishing, says Ambassador David Balton, who spearheaded the U.S.-led initiative. Whereas some fish may thrive in the new Arctic, other stocks could crash.

A cautionary tale, says Ed Farley of NOAA's Alaska Fisheries Science Center in Juneau, is the hit that Alaska's half-billion-dollar walleye pollock industry took as the ocean warmed steadily between 2004 and 2008. The catch declined 40%, he notes, most likely because smaller, less nutritious zooplankton became more prevalent in the warmer waters, stunting the growth and winter fitness of young pollock.

One way to promote ecosystem resilience in the Arctic might be to safeguard the last areas where sea ice is expected to persist as the planet warms. The World Wildlife Fund (WWF) has called for heightened management of this "lasting ice area," mostly around Canada's high Arctic islands and northwest Greenland. That could give some hope for bears and other embattled species, says WWF's Clive Tesar in Ottawa.

Enstipp, meanwhile, fears that little auks are in for a rough ride. As his month in Ny-Ålesund comes to a close, he got great footage of the birds hunting like mad underwater. But they never switched over to filter feeding. If smaller copepods continue to gain a foothold, he says, "this might be very challenging for little auks to cope with energetically." And that could mean yet another species fighting for survival in the changing Arctic. ■

PHOTO: DR. SONAL CHOUDHARY

A Ny-Ålesund neighbor makes a house call.

Don't mess with the bears

By **Eli Kintisch**, *in Ny-Ålesund, Norway*

On a sunny summer evening here on the edge of the Arctic Circle, I'm Skyping with a friend back home from my tiny dormitory room at the Ny-Ålesund research station when I hear the pop of a pistol outside. A polar bear, I wonder? When scientists posted to the world's most northern research station, on Norway's Svalbard archipelago, leave the base, they carry flares and guns to scare off any bears they encounter—or, if their own life is threatened, to kill them. As instructed during the bear safety briefing I received upon arrival, I stay indoors.

At breakfast the next day, the dining hall is abuzz over the bear. It had ignored the flare gunshot I'd heard, forcing station managers to trail it for an hour until it wandered off the base. But not before someone posted a video on YouTube.

The episode illustrates a growing phenomenon in the Arctic: polar bears foraging on land as their primary habitat, sea ice, retreats. Normally, the bears subsist mainly on seals, snatched at holes in the ice where they surface for air. With less ice for such ambushes, polar bears are increasingly seeking carrion and bird eggs on land.

Later that morning, ecologist Maarten Loonen of the Netherlands Arctic Station on Spitsbergen takes me on an inflatable speedboat around nearby Blomstrand Island, where a bear was sighted the day before. We find a safe place to dock and Loonen turns to his student, Ross Wetherbee, who is carrying a rifle. "If there's trouble, you prepared to shoot?" he asks. Wetherbee nods.

Over the next hour, we count 31 bloodied and broken eggshells, mostly from eider ducks, and collect samples from mounds of greenish gray bear diarrhea. Later, on his blog, Loonen speculates about why the scat was so runny: "The polar bear is used to a very fatty diet. Eggs are full of protein … He must have had some stomach ache."

Four million people live north of the Arctic Circle; only one or two polar bear attacks are reported a year. But more frequent encounters at Svalbard have changed the way scientists work. During fieldwork nowadays, researchers often take turns standing watch for bears, meaning one less set of hands to collect samples. For overnight outings, wooden huts have largely replaced tents. And Loonen has a stern warning for students. "Anyone who photographs a bear will get sent home immediately," he tells them. "It's best to be a little afraid." ■

Efficient electron extraction p. 587 ▸

Deepwater Horizon's environmental legacy p. 592

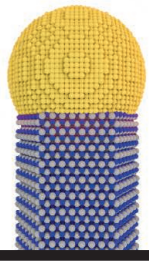

PERSPECTIVES

BIOLOGICAL ADHESIVES

Positive charges and underwater adhesion

Mussels stick under water by using their own ions to combat the salt around them

By **Jonathan J. Wilker**[1,2]

When visiting a beach, we can see that mussels, oysters, and barnacles attach themselves to rocks even while being pounded by waves. These organisms remain affixed by secreting adhesives. Human efforts to make such wet-setting glues are often foiled by the presence of water. Instructions on tubes of adhesives remind us that the surfaces must be clean and dry, given that our materials interact better with water than with the pieces of a broken dish. On page 628 of this issue, Maier *et al.* (*1*) have divulged a potentially key part of the underwater adhesion story. Mussels appear to gain surface access for glues by using their own protein-based ions to outcompete the ions in their saltwater environment.

When mussels identify an inviting location to settle down, they deposit a mixture of proteins that contains the rare amino acid 3,4-dihydroxyphenylalanine (Dopa). The catechol side chain of Dopa (i.e., 1,2-dihydroxybenzene) can bond onto rocky substrates via hydrogen bonding and metal chelation to provide surface adhesion (*2*, *3*). Oxidation of Dopa to a semiquinone or

PHOTO: ANDREW FULLER

a quinone initiates coupling chemistry to bring about covalent bonding for creating cohesion within the material. Iron bound by Dopa is needed for these processes, both in the adhesive plaques (*4*) and threads (*5*) of the animal's attachment assembly.

Other marine microorganisms such as bacteria also require iron to survive and have developed an approach for scavenging the needed metals from their surroundings. Siderophores are small molecules excreted into the water for capturing iron and pulling it back into the cells (*6*). These siderophores often rely upon catechol groups for binding iron. Although bacteria and mussels use their catechol chemistries for different purposes, Maier *et al.* have now made an intellectual bridge between these phenomena to gain insight into fundamental chemical processes that control underwater adhesion.

Siderophores were used in experimental studies to represent macromolecular adhesive proteins. A surface forces apparatus measured the energies of pulling apart two mica surfaces on length scales of 1 to 5 nm. Of particular concern was the subset of mussel proteins known to reside at the interface between animal and rock. These proteins contain high levels of lysine and arginine that make them positively charged. Have mussels created a cationic glue for binding to anionic, inorganic surfaces? To find out, three classes of siderophore molecules were made that had only catechols, only cations, or both catechols and cations.

Adhesion energies in salt water were the highest when both catechols and positive charges were part of the molecule. Although siderophores bearing cations alone also showed attachment, the strength was only ~15% of that when coupled to catechols. By themselves, catechols barely bonded at all. A surprise here is that the combination of catechols and cations yielded greater binding than the sum of the individual components. A type of synergy appears to be present when binding a surface submerged in sea water.

Having only catechols in the molecule and no cations resulted in appreciable bonding, but only when the environment was pure water, not salt water. On their own, catechols appear unable to drill through the barrier of hydrated cations associated atop anionic surfaces in the sea. Cations within the compounds studied here, and by extension in mussel adhesive proteins, seem to be present for the purpose of clearing surfaces of bound salts and making way for catechol adhesion.

Deciphering the detailed workings of biology is always captivating, especially when the insights influence how we design synthetic materials. Mussel proteins have been inspiring the development of several polymer systems with pendant catechol groups. These cutting-edge adhesives can sometimes bond more strongly than our favorite store-bought products such as Super Glue (*7*) and even function well under water (*8*).

Perhaps given the magnitude of the challenge, little has been reported on synthetic catechol adhesives for substrates submerged in sea water. In one example, a combination of catechols and positive charges did not increase binding, although the lysine groups may not have colocalized near the catechols within these hydrogels (*9*). Bulk adhesion in sea water has been studied with a polymeric adhesive containing catechols and varying amounts of ammonium cations (*10*). Bonding increased when cations were added into the polymer. However, incorporation of cations actually decreased adhesion when the substrates were in air rather than a salty environment. Such macroscopic results are consistent with—and now explained by—the molecular-level study of Maier *et al.*

The classic adhesive chemistries of acrylates, epoxies, and urethanes practically cower when facing waterlogged surfaces or environments. These recent insights may herald the availability of tailored adhesives for different wet environments. The hardware store may have one aisle for mussel-mimicking glues with both catechols and cations for when you need to bond parts in salt water. For gluing in pure water or air, visit the aisle with catechols but no added positive charges. Before we can buy such materials at the store, many questions remain. How much charge yields the best adhesion? Why are mussel proteins in the bulk of the adhesive, not just at the surface, also cationic? Even in pure water, how can catechols find a way past surface-associated waters to bind substrates? Finally, is the cationic adhesive strategy used by mussels a general theme throughout marine biology, or just one solution? ■

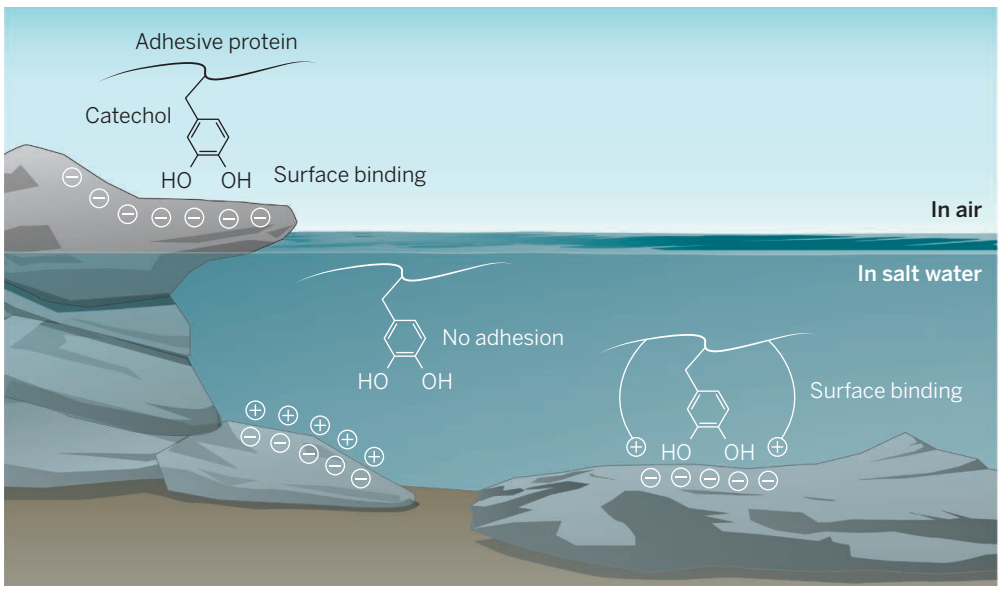

Sticking in the salty seas. Mussels have devised clever strategies for binding to rocks. Catechol-containing adhesive proteins attach to anionic surfaces when in air or pure water. Maier *et al.* have found that in salt water, surface-bound cations deter access to proteins. To wipe the surface clean, mussel proteins contain their own cations for displacing salts. Catechols, and the animals, can then stick.

[1]*Department of Chemistry, Purdue University, West Lafayette, IN 47907, USA.* [2]*School of Materials Engineering, Purdue University, West Lafayette, IN 47907, USA.*
E-mail: wilker@purdue.edu

REFERENCES AND NOTES

1. G. P. Maier, M. V. Rapp, J. H. Waite, J. N. Israelachvili, A. Butler, *Science* **349**, 628 (2015).
2. S. A. Mian *et al.*, *J. Phys. Chem. C* **114**, 20793 (2010).
3. J. Yu *et al.*, *Nat. Chem. Biol.* **7**, 588 (2011).
4. M. J. Sever, J. T. Weisser, J. Monahan, S. Srinivasan, J. J. Wilker, *Angew. Chem. Int. Ed.* **43**, 448 (2004).
5. M. J. Harrington, A. Masic, N. Holten-Andersen, J. H. Waite, P. Fratzl, *Science* **328**, 216 (2010).
6. M. P. Kem, A. Butler, *Biometals* **28**, 445 (2015).
7. H. J. Meredith *et al.*, *Adv. Funct. Mater.* **24**, 3259 (2014).
8. H. Shao, R. J. Stewart, *Adv. Mater.* **22**, 729 (2010).
9. B. P. Lee *et al.*, *Macromolecules* **39**, 1740 (2006).
10. J. D. White, J. J. Wilker, *Macromolecules* **44**, 5085 (2011).

ACKNOWLEDGMENTS

Thanks to C. Del Grosso for help with the illustration. Support provided by NSF (grants CHE-0952928, DMR-1309787) and Office of Naval Research (grants N000141310245, N000141310327) is gratefully appreciated.

10.1126/science.aac8174

WATER

Water security: Gray or green?

Building engineered structures, such as dams and dikes, has been the conventional approach to water management. Some suggest that such "gray" infrastructure make way for "green" ecosystem-based approaches. In this second of three debates, *Science* invited arguments for how these approaches can address the challenge of building the water security of rapidly growing societies worldwide.

Manage water in a green way

By **Margaret A. Palmer,[1]* Junguo Liu,[2,3]* John H. Matthews,[4] Musonda Mumba,[5] Paolo D'Odorico[1,6]**

POLICY

Reliance on "hard," human-engineered structures—"gray" infrastructure—has been the conventional way to manage water needs for economic development. But building dams, piping water, and constructing protective barriers is capital intensive and may address only a few water problems (*1*). Gray infrastructure often damages or eliminates biophysical processes necessary to sustain people, ecosystems and habitats, and livelihoods. Consequently, there is renewed focus on "green" infrastructure, which can be more flexible and cost effective for providing benefits besides water provision. Supplementing or integrating gray infrastructure with biophysical systems is critical to meeting current and future water needs. Gray and green infrastructures combined are synergistic and can have superior results to one or the other.

Green infrastructure is a network of natural or seminatural features that has the same objectives as gray infrastructure. Gray infrastructure may always be needed to pipe and store water, but careful planning can limit its magnitude and extent. Green infrastructure—wetlands, healthy soils and forest ecosystems, as well as snowpack and its contributions to runoff—supplies clean drinking water, regulates flooding, controls erosion, and "stores" water for hydropower and irrigation.

For thousands of years, civilizations have been capturing and distributing water by combining natural processes, adaptive approaches, technologies with low external input, and sophisticated hydraulic and hydrological knowledge (*2*). Today, some developing countries create small-scale, environmentally sustainable water projects without large dams, massive infrastructure investments, or systems that depend on groundwater (*3*).

Green approaches to crop and soil management can reduce evaporative losses of water from fields (*4*). Rainwater harvesting and small, farm-scale reservoirs allow more efficient use of water in agriculture (*4*). Smallholders can access these methods, whereas large-scale irrigation projects benefit fewer local people. Such approaches can enhance farmers' resilience and long-term adaptation to climate change.

Coastlines can be protected by conserving coastal sand dunes, mangrove swamps, salt marshes, and coral and/or oyster reefs. Although loss of these buffers can be irreversible and has led to wide use of built structures, soft engineering, ecological restoration, and combined approaches are increasingly being used (*5*). In the Netherlands, recent approaches rely on coastal geomorphological processes that reinforce ecological and human benefits while buffering impacts from sea-level rise and increasingly powerful storms (*6*).

Although green infrastructure is not a panacea, it has fewer negative impacts than large water-infrastructure projects that displace local people, destroy habitat, or extirpate or shift fisheries (*7*, *8*). Green infrastructures allow for more flexibility and fewer environmental impacts.

COSTS AND BENEFITS. Most national water-management strategies now include ecosystems as natural capital, emphasizing the specific functions they can play economically. Green infrastructure, efficiency improvements, use of reclaimed wastewater, and policy instruments are proposed as more sustainable and affordable alternatives to tradi-

tional water development schemes. Yet more is known about the costs and effectiveness of gray infrastructure in a development context.

Economic efficiency, typically used to estimate the cost of gray projects, can lead to underestimates if changing environmental, economic, or social conditions are not taken into account (*9*). For example, although large dams may produce energy and protect the nearby populace and fields from floods, an estimated three out of four dam projects have cost overruns, on average, 96% greater than estimated (*10*). Underestimates are compounded if the burden of potential remediation costs is not considered, such as removal of contaminated sediments.

Gray water infrastructure is not always reliable; for example, levees lead to increased flood levels downstream (*11*). Levees can give a false sense of security that favors human encroachment in floodplains and, consequently, more flood damage than when levees are absent.

Evaluations of the economic benefits of green options that consider a range of social and environmental uncertainty, have, for example, ranked wetlands, tidal marshes, and coral reefs as particularly valuable (*12*). However, few studies have compared costs of green versus gray approaches, e.g., questioning the wisdom of replacing mangroves and corals with seawalls and breakwaters in peninsular Malaysia (*13*).

RESEARCH FOREFRONTS. The developed world has studied urban green infrastructure, but more research is needed to predict the performance of a network of structures within different environmental contexts (*14*). Even when existing finance, risk, and investment theories can be combined to compare gray and green (*15*), critical biophysical performance data are needed.

A new generation of "sociohydrologic" models is exploring social acceptability and biophysical trade-offs for different configurations of infrastructure. Testing and validation using case studies and data on social and biophysical drivers and ecological constraints will be required for broad application (*16*).

Most forest restoration programs are based on the assumption that forest area is a proxy for ecosystem services based on rainfall and water use. Reforestation can provide water regulation benefits by reducing streamflow variability and peak flows (*17*) and, in some cases, can enhance soil water storage (*4*); yet water flows that result from reforestation in larger tropical basins are rarely quantified. Modeling studies suggest that large-scale [i.e., $>10^4$ to 10^5 km^2 (*18*)] deforestation can reduce rainfall through changes in the surface energy balance and evapotranspiration; this effect, however, depends on the geography and other factors (*19*). Work is still needed to determine whether large-scale forest restoration could become a valuable approach to increase rainfall and water yield.

ADOPTION. When reliability needs are high and/or tolerance for failure is low, gray water infrastructure probably represents the most effective approach to meeting the needs of developing countries. However, gray infrastructure can result in substantial damage to ecosystems and livelihoods; thus green infrastructure may represent a safer, more conservative pathway. The multiple benefits of green infrastructure are not broadly recognized, and the lack of cost-benefit data increases perceived risks. However, ongoing geographic shifts in agricultural production, needed growth in developing countries, and uncertainty about future climates provide an opportunity to renegotiate how we quantify sustainable infrastructure over long periods and express trade-offs between environmental and economic parameters (*12*). ■

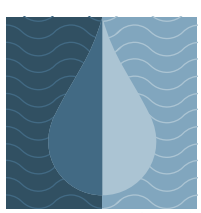

WATER DEBATE SERIES

[1]National Socio-Environmental Synthesis Center, University of Maryland, Annapolis, MD 21401, USA. [2]School of Nature Conservation, Beijing Forestry University, Beijing 10083, China. [3]School of Environmental Science and Engineering, South University of Science and Technology of China, Shenzhen 518055, China. [4]Alliance for Global Water Adaptation, Corvallis, OR 97330, USA. [5]United Nations Environment Programme, Nairobi, Kenya. [6]University of Virginia, Charlottesville, VA 22904, USA.
*Corresponding author. E-mail: mpalmer@umd.edu (M.A.P.); junguo.liu@gmail.com (J.L.)

REFERENCES AND NOTES

1. J. Liu *et al.*, *Glob. Environ. Change* **23**, 633 (2013).
2. C. Ortloff, *Water Engineering in the Ancient World* (Oxford Univ. Press, New York, 2009).
3. W. Critchley, G. Negi, M. Brommer, in *Conserving Land, Protecting Water*, D. Bossio, K. Geheb, Eds. (CAB International, Cambridge, 2008), pp. 107–119.
4. J. Rockström *et al.*, *Water Resilience for Human Prosperity* (Cambridge Univ. Press, Cambridge, 2014).
5. S. Luo *et al.*, *Ocean Coast. Manage.* **103**, 134 (2015).
6. M. J. Stive *et al.*, *J. Coast. Res.* **290**, 1001 (2013).
7. G. Ziv, E. Baran, S. Nam, I. Rodríguez-Iturbe, S. A. Levin, *Proc. Natl. Acad. Sci. U.S.A.* **109**, 5609 (2012).
8. M. C. Galizia, C. Schilis-Gallego, M. Cabra, "Ten years of World Bank resettlement data" (ICIJ: The Center for Public Integrity, Washington, DC, 2015); bit.ly/WBankdisplaced.
9. E. Z. Stakhiv, *J. Am. Water Resour. Assoc.* **47**, 1183 (2011).
10. A. Ansar, B. Flyvbjerg, A. Budzier, D. Lunn, *Energy Policy* **69**, 43 (2014).
11. R. A. Heine, N. Pinter, *Hydrol. Processes* **26**, 3225 (2012).
12. D. Russi *et al.*, *The Economics of Ecosystems and Biodiversity (TEEB) for Water and Wetlands* (Institute for European Environmental Policy, London and Brussels, 2013)
13. F. Moberg, P. Ronnback, *Ocean Coast. Manage.* **46**, 27 (2003).
14. B. Koch, C. M. Febria, M. Gevrey, L. A. Wainger, M. A. Palmer, *J. Am. Water Resour. Assoc.* **50**, 1594 (2014).
15. J. Talberth *et al.*, *Soln. J.* **40**(1), na (2013) www.thesolutionsjournal.org/node/1241/.
16. T. J. Troy, M. Pavao-Zuckerman, T. P. Evans, *Water Resour. Res.* **51**, 4806 (2015).
17. M. C. Roa-García, S. Brown, H. Schreier, L. M. Lavkulich, *Water Resour. Res.* **47**, W05510 (2011).
18. D. Lawrence, K. Vandecar, *Nat. Clim. Chem.* **5**, 27 (2014).
19. G. B. Bonan, *Ecological Climatology* (Cambridge Univ. Press, Cambridge, 2008).

ACKNOWLEDGMENTS

Support for this paper was provided by the National Socio-Environmental Synthesis Center, NSF DBI-1052875, and the USA-China International S&T Cooperation from MoST, China 2012DFA91350.

10.1126/science.aac7778

Built infrastructure is essential

By **Mike Muller,[1]* Asit Biswas,[2,3] Roberto Martin-Hurtado,[4] Cecilia Tortajada[2,3]**

Built water infrastructure supported the evolution of all human societies and will remain an integral part of socioeconomic development and modernization. Some postindustrial societies not only seek to "preserve" existing aquatic ecosystems in their otherwise transformed landscapes but also insist that others do the same. They suggest that "green infrastructure" can provide "equivalent or similar benefits to conventional (built) 'gray' water infrastructure" (*1*).

Fast developing countries have a different perspective. For them, built infrastructure underpins "water security": enough water of adequate quality, reliably available to meet health, livelihoods, ecosystems, and production needs, as well as protection from water's destructive extremes (*2*). Their challenge is to enable an expanding global population, seeking a better quality of life, to determine the nature of their new environment, not simply to preserve the old.

21ST-CENTURY CHALLENGES. By 2050, water systems will have to support a global population of 9.6 billion, up from 7.2 billion in 2013 (*3*), most in expanding cities far larger than those of Europe and North America. More people and property will need infrastructure for services far beyond the capacity of "green infrastructure," based on natural ecosystems, to provide.

The OECD estimates (*4*) that global water abstraction for domestic and industrial purposes will more than double by 2050. Improved efficiencies may help (a 14% reduction in agricultural demand is forecast on this basis), but the world in 2050 will need more water infrastructure.

Large conurbations have long exceeded the capacity of local sources, and extensive infrastructure is required to capture, store, transmit, treat, and distribute water to them. Even a mature society like the USA needs to invest almost $400 billion in its existing built infrastructure between 2011 and 2030 just to sustain drinking water supplies (*5*). The urban populations of China and India are expected to grow by 292 million and 404 million people, respectively, between 2014 and 2050 (*6*), with Africa and Latin America not far behind. These populations have access to better technologies and information, but their climate variability and extremes limit the potential contribution of "green" infrastructure and require built infrastructure to achieve water security.

Interventions needed to achieve water security depend not just on local specifics of topography and climate but also on institutional capacities, policies, economics, and politics. Global warming will reduce flows from water stored in Andean glaciers. So trans-Andean transfers through short tunnels from high-level dams in the Amazon and Orinoco basins are logical responses for growing cities along South America's arid Pacific coastal region.

"For [fast-developing countries], built infrastructure underpins 'water security'"

The 10 major rivers flowing from the Hindu Kush Himalayas underpin water, energy, food, and ecological security for 1.3 billion people. Only carefully judged infrastructure investments can provide water security for, for instance, the 50 million people in Bangladesh vulnerable to the calamitous coincidence of river flooding and storm surges.

SHIFTING CHALLENGES. Despite obvious needs, water projects are often opposed because they threaten poor people's livelihoods and the environment (*7*). In societies with water security, this opposition reflects changing social priorities. But "green infrastructure" often fails to achieve its goals.

In Britain, proposals to reduce sewage spillages into the Thames river using "green engineering" techniques were "not considered to be technically feasible" (*8*, *9*). Instead, a massive 25-km tunnel is being built to contain contaminated stormwater and divert it for treatment.

Controversy surrounded South Korea's Four Rivers Restoration project; although promoted as a "green economy" project, it was criticized as "an ecological disaster" (*10*). Yet only a package of dams, dykes, and hydropower plants could reduce deadly flooding and sustain land and water availability.

Environmental concerns halted a century of infrastructure development in Spain. A transfer from the Ebro River to water-short areas, proposed by the 1998 National Hydraulic Plan, was later rejected on economic, environmental, and political grounds (*11*). But when drought struck in 2008, Barcelona had to import water by ship, and farmers refused to pay for desalination plants, built as an alternative. Australia suffered similarly, and both countries are now analyzing the limitations of green infrastructure and the "dams versus desalination" dilemma (*12*).

Rapidly growing developing countries cannot afford risky experiments or high-cost alternatives. Although potable water needs are being met in most urban areas, sanitation and wastewater treatment are daunting tasks requiring even more investment.

These countries have followed precedent and public preferences, giving initial priority to infrastructure for water supply, irrigation, energy, and flood protection, followed by investments in wastewater management and, finally, other environmental improvements.

This sequence makes sense, given the vicious cycle of water insecurity, in which national economies cannot support the infrastructure investments needed, in part, because water security has not yet been achieved (*13*). In Africa, demands from water-secure communities elsewhere for green alternatives have delayed economic growth and social development (*14*). Economic water scarcity (*15*) is exemplified by the city of Cherrapunji, India, which, despite an annual rainfall of 12,000 mm, suffers severe water shortages during dry months because of inadequate storage.

CHANGING CLIMATES AND PRIORITIES. Over time, societies' needs for water infrastructure change. The Netherlands, whose existence depends on built water infrastructures, can now make "more room for the rivers," including flooding reclaimed polders, because agricultural intensification reduced the demand for agricultural land.

China's Three Gorges Dam symbolizes the infrastructure required to sustain prosperous large societies in the 21st century. It had social and environmental costs but protects millions of people from floods; supports economic development through improved inland navigation; and generates more emission-free electricity than most European countries (*16*). It also helps to integrate wind and solar power into China's electric grids, building resilience while mitigating climate change.

In this Anthropocene world, the primary concern should be to ensure that infrastructure interventions are part of a broader process of "ecological modernization" (*17*) that meets people's aspirations within an altered but sustainable and socially acceptable ecological framework. ■

[1]School of Governance, University of the Witwatersrand, Johannesburg, South Africa. [2]Lee Kuan Yew School of Public Policy, Singapore, Singapore. [3]Cofounder, Third World Centre for Water Management, Atizapán, Mexico. [4]Alboran Consulting, London, UK.
*Corresponding author. E-mail: mike.muller@wits.ac.za

REFERENCES AND NOTES

1. UN Environment Programme, *Green Infrastructure Guide for Water Management* (UNEP, Nairobi, 2014).
2. D. Grey, C. W. Sadoff, *Water Policy* **9**, 545 (2007).
3. Department of Economic and Social Affairs, Population Division, United Nations, *World Population Prospects: The 2012 Revision, Volume I: Comprehensive Tables* (ST/ESA/SER.A/336, UN, New York, 2012).
4. Organization for Economic Cooperation and Development, *Environmental Outlook to 2050* (OECD Publishing, Paris, 2012).
5. Office of Water, U.S. Environmental Protection Agency, "Drinking water infrastructure needs survey and assessment: Fifth report to Congress" (4606M EPA 816-R-13-006, EPA, Washington, DC, 2013).
6. Department of Economic and Social Affairs, UN Population Division, "World urbanization prospects: The 2014 revision: Highlights" (ST/ESA/SER.A/352, UN, New York, 2014).
7. C. Tortajada, D. Altinbilek, A. K. Biswas, Eds., *Impacts of Large Dams* (Springer, Berlin, 2012).
8. C. Binnie, *Thames Tideway Tunnel: Costs and Benefits Analysis* (Clean Thames Now and Always, UK, 2014) http://bit.ly/ThamesTunnelC-B.
9. National Audit Office, "Thames Tideway Tunnel: Early review of potential risks to value for money" (UK Audit Office, London, 2014).
10. D. Normile, *Science* **327**, 1568 (2010).
11. A. K. Biswas, C. Tortajada, *Int. J. Water Resour. Dev.* **19**, 377 (2003).
12. H. Scarborough, O. Sahin, M. Porter, R. Stewart, *Desalination* **358**, 61 (2015).
13. C. Brown *et al.*, "An empirical analysis of the effects of climate variables on national level economic growth" (Policy Research Working Paper Series, World Bank, Washington, DC, 2010).
14. M. Muller, in *Africa in Focus: Governance in the 21st Century*, K. Kondlo and C. Ejiogu, Eds. (HSRC Press, Pretoria, 2011); http://bit.ly/HSRCAfrGov.
15. D. Seckler, R. Barker, U. Amarasinghe, *Int. J. Water Resour. Dev.* **15**, 29 (1999).
16. Y. Zhao, B. F. Wu, Y. Zeng, *Biogeosciences* **10**, 1219 (2013).
17. A. P. Mol, G. Spaargaren, D. A. Sonnenfeld, in *Ökologische Modernisierung-Zur Geschichte und Gegenwart eines Konzepts* in *Umweltpolitik und Sozialwissenschaften* (Campus Verlag, Frankfurt, 2014), pp. 35–66.

10.1126/science.aac7606

PHYSICS

Plasmons at the interface

Extraction of light-induced electrons is enhanced by interface control

By **Matthew J. Kale**[1]
and **Phillip Christopher**[1,2]

Absorption of photons by solid materials is critical for applications such as photovoltaics (*1*), photocatalysis (*2*), and sensors (*3*). Fundamental to these technologies is the design of materials that can efficiently absorb photons of desired wavelengths and direct the separation and transport of the generated charge carriers [electrons (negative) and holes (positive)] to their respective collectors. Materials with high concentrations of free conducting electrons, such as coinage metals (Ag, Au, and Cu), have attracted attention for these applications because of their tunable ability to strongly concentrate a light flux in small volumes via the excitation of resonant surface plasmons. However, the lifetime of useful electrons and holes generated in metals upon the decay of surface plasmons is on the order of 1 ps, which limits their efficient collection. On page 632 of this issue, Wu *et al.* (*4*) overcome this limitation by demonstrating a direct, instantaneous transfer of plasmon-derived electrons into interfacial semiconductors that allows for efficient solar energy harvesting across a broad range of photon energies.

Excitation of resonant surface plasmons occurs when photons coherently oscillate with low-energy electrons in a metal, against a background of positively charged nuclei. On nanostructures with characteristic geometries below ~30 nm, coherent plasmon oscillations decay through Landau damping. In the Landau damping process, the loss of plasmon coherence excites electronic transitions in the metal, producing electron-hole pairs with a total energy equivalent to the original photon energy (see the figure inset, left). Primary electrons and holes produced during Landau damping lose energy on the time scale of tens to hundreds of femtoseconds by scattering off ground state electrons and holes (*5*). Because of ultrafast energy dissipation time scales, photon energy harvesting technologies based on surface plasmon excitation and decay must involve the production of electrons and holes with tailored energies that are quickly and efficiently transferred to the collectors.

Differences in electron and hole energies produced by plasmon decay for various metal nanostructures in inert environments can be analyzed on the basis of known band structures of noble metals and provide potential for controlling charge transfer to collectors (*6*). However, bond formation between metal nanostructures and adsorbates or solid-state materials complicates the picture, owing to hybridization of metal and interfacial species' electronic states. Wu *et al.* take an important step in understanding plasmon-interfacial interactions by demonstrating that Au/CdSe interfaces perturb the Au surface plasmons to facilitate direct injection of electrons into the CdSe conduction band upon plasmon decay. The interfacial plasmon decay process effectively separates electrons from holes, which are left behind in the Au. Direct plasmon-mediated interfacial charge transfer is more efficient for injecting plasmon-derived charge carriers into semiconductors than the typically assumed indirect mechanism of electron and hole generation in the metal by Landau damping, followed by transfer through tunneling or traversing the Schottky barrier (see the figure inset, left) (*3*, *7*).

The impact of interface formation between plasmonic nanostructures and surrounding environments is often discussed in terms of the encompassing matrix dielectric function. This ignores the modifying impact of interfacial chemical bond formation on valence metal electrons, which are responsible for resonant surface plasmon oscillation and decay, and cannot account for observed reductions in plasmon lifetime (plasmon resonance broadening). The mechanism of chemical interface damping has also been used to describe interface-induced changes in surface plasmon resonances (*8*). In this mechanism, interfacial bond formation introduces new

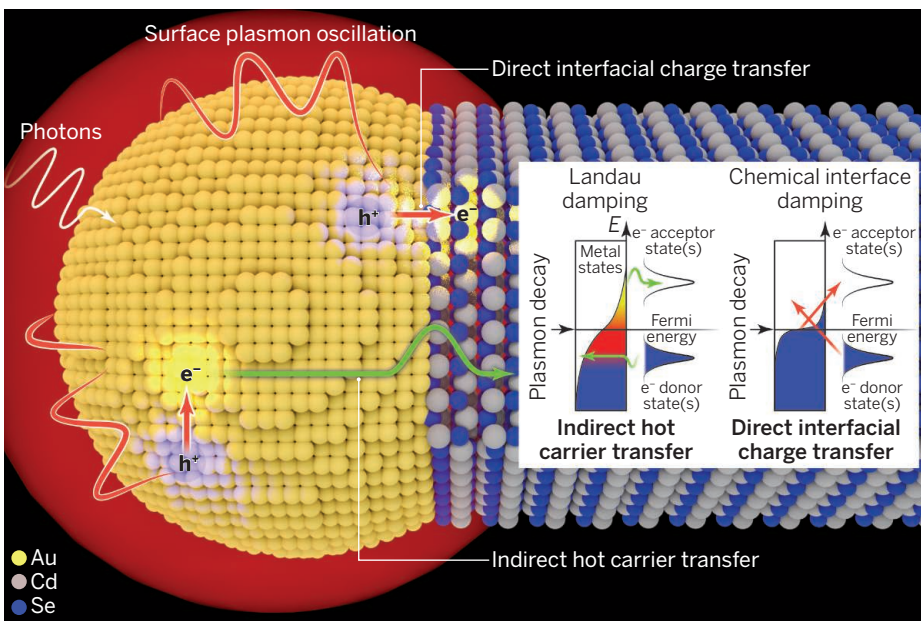

Interfacial charge transfer. Photons excite collective surface plasmon oscillations on an Au-tipped CdSe nanorod. Electrons are transferred to the CdSe following plasmon decay indirectly through hot carrier generation in the Au by Landau damping, diffusing to the Au/CdSe interface and traversing the Schottky barrier. Alternatively, plasmon decay causes direct interfacial charge transfer between hybridized Au and CdSe states via chemical interface damping. The inset shows an energy diagram of plasmon-induced charge transfer through (left) Landau damping, where upon plasmon decay, the high-energy tail of a hot electron distribution can transfer across an interface into electron acceptor state (or hot holes can transfer into donor states), and (right) chemical interface damping, where surface plasmon decay occurs by direct interfacial electronic transitions.

[1]*Department of Chemical and Environmental Engineering, University of California, Riverside, Riverside, CA 92521, USA.* [2]*Program in Materials Science, University of California, Riverside, Riverside, CA 92521, USA. E-mail: christopher@engr.ucr.edu*

ILLUSTRATION: MATTHEW J. KALE

electron acceptor and donor states that decrease the lifetime of surface plasmons by providing decay pathways via interfacial electronic transitions (see the figure inset, right). Wu *et al.* observe extreme chemical interface damping where electronic transitions at the Au/CdSe interface decrease the Au plasmon lifetime and, as a result, the plasmonic light concentration strength. Recent results show that similar electronic transitions exist at metal-adsorbate interfaces and enable control of catalytic processes, indicating that chemical interface damping may be critical for efficiently activating adsorbed molecules, and driving catalysis on plasmonic nanostructures (*9*, *10*). This reinforces an important point—that any covalent bond formation to plasmonic nanostructures will have an impact on plasmon excitation and decay processes through chemical interface damping.

The results of Wu *et al.* solidify the importance of atomistic insights into electronic transitions across plasmonic metal interfaces for enabling increased charge separation efficiency at metal-semiconductor interfaces and efficient control of catalysis. The fraction of plasmons that decay via chemical interface damping, compared to Landau damping into the metal, will be specific to plasmonic nanostructure geometry and the nature of metal-interface hybridization. As originally postulated in the chemical interface damping mechanism, direct interfacial charge transfer pathways damp the strength of plasmonic light concentration (the feature that makes plasmonic nanostructures potentially interesting for solar energy conversion). This suggests that the efficient use of plasmon-derived charge carriers will require a balance between the strength of plasmonic light concentration and efficiency of interfacial charge transport and that once again we will turn to hot spots at plasmonic nanoparticle junctions for enhancing light-matter interactions (*11*). ■

REFERENCES

1. H. A. Atwater, A. Polman, *Nat. Mater.* **9**, 205 (2010).
2. P. Christopher, H. Xin, S. Linic, *Nat. Chem.* **3**, 467 (2011).
3. M. W. Knight, H. Sobhani, P. Nordlander, N. J. Halas, *Science* **332**, 702 (2011).
4. K. Wu, J. Chen, J. R. McBride, T. Lian, *Science* **349**, 632 (2015).
5. C. Voisin *et al.*, *Phys. Rev. Lett.* **85**, 2200 (2000).
6. A. O. Govorov, H. Zhang, Y. K. Gun'ko, *J. Phys. Chem. C* **117**, 16616 (2013).
7. S. Mubeen *et al.*, *Nat. Nanotechnol.* **8**, 247 (2013).
8. H. Hövel, S. Fritz, A. Hilger, U. Kreibig, M. Vollmer, *Phys. Rev. B* **48**, 18178 (1993).
9. H. Petek, M. J. Weida, H. Nagano, S. Ogawa, *Science* **288**, 1402 (2000).
10. M. J. Kale, T. Avanesian, H. Xin, J. Yan, P. Christopher, *Nano Lett.* **14**, 5405 (2014).
11. P. Christopher, H. Xin, A. Marimuthu, S. Linic, *Nat. Mater.* **11**, 1044 (2012).

10.1126/science.aac8522

NATURAL HAZARDS

Building land with a rising sea

Cost-efficient nature-based solutions can help to sustain coastal societies

By **Stijn Temmerman**[1] *and* **Matthew L. Kirwan**[2]

Coastal lowlands are increasingly exposed to flood risks from sea-level rise and extreme weather events (*1*). Megacities like Shanghai, London, New York, and Bangkok that lie in vast river deltas are particularly vulnerable. Dramatic flood disasters include the Indian Ocean tsunami in 2004, Hurricane Katrina in New Orleans in 2005, Hurricane Sandy in New York in 2012, and Typhoon Haiyan in the Philippines in 2013. Managing the risks of such disasters requires investments in short-term emergency response and long-term flood protection (*2*), including nature- or ecosystem-based engineering (*3*, *4*). On page 638 of this issue, Tessler *et al.* (*5*) show that sea-level rise, increasing climate extremes, population growth, and human-induced sinking of deltas threaten the sustainability of many major deltas around the world.

Investments in coastal and river engineering, such as the building of dikes, levees, and dams, are often seen as the ultimate solution to combat flood risks and shoreline erosion. However, Tessler *et al.* reach a rather different conclusion: Deltas in wealthy countries, which can currently reduce risks by costly engineering solutions, are likely to see the strongest risk increase in the long term, when energy becomes more expensive. Prominent examples of engineered deltas with compromised long-term sustainability, according to the authors, are the Mississippi delta in the United States, the Rhine delta in the Netherlands, and deltas in East Asia where engineering is deployed on vast scales (*6*).

PHOTO: JOOP VAN HOUDT/RIJKSWATERSTAAT

Nature-based adaptation to rising sea level. This aerial view of part of the Rhine-Meuse-Scheldt delta in the Netherlands and Belgium shows natural wetlands that build up land with rising sea level, thereby contributing to flood protection of developed lowlands in the back.

Apart from the socioeconomic constraints highlighted by Tessler *et al.*, there are additional limitations to conventional engineering. Although it provides effective flood and erosion protection on time scales of years to decades, it disturbs natural delta processes in ways that accelerate local sea-level rise and increase long-term flood risks. A natural delta before engineering (see the figure, panel A) consists of a network of river channels surrounded by wetlands that are regularly inundated by tides and river flooding. Sand and mud supplied during inundations are trapped in the wetland vegetation, a key natural process that has enabled the vertical building and maintenance of deltas in balance with sea-level rise for thousands of years (*7*).

With human settlement, deltaic wetlands are converted into agricultural, urban, and industrial land. In these deltas, flood-protecting structures such as dikes directly fringe the river channels, leaving almost no space for natural wetlands (see the figure, panel B). When the wetlands are disconnected from the rivers, the land no longer builds up with sea-level rise. Furthermore, upstream dams often reduce the supply of riverine sediment, slowing down the land-building process in remaining wetlands (*4*). Deltas are also highly susceptible to land subsidence, which is the sinking of land due to soil compaction and which is exacerbated by human activities like soil drainage (*4*).

In the Mississippi delta, human disruption to natural delta-building processes are deemed responsible for rapid submergence of the delta plain and subsequent land loss rates as high as 100 km^2 per year since 1900 (*8*). In the Netherlands, after centuries of soil drainage and land sinking, 9 million people now live below sea level behind costly dikes. In the Ganges-Brahmaputra delta in Bangladesh and India (with 170 million people, the most populated delta on Earth), land that was embanked in the 1960s now lies 1 to 1.5 m lower than remaining wetlands (*9*).

Wetland embankment also triggers extra sea-level rise, because storage area for flood

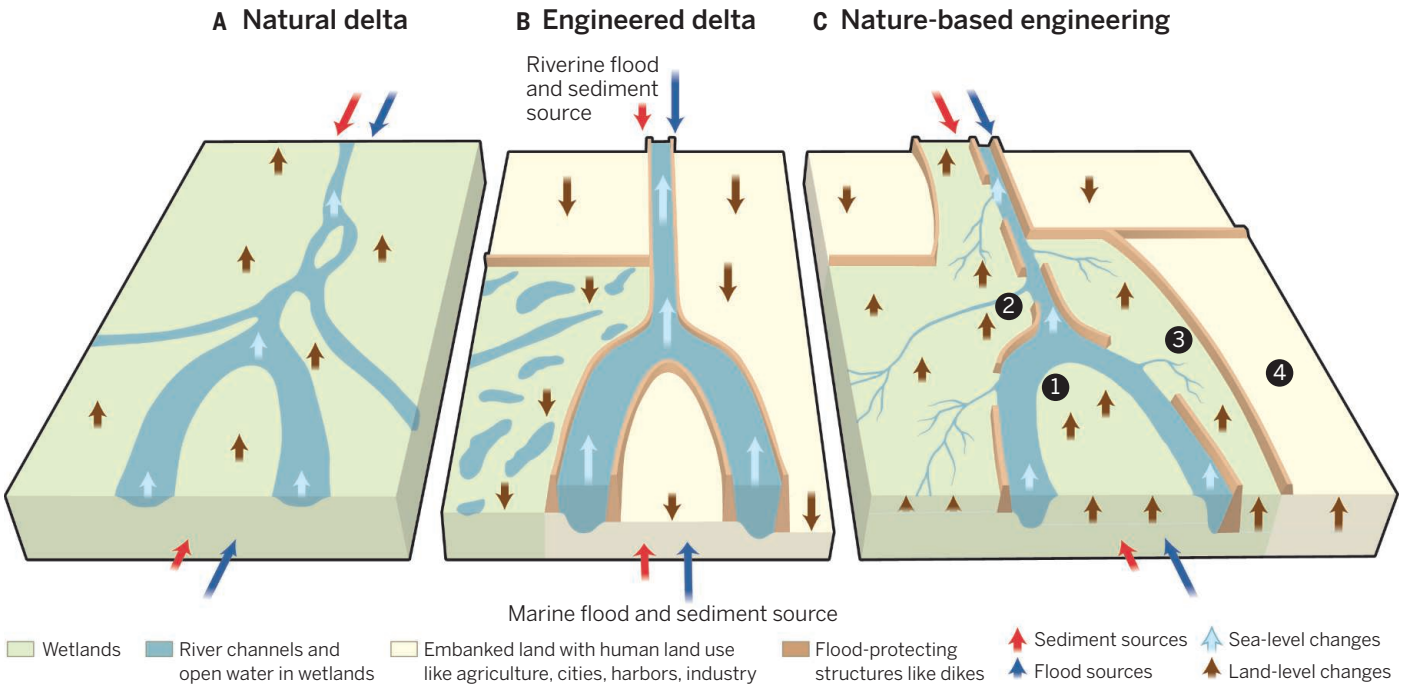

Sinking or rising deltas. In natural deltas (**A**), land can rise in balance with sea level through sediment accumulation in regularly inundated wetlands. In deltas with conventional engineering (**B**), land rise through sedimentation is prevented by flood-protecting structures like dikes and upstream river dams; land sinks due to human activities like soil drainage; and extreme water levels rise due to loss of wetlands. As Tessler *et al*. show, reliance on conventional engineering of this kind poses a risk to populations living in deltas around the world.In contrast, we propose that nature-based engineering solutions (**C**) can help to maintain land-building processes and flood storage through wetland conservation and restoration, for instance by dike removal (1), controlled dike breaching and river diversions (2), and temporary dike breaching and subsequent re-embankment (3) and (4).

waters is lost, causing water levels to rise faster in the remaining channels of a delta. In the Ganges-Brahmaputra delta, this has contributed to an effective sea-level rise of 17 mm per year since 1960; near the coast, this rate is 10 mm per year (*10*). Similarly in the Rhine-Meuse-Scheldt delta, effective sea-level rise is up to 15 mm per year since 1930, which is five times the rate at the coast (*3*).

Conventional engineering thus unintentionally exacerbates long-term flood risks and compromises the sustainability of delta communities. In contrast, new nature-based engineering solutions should include the restoration of large wetlands between rivers and human settlements, which can provide extra water storage, slow down flood propagation, and reduce flood risks in populated parts of a delta (*3*) (see the figure, panel C). At the same time, restored wetlands have a high capacity to build up sediments, regain elevation on formerly embanked and lowered land (*11*), and survive long-term sea-level rise (*7*). Unlike conventional engineering, which Tessler *et al.* argue will become more expensive in the future, nature-based solutions are largely self-sustaining and cost-efficient (*3*) and could therefore make deltas less vulnerable to rising energy costs.

Ecosystem-based engineering projects are just beginning to be designed and implemented (*3*, *4*). In the Mississippi delta, there are ambitious plans to divert sediment-laden river water back onto the delta plain (see 2 in the figure) (*4*, *8*). These efforts would build or prevent the loss of more than 500,000 ha of wetlands and contribute to reducing annual flooding damage to New Orleans and coastal Louisiana by US$5.3 to $18 billion in 50 years (*12*). Projects designed to stimulate natural wetland-building processes with sediment delivered through river diversions are estimated to cost about 10 times less than projects with conventional sediment delivery by barge or pipeline (*12*).

In the Belgian part of the Rhine-Meuse-Scheldt delta (see the photo), around 4000 ha of historically embanked floodplains will be restored by 2030. These efforts should lower a 1-in-100-year storm surge by 60 to 80 cm and are more cost-efficient than conventional heightening of dikes (*12*). In Bangladesh, unintended dike breaching caused rapid elevation gain of several decimeters within 2 years of tidal flooding, inspiring scientists to propose temporary controlled dike breaches as a method to regain elevation on formerly embanked and lowered land (*9*). Once the land would be built up, it could be re-embanked, and human land use such as agriculture could start again (see 3 and 4 in the figure).

Building land with a rising sea and a growing coastal population requires strategies that combine conventional engineering with the restoration and maintenance of wetlands and natural delta-building processes. Advances in ecosystem-based engineering may mitigate the risks associated with conventional engineering and rising energy costs. The few existing examples, however, are too recently implemented to fully evaluate their long-term success. More proof-of-concept projects with extensive monitoring are urgently needed in the search for science-based solutions to safeguard delta societies around the world. ■

[1]*Ecosystem Management Research Group, University of Antwerp, B2000 Antwerp, Belgium.* [2]*Virginia Institute of Marine Science, College of William and Mary, Gloucester Point, VA 23062, USA. E-mail: kirwan@vims.edu, stijn.temmerman@uantwerpen.be*

ILLUSTRATION: ADAPTED BY P. HUEY/*SCIENCE*

REFERENCES

1. J. Hinkel *et al.*, *Proc. Natl. Acad. Sci. U.S.A.* **111**, 3292 (2014).
2. E. B. Barbier, *Science* **345**, 1250 (2014).
3. S. Temmerman *et al.*, *Nature* **504**, 79 (2013).
4. L. Giosan *et al.*, *Nature* **516**, 31 (2014).
5. Z. D. Tessler *et al.*, *Science* **349**, 638 (2015).
6. Z. Ma *et al.*, *Science* **346**, 912 (2014).
7. M. L. Kirwan, J. P. Megonigal, *Nature* **504**, 53 (2013).
8. J. W. Day Jr. *et al.*, *Science* **315**, 1679 (2007).
9. L. W. Auerbach *et al.*, *Nature Climate Change* **5**, 153 (2015).
10. J. Pethick, J. D. Orford, *Global Planet. Change* **111**, 237 (2013).
11. W. Vandenbruwaene *et al.*, *Geomorphology* **130**, 115 (2011).
12. CPRA, "Louisiana's Comprehensive Master Plan for a Sustainable Coast" (Louisiana Coastal Protection and Restoration Authority, Baton Rouge, 2012).
13. P. Meire *et al.*, *ECSA Bull.* **62**, 19 (2014).

10.1126/science.aac8312

OPTOGENETICS

Expanding the optogenetics toolkit

A naturally occurring channel for inhibitory optogenetics is discovered

By Andre Berndt[1] and Karl Deisseroth[1,2,3]

Many microbial opsin genes encode proteins that, upon absorption of a photon, move ions across the cell membrane. The resulting ion flow can activate, inhibit, or modulate cells depending on the type, direction, and quantity of the ion being conducted (*1*). For optogenetic experiments, expressing these proteins has been useful for providing activity patterns to targeted cells (*1*, *2*). On page 647 of this issue, Govorunova *et al.* (*3*) report a potent new opsin from the microbe *Guillardia theta* that can inhibit target cells. The discovery of this channelrhodopsin punctuates the long search for a naturally occurring, light-activated ion channel with utility for inhibition in optogenetic studies.

Most channelrhodopsin proteins allow cations in the cellular milieu to flow down electrochemical gradients across the membrane in response to light (*4*). This translates into an excitatory stimulus for the opsin-expressing cell. In many cases, however, inhibiting the targeted cells is also of scientific value, for which light-activated potassium or chloride ion channels would be well-suited. However, for more than 12 years after the initial description of ion conductances of channelrhodopsins (*4*, *5*), and for more than 7 years after initial reports of channel engineering and genomic screening (*6*) to create or identify channelrhodopsins with new properties—and despite intense efforts on both the genomic and channel engineering fronts—no potassium- or chloride-selective channelrhodopsins had emerged (*7*).

To overcome this obstacle, microbial opsins encoding chloride or proton pumps have been used, giving rise to many discoveries on the neural circuit control of behavior. However, these are less efficient than channels, moving only one ion per photon instead of the hundreds that channels can allow. The crystal structure of channelrhodopsin (*8*) allowed rational modification of the channel pore (*9*) and mutagenesis of amino acids involved in the photocycle (*10*), to generate inhibitory chloride channels. Both engineered channelrhodopsins [inhibitory C1C2 (iC1C2) and slow chloride-conducting channelrhodopsin (SloChloC), respectively] exclude sodium and potassium ions, but conduct chloride, thus effectively inhibiting action potentials in cultured neurons (*9*, *10*).

Genomic studies had identified and characterized microbial opsins from *Guillardia* (*7*), but the new family members reported by Govorunova *et al.* [called *Guillardia theta* anion channelrhodopsin 1 (*Gt*ACR1) and *Gt*ACR2] show markedly reduced primary-sequence homology and unusual chloride selectivity. Like the engineered chloride channels (*9*, *10*), *Gt*ACR2 allows light-induced blockade of action potentials in cultured neurons. Two other properties of the *Gt*ACRs deserve mention: large photocurrents and high light sensitivity.

The photocurrents arising from *Gt*ACR2 are among the largest that have been reported with any microbial opsin (many nanoamperes of current in single mammalian cells). This implies especially robust expression (many channels per cell) and perhaps especially strong single-channel conductance as well. Although *Gt*ACR2 in neurons was challenged with relatively moderate action potential–inducing stimulation, its large inhibitory photocurrent

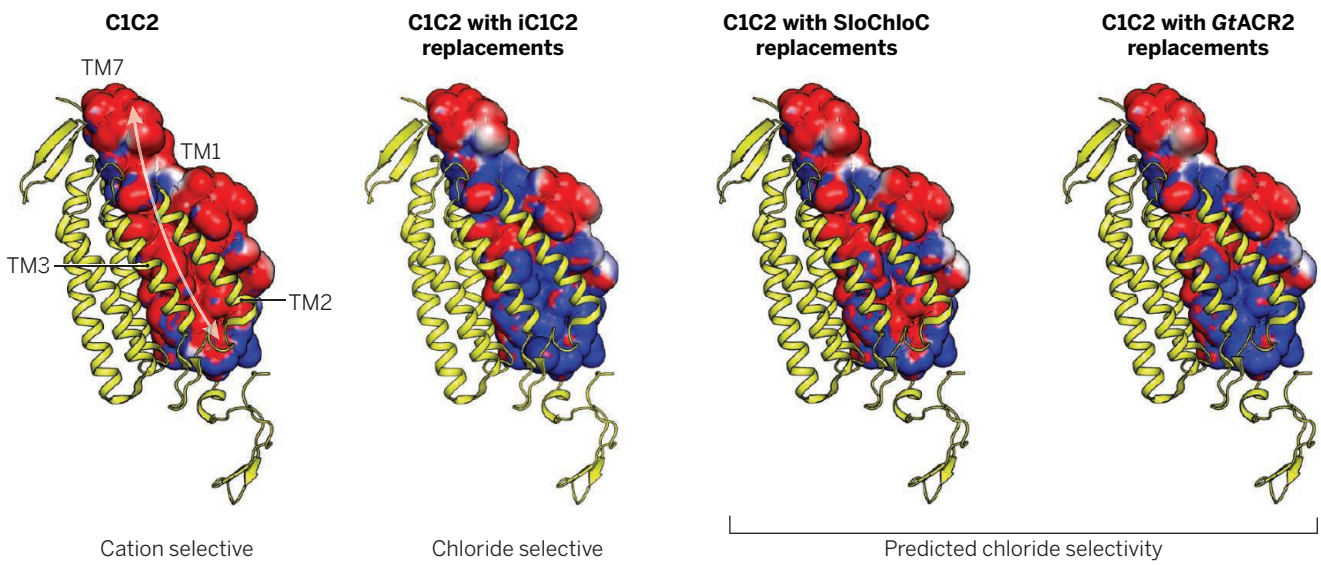

Conductivity in channelrhodopsins. The wild-type channel C1C2 [Protein Data Bank: 3UG9 (*8*)] does not conduct chloride (*9*). The ion-conducting pore is formed by four transmembrane helices (TM 1, 2, 3, 7). In the modified structures shown, residues facing the ion-conducting pore in C1C2 are replaced to demonstrate the putative impact on the electrostatic surface potential of helices 1 and 7; side-chain positioning (except for the shown closed state of C1C2) (*8*) and electrostatics are not known and could vary in the open state as well. Structures were generated with PyMOL 1.7 and surface potentials were calculated with the APBS Tool 2.1 (*14*) assuming full deprotonation of acidic and full protonation of basic residues. Red and blue represent putative electrostatic potential of $-1\,kT/e$ and $+1\,kT/e$, respectively. k, Boltzmann's constant; T, temperature; e, elementary charge.

[1]Department of Bioengineering, Stanford University, Stanford, CA, USA. [2]Department of Psychiatry and Behavioral Sciences, Stanford University, Stanford, CA, USA. [3]Howard Hughes Medical Institute, Stanford University, Stanford, CA, USA. E-mail: deissero@stanford.edu

amplitude may present a major upside for preventing action potentials driven by very strong synaptic input.

Also of interest is the low light intensity that can be employed. Govorunova *et al.* used an irradiance value of 0.026 mW/mm^2 to inhibit action potentials in neurons, which is about two orders of magnitude weaker than might be used to saturate widely used channelrhodopsins (*11*). In optogenetics, the operational light sensitivity of targeted cells can be decomposed into several contributing factors (*11*), ranging from quantum efficiency of the photosensitive protein molecule itself (the likelihood of successful absorption of a photon arriving within the protein's spatial cross-section, leading to photocycle initiation), to the density of proteins on the cell membrane (which is itself related to expression level and trafficking efficiency), to the kinetics of deactivation (slowed deactivation kinetics allow accumulation of proteins in the active state within a cell, and therefore longer light pulses can be effective at orders-of-magnitude lower irradiance values for slow-deactivating opsins). All of these factors could be operative for *Gt*ACR2. However, quantum efficiencies are already thought to be fairly high for wild-type channelrhodopsins (~0.5, leaving little room for orders-of-magnitude improvement). In addition, *Gt*ACR2 protein density in the membrane is presumably high, as reflected in the large photocurrents, but again perhaps not alone high enough to explain the sensitivity. Also, deactivation kinetics of *Gt*ACR2 (>40 ms) are somewhat slower than fast inhibitory pumps (~4 ms exhibited by cells expressing the chloride pump halorhodopsin eNpHR3.0) (*11*, *12*) or inhibitory channels (~10 ms for the dominant fast component of iC1C2) (*9*). It may be that high expression is the dominant contributor to the effective light sensitivity reported by Govorunova *et al.*, which will be fascinating to explore further but is, in principle, of high utility regardless of mechanism.

Are the slower off-kinetics problematic in other ways? For hypothetical experiments involving, for example, the deletion of single action potentials (spikes) from within >25-Hz trains, deactivation kinetics of >40 ms could be problematic. But most experiments with inhibition do not involve deleting a single spike within a high-frequency train (for which fast pumps or channels like eNpHR3.0 and iC1C2 would be used), but rather involve more sustained inhibition. The photocurrents of *Gt*ACR2 show suitable properties for such longer-term experiments, including temporal stationarity and large amplitude. Other factors could guide selection (for use in optogenetics) of a chloride pump over a chloride channel—for example, in cases where chloride gradients might be inverted as in developmental or pathological situations, and certain cell types or subcellular compartments. In these cases, even perfect chloride conductance and strong currents will not lead to better inhibition. Instead, excitation will result, indicating that chloride pumps would be a better choice. Pumps have their own challenges and can cause membrane instability if hyperpolarization that is too strong is achieved (*11*). It will be interesting to observe the extent of hyperpolarization elicited by the robust photocurrents of *Gt*ACR2 in typical application settings.

"The discovery of this channelrhodopsin punctuates the long search for a naturally occurring, light-activated ion channel with utility for inhibition in optogenetic studies."

What are the next steps for the field? Individual optogenetic tools have frequently shown promise in vitro, but unpredictably encountered fundamental problems in the longer-term in vivo expression setting. It will be essential to actually test, for optogenetics, all of the new chloride channels (both engineered and naturally occurring) in intact tissue, in different cell types, and under different chloride concentrations. A large upside is possible for *Gt*ACR2, as many opportunities have not yet been leveraged, including adding the mutations from step-function opsins [for higher light sensitivity (*11*, *13*)], adding surface-membrane and neurite trafficking sequences for higher expression levels (*11*–*13*), and adding mutations for accelerating kinetics further (*11*, *13*).

Knowing that channelrhodopsins can be chloride-selective to an extent that allows action potential inhibition (*2*, *9*, *10*) has been useful for understanding the proteins themselves, and now poses additional intriguing biophysical and structure-function questions. Solving the crystal structures of both the engineered and naturally occurring chloride channels will be necessary, to understand if shared or distinct pore configurations and related selectivity mechanisms are at work.

In particular, the crystal structure of channelrhodopsin (*8*)—with a large relatively disordered pore, absence of bound ions, and conduction pathway lined with residues expected to be negatively charged or polar—suggested an electrostatic model for cation-selective pore function that was empirically tested, and successfully led to creation of anion selectivity (*9*). Obtaining the structure of *Gt*ACR2 will be interesting in this regard; although *Gt*ACR2 is chloride selective while retaining a glutamate residue (E90) (*2*), which iC1C2 (*9*) and SloChloC (*10*) lack, certain pore similarities between iC1C2 and *Gt*ACR2 support the net electrostatic model (see the figure) with numerous replacements of pore-facing glutamate residues corresponding to the original C1C2 channelrhodopsin with noncharged residues in *Gt*ACR2 (including *Gt*ACR2 serine 57, threonine 67, alanine 71, and serine 93). Interestingly, the serine 93 site corresponds to a similar threonine in the chloride pump halorhodopsin from *Halobacterium salinarum*, where this residue is near the chloride ion binding site.

Structural information and molecular dynamics studies on *Gt*ACR2 will also enable understanding of the central and cytosolic pore gates of the closed-state channelrhodopsin structure, especially because tyrosine 109 of the C1C2 cytosolic gate is represented by methionine in *Gt*ACR2, while another contributing residue to this site in C1C2 (histidine 173) is replaced by tryptophan in *Gt*ACR2. These presumptive gates might still operate in *Gt*ACR2, but replacement of the cytosolic gate tyrosine by methionine suggests a substantial disturbance of that pore site, which based on the closed-state structure could contribute considerably to enhanced conductance. Complementation of crystal structures with spectroscopic studies and molecular dynamics simulations will be of value for deeper understanding of intermediate states. These and many other basic biophysical questions will go hand in hand with exploring the opportunities for optogenetics—both avenues representing intriguing directions arising from identification of *Gt*ACRs. ■

REFERENCES AND NOTES

1. K. Deisseroth, *Nature* **505**, 309 (2014).
2. L. Grosenick, J. H. Marshel, K. Deisseroth, *Neuron* **86**, 106 (2015).
3. E. G. Govorunova, O. A. Sineshchekov, R. Janz, X. Liu, J. L. Spudich, *Science* **349**, 647 (2015).
4. G. Nagel *et al.*, *Science* **296**, 2395 (2002).
5. G. Nagel *et al.*, *Proc. Natl. Acad. Sci. U.S.A.* **100**, 13940 (2003).
6. F. Zhang *et al.*, *Nat. Neurosci.* **11**, 631 (2008).
7. F. Zhang *et al.*, *Cell* **147**, 1446 (2011).
8. H. E. Kato *et al.*, *Nature* **482**, 369 (2012).
9. A. Berndt, S. Y. Lee, C. Ramakrishnan, K. Deisseroth, *Science* **344**, 420 (2014).
10. J. Wietek *et al.*, *Science* **344**, 409 (2014).
11. J. Mattis *et al.*, *Nat. Methods* **9**, 159 (2012).
12. V. Gradinaru *et al.*, *Cell* **141**, 154 (2010).
13. O. Yizhar *et al.*, *Nature* **477**, 171 (2011).
14. N. A. Baker, D. Sept, S. Joseph, M. J. Holst, J. A. McCammon, *Proc. Natl. Acad. Sci. U.S.A.* **98**, 10037 (2001).

ACKNOWLEDGMENTS

We thank S. Y. Lee, H. Kato, Y. S. Kim, and C. Ramakrishnan for helpful comments.

10.1126/science.aac7889

MARINE SCIENCE

Deepwater Horizon, 5 years on

Baseline environmental data are crucial for understanding the impacts of oil spills

By **Samantha B. Joye**

On 20 April 2010, an explosion on the Deepwater Horizon drilling unit initiated an uncontrolled release of oil and gas from the Macondo seafloor well into the Gulf of Mexico that lasted for 87 days. Documenting and tracking the ecological, environmental, and human impacts of the Deepwater Horizon oil-well blowout has proved a considerable challenge. Nonetheless, valuable lessons continue to be learned, and data are revealing broad and substantial impacts on the Gulf ecosystem across a range of scales.

The Macondo well discharged at least 5 million barrels of oil (~210 million gallons) (*1*–*3*) and at least 250,000 metric tons of natural gas, largely methane. The error associated with estimates of oil and gas discharge is large, e.g., ranging from 50,000 to 70,000 barrels of oil per day (*3*), because the discharge rate was not quantified immediately or continuously. The absolute magnitude of the discharge is therefore not known. Yet, robust discharge values are required for staging an effective response, constraining the distribution of oil and gas in the environment, and evaluating environmental impacts. They are also critical for formulating and closing the hydrocarbon budget.

In the case of the Deepwater Horizon incident, lack of an accurate discharge rate almost certainly hindered the early response efforts, which assumed a discharge rate of 1000 to 5000 barrels of oil per day, a gross underestimate of the actual discharge (*4*). Higher estimates of 26,500 barrels of oil per day were obtained in mid-May on the basis of remote-sensing data (*4*); however, this estimate only considered oil floating on the surface, not oil dissolved in the Gulf's deep waters. By late May, it was clear that a substantial fraction of the discharged oil was in the deep-water plume (*5*). Discharge was quantified in situ with state-of-the art acoustic scintillation technology only once, on 31 May 2010, about 6 weeks after blowout began (*1*).

Oil and gas discharge from the wellhead is best visualized as a point source that ejected hydrocarbons at a rapid rate, leading to dispersion of oil into droplets and facilitating the formation of deep-water plumes enriched in oil, dissolved gas, and gas hydrate at depths between 900 and 1200 m (*2*, *6*). Plumes were detected with sophisticated chemical sensors lowered through or introduced into the affected waters. Best estimates now suggest that all discharged gas and up to half of the discharged oil (*2*, *3*) [see the figure, bottom] were entrained in the Gulf's deep waters. The fate of the oil and gas in the deep-water plumes can only be estimated from oxygen anomalies (*7*), because few direct measurements of hydrocarbon oxidation rates (except methane) were performed in surface or deep water. Microbially mediated processes facilitated the formation and deposition of oil-containing organic matter (*8*). Quantification of oil-containing organic matter in deep-sea sediments permitted an indirect estimation of the mass of oil-derived material deposited on the seabed (*9*) (see the figure).

> ***"The Deepwater Horizon disaster represented a new type of oil spill: an uncontrolled offshore deep-water discharge that was very difficult to contain."***

Using available estimates of petrocarbon oxidation, assimilation (*7*), and sedimentation (*9*), the fate of roughly 45 to 76% of the discharged hydrocarbons can be constrained (see the figure). The remaining hydrocarbons may have been respired in the upper regions of the ocean and deposited on coastal marshes or beaches, or they may remain in Gulf waters at undetectable levels. There are few direct measurements of hydrocarbon oxidation rates, mainly because sensitive radiotracer methods to quantify oil biodegradation rates in ocean water were lacking at the time. This, together with the absence of sedimentation rate measurements during the incident, makes it difficult to further constrain the fate of oil.

The Deepwater Horizon incident represented an unprecedented hydrocarbon discharge into open ocean waters. It is also historical because of the unparalleled application of chemical dispersants, both at the sea surface and deep below the surface at the discharging wellhead. The utility of chemical dispersants to stimulate hydrocarbon biodegradation by breaking up surface oil slicks into smaller-sized oil droplets remains debated (*10*, *11*). It remains unclear whether the benefits of dispersant application—increased dissolution of oil in offshore waters, reduction of oil delivery to shorelines, and presumed facilitation of hydrocarbon oxidation—offset the documented negative environmental impacts (*12*). To resolve present uncertainties, experiments conducted under conditions that reflect realistic open-ocean environmental conditions and reasonable concentrations of dissolved oil and dispersant are needed for a wide variety of biological organisms, from microorganisms to larval forms of fish, invertebrates, and corals to adult animals. Only with these data in hand can more-informed decisions on dispersant application be made.

The hydrocarbon infusion drove remarkable shifts in the Gulf's water column microbial communities and negatively affected multiple levels of the Gulf's food web, from the microscopic plankton at the base to pelagic fish and top predators, such as dolphins (*13*). Inhibition of zooplankton by oil and/or dispersants during 2010 (*12*) may have blocked trophic transfer of carbon up the food web, which, along with the negative impacts of oil on larval fish populations, could lead to cascading affects at higher trophic levels that are not yet apparent in catch data. The oil infusion also had profound effects on natural communities along the shoreline and on the deep seabed (e.g., cold-water corals).

The Deepwater Horizon disaster represented a new type of oil spill: an uncontrolled offshore deep-water discharge that was very difficult to contain. The incident brought to the forefront many unexpected aspects of hydrocarbon dynamics that were not revealed by previous shallow water spills, such as the Exxon Valdez spill in Alaska. We now know that in the case of a deep-water blowout, as much as 50% of the discharged oil and essentially all of the discharged gas will be sequestered in deep-water plumes (*2*, *3*). Given the magnitude of deep-water oil and gas, consistent tracking and monitoring of its distribution and fate, including direct measurements of degradation rates, should be a priority in future response scenarios. Robust and consistent documentation of the discharge rate is critical for developing the oil budget and constraining the fate of oil and gas.

Department of Marine Sciences, University of Georgia, Athens GA 30602-3636 USA. E-mail: mjoye@uga.edu

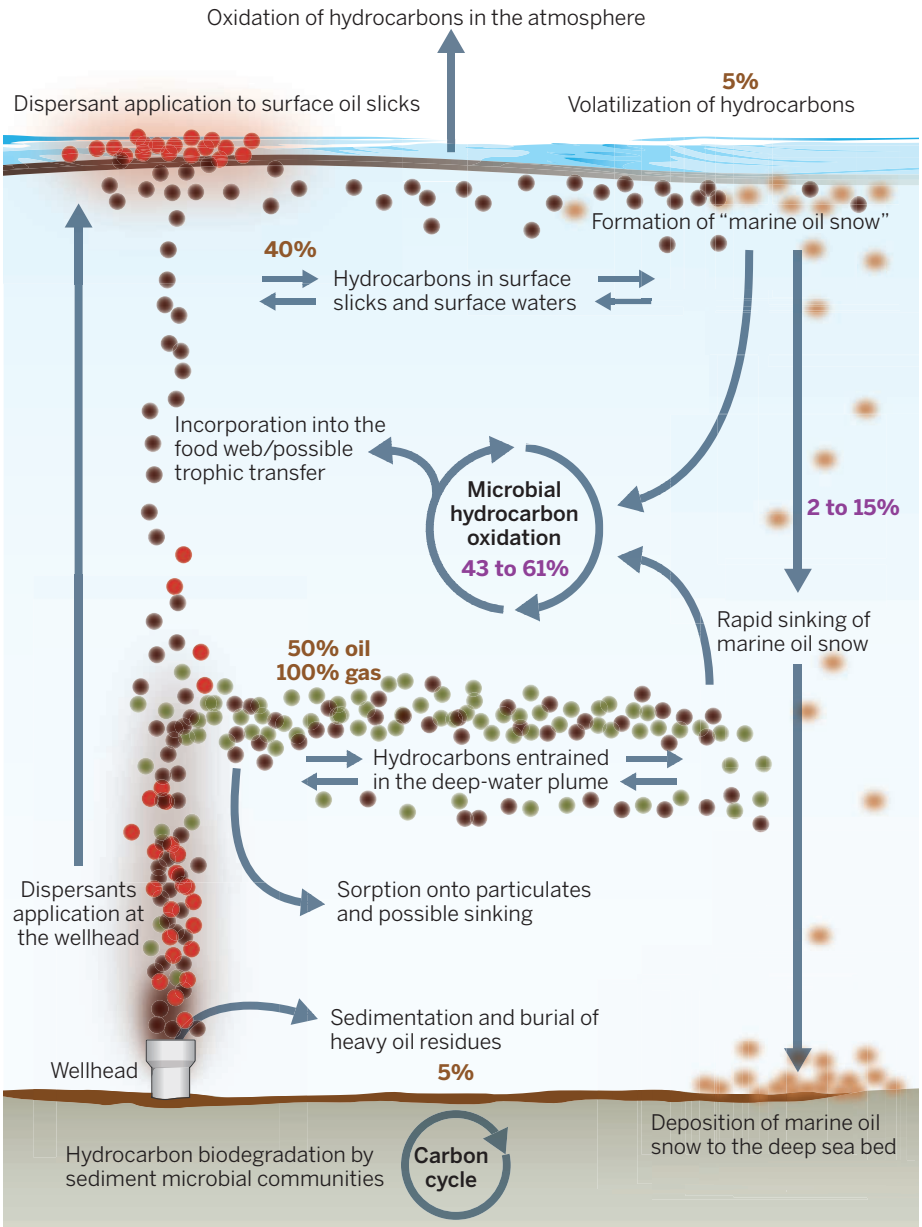

Where did the oil and gas go? The percentages given in brown in the figure reflect the approximate distribution of oil (brown circles) and gas (green circles) during the Deepwater Horizon well blowout (*2*–*4*); dispersant addition is noted by red circles. Available data (purple percentages) suggest that the long-term fate is known for only 45 to 76% of the discharged hydrocarbons (*7*–*9*). Some of the unaccounted-for oil may have been deposited in coastal marshes or beaches (not shown on the figure). Vertical and horizontal aspects are not to scale.

ILLUSTRATION: ADAPTED FROM (*10*)

Before the Deepwater Horizon incident, sedimentation was not considered an important fate of oil, and it was not considered in the Deepwater Horizon oil budget (*2*). However, recent data show that 2 to 15% of the discharged oil was deposited on the seabed (*9*). Quantifying sedimentation rates at multiple sites over short time scales in a large area is possible through use of inexpensive particle interception traps deployed at the base of the mixed layer. In contrast, quantifying sedimentation rates at the seabed or at deeper depths in the water column requires more expensive moored (Kiel) sediment traps. Both types of traps—deployed in a targeted fashion based on available surface oil distribution and physical oceanographic data—would be needed to quantify the extent of oil sedimentation to the seabed during a future incident like the Deepwater Horizon spill.

Given the expansion of oil and gas drilling into ~1500-m deep waters—deeper than the Macondo wellhead—in the Gulf of Mexico and offshore Brazil and West Africa, the likelihood of another incident is a real threat. Ecological changes can occur slowly or sporadically and are only apparent and quantifiable through consistent long-term observation. The absence of long-term monitoring data hamstrings the ability of the scientific community to assess natural environmental change, manage the environment in a sustainable fashion, and document anthropogenic perturbations (*14*). Scientists from many disciplines responded in force to the Deepwater Horizon disaster, providing a plethora of data that helped quantify the discharge rate, advanced the understanding of oil and gas distribution, and identified environmental affects (*15*), but the lack of baseline data made it difficult to constrain and, in some cases, verify, environmental impacts.

We can and we must do better. Environmental baselines are sorely lacking across the Gulf of Mexico ecosystem and other environments that are or may soon be affected by hydrocarbon extraction, such as the Arctic Ocean basin. Without environmental baselines, assessing acute and chronic impacts is nearly impossible. Examples of baselines that should be obtained include the range and dynamics of sedimentation rates across open-water environments disturbed by deep-water drilling; better constrained distributions of oil and gas in the Gulf and other systems that derive from natural seepage; elucidating the capacity and regulation of the native pelagic microbial communities that degrade oil and gas; and describing biological community dynamics in the water column and along the seabed [e.g., from the microbial communities at the base of the food web to fish; marine mammals; and seabed communities, such as cold-water corals]. Such data would advance the understanding of ecosystems affected by hydrocarbon extraction and would provide for a more-informed impact assessment. It is also imperative that methods for in situ daily flow-rate monitoring are in place for any deep-water drilling site; these methods must be calibrated and must not interfere with well control operations. ■

REFERENCES

1. R. Camilli *et al.*, *Proc. Natl. Acad. Sci. U.S.A.* **109**, 20235 (2012).
2. T. B. Ryerson *et al.*, *Proc. Natl. Acad. Sci. U.S.A.* **109**, 20246 (2012).
3. M. K. McNutt *et al.*, *Proc. Natl. Acad. Sci. U.S.A.* **109**, 20260 (2012).
4. I. MacDonald, *Significance* **7**, 149 (2010).
5. R. Camilli *et al.*, *Science* **330**, 201 (2010).
6. S. B. Joye *et al.*, *Nat. Geosci.* **4**, 160 (2011).
7. M. Du, J. D. Kessler, *Environ. Sci. Technol.* **46**, 10499 (2012).
8. U. Passow, *Deep Sea Res. Part II Top. Stud. Oceanogr.* 10.1016/j.dsr2.2014.10.001 (2014).
9. D. L. Valentine *et al.*, *Proc. Natl. Acad. Sci. U.S.A.* **111**, 15906 (2014).
10. S. Kleindienst *et al.*, *Nat. Rev. Microbiol.* **13**, 388 (2015).
11. R. C. Prince, *Environ. Sci. Technol.* **49**, 6376 (2015).
12. R. Almeda, C. Hyatt, E. J. Buskey, *Ecotoxicol. Environ. Saf.* **106**, 76 (2014).
13. S. Venn-Watson *et al.*, *PLOS ONE* **10**, e0126538 (2015).
14. J. P. Magnuson, *Bioscience* **40**, 495 (1990).
15. J. Lubchenco *et al.*, *Proc. Natl. Acad. Sci. U.S.A.* **109**, 20212 (2012).

10.1126/science.aab4133

BOOKS *et al.*

ECOLOGY

The field guide, rebooted

Identifying species in the field? There's an app for that

By **Gregory R. Goldsmith**

The field guide as we know it has not changed much since it was invented more than 100 years ago. It is a list of species and a description of their respective attributes, accompanied by some illustrations. More recent field guides also include maps of expected species distributions. However, publishing on paper imposes some limits on the information that can be included. A paper field guide can either be comprehensive in its consideration of every species in a taxon or consider multiple taxa without including every single species. This information can only be organized in one way and with one or two indices.

Map of Life joins a small but growing number of mobile applications seeking to reimagine the field guide by combining big data and mobile technology. The project, first launched in 2012 as a web-based platform for compiling range maps of all living plant and animal species, is directed by Walter Jetz at Yale University in collaboration with Rob Guralnick at the University of Florida. The application, released earlier this year, is available free on both iOS and Android platforms in six different languages.

The application is ambitious in its scope, seeking to provide a guide to all local species, no matter where the user is located on the planet. In contrast to the long tradition of field guides authored by expert natural historians, *Map of Life* draws on collective wisdom, amalgamating global data sets of species observations from published sources and using a series of modeling techniques to convert them into species range maps. By combining these data with information from the mobile device's location services (e.g., GPS), the application creates a list of species the user can expect to encounter. This information can be sorted, searched, and filtered to make a field guide relevant to the user's particular interests.

Species from the list can be explored with pictures, descriptions, and range maps. Distinguishing among birds in a nearby lake, for example, was simple and intuitive. However, the list of taxa provided by the application is only as comprehensive and accurate as the data sets from which it draws. While walking around an alpine meadow in full bloom, I discovered that the application does not currently include any flowering plant species for that location.

I was also unable to identify the species I observed when I turned into a forested valley, because data access depends on a wireless Internet connection. Luckily, the application's mapping interface makes it easy to access lists of species for any location, so it is possible to identify a species before or after a day in the field.

The current problems with connectivity intrinsic to all mobile applications will inevitably fade. *Map of Life* comes with a crowdsourcing twist to address these issues of data availability. Following in the footsteps of *iNaturalist* (www.inaturalist.org), a standard-bearer for natural history mobile applications, it allows users to instantly contribute their own geolocated, time-stamped species observations, although the process by which they are vetted and used to revise the species range maps has not yet been completed. (The observations I added can be viewed on a dashboard on the *Map of Life* website.) The ability to add an observation is currently limited to only those species that already exist in the database, but it is nevertheless the foundation for the application's self-sustaining development.

In addition to being able to add observations about species encountered, the user is also able to note which expected species were not encountered. I was struck by all of the species that were expected to occur but were not present as I walked around the city where I live, a compelling reminder of our impact on the planet's biodiversity.

The long-term utility and sustainability of natural history mobile applications remain to be seen. The use of data generated from public funding makes it imperative that such applications are provided free, yet their development remains resource intensive. Traditionally, the sales of the field guide helped recoup the cost of its production. An alternative revenue model is not yet obvious. Moreover, the efficacy of mobile applications with regard to improving knowledge and attitudes about biodiversity, relative to paper field guides, remains largely unexplored. However, Jetz already reports an average of more than 500 unique daily users, a very promising sign that the application is garnering considerable attention.

With the advent of *Map of Life*, one can't help but imagine a future of locally relevant, on-demand field guides. One can imagine, for example, a user in the Brazilian Pantanal looking at a list of local bird species at the same time that a user in an Australian rainforest shares an observation of a butterfly—and with that comes the possibility of imagining a whole new generation exploring the planet's biodiversity.

The reviewer is in the Ecosystem Fluxes Group, Laboratory for Atmospheric Chemistry, Paul Scherrer Institute, Villigen 5232, Switzerland. E-mail: gregory.goldsmith@psi.ch

Map of Life
iOS/Android compatible, 2015.
http://mol.org

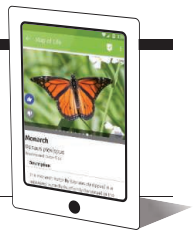

10.1126/science.aac7810

PHOTO: LZF/THINKSTOCK

NEUROSCIENCE

Identity crisis

A scientific exploration of our sense of self

By **Oliver Vikbladh**

Peering down at what should have been my own body, all I saw were the shiny legs and lifeless torso of a plastic humanoid figure. I wore a pair of futuristic virtual-reality glasses, and through them I watched a live video feed from a camera mounted on the head of the manikin. The experimenter started synchronously tapping my chest and the synthetic torso. At first, nothing happened. But then, suddenly, it felt as though my body became one with the plastic figure.

This strange episode occurred a few years ago while I was working at the Karolinska Institute in Stockholm. I had agreed to take part in an experiment in the lab of Henrik Ehrsson, a professor of neuroscience who uses illusions and neuroimaging to investigate why we perceive our body as distinct from the world. This was my first encounter with the "new science of the self" that is the topic of Anil Ananthaswamy's *The Man Who Wasn't There*. The book explores the innovative work of researchers, including Ehrsson, who leverage theoretical, methodological, and clinical advances in neuroscience and psychology to investigate the "I" that exists in our minds.

"Those of us who inhabit our bodies seamlessly … may not value what we have," Ananthaswamy writes. To probe the true nature of the self, he has traveled around the world to interview academics, clinicians, and individuals who suffer from neurological and psychiatric conditions in which an aspect of self-identity has been disturbed. Each disorder, he argues, "illuminates some sliver of the self," and by studying them, we can begin to grasp the elusive "I."

The gallery of personal, often tender, portraits of patients is impressive and reminiscent of the writings of Oliver Sacks. We are introduced, for example, to Laurie from Bristol, England, whose schizophrenia deprives her of feeling like the owner of her actions. Allan, from California, has lost his sense of personal narrative to Alzheimer's. And then there is the man Ananthaswamy calls David. David suffers from body integrity identity disorder, a rare condition in which sufferers feel as though one or more of their limbs do not belong to them. In a gripping chapter, Ananthaswamy joins David as he travels to Asia for an "off-the-books" leg amputation. After the deed is done Ananthaswamy explains: "I sensed relief, happiness.... It was as if for the first time in his life, David was whole." But, given that David had never met with a psychiatrist, I found myself wondering how Ananthaswamy can be so sure that this is truly a happy ending.

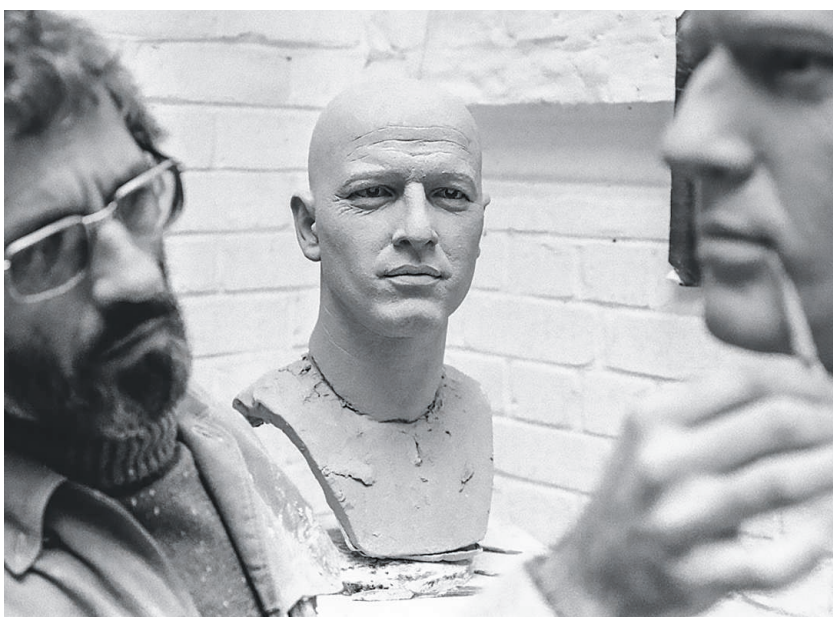

Compelling anecdotes and cutting-edge research challenge our understanding of the human self.

A skilled science journalist, Ananthaswamy excels at making theoretical concepts and experimental procedures both comprehensible and compelling. Using anecdotes and personal observations, he places the people and the science in a broader context by drawing connections to philosophy, sociology, art, and spirituality. We learn about Dostoevsky's ecstatic epileptic seizures, what the sociologist Pierre Bourdieu's concept of "the habitus" might tell us about Alzheimer's patients, and how Indian Buddhist folklore questions the very existence of a self.

The Man Who Wasn't There
Investigations into the Strange New Science of the Self
Anil Ananthaswamy
Dutton, 2015. 317 pp.

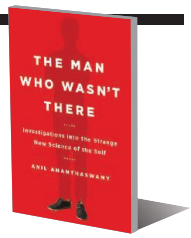

Synthesizing this rambunctious collection of interviews, theories, stories, and observations into a coherent account is a formidable job, however. One challenge is that "the self" is a multifaceted concept. The book explores a vast range of theoretical constructs, including the "narrative self" that emerges from the stories we tell about ourselves, the "interpersonal self" that comes from our interactions with other people, and "embodied selfhood," a sense of self that is carried by our bodily habits, gestures, and actions. Unfortunately, Ananthaswamy doesn't always succeed in connecting or relating their meanings across chapters and, given the enormous breadth of material presented, some of his arguments lack enough precision and depth to be fully convincing.

Another challenge confronting Ananthaswamy is that the science of most of these disorders is still very young. The theories explored are therefore often speculative, and on occasion, the evidence presented is limited to listing which brain areas "showed activity" in the brain scanner, without necessarily supplying any developed framework to interpret the results. This doesn't mean that the book isn't thought-provoking—it covers plenty of fascinating research. But neuroscience is still working toward the kind of mechanistic appreciation of the brain that may allow us to understand and ultimately cure these "maladies of the self."

Perhaps somewhat premature in its conception, but with curiosity and heart, *The Man Who Wasn't There* outlines the early progress of a captivating research field that is likely to redefine the way we think about both science and ourselves.

10.1126/science.aac6681

The reviewer is at the Center for Neural Science, New York University, New York, NY 10003, USA. E-mail: omv208@nyu.edu

PHOTO: SELWYN TAIT/CORBIS IMAGES

LETTERS

Edited by **Jennifer Sills**

Selling First Nations down the river

OIL AND GAS interests and the government recently offered a First Nation in the Skeena River estuary (BC, Canada) $1 billion to consent to construction of a controversial terminal to load fossil fuels onto tankers (*1*). The proposal highlights a troubling blind spot in Canada's environmental decision-making. This gap could enable decisions that insufficiently consider risks to both environment and people. Science can help decrease these blind spots.

The second-largest salmon producer in Canada, the Skeena River has supported First Nation fisheries for 5 millennia (*2*). Its estuary is a nursery for hundreds of millions of young salmon annually as they graduate from freshwater to sea (*2*). It is also situated between fossil fuel reserves in interior Canada and ocean-access to Asian markets. Multinational companies have proposed pipelines to and terminals in the estuary, and are currently assessing the environmental impacts on constitutionally protected (*3*) aboriginal fisheries. Previous research indicates that industrialized estuaries depress salmon survival (*4*). Although terminal proponents and the government have recognized interests of First Nations from the estuary during environmental assessment, they have ignored interests of upriver First Nations who also harvest salmon (*5*).

Salmon migrate thousands of kilometers during their life. We have shown that the proposed development area supports particularly high abundances of juvenile salmon from more than 40 populations that are harvested in at least 10 First Nations territories throughout the Skeena watershed and beyond (*6*, *7*). This is twice the number of First Nations groups that industry proponents identified as needing to be consulted (*5*).

These data reveal a striking mismatch between the narrow consideration of aboriginal rights and environmental risks and the true scale of environmental connections, which needs to be addressed by the Canadian Environmental Assessment Agency (CEAA) and industrial proponents. The terminal application is being evaluated by CEAA without consideration of upriver First Nations (*5*). Moreover, despite the resounding rejection of the $1 billion by the estuary First Nation due to environmental and cultural concerns, the government has ratified fiscal agreements with terminal proponents (*8*). The Skeena Watershed is united by salmon; First Nations throughout the watershed should be involved in decisions that could damage their fisheries.

Identifying the proper spatial scale for environmental decision-making is a fundamental challenge for environmental policy and ethics. Whether it is migratory animals like salmon that transmit impacts, hydroelectric dams that deprive downstream farming communities of water (*9*), or carbon emissions from industrialized countries that raise ocean levels and threaten low-lying islands (*10*), decisions can impact distant ecosystems and people. Science can and should inform the scale at which environmental decision-makers weigh risks to the environment and human rights against potential economic benefits.

Jonathan W. Moore,[1]* Charmaine Carr-Harris,[2] Allen S. Gottesfeld,[3] Donna MacIntyre,[3] David Radies,[4] Mark Cleveland,[5] Chris Barnes,[2,6]† Walter Joseph,[7] Glen Williams,[5] Jennifer Gordon,[8] Bill Shepert[8]

[1]Earth2Ocean Research Group, Department of Biological Sciences, Simon Fraser University, Burnaby, BC V5A 1S6, Canada. [2]Skeena Fisheries Commission, Kispiox, BC V0J 1Y4, Canada. [3]Lake Babine Nation, Burns Lake, BC V0J 1E0, Canada. [4]Takla Lake Nation, Prince George, BC V2L 2Y9, Canada. [5]Gitanyow, Kitwanga, BC V0J 2A0, Canada. [6]Gitxsan Watershed Authorities, Hazelton, BC V0J 1Y0, Canada. [7]Wet'suwet'en, Smithers, BC V0J 2N1, Canada. [8]Lax Kw'alaams Fisheries, Lax Kw'alaams, BC V0V 1H0, Canada.

*Corresponding author. E-mail: jwmoore@sfu.ca

†Deceased

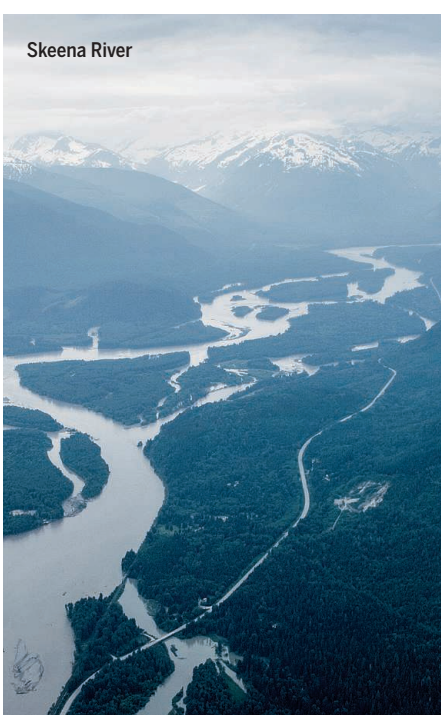

Skeena River

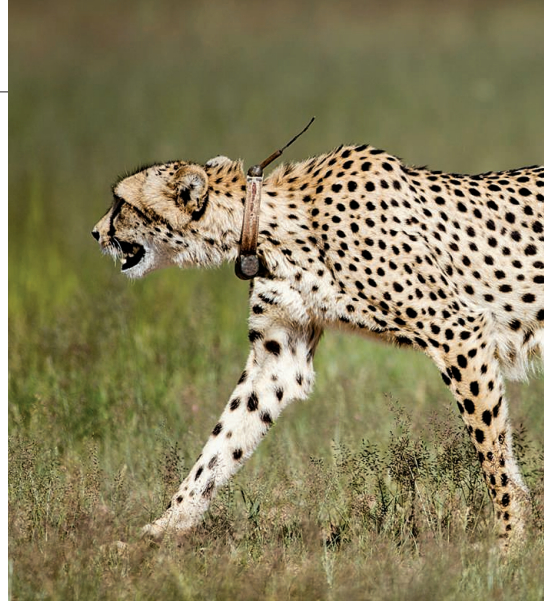

REFERENCES

1. Lax Kw'alaams Band, LNG Benefits (http://laxkwalaams.ca/wp-content/uploads/2015/04/Bulletin-2-Benefits-Summary-01054439.pdf).
2. A. S. Gottesfeld, K. A. Rabnett, *Skeena River Fish and Their Habitat* (Ecotrust, Portland, OR, 2008).
3. Government of Canada, Constitution Act, 1982, schedule B to the Canada Act 1982 (UK) c. 11, Section 35 (1982).
4. A. Magnusson, R. Hilborn, *Estuaries* **26**, 1035 (2003).
5. Stantec Consulting Ltd., *Pacific Northwest LNG Environmental Assessment Certificate Application* (Burnaby, BC, 2014).
6. C. Carr-Harris, A. S. Gottesfeld, J. W. Moore, *PLOS ONE* **10**, e0118988 (2015).
7. C. Carr-Harris, A. S. Gottesfeld, J. W. Moore, "Genetically-identified salmon from Flora Bank region, Skeena River estuary, 2013 and 2014" (http://moorelab.wix.com/moorelab#!flora-bank-salmon/cvyk).
8. Bill 30: Liquefied Natural Gas Project Agreements Act. (2015). 1st Reading July 21, 2015, 40th Parliament, 4th session. Retrieved from: www.leg.bc.ca/40th4th/1stread/gov30-1.htm.
9. E. P. Glenn, C. Lee, R. Felgar, S. Zengel, *Conserv. Biol.* **10**, 1175 (1995).
10. J. Barnett, W. N. Adger, *Clim. Change* **61**, 321 (2003).

Animal telemetry: Tagging effects

THE 12 JUNE Reviews by R. Kays *et al.* ("Terrestrial animal tracking as an eye on life and planet," p. 1222) and N. E. Hussey *et al.* ("Aquatic animal telemetry: A panoramic window into the underwater world," p. 1221) highlight some challenges to the future of terrestrial and aquatic telemetry studies, respectively, focusing on issues related to global collaboration and data sharing. Kays *et al.* also mention the need to continually improve animal-mounted sensors to minimize impacts of tags on animals. However, the gaps in our understanding of impacts associated with attaching instruments to animals are not given substantial consideration in either Review.

Potential impacts may be associated with capture/immobilization stress (*1*), increased drag (and its associated impacts on energy expenditure and locomotor performance)

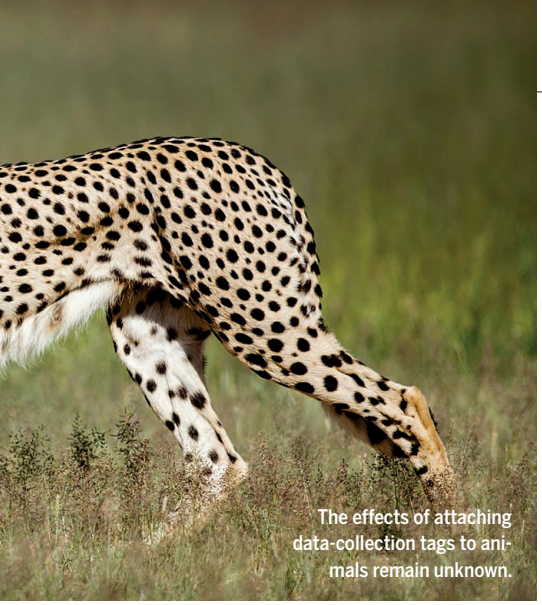

The effects of attaching data-collection tags to animals remain unknown.

from external tags on aquatic and flying animals (*2*), behavioral modifications (*3*), and even environmental impacts such as biofouling (the accumulation of microorganisms or plants on wet surfaces) (*4*). The requirement for more studies assessing tagging impacts has been recognized for some time [e.g., (*5*)]. Some recent papers reported impacts ranging from negligible (*6*, *7*) to substantial (*8, 9*), but the paucity of such studies remains. In fact, in a review of papers reporting results from biologging deployments on free-ranging marine mammals (1965 to 2013; n = 620), I only found 14 papers explicitly aimed to quantify potential impacts associated with instrument deployments (*10*). The knowledge contributions of telemetry studies are undeniable and auspicious, but adequately measuring and minimizing possible negative instrument effects remain important challenges and should receive increased research interest.

Trevor McIntyre

Mammal Research Institute, Department of Zoology and Entomology, University of Pretoria, Hatfield 0028, South Africa. E-mail: tmcintyre@zoology.up.ac.za

REFERENCES

1. A. M. M. Baylis *et al.*, *Mar. Mammal. Sci.* **31**, 322 (2015).
2. C. Tudorache *et al.*, *PLOS ONE* **9**, e112280 (2014).
3. J. M. van der Hoop *et al.*, *J. Exp. Biol.* **217**, 4229 (2014).
4. R. R. Reisinger *et al.*, *Polar Biol.* **33**, 561 (2010).
5. R. P. Wilson, C. R. McMahon, *Front. Ecol. Environ.* **4**, 147 (2006).
6. R. R. Reisinger *et al.*, *PLOS ONE* **9**, e111835 (2014).
7. Y. Kim *et al.*, *Mar. Ornithol.* **42**, 63 (2014).
8. S. P. Vandenabeele *et al.*, *Mar. Ecol. Prog. Ser.* **519**, 239 (2015).
9. A. L. Rasiulis *et al.*, *J. Wildl. Manage.* **78**, 953 (2014).
10. T. McIntyre, *Afr. J. Mar. Sci.* **36**, 409 (2014).

Animal telemetry: Follow the insects

UNDERSTANDING animal movements is crucial for ecology, evolution, and global change. Miniaturized tracking tags have created unprecedented opportunities for advancing knowledge on animal movements. R. Kays *et al.* ("Terrestrial animal tracking as an eye on life and planet," Review, 12 June, p. 1222) summarize breakthroughs with modern Global Positioning System (GPS) devices and suggest that GPS tracking with global communication functionality will allow monitoring of the planet and its ecosystem services. However, this approach is limited by its taxonomic focus on vertebrates (especially birds and mammals). Assuming a global estimate of 5 to 8 million species of insects and other arthropods on Earth (*1*, *2*), the tracking of even 15,000 bird and mammal species would only cover 0.2 to 0.3% of all terrestrial animal species on Earth.

Insects are the most species-rich and abundant terrestrial animals, and they play key roles in ecosystem services (e.g., pollination), food production (e.g., pests), and pathogen spread (e.g., insect-transmitted plant diseases). Conventional (battery-powered) radio tags have now become small enough to allow the telemetry of large insects (*3*), but modern GPS devices remain too heavy for automated, large-scale, and high-resolution insect tracking. The "eye on life and planet" with GPS tags will therefore be blind to the vast majority of animal movements on Earth.

Since only a tiny fraction of animal diversity can be tracked with GPS devices, renewed efforts and additional funding are needed for tracking insect movements across taxa and regions. Manual radio tracking, harmonic radar, and the development of automated tracking systems are crucial for quantifying insect movement at landscape scales (*3–5*), and aerial radio telemetry (*6*) as well as vertical-beam entomological and weather radars (*7–9*) can reveal regional- to continental-scale insect migrations. Monitoring our changing planet requires not only the tracking of vertebrates, but also the myriad movements of insects.

W. Daniel Kissling

Institute for Biodiversity and Ecosystem Dynamics (IBED), University of Amsterdam, 1090 GE Netherlands. E-mail: wdkissling@gmail.com

REFERENCES

1. C. Mora, D. P. Tittensor, S. Adl, A. G. B. Simpson, B. Worm, *PLOS Biol* **9**, e1001127 (2011).
2. M. J. Caley, R. Fisher, K. Mengersen, *Trends Ecol. Evol.* **29**, 187 (2014).
3. W. D. Kissling, D. E. Pattemore, M. Hagen, *Biol. Rev.* **89**, 511 (2014).
4. R. Kays *et al.*, *Comput. J.* **54**, 1931 (2011).
5. J. L. Osborne *et al.*, *J. Appl. Ecol.* **36**, 519 (1999).
6. M. Wikelski *et al.*, *Biol. Lett.* **2**, 325 (2006).
7. J. W. Chapman, D. R. Reynolds, K. Wilson, *Ecol. Lett.* **18**, 287 (2015).
8. J. Shamoun-Baranes *et al.*, *Movement Ecol.* **2**, 9 (2014).
9. J. W. Chapman, V. A. Drake, D. R. Reynolds, *Annu. Rev. Entomol.* **56**, 337 (2011).

RESEARCH

Parkinson's, Alzheimer's, and prions

Goedert et al., *p. 601*

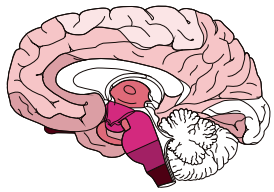

IN *SCIENCE* JOURNALS

Edited by **Nick Wigginton**

Vertical pupils allow cats and other predators to better stalk their prey

EVOLUTIONARY BIOLOGY

The benefits of pupil orientation

Slit-eyed animals have either vertical or horizontal pupils. It is unclear whether one orientation conveys any sort of competitive advantage over the other, and if so, under what circumstances. Banks *et al*. suggest that the optics of vertical pupil slits generally benefit predators, whereas the optics of horizontal slits benefit prey. Vertical slits are better for estimating object distance and distances along the ground—perfect for a predator stalking its prey. In contrast, horizontal slits are better for seeing objects on the horizon—ideal for prey seeing an approaching predator and deciding which way to flee. — SN

Sci. Adv. **1**, el500391

NEUROSCIENCE

Silencing neurons using optogenetics

Rhodopsin light-sensitive ion channels from green algae provide a powerful tool to control neuronal circuits. Rhodopsin cation channels effectively depolarize neurons and cause the firing of short-lived electrical membrane potentials. Govorunova *et al*. describe algal channels that do the opposite; that is, they hyperpolarize or silence particular neurons (see the Perspective by Berndt and Deisseroth). These cation channels provide greater light sensitivity than that of existing hyperpolarizing light-activated channels, operate rapidly, and selectively conduct only anions. This approach is an ideal complement to the widely used technique of creating light-sensitive neurons through the expression of rhodopsin cation channels. — LBR

Science, this issue p. 647; see also p. 590

STATISTICS

Testing hypotheses privately

Large data sets offer a vast scope for testing already-formulated ideas and exploring new ones. Unfortunately, researchers who attempt to do both on the same data set run the risk of making false discoveries, even when testing and exploration are carried out on distinct subsets of data. Based on ideas drawn from differential privacy, Dwork *et al*. now provide a theoretical solution. Ideas are tested against aggregate information, whereas individual data set components remain confidential. Preserving that privacy also preserves statistical inference validity. — GJC

Science, this issue p. 636

BIOLOGICAL ADHESIVES

Keeping it sticky when wet

Some biological molecules are remarkably sticky, even to surfaces submerged in water. Mussel adhesion, for example, is based on the overproduction of dihydroxyphenylalanine (DOPA) and proteins with a high abundance of cationic amine residues such as lysine. Using bacterial iron chelators consisting of paired DOPA and lysine groups as analogs for the mussel proteins, Maier *et al*. show that these two functional groups synergistically enhance interfacial adhesion (see the Perspective by Wilker). The lysine appears to displace hydrated cations from the surface, thus giving a dry patch for better adhesion. — MSL

Science, this issue p. 628; see also p. 582

PALEOECOLOGY

Climate killed off the megafauna

The causes of the Pleistocene extinctions of large numbers of megafaunal species in the Northern Hemisphere remain unclear. A range of evidence points to human hunting, climate change, or a combination of both. Using ancient DNA and detailed paleoclimate data, Cooper *et al*. report a close relationship between Pleistocene megafaunal extinction events and rapid warming events at the start of interstadial periods. Their

analysis strengthens the case for climate change as the key driver of megafaunal extinctions, with human impacts playing a secondary role. — AMS

Science, this issue p. 602

HUMORAL IMMUNITY

B cells have a need for speed

High-affinity antibodies provide long-lasting protective immunity against many infections. Generating such antibodies requires help, in the form of T cells, which interact with antibody-producing B cells. As B cells proliferate and mutate their antibody genes, T cells select the cells producing high-affinity antibodies. Gitlin *et al*. show in mice that B cells that receive T cell help transit through the cell cycle more quickly by increasing the speed at which replication forks progress. Such a rapid cell cycle transition gives high-affinity B cells a selective advantage. — KLM

Science, this issue p. 643

TOPOLOGICAL MATTER

Weyl physics emerges in the laboratory

Weyl fermions—massless particles with half-integer spin—were once mistakenly thought to describe neutrinos. Although not yet observed among elementary particles, Weyl fermions may exist as collective excitations in so-called Weyl semimetals. These materials have an unusual band structure in which the linearly dispersing valence and conduction bands meet at discrete "Weyl points." Xu *et al*. used photoemission spectroscopy to identify TaAs as a Weyl semimetal capable of hosting Weyl fermions. In a complementary study, Lu *et al*. detected the characteristic Weyl points in a photonic crystal. The observation of Weyl physics may enable the discovery of exotic fundamental phenomena. — JS

Science, this issue p. 613 and 622

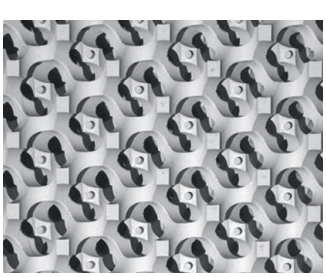

Surface of a 3D photonic crystal with four Weyl points in the band structure

PHOTO: (FROM TOP) DAVID MARTINEZ-DELGADO (MPIA) & GABRIEL PEREZ (IAC); LING LU

STROKE TREATMENT

Randomized clinical trials for mice

To ensure valid conclusions for formal drug approval, the design and analysis of clinical trials are very stringent. Llovera *et al*. applied the criteria of the gold-standard randomized controlled clinical trial to a preclinical investigation in mice. They tested an antibody to CD49d, which inhibits leukocyte migration into the brain, in two mouse models of stroke. Their six-center randomized controlled study showed that the antibody reduced both leukocyte invasion and infarct volume after a small cortical stroke, but had no effect on larger injuries. — KLK

Sci. Transl. Med. **7**, 299ra121 (2015).

ENVIRONMENTAL SCIENCE

Deltas are growing centers of risk

Population growth, urbanization, and rising sea levels are placing populations living in delta regions under increased risk. The future resiliency and potential for adaptation by these populations depend on a number of socioeconomic and geophysical factors. Tessler *et al*. examined 48 deltas from around the globe to assess changes in regional vulnerability (see the Perspective by Temmerman). Some deltas in countries with a high gross domestic product will be initially more resilient to these changes, because they can perform expensive maintenance on infrastructure. However, short-term policies will become unsustainable if unaccompanied by long-term investments in all delta regions. — NW

Science, this issue p. 638; see also p. 588

IN OTHER JOURNALS

Edited by **Sacha Vignieri** *and* **Jesse Smith**

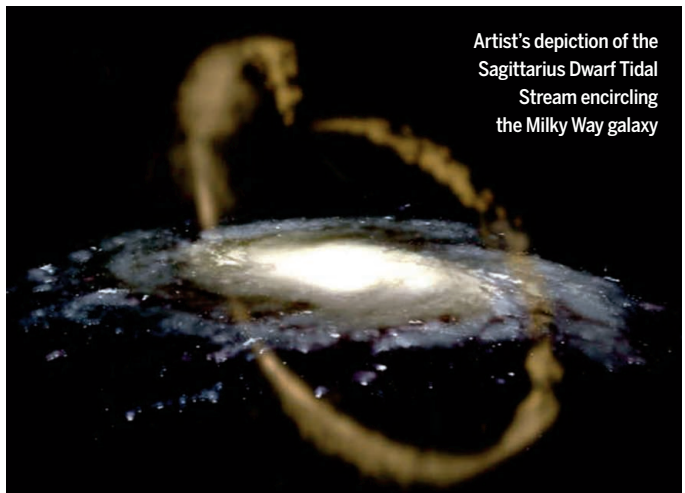

Artist's depiction of the Sagittarius Dwarf Tidal Stream encircling the Milky Way galaxy

GALACTIC ARCHAEOLOGY

Exposing an act of galactic cannibalism

Our Milky Way galaxy contains two streams of stars that have been stripped by its gravity from the neighboring Sagittarius Dwarf Spheroidal Galaxy (Sgr dSph). de Boer *et al*. have disentangled the streams from the surrounding Milky Way and analyzed their star formation history. No stars are younger than 6 billion years old, indicating when they were ripped from the Sgr dSph. The streams also reveal how the stars originally formed in the Sgr dSph, including the moment when type Ia supernovae began enriching the galaxy. This galactic archaeology will help us understand how the Milky Way grew by consuming smaller galaxies. — KTS

Mon. Not. R. Astron. Soc. **451**, 3489 (2015).

PATERNAL CHROMATIN

Biparental control in remodeling sperm

Maternally and paternally inherited animal genomes reorganize and replicate before entering the first zygotic mitosis. Maternally deposited proteins in the egg recondition the sperm DNA; however, Levine *et al*. show that paternal factors are also involved. The *Drosophila* testis-specific protein HP1E localizes to paternal chromosomes and controls sperm DNA reorganization to prime it for embryonic chromosome segregation. Elimination of HP1E in males results in male sterility. Hence, proteins from both parents prime sperm DNA so it can be synchronized with the maternal genome for the first zygotic mitosis. — BAP

eLife 10.7554/eLife.07378 (2015).

PSYCHOLOGY

Believing you know is not the same as knowing

Impossibly large numbers of people believe that they are above average drivers; similarly, people often think that they understand how GPS works, but then cannot provide a persuasive explanation. Atir *et al*. add the phenomenon of overclaiming to this list of metacognitive judgments. They find that crowdsourced workers claim

Wild legumes, like this red clover, need mycorrhizal fungi to help their Nitrogen fixing symbionts during growth

MICROBIOME

Belowground-aboveground

Symbiotic microorganisms, such as nitrogen-fixing bacteria and phosphorus-transferring fungi (mycorrhizae), are vital for plant growth in wild systems. The symbionts may scavenge rare nutrients for plants, but how do they interact? Van der Heijden *et al.* systematically simulated the plant-symbiont communities found in sand dunes in experimental microcosms kept free of contaminating organisms. For wild legume (peas, beans, and their relatives) seedlings, hosting nitrogen-fixing bacteria alone was not enough to guarantee growth; mycorrhizal fungi supplying phosphorous had to be present too. This synergism becomes apparent only when plants live on a nutritional edge. — CA

ISME 10.1038/ismej.2015.120 (2015).

to know or to be familiar with nonexistent financial ("fixed-rate deduction") or biological ("metatoxins") terms and that this occurs in proportion to their self-assessed knowledge about the topic. Moreover, telling people in advance that some terms did not exist had no effect on how many they claimed to know. — GJC

Psychol. Sci. **26**, 10.1177/0956797615588195 (2015).

SOLAR CELLS

Healing perovskite thin films

Inorganic-organic perovskite thin films function best in solar cells when they are free of defects and grain boundaries, but the as-synthesized films are often rough and highly polycrystalline. Zhou *et al*. now show that methyl ammonium lead iodide ($CH_3NH_3PbI_3$) rapidly reacts with gas-phase methylamine (CH_3NH_2) to form a liquid, and then reforms a solid film after degassing. Processed films decreased in root mean square roughness by about a factor of 25, and their overall power conversion efficiency in solar cells increased from 5.0 to 14.5% after treatment. — PDS

Angew. Chem. Int. Ed. 10.1002/anie.201504379 (2015).

In the spiny chromis damselfish, genes involved in metabolism, immunity, and development are up-regulated in cross-generational adaptation to warming

CLIMATE ADAPTATION

How to adapt to climate change

Climate change is imposing increases in temperature on a wide variety of species. Such warming conditions may be particularly challenging for aquatic animals, for which warming waters bring not only temperature increases but also associated oxygen limitations. Some species have displayed an ability to adapt to warming conditions across generations. Veilleux *et al.* looked at the transcriptome of parents and offspring in a Pacific damselfish, *Acanthochromis polyacanthus*, and found three suites of genes whose expression was altered during transgenerational exposure to increased temperatures. These included genes involved in metabolism, immune response, and tissue development. Notably, heat-shock gene expression did not change, suggesting that these markers of immediate response to increased temperatures may not be involved in longer-term adaptation. — SNV

Nat. Clim. Change 10.138/nclimate2724 (2015).

CLIMATE CHANGE

Whither carbon capture and storage?

Carbon capture and storage (CCS) is widely considered an essential aspect of efforts to limit global warming. Yet efforts to develop CCS technology are progressing slowly, and no full-scale power plant with CCS is in operation. Maddali *et al.* analyze the costs and risks associated with CCS and model the effects of its delayed implementation using a dynamic nonlinear simulation tool. Based on a number of emissions and mitigation scenarios, the authors conclude that CCS is not sufficiently mature and, in its current form, is too expensive to contribute significantly to global climate change mitigation. Other mitigation strategies must therefore be developed urgently. — JFU

Environ. Sci. Technol. 10.1021/acs.est.5b00839 (2015).

PHOTO: (FROM TOP) FRANZ SCHUBIGER, AGROSCOPE; © FLPA/COLIN MARSHALL/FLPA/CORBIS

Edited by **Nick Wigginton**

NEURODEGENERATION

Converging paradigms in neurodegeneration

Parkinson's disease and Alzheimer's disease are progressive neurodegenerative diseases with increasing prevalence in our aging populations. Recent evidence suggests that some of the molecular mechanisms involved in the pathology of these diseases have similarities to those observed in infectious prion diseases such as bovine spongiform encephalopathy (mad cow disease). Goedert reviews how the spread of a variety of pathological protein aggregates is involved in neurodegenerative disease. — SMH

Science, this issue p. 601

CHARGE TRANSFER

Improving electron harvesting

Small metal nanostructures generate electrons from light by creating surface plasmons, which can transfer "hot electrons" to a semiconductor. The efficiency of this process, however, is often low because of electron-electron scattering. Wu *et al*. demonstrate a pathway that allows the plasmon to directly excite an electron in a strongly coupled semiconductor acceptor (see the Perspective by Kale). Cadmiun selenide nanorods bearing gold nanoparticles on their ends strongly damped plasmons via interfacial electron transfer with a quantum efficiency exceeding 24%. — PDS

Science, this issue p. 632; see also p. 587

IMMUNODEFICIENCIES

A surprising immune twist for RORC

The immune system needs its full array of soldiers—including cells and the molecules they secrete—to optimally protect the host. When this isn't the case, minor infections can become chronic or even deadly. Markle *et al*. report the discovery of seven individuals carrying loss-of-function mutations in RORC, which encodes the transcription factors RORγ and RORγT. These individuals lacked immune cells that produce the cytokine interleukin-17, causing them to suffer from chronic candidiasis. RORC-deficient individuals also exhibited impaired immunity to mycobacterium, probably due to reduced production of the cytokine interferon-γ, a molecule not known to require RORC for its induction. — KLM

Science, this issue p. 606

ROCK PHYSICS

Cementing Roman concrete to a caldera

Ancient concrete would seem to have little to do with volcano geology. However, Vanorio and Kanitpanyacharoen found similarities between the caprock of the Campi Flegrei caldera near Naples, Italy, and the Roman-era concrete for which the region was known. Both materials require a similar set of chemical reactions to give it the high strength caused by microstructures of intertwining fibrous minerals. The high strength of the natural rock explains the ability of the caldera to withstand periods of high-rate uplift without eruption. The Romans living in the caldera, where the town of Pozzuoli is today, may have been trying to mimic nature to produce this iconic material. — BG

Science, this issue p. 617

NEURODEGENERATION

Mechanistic surprise in ALS-FTD

Intense efforts have focused on identifying therapeutic targets for misfolded proteins that cause amyotrophic lateral sclerosis and frontotemporal dementia (ALS-FTD). Ling *et al*. show that the main culprit of proteinopathy, TDP-43, acts as a splicing suppressor of nonconserved cryptic exons. These exons often disrupt messenger RNA translation and promote nonsense-mediated decay. When TDP-43 was depleted in cells, a set of nonconserved cryptic exons spliced into target RNAs, leading to down-regulation of corresponding proteins critical for cellular function. Repression of cryptic exons prevented cell death in TDP-43–null cells. Because brains of ALS-FTD cases showed evidence of missplicing of cryptic exons, failure in these regions may underlie TDP-43 proteinopathy. — SMH

Science, this issue p. 650

DEVICE TECHNOLOGY

Making better contacts

A key issue in fabricating transistors is making a good electrical contact to the semiconductor gate material. For two-dimensional materials, one route is through a phase transition that converts a hexagonally packed semiconductor phase into a distorted octahedrally packed metallic phase. Cho *et al*. show that laser heating of molybdenum telluride ($MoTe_2$) achieves this conversion through the creation of Te vacancies. The phase transition improves charge carrier mobility while maintaining the low resistance necessary for improved transistor function. — PDS

Science, this issue p. 625

CANCER

Semaphorin signals guide metastases

Tumors of patients with metastatic pancreatic ductal adenocarcinoma (PDAC) contain elevated levels of semaphorin 3D, which guides the growth of new blood vessels. Foley *et al*. found that the protein annexin A2 increased the release of semaphorin from tumor cells from a genetic mouse model of PDAC and promoted migration in these cells. Knockdown of annexin A2 in PDAC cells decreased the ability of these cells to colonize the liver and lungs when injected into mice. These prometastatic effects of annexin A2 did not involve changes in tumor vascularization. — LKF

Sci. Signal. **8**, ra77 (2015).

ENVIRONMENTAL SCIENCE

Lessons from Deepwater Horizon

The explosion and sinking of the Deepwater Horizon drilling unit caused the largest accidental marine oil spill to date. For almost 3 months in 2010, oil and gas flooded into the Gulf of Mexico. In contrast to previous spills, much of the oil and gas formed deep-water plumes. However, Joye explains how accurate data are lacking on both the amount and ultimate fate of the oil and gas emitted from the well. As deep-water oil and gas exploration continues around the world, ecological baseline data and the implementation of daily flow rate measurements from wells should be a high priority. — JFU

Science, this issue p. 592

REVIEW SUMMARY

NEURODEGENERATION

Alzheimer's and Parkinson's diseases: The prion concept in relation to assembled Aβ, tau, and α-synuclein

Michel Goedert*

BACKGROUND: Alzheimer's disease (AD) and Parkinson's disease (PD) are the most common human neurodegenerative diseases. AD is primarily a dementing disease, and PD is a movement disorder. Together, they affect around 50 million people worldwide, with the vast majority of disease cases being sporadic. Their incidence increases with age. Like most neurodegenerative diseases, AD and PD are caused by the aggregation of a small number of proteins, with filament assemblies constituting the end-point of protein aggregation. AD is characterized by the presence of abundant extracellular plaques made of amyloid assemblies of Aβ peptides and intraneuronal inclusions made of assembled tau protein. Some dominantly inherited cases of AD are caused by mutations in the gene encoding the amyloid precursor protein (APP), the cleavage of which gives rise to Aβ. In these cases, dysfunction of APP precedes dysfunction of tau. In contrast, mutations in *MAPT*, the tau gene, give rise to dominantly inherited frontotemporal dementia and parkinsonism, with abundant tau inclusions in the absence of Aβ plaques. Extrapolation to the much more common sporadic cases of AD has given rise to the amyloid cascade hypothesis, which postulates that Aβ aggregation causes the formation of tau inclusions, synaptic dysfunction, nerve cell death, and brain shrinkage. However, tau inclusions correlate better with cognitive impairment, and Aβ may exert its effects through tau. Strategies targeting the formation of Aβ and tau assemblies are valuable for the development of mechanism-based therapies. Unlike AD, in which two distinct amyloid assemblies are present, PD is characterized by intracellular deposits, Lewy bodies and neurites, both composed of the protein α-synuclein. Dominantly inherited forms of PD are caused by mutations in *SNCA*, the α-synuclein gene. More than 95% of those diagnosed with PD have Lewy inclusions.

ON OUR WEB SITE

Read the full article at http://dx.doi.org/10.1126/science.1255555

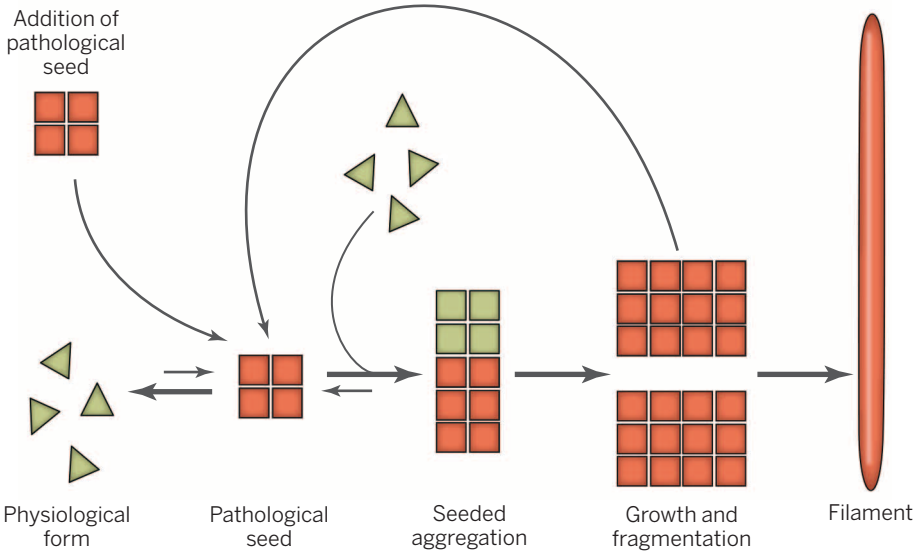

A pathological pathway leading from soluble proteins to insoluble filaments. This pathway is at the heart of human neurodegenerative diseases, including Alzheimer's and Parkinson's diseases. The formation of pathological seeds is a rare and energetically unfavourable event, which requires exposure of backbone amide groups and a high protein concentration. Once a seed has formed, single molecules can change shape and join the growing aggregates. Seed addition induces rapid assembly of the soluble protein. Fragmentation generates new seeds, accelerating the formation of aggregates. Filaments represent the endpoints of aggregation. They are typically unbranched, with a diameter of ~10 nm, and can be several micrometers long. This drawing is not to scale. [Adapted from S. K. Fritschi *et al.*, in *Proteopathic Seeds and Neurodegenerative Diseases*, M. Jucker, Y. Christen Eds. (Springer, Berlin, 2013), pp. 61–69].

ADVANCES: For many years, the mechanisms underlying AD and PD were widely believed to be cell-autonomous. This implies that the same molecular events, such as the formation of tau and α-synuclein assemblies, occur independently in a large number of cells in an otherwise healthy brain. Recent findings have suggested instead that non–cell-autonomous processes play an important part in AD and PD. Inclusions are thought to form in a small number of cells and—given enough time and, perhaps, a genetic predisposition—spread in a deterministic manner to distant brain regions. The formation of the first Aβ, tau, and α-synuclein inclusions is probably stochastic, with most seeds being degraded. Distinct molecular conformers of aggregated proteins (or strains) may underlie clinically different diseases. This is reminiscent of human prion diseases, such as Creutzfeldt-Jakob disease (CJD). However, there is reluctance to use the term prion for the inclusions of AD and PD. The main reasons are that in contrast to Kuru and CJD, transmission of AD and PD has not been demonstrated between individuals, and most experimental studies have used transgenic animals that overexpress disease proteins.

OUTLOOK: The prion concept appears to apply to all human neurodegenerative diseases with abnormal protein assemblies, including AD and PD. This has brought unity to the field and changed the way we think about these diseases. It has been known for some time that a seed can template aggregation of the homologous protein. However, the ability of protein aggregates to spread through the nervous system had previously been underappreciated. At a practical level, the new findings are helping to elucidate the mechanisms underlying disease, which may have therapeutic implications in all cases. It will be important to identify the molecular species of assembled host proteins responsible for propagation and neurotoxicity. ■

Laboratory of Molecular Biology, Medical Research Council, Francis Crick Avenue, Cambridge CB2 0QH, UK.
*Corresponding author. E-mail: mg@mrc-lmb.cam.ac.uk
Cite this paper as M. Goedert, *Science* 349, 1255555 (2015). DOI: 10.1126/science.1255555

REVIEW

NEURODEGENERATION

Alzheimer's and Parkinson's diseases: The prion concept in relation to assembled Aβ, tau, and α-synuclein

Michel Goedert*

The pathological assembly of Aβ, tau, and α-synuclein is at the heart of Alzheimer's and Parkinson's diseases. Extracellular deposits of Aβ and intraneuronal tau inclusions define Alzheimer's disease, whereas intracellular inclusions of α-synuclein make up the Lewy pathology of Parkinson's disease. Most cases of disease are sporadic, but some are inherited in a dominant manner. Mutations frequently occur in the genes encoding Aβ, tau, and α-synuclein. Overexpression of these mutant proteins can give rise to disease-associated phenotypes. Protein assembly begins in specific regions of the brain during the process of Alzheimer's and Parkinson's diseases, from where it spreads to other areas.

More than 100 years ago, Alois Alzheimer, Oskar Fischer and Friedrich Lewy described the inclusions of Alzheimer's disease (AD) and Parkinson's disease (PD), but their constituent proteins were only identified over the past 31 years (*1*, *2*). In AD, these inclusions are amyloid plaques and neurofibrillary lesions, whereas in PD, they are Lewy bodies and neurites.

In the 1980s, β-amyloid (Aβ) peptides, cleavage products of the amyloid precursor protein (APP), were discovered as the major component of amyloid plaques and cerebral vascular inclusions, whereas tau protein was identified as the major component of the neurofibrillary lesions of AD. In the 1990s, α-synuclein was found to make up Lewy bodies and neurites. The study of rare, dominantly inherited cases was essential for understanding the aetiologies of AD and PD. Extrapolation to the much more common sporadic cases underpins most current thinking. In 1991, a missense mutation in the amyloid precursor protein gene (*APP*) that encodes Aβ was shown to cause AD (*3*), and in 1998, mutations in *MAPT*, the tau gene, were reported to cause frontotemporal dementia and parkinsonism (*4*–*6*). In 1997, a missense mutation in *SNCA*, the α-synuclein gene, was shown to cause PD (*7*). More recently, it has become apparent that AD and PD are caused by protein assemblies that adopt alternative conformations and become self-propagating, like prions (*8*, *9*).

Alzheimer's and Parkinson's diseases

AD is the most common neurodegenerative disease. It is defined clinically by a progressive decline in memory and other cognitive functions, and neuropathologically by brain atrophy and the accumulation of abundant extracellular Aβ plaques and intraneuronal neurofibrillary tau lesions (Fig. 1A) (*1*). As shown with electron microscopy, plaques and neurofibrillary lesions are made of abnormal filaments with the fine structure of amyloid (Fig. 1B). They are unbranched and have a diameter of ~10 nm, with a length of up to several micrometers (*10*). Each amyloid filament exhibits characteristic dye-binding properties and consists of several protofilaments with β-sheet structures that are stabilized through hydrogen bonding. The in-register, parallel β-sheet organization predominates in amyloid filaments. The crystal structures of amyloidogenic peptides have shown that amino acid side-chains complement each other across the sheet-sheet interface and that the space between sheets is devoid of water (dry steric-zipper) (Fig. 1C) (*11*, *12*). Non-filamentous aggregates are also present (*1*, *8*). They are β-sheet–rich but transient and are objects of intense investigation (*13*).

Aggregates formed by a given peptide or protein are polymorphic, in that they can adopt multiple molecular structures, which retain their properties after repeated passaging between animals (*14*). Whereas abundant Aβ plaques and cerebral vascular deposits are specific for AD, filamentous tau inclusions are also characteristic of other neurodegenerative diseases, including chronic traumatic encephalopathy (CTE), progressive supranuclear palsy (PSP), corticobasal degeneration (CBD), argyrophilic grain disease (AGD), Pick's disease, and frontotemporal dementia and parkinsonism linked to chromosome 17 (FTDP-17T) (*1*). In some of these diseases, tau inclusions are also found in glial cells.

PD is the second-most common neurodegenerative disease and the most common movement disorder. Patients exhibit bradykinesia that worsens over time, in conjunction with one of three additional features: rigidity, resting tremor, or gait disturbance (*15*). PD is characterized by the widespread degeneration of subcortical structures of the brain, especially dopaminergic neurons in the substantia nigra. They contain Lewy pathology, which is made of abnormal filaments composed of α-synuclein (Fig. 1D). More than 95% of those who fulfill the clinical criteria of PD have Lewy pathology. PD-dementia and dementia with Lewy bodies (DLB) form part of the biological spectrum of PD. α-Synuclein is also the major component of glial cytoplasmic inclusions (GCIs) (*16*–*18*), or Papp-Lantos bodies (*19*), filamentous inclusions that define multiple system atrophy (MSA), a movement disorder characterized by cerebellar ataxia, parkinsonism, and autonomic dysfunction. In MSA, unlike PD and DLB, many α-synuclein inclusions are also found in glial cells (oligodendrocytes and Schwann cells) (*20*, *21*).

Links with prion diseases

Following radioinactivation studies, which suggested that the agent of scrapie may replicate without nucleic acid (*22*, *23*), its purification led to the identification of the prion protein (PrP) and showed that the scrapie agent was devoid of nucleic acid (*24*). To distinguish protein pathogens from viruses, the term "prion" (proteinaceous infectious particle) was introduced (*25*). Human prion diseases include Kuru, Creutzfeldt-Jakob disease (CJD), Gerstmann-Sträussler-Scheinker (GSS) disease, and fatal insomnia. Scrapie, bovine spongiform encephalopathy (BSE), and chronic wasting disease (CWD) are the most common prion diseases in animals. A polymorphism at codon 129 of human *PRNP*, where M or V is encoded, is a susceptibility factor for prion diseases (*26*). Cases of variant CJD (vCJD), which humans acquire through the consumption of BSE-contaminated food products, have so far almost all been M/M (*27*).

With the identification of causative mutations in *PRNP* (Fig. 2A), a possible explanation for dominantly inherited and sporadic cases of CJD emerged (*28*–*30*). Mutations were surmised to lower the energy barrier for conversion of the cellular form of PrP (PrP^{C}) to its scrapie form (PrP^{Sc}). Once a sufficient number of PrP^{Sc} molecules has formed, the conversion of PrP^{C} to PrP^{Sc} occurs readily. Upon introduction into a new host, PrP^{Sc} seeds convert PrP^{C}, which explains how prion diseases can be infectious. In some prion isolates, the majority of infectivity is protease-sensitive. Variable protease-sensitive prionopathy accounts for 2 to 3% of cases of sporadic disease (*31*). More needs to be learned about the sites of prion conversion and the mechanisms of intercellular propagation. The transfer of pathology from one neuron to another appears to occur trans-synaptically. The scrapie agent spreads through the visual system after retinal injection (*32*).

Findings from multiple studies have shown that strain-specific properties are maintained upon serial passaging between animals and are enciphered in the conformation of misfolded prion protein (*33*). Structural differences have been

Laboratory of Molecular Biology, Medical Research Council, Francis Crick Avenue, Cambridge CB2 0QH, UK.
*Corresponding author. E-mail: mg@mrc-lmb.cam.ac.uk

demonstrated between two strains of yeast prions (34). In sporadic diseases, the formation of misfolded prion protein is hypothesized to be stochastic, with prions forming randomly but being usually degraded. The age-dependence of prion diseases, and neurodegenerative diseases more generally, may be the result of a decrease in the efficiency of protein quality-control systems (35).

Mutations in *PRNP* account for ~10% of cases of CJD, with 90% being sporadic. This is reminiscent of AD and PD, in which dominantly inherited mutations account for a minority of cases, with the majority being sporadic. Heterozygous G127V PrP confers resistance against Kuru, with V127 being only found in conjunction with M129 (36). Mice heterozygous for human PrP V127 are resistant to Kuru and CJD but not vCJD prions. Remarkably, homozygous mice are resistant to all prion strains (37).

Initially, the prion concept was confined to a small group of diseases, typified by scrapie and CJD, in which PrP, a glycolipid-anchored sialoglycoprotein, adopts a conformation rich in β-sheet (38). Similar conformational changes have been observed for Aβ, tau, and α-synuclein upon assembly. The prion concept may thus also apply to AD and PD. After injection of misfolded prion protein into the brain, a large increase in the titer of infectivity is observed. It remains to be seen whether this is also the case of assembled Aβ, tau, and α-synuclein.

There is reluctance to use the term prion with respect to the inclusions of AD and PD. The main reason is that in contrast to Kuru and CJD, transmission of AD and PD between individuals has not been demonstrated. However, only ~1% of cases of CJD are acquired, with 99% being sporadic or inherited. The infectious cases in humans have occurred under unusual circumstances, such as ritualistic cannibalism, consumption of BSE-contaminated food products, injection of cadaveric growth hormone and gonadotropin, blood transfusions, corneal transplants, and dura mater grafts, as well as implantation of improperly sterilized depth electrodes.

When prions enter the gastrointestinal tract, they have a reduced ability to cause disease, compared with their injection into the brain (39). However, strain-dependent variations in the efficiencies of oral infection have been described (40). This notwithstanding, the number of humans exposed to BSE prions has been much greater than the fewer than 250 who have died of vCJD. Clearly, human prion diseases are not easily communicable or contagious.

It remains to be seen whether the apparent lack of infectivity of AD and PD can be attributed to the more fragile nature of Aβ, tau, and α-synuclein assemblies, as compared with misfolded prion protein, or to other properties. Yet in the brain (at least of overexpressing animals), many characteristics are shared with PrP^{Sc}. Thus, both PrP^{Sc} and assembled Aβ bound tightly to stainless-steel wires, and after their brain implantation, replication occurred, and prion-specific pathological changes ensued (41, 42). Assembled Aβ and α-synuclein were also resistant to inactivation by formaldehyde (43, 44).

For prion diseases, the molecular species responsible for infectivity and toxicity appear to be different (45–47). Subclinical states and large amounts of PrP^{Sc} have been described, as has neurodegeneration in the presence of small amounts of PrP^{Sc}. Removal of the glycosylphosphatidylinositol anchor of PrP reduces neurotoxicity, despite the accumulation of abundant extracellular PrP^{Sc}. It has been proposed that neurodegeneration is mediated by a toxic form of PrP, called PrP^{L}, that is distinct from PrP^{Sc}, but whose formation is catalyzed by PrP^{Sc} (47). Although the molecular species responsible for toxicity are not well defined, they may be crucial for activating one or more downstream pathways. Targeting the unfolded protein response in mice overexpressing PrP has been reported to prevent neurodegeneration (48).

Assemblies of Aβ, tau, and α-synuclein

Aβ

APP encodes a widely expressed type 1 transmembrane glycoprotein that is alternatively spliced to produce three major transcripts: APP695, APP751, and APP770 (49, 50), with APP695 being the major isoform in neurons. Aβ is produced from APP through sequential endoproteolytic cleavage, with its N terminus being located in the extracellular domain and its C terminus in the transmembrane region. The enzymes, which cut APP to produce Aβ, are the β- and γ-secretases.

β-Secretase features in the initial and rate-limiting step, giving rise to the N terminus of Aβ. It removes the majority of the extracellular portion of the protein, leaving the C-terminal part of APP. BACE1 (β-site APP cleaving enzyme 1), a type I transmembrane aspartyl protease, which has its active site in the extracellular space, is the β-secretase.

γ-Secretase, which gives rise to the C terminus of Aβ, is a membrane-embedded aspartyl protease, which cleaves many transmembrane proteins, including APP and Notch. The γ-secretase complex consists of four proteins: presenilin (PS), presenilin enhancer-2 (Pen-2), anterior pharynx-defective (Aph-1), and nicastrin. PS, an aspartyl protease, forms the catalytic core of the complex. It comprises nine transmembrane (TM) domains, with the two catalytic aspartates located in domains 6 and 7. Upon assembly of the complex, PS undergoes proteolysis between these two domains to form the catalytically active γ-secretase. Pen-2 facilitates the maturation of PS, whereas Aph-1 stabilizes the complex. Nicastrin, which comprises two thirds of the 170-kD protein complex, may be a receptor for γ-secretase substrates. The human γ-secretase complex consists of a horseshoe-shaped domain of TM segments and a large

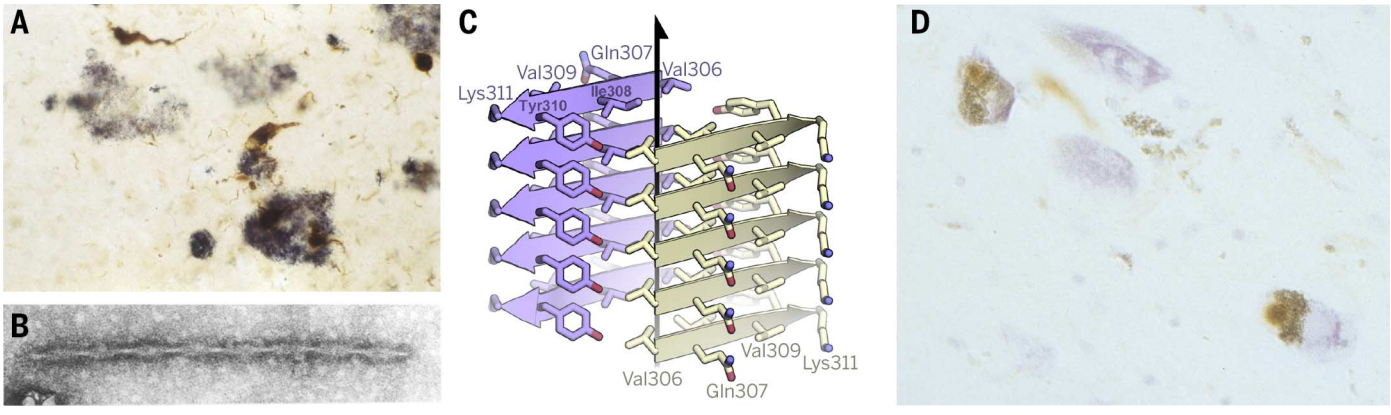

Fig. 1. The assemblies of AD and PD. (**A**) Light microscopic picture of Aβ plaques (blue) and neurofibrillary tau lesions (brown) in the cerebral cortex in AD. (**B**) Electron micrograph of a paired helical tau filament from AD. The cross-over spacing is ~80 nm. Paired helical filaments form the majority of tau filaments, with straight filaments being in the minority. [Reproduced with permission from (138), with permission] (**C**) Steric-zipper crystal structure of the hexapeptide VQIVYK (residues 306 to 311) from the core of tau filaments, which is required for aggregation. Two β-sheets are shown (gray and blue), with the β-strands being parallel within each sheet, and antiparallel between sheets. A tau filament consists of thousands of β-strands, five of which are given for each sheet. The peptide backbones are shown as arrows. Protruding from each sheet are the amino acid side chains. The black arrow marks the filament axis. (**D**) Light microscopic picture of Lewy bodies and Lewy neurites made of α-synuclein (brown) in the substantia nigra in PD. [Reproduced with permission from (139)]

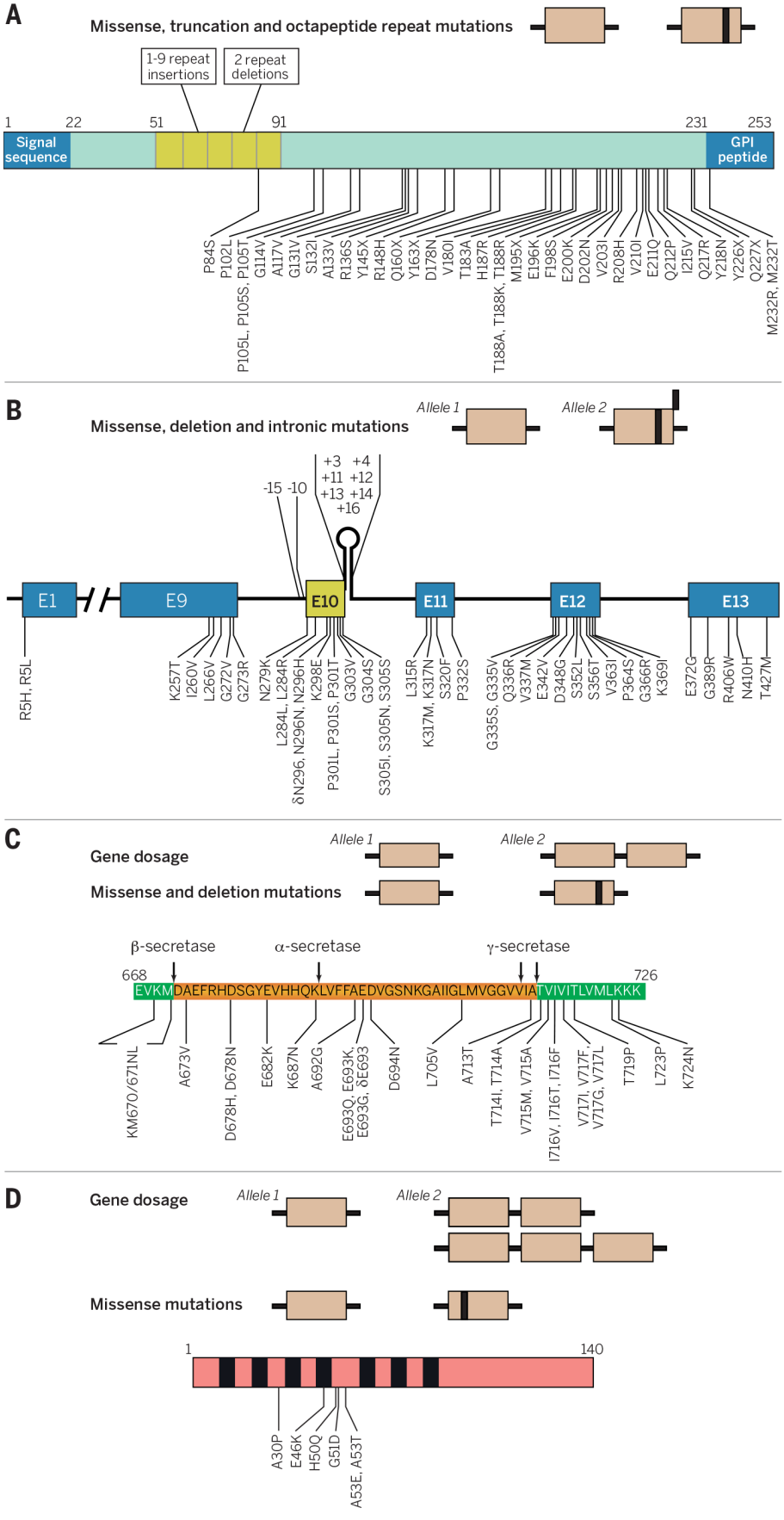

Fig. 2. Mutations in *PRNP*, *MAPT*, *APP*, and *SNCA* that cause human neurodegenerative diseases. (**A**) Missense mutations, truncation mutations, and changes in the numbers of octapeptide repeats in *PRNP*, the prion protein gene, cause dominantly inherited forms of CJD, fatal familial insomnia and GSS disease. Thirty-three missense mutations and six truncation mutations are shown. The number of octapeptide repeats (in yellow) can increase through insertion or decrease through deletion. The methionine/valine polymorphism at codon 129 is important. In human prion diseases with mutations P102L, P105L, P105S, A117V, D178N, H187R, T188R, F198S, E200K, D202N, Q217R, Y218N, Y226X, and Q227X, the sequence was valine at codon 129 of the mutant allele. In many cases with mutations P102L, D178N and E200K, the amino acid at codon 129 of the mutant allele was methionine. (Single-letter abbreviations for the amino acid residues are as follows: A, Ala; C, Cys; D, Asp; E, Glu; F, Phe; G, Gly; H, His; I, Ile; K, Lys; L, Leu; M, Met; N, Asn; P, Pro; Q, Gln; R, Arg; S, Ser; T, Thr; V, Val; W, Trp; and Y, Tyr. In the mutants, other amino acids were substituted at certain locations; for example, G127V indicates that glycine at position 127 was replaced by valine.) The signal sequence and glycosylphosphatidylinositol (GPI) peptide are indicated (in blue). (**B**) Missense, deletion, and intronic mutations in *MAPT*, the tau gene, cause dominantly inherited frontotemporal dementia and parkinsonism linked to chromosome 17 (FTDP-17T). Exons 1 (E1) and E9 to E13 are shown schematically (not to scale). E9 to E12 encode the four tau repeats, with E10 (in yellow) being alternatively spliced. Forty-four coding region mutations and nine intronic mutations flanking E10 are shown. (**C**) Duplication of *APP*, the amyloid precursor protein gene, as well as missense and deletion mutations (black box) in *APP* cause dominantly inherited AD and cerebral amyloid angiopathy. Twenty-eight missense and deletion mutations in *APP* are shown. The Aβ sequence is shown in brown, with the flanking sequences of APP shown in green (numbering according to the 770 amino acid isoform). (**D**) Multiplications of *SNCA*, the α-synuclein gene, and missense mutations (black box) in *SNCA* cause dominantly inherited forms of PD and dementia with Lewy bodies. Six missense mutations are shown. The black bars indicate the imperfect repeats in the amino-terminal half of α-synuclein.

extracellular domain (*51*, *52*). Nicastrin, Aph-1, and the C-terminal part of PS are located at the thick end of the horseshoe, with Pen-2 and the N-terminal part of PS being located at its thin end. Because of the existence of two PS (PS1 and PS2) and Aph-1 (Aph-1A and Aph-1B) variants, there are at least four different human γ-secretase complexes, cleavage by which results in different Aβ profiles (*53*). The processing of APP by γ-secretase is not restricted to a single site. It is cleaved several times, at the ε-, ζ-, and γ-sites that are separated by approximately three amino acids. The final cleavage occurs between amino acids 37 and 43, giving rise to Aβ37, Aβ38, Aβ39, Aβ40, Aβ42, and Aβ43, with Aβ40 being the predominant species. However, Aβ42 is more aggregation-prone and believed to be the toxic building block of Aβ assemblies. The most abundant γ-secretase complex comprises PS1, Pen-2, Aph-1A, and nicastrin.

A third enzyme, α-secretase, cleaves between residues 16 and 17 of Aβ. ADAM10 (a disintegrin and metalloprotease) is the major α-secretase in neurons. Most APP is cleaved by the α- and γ-secretases, resulting in nonpathogenic fragments, but some is cut by β- and γ-secretases to generate Aβ. Cell-surface APP is endocytosed, resulting in the endosomal production of Aβ and its secretion into the extracellular space.

Once a Kuru-like syndrome had been transmitted from humans to chimpanzees (*54*), work was undertaken to determine whether AD and PD were transmissible. No convincing evidence of brain dysfunction was obtained (*55*). In the 1990s, the intracerebral injection of brain homogenates from AD patients was shown to cause deposition of Aβ in marmoset monkeys after 6 to 7 years (*56*). A separate approach used mice overexpressing human mutant APP, resulting in the formation of Aβ plaques. Intracerebral and intraperitoneal inoculations of AD brain homogenates accelerated the deposition of plaques (*57*–*59*). Subsequently, assembled synthetic Aβ was injected intracerebrally into young transgenic mice, where it gave rise to Aβ amyloidosis (*60*). Strictly speaking, these experiments described the acceleration of a process that occurs anyway. However, the induction of Aβ deposition after the intracerebral injection of Aβ amyloid in transgenic rodents that do not normally develop pathology has also been described (*61*). In human brain, Aβ plaques are initially found in basal temporal and orbitofrontal neocortex (*62*–*64*). They appear later throughout the neocortex, as well as in hippocampal formation, diencephalon, and basal ganglia. In severe cases of AD, Aβ plaques are also found in brainstem and cerebellum (Fig. 3).

Modifying the conditions for peptide assembly resulted in different conformers of assembled Aβ, akin to prions (*65*). One strain of Aβ42 induced small plaques composed almost exclusively of Aβ42, whereas another produced large plaques composed of both Aβ40 and Aβ42. Moreover, transgenic mice injected with brain extracts from individuals with AD caused by different *APP* mutations formed distinct Aβ aggregates (*66*). These properties were maintained upon serial passaging in mice.

Tau

In adult human brain, six tau isoforms ranging from 352 to 441 amino acids are produced from one gene through alternative mRNA splicing (*1*). Three isoforms have three repeats each, and three isoforms have four repeats each. The repeats and some adjoining sequences constitute the microtubule-binding domains of tau. They also make up the core of tau filaments. In AD and CTE brains, all six isoforms are present in the filaments. In other diseases—such as PSP, CBD, and AGD—tau isoforms with four repeats are found. In Pick's disease, three-repeat tau isoforms predominate in the inclusions. Unlike AD, these diseases lack Aβ pathology.

Despite the fact that mutations in *APP*, but not *MAPT*, cause inherited AD, neurofibrillary lesions are required for the development of dementia (*62*, *67*). People with abundant Aβ plaques, but no or only few neurofibrillary lesions, do not have AD. The overexpression of mutant human tau in the brains of transgenic mice recapitulates molecular and cellular features of tauopathies, including filament formation and neurodegeneration. The crossing of lines expressing mutant tau with lines expressing mutant APP resulted in enhanced tau pathology (*68*). However, unlike in inherited AD, human tau was mutant. Three-dimensional cultures of human neural stem cells transfected with mutant *APP* have been reported to develop

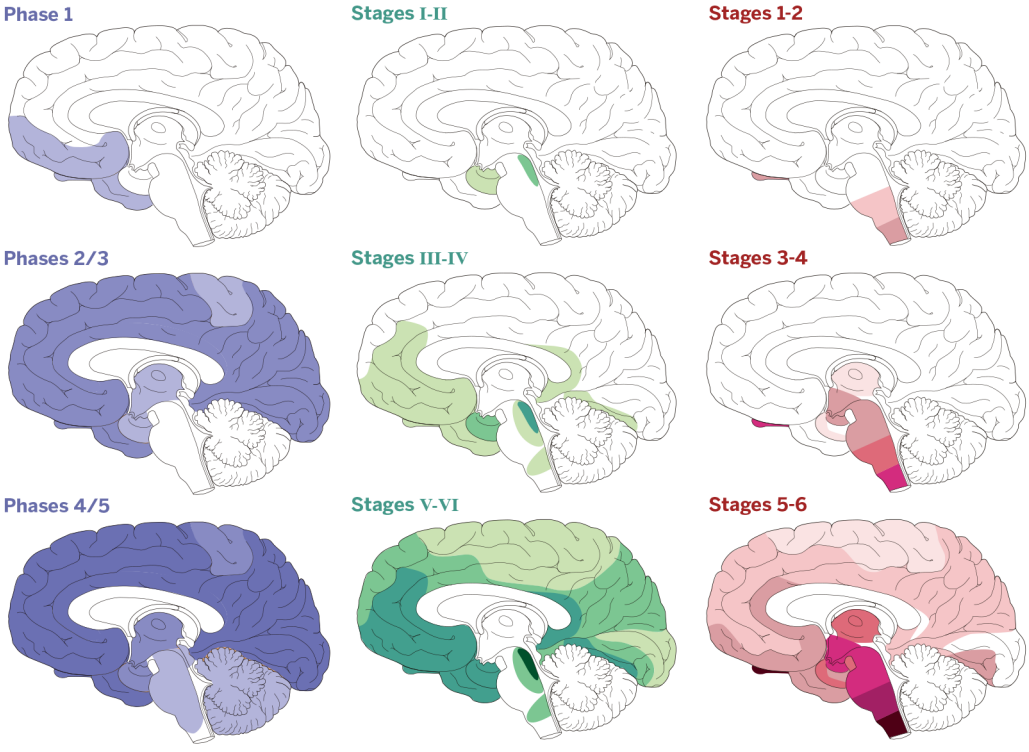

Fig. 3. Propagation of Aβ, tau, and α-synuclein inclusions in human brain. (**Left**) (Blue) Aβ plaques develop first in one or more sites in the basal temporal and orbitofrontal neocortex (phase 1). They are observed later throughout the neocortex, in hippocampal formation, amygdala, diencephalon, and basal ganglia (phases 2 and 3). In severe cases of AD, Aβ plaques are also found in mesencephalon, lower brainstem, and cerebellar cortex (phases 4 and 5). (**Middle**) (Green) Tau inclusions develop in the locus coeruleus, as well as in the transentorhinal and entorhinal regions (stages I and II). This is followed by the presence of tau inclusions in the hippocampal formation and some parts of the neocortex (stages III and IV), followed by large parts of the neocortex (stages V and VI). (**Right**) (Red) α-Synuclein-positive Lewy pathology ascends from the brainstem. The first inclusions are present in the olfactory bulb and the dorsal motor nucleus of the vagal and glossopharyngeal nerves of the medulla oblongata (stages 1 and 2). From the brainstem, the pathology spreads through the pons to midbrain and basal forebrain (stages 3 and 4), followed by the neocortex (stages 5 and 6). [Fig. 3 is based on the work of H. Braak, K. Del Tredici, and collaborators. Adapted, with permission, from (*9*, *64*)]

amyloid plaques and inclusions made of wild-type tau (69). Tau appears to be necessary for Aβ-induced toxicity, and the hyperexcitability of nerve cells caused by exposure to Aβ was reduced in the absence of tau (70).

The role of tau in neurodegeneration became clear with the identification of causative mutations in *MAPT* in FTDP-17T (Fig. 2B) (4–6). Filamentous tau inclusions are present, in the absence of Aβ deposits. Mutations fall into two largely nonoverlapping groups: those that influence the alternative splicing of tau pre-mRNA and those whose primary effect is at the protein level (1). Most missense mutations reduce the ability of tau to interact with microtubules. Some mutations also promote tau assembly into filaments. Intronic mutations and some coding region mutations lead to the relative overproduction of four-repeat tau.

In populations of European descent, *MAPT* is characterized by two haplotypes that result from a 900-kb inversion (*H1*) or noninversion (*H2*) polymorphism (71). Inheritance of the *H1* haplotype is a risk factor for PSP, CBD, PD, and MSA. The association between the *H1* haplotype and PSP had a higher odds-ratio than that between *APOEε4* and sporadic AD (72).

Several lines of investigation have shown that assembled tau can behave like a prion. In the human brain, neurofibrillary lesions appear to spread along neural pathways from one brain region to another (62, 73). During the process of sporadic AD, they first appear in locus coeruleus and entorhinal cortex, followed by hippocampal formation and large parts of the neocortex (Fig. 3). Tau inclusions follow the opposite direction to Aβ plaques, which form first in the neocortex. The symptoms of AD are present, when abundant tau inclusions and Aβ deposits are found in neocortex (74, 75). Tau deposition in entorhinal cortex and hippocampus is probably necessary, but not sufficient, for the development of AD (76). It remains to be determined whether Aβ plaques and tau inclusions form independently and when they become self-sustaining. It is also not clear whether one type of inclusion influences the spreading of the other. Interpretation is limited by the ability to visualize only a subset of aggregates. A pathological pathway leads from misfolded proteins to filaments, with a number of intermediates. The roles of the latter in the propagation of pathology and aggregate neurotoxicity need to be better understood. Positron emission tomography ligands can visualize Aβ and tau pathologies in living brains; if their spatial resolution can be improved, it will become possible to follow the sequential spreading of protein inclusions.

In AGD, tau inclusions are initially restricted to the ambient gyrus, from where the pathological process extends to the anterior and posterior temporal lobe, followed by septum, insular cortex, and anterior cingulate cortex (77). In CTE, tau inclusions form first in the depths of some cortical sulci, close to the perivascular spaces. They are later found throughout cerebral cortex, diencephalon, basal ganglia, brainstem, and spinal cord (78).

Intracerebral injection of human mutant tau inclusions into the brains of mice transgenic for wild-type human tau induced the formation of inclusions that spread to distant brain regions (79). Similar results were obtained when presymptomatic mice transgenic for human mutant tau were injected (80). Tauopathy was also observed in wild-type mice after seeding with human brain aggregates, although there was a lower density of aggregates than after seeding in transgenic human tau mice (81). A substantial species barrier was not present because human mutant tau seeds were reported to induce aggregation of wild-type murine tau (82, 83). Intraperitoneal injections of tau inclusions into presymptomatic transgenic mice promoted the formation of tau inclusions in brain, albeit less efficiently than after intracerebral injection (84).

Distinct conformers of assembled tau exist, reminiscent of prion strains (81, 85–87). This may explain the variety of human tauopathies. It is also supported by the presence of distinct tau filament morphologies in cases of FTDP-17T with different *MAPT* mutations (Fig. 4) (88). Network connectivity studies using functional magnetic resonance imaging have provided evidence that different tauopathies may be caused by distinct molecular conformers of assembled tau, akin to prion strains (89). This may explain the selective neuronal vulnerability characteristic of individual tauopathies, with different disease processes beginning in different brain cells, from where they spread to connected regions. Host factors may also play an important role (90).

Studies in cultured cells have shown the intercellular transfer of tau assemblies and the adoption of alternative conformations that became self-propagating (91, 92). Tau seeds were taken up and induced tau assembly in the cytoplasm. Monomeric tau was ineffective, and expressed tau could only be seeded if it was capable of aggregation (86). Internalization required the presence of sulphated glycosaminoglycans at the cell surface. Distinct seeded assemblies made of four tau repeats formed in human embryonic kidney (HEK) 293 cells (85); they could be distinguished upon injection into the brain of presymptomatic transgenic mice, from where they could be passaged. When HEK293 cells expressing four tau repeats were seeded, inclusions formed that were identical to those initially present.

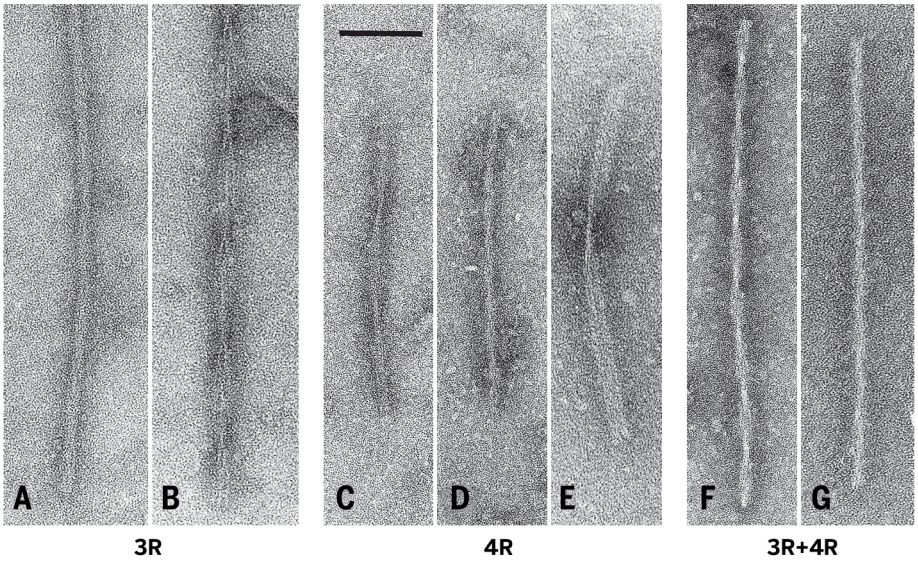

Fig. 4. Morphologies of tau filaments from cases of frontotemporal dementia and parkinsonism linked to chromosome 17 caused by *MAPT* mutations (FTDP-17T). (**A** and **B**) Neuronal tau filaments from a tauopathy with abundant Pick body–like inclusions and a G389R mutation in *MAPT*. (A) Straight filaments form the majority species, and (B) strongly stranded twisted filaments are in the minority. The filaments in (A) and (B) are made of three-repeat (3R) tau. (**C** to **E**) Tau filaments from a case with neuronal and glial tau inclusions and a P301L mutation in *MAPT*. (C) Narrow twisted ribbons and (D) occasional rope-like filaments are present. (E) Familial multiple system tauopathy with presenile dementia and other cases caused by *MAPT* mutations in the intron after E10 are characterized by wide twisted ribbons and neuronal and glial tau inclusions. The filaments in (C) to (E) are made of four-repeat (4R) tau. (**F** and **G**) Tau filaments from a case with a V337M mutation in *MAPT*. (F) Paired helical and (G) straight filaments are present as in AD. The tau pathology is largely neuronal. The filaments in (F) and (G) are made of 3R and 4R tau. Scale bar, 100 nm. [Adapted, with permission, from (88)]

α-Synuclein

This is an abundant 140–amino acid protein that is highly enriched in presynaptic nerve terminals (93). α-Synuclein binds to lipids through its amino-terminal part, when it multimerizes and becomes α-helical. It can also self-assemble through this region, which forms the core of the β-sheet–rich disease filaments. In nerve

terminals, α-synuclein binds to the external surface of synaptic vesicles, where it is thought to play a role in neurotransmission. The membrane-bound form of α-synuclein is present in equilibrium with a cytosolic form. In nerve cells, membrane binding inhibits α-synuclein aggregation (*94*).

Like Aβ and tau, α-synuclein assembles into a β-sheet–rich conformation that is able to seed aggregation of soluble α-synuclein in transfected cells (*92*, *95*). Neuropathological studies have shown that Lewy pathology spreads along neural pathways in the brain, beginning in the dorsal motor nucleus of the glossopharyngeal and vagal nerves, the olfactory bulb, and the anterior olfactory nucleus (Fig. 3) (*96*, *97*). Lewy inclusions are also found in spinal cord, autonomic ganglia, and the enteric nervous system (*2*). It is not clear whether this is indicative of brain-to-gut or gut-to-brain spreading. The latter would be analogous to vCJD. In support of gut-to-brain spreading, vagotomy has been associated with a reduced risk of PD (*98*).

In the 1970s and 1980s, some patients with idiopathic PD received intrastriatal grafts of human foetal dopaminergic neurons. After 10 to 22 years, a proportion of the grafted neurons contained Lewy pathology (*99*, *100*). It is not known how these young neurons, from donors genetically unrelated to their hosts, acquired Lewy pathology. One possibility is that aggregated α-synuclein transferred from the host brain to the grafted cells, where it seeded the aggregation of soluble α-synuclein. It has been suggested that α-synuclein prions from the host PD brain passed into the grafted cells, where they templated the conversion of soluble α-synuclein (*101*). This is reminiscent of infectious cases of human prion diseases.

In transgenic mice, human α-synuclein can transit to nerve cells grafted into the striatum (*102*). Moreover, the acceleration of α-synuclein aggregation has been described in the brains of presymptomatic transgenic mice, in conjunction with an earlier onset of neurological symptoms, after the intracerebral inoculation of brain tissue from symptomatic mice (*103*). Unlike induced Aβ and tau assemblies, the formation of α-synuclein inclusions was accompanied by neurodegeneration. Evidence for assembled α-synuclein behaving like a prion has come from the injection of MSA brain extracts into heterozygous mice transgenic for A53T human α-synuclein, which express the human mutant protein predominantly in nerve cells (*104*). Intracerebral injection led to the death of the mice and the development of abundant α-synuclein inclusions. Noninjected mice did not develop inclusions or disease. Unlike in MSA, in which they are mainly found in glial cells, inclusions were present in nerve cells. After injection into the hind limb muscle of transgenic mice, recombinant α-synuclein assemblies also induced cerebral α-synuclein aggregation and disease symptoms (*105*). Transection of the sciatic nerve mitigated these effects. Spreading of α-synuclein aggregates from the periphery to the brain has been demonstrated in wild-type rats (*106*, *107*). However, it remains to be shown that these aggregates can seed aggregation of endogenous α-synuclein.

Intrastriatal injection of mouse recombinant α-synuclein assemblies into wild-type mice gave rise to α-synuclein inclusions and some brain dysfunction (*108*). The same fibrils induced the formation of α-synuclein inclusions in primary cortical neurons from wild-type mice. Intranigral injection of α-synuclein assemblies from the brains of DLB patients into wild-type mice resulted in the formation of inclusions of mouse α-synuclein (*109*).

Morphological differences between disease-associated α-synuclein filaments have been described (*17*). Polymorphs of recombinant aggregated α-synuclein in the form of ribbons or fibrils have been reported (*107*, *110*). When injected into the rat substantia nigra, ribbons gave rise to Lewy pathology, whereas fibrils, which did not seed Lewy pathology, led to a loss of dopaminergic neurons. It remains to be seen whether ribbons and fibrils of α-synuclein have their counterparts in human diseases. In separate work (*111*), some α-synuclein filaments seeded both tau and α-synuclein aggregation, whereas others seeded only α-synuclein aggregation. These conformers of aggregated α-synuclein exhibited different properties after proteinase K digestion. They were like prion strains in that they exhibited structural variations, differences in seeding properties, and heritability of phenotypic traits.

Genetics of AD

Mapping of *APP* to chromosome 21—together with the presence of abundant plaques and neurofibrillary lesions in most elderly individuals with Down's syndrome caused by three, rather than the usual two, copies of chromosome 21—suggested an important role for Aβ in AD. In 1991, the first mutation in *APP* that causes AD was identified (*3*). Mutations in *APP* are located near the β- and γ-secretase cleavage sites, as well as within Aβ (Fig. 2C) (*112*). Mutations near the β-secretase cleavage site increase production of Aβ, whereas those near the γ-secretase cleavage site result in an increased ratio of Aβ42 to Aβ40. Mutations within Aβ increase rates of aggregation, suggesting that familial AD is initiated by the aggregation of Aβ. Dominantly inherited duplications of the *APP* locus also give rise to AD.

Mutations in *PS1* and *PS2* are the most common cause of inherited AD (*113*, *114*). Mutations in the genes encoding other γ-secretase components have not been associated with AD. Like the *APP* mutations near the γ-secretase cleavage site, *PS* mutations increase the ratio of Aβ42 to Aβ40, resulting in a gain-of-toxic function. Haploinsufficiency of the γ-secretase complex gives rise to acne inversa, not AD (*115*). No disease-causing mutations have been identified in *BACE1*. However, the A673T variant of APP, which is located near the BACE1 cleavage site (position 2 of Aβ), is overrepresented in Icelandic controls when compared with AD (*116*). The A673T mutation interferes with the BACE1 cleavage of APP and causes a reduction in Aβ40 and Aβ42. Reducing BACE1 cleavage may thus protect against late-onset AD. However, APP with the A673T mutation also appeared to protect against cognitive decline that was not caused by AD.

Inheritance of the *ε4* allele of apolipoprotein E (*APOE*) is the major risk factor for late-onset AD. It increases disease risk in a dose-dependent manner and lowers the age of onset, as first shown in 1993 (*117*). APOE comprises 299 amino acids and exists as three isoforms based on the presence of C or R at positions 112 and 158: APOE2 (C/C), APOE3 (C/R), and APOE4 (R/R) (*118*). One copy of APOE4 increases the risk of AD by about four-fold (compared with the more common *APOEε3*/*APOE3ε3* genotype), whereas two copies of APOE4 increase the risk of AD by about 12-fold. The mechanism by which the amino acid difference between APOE3 and APOE4 at position 112 (C or R) increases the risk of AD remains to be established.

Only ~40% of individuals with AD carry an *APOEε4* allele, suggesting the existence of additional genetic risk factors. Genome-wide association studies (GWASs) have identified about 20 additional risk factors (*119*, *120*). The effects of these common alleles are smaller than those of *APOE*. However, they make it possible to identify biological pathways involved in the pathogenesis of AD. Several loci play a role in the immune system, whereas others are involved in endocytosis and lipid biology.

There are also rarer risk alleles with large effects. Heterozygous missense mutations in the gene encoding triggering receptor expressed on myeloid 2 cells (*TREM2*) increase the risk of AD by about threefold (*121*, *122*). *APP* and *PSEN* have so far not been identified in GWASs. This may be because Aβ clearance is impaired in sporadic AD (*123*), whereas Aβ species are overproduced in dominantly inherited AD (*124*).

Genetics of PD

Dominantly inherited forms of PD and DLB are caused by missense mutations in *SNCA* (*7*) or multiplications (duplications and triplications) of the gene (Fig. 2D) (*125*). Six missense mutations have been described in the amino-terminal region of α-synuclein. Penetrance in duplication cases was of the order of 40%, whereas it was close to 100% for triplications and missense mutations. Lewy pathology was present. Mutations causing MSA have not been identified, although the neuropathologies associated with some mutations in *SNCA* had features of MSA (*126*, *127*). Lewy body diseases and MSA are probably linked.

Heterozygous mutations in the gene encoding leucine-rich repeat kinase 2 (*LRRK2*) give rise to dominantly inherited PD (*128*, *129*). LRRK2 is a protein of 2527 amino acids with two enzymatic activities (guanosine triphosphatase and protein kinase) and multiple protein-protein interaction domains. Disease penetrance is incomplete. In most patients, *LRRK2* mutations are associated with the deposition of α-synuclein. LRRK2 is expressed at high levels in monocytes, suggesting a role in the innate immune system (*130*).

PD is a motor syndrome with levodopa-responsive parkinsonism, in conjunction with

α-synuclein–positive Lewy pathology and dopaminergic nerve cell loss in the substantia nigra (*2*). Because parkinsonism can be present in the absence of Lewy pathology, multiple mechanisms may cause the degeneration of dopaminergic neurons of the substantia nigra. They can be associated with tau inclusions, as in FTDP-17T and postencephalitic parkinsonism, or polyglutamine inclusions, as in some spinocerebellar ataxias. A separate pathway involves primary mitochondrial dysfunction and defective mitophagy, as in juvenile-onset recessive parkinsonism caused by loss-of-function mutations in *PARKIN*, *PINK1*, and *DJ1*.

Loss-of-function mutations in the gene encoding glucocerebrosidase (*GBA*) cause Gaucher's disease and are characterized by the lysosomal accumulation of glycosylceramide. Gaucher's disease appears to predispose to PD (*131*). Heterozygous *GBA* mutation carriers without Gaucher's disease have an increased risk of developing PD, and patients with PD are five times more likely to carry a *GBA* mutation than age-matched controls. *GBA* mutations enhance, but do not initiate, the aggregation of α-synuclein. They do not appear to predispose to MSA.

GWASs have shown that variability in *SNCA*, *LRRK2*, *GAK* (cyclin G-associated kinase), and *MAPT* are risk factors for sporadic PD (*132*, *133*). Variants in *SNCA* probably increase expression. They are also a risk factor for MSA, as is variability in *MAPT*. The latter suggests an interaction between tau and α-synuclein that is probably independent of tau assembly.

Conclusion

Transcellular propagation of protein pathogens, reminiscent of the spread of viruses, represents an unprecedented concept of disease. It is now known to extend beyond CJD, to include AD and PD, which are the most common neurodegenerative diseases. For all three diseases, there is a long prodromal phase, during which neurodegenerative changes develop and eventually lead to brain dysfunction. The interval between the formation of the first protein inclusions and the appearance of disease symptoms may offer a therapeutic window, provided sufficiently sensitive diagnostic techniques can be developed. Other protein pathogens, such as aggregates of TDP-43 and mutant superoxide dismutase 1, exhibit similar properties (*134*–*136*).

Progress in deciphering the molecular pathogenesis of AD and PD is offering new approaches for the development of effective therapies. At present, there is no drug that prevents or halts a neurodegenerative disease. Understanding the events that lead to the formation of inclusions may provide insights into where they begin to behave like prions and their routes of transneuronal spread. The role of glial cells in the spreading of pathology also remains to be established. Moreover, the initial events are likely to determine the particular strains that are produced. This may be critical for developing therapies because drug-resistant prions have been described (*137*). Individuals with disease-causing mutations in *APP*, *MAPT*, or *SNCA* will be candidates for prophylactic treatment. Hopefully, neuroimaging techniques able to detect small numbers of inclusions will be developed in order to diagnose and evaluate patients long before the appearance of clinical signs. On the basis of the progress described here, the prevention of neurodegenerative diseases using presymptomatic therapies may become a reality in the not too distant future.

REFERENCES AND NOTES

1. M. Goedert, M. G. Spillantini, A century of Alzheimer's disease. *Science* **314**, 777–781 (2006). doi: 10.1126/science.1132814; pmid: 17082447
2. M. Goedert, M. G. Spillantini, K. Del Tredici, H. Braak, 100 years of Lewy pathology. *Nat. Rev. Neurol.* **9**, 13–24 (2013). doi: 10.1038/nrneurol.2012.242; pmid: 23183883
3. A. Goate *et al*., Segregation of a missense mutation in the amyloid precursor protein gene with familial Alzheimer's disease, *Nature* **349**, 704–706 (1991).
4. P. Poorkaj *et al*., Tau is a candidate gene for chromosome 17 frontotemporal dementia. *Ann. Neurol.* **43**, 815–825 (1998). doi: 10.1002/ana.410430617; pmid: 9629852
5. M. Hutton *et al*., Association of missense and 5′-splice-site mutations in *tau* with the inherited dementia FTDP-17. *Nature* **393**, 702–705 (1998). doi: 10.1038/31508; pmid: 9641683
6. M. G. Spillantini *et al*., Mutation in the tau gene in familial multiple system tauopathy with presenile dementia. *Proc. Natl. Acad. Sci. U.S.A.* **95**, 7737–7741 (1998). doi: 10.1073/pnas.95.13.7737; pmid: 9636220
7. M. H. Polymeropoulos *et al*., Mutation in the alpha-synuclein gene identified in families with Parkinson's disease. *Science* **276**, 2045–2047 (1997). doi: 10.1126/science.276.5321.2045; pmid: 9197268
8. M. Jucker, L. C. Walker, Self-propagation of pathogenic protein aggregates in neurodegenerative diseases. *Nature* **501**, 45–51 (2013). doi: 10.1038/nature12481; pmid: 24005412
9. M. Goedert, B. Falcon, F. Clavaguera, M. Tolnay, Prion-like mechanisms in the pathogenesis of tauopathies and synucleinopathies. *Curr. Neurol. Neurosci. Rep.* **14**, 495 (2014). doi: 10.1007/s11910-014-0495-z; pmid: 25218483
10. D. Eisenberg, M. Jucker, The amyloid state of proteins in human diseases. *Cell* **148**, 1188–1203 (2012). doi: 10.1016/j.cell.2012.02.022; pmid: 22424229
11. R. Nelson *et al*., Structure of the cross-β spine of amyloid-like fibrils. *Nature* **435**, 773–778 (2005). doi: 10.1038/nature03680; pmid: 15944695
12. M. R. Sawaya *et al*., Atomic structures of amyloid cross-β spines reveal varied steric zippers. *Nature* **447**, 453–457 (2007). doi: 10.1038/nature05695; pmid: 17468747
13. A. Laganowsky *et al*., Atomic view of a toxic amyloid small oligomer. *Science* **335**, 1228–1231 (2012). doi: 10.1126/science.1213151; pmid: 22403391
14. A. T. Petkova *et al*., Self-propagating, molecular-level polymorphism in Alzheimer's β-amyloid fibrils. *Science* **307**, 262–265 (2005). doi: 10.1126/science.1105850; pmid: 15653506
15. P. Jenner *et al*., Parkinson's disease—The debate on the clinical phenomenology, aetiology, pathology and pathogenesis. *J. Parkinson's Dis.* **3**, 1 (2013).
16. K. Wakabayashi, M. Yoshimoto, S. Tsuji, H. Takahashi, Alpha-synuclein immunoreactivity in glial cytoplasmic inclusions in multiple system atrophy. *Neurosci. Lett.* **249**, 180–182 (1998). doi: 10.1016/S0304-3940(98)00407-8; pmid: 9682846
17. M. G. Spillantini *et al*., Filamentous α-synuclein inclusions link multiple system atrophy with Parkinson's disease and dementia with Lewy bodies. *Neurosci. Lett.* **251**, 205–208 (1998). doi: 10.1016/S0304-3940(98)00504-7; pmid: 9726379
18. P. H. Tu *et al*., Glial cytoplasmic inclusions in white matter oligodendrocytes of multiple system atrophy brains contain insoluble α-synuclein. *Ann. Neurol.* **44**, 415–422 (1998). doi: 10.1002/ana.410440324; pmid: 9749615
19. M. I. Papp, J. E. Kahn, P. L. Lantos, Glial cytoplasmic inclusions in the CNS of patients with multiple system atrophy (striatonigral degeneration, olivopontocerebellar atrophy and Shy-Drager syndrome). *J. Neurol. Sci.* **94**, 79–100 (1989). doi: 10.1016/0022-510X(89)90219-0; pmid: 2559165
20. A. Fanciulli, G. K. Wenning, Multiple-system atrophy. *N. Engl. J. Med.* **372**, 249–263 (2015). doi: 10.1056/NEJMra1311488; pmid: 25587949
21. K. Nakamura *et al*., Filamentous aggregations of phosphorylated α-synuclein in Schwann cells (Schwann cell cytoplasmic inclusions) in multiple system atrophy. *Acta Neuropathol. Commun.* **3**, 29 (2015). doi: 10.1186/s40478-015-0208-0; pmid: 25990096
22. T. Alper, D. A. Haig, M. C. Clarke, The exceptionally small size of the scrapie agent. *Biochem. Biophys. Res. Commun.* **22**, 278–284 (1966). doi: 10.1016/0006-291X(66)90478-5; pmid: 4957205
23. T. Alper, W. A. Cramp, D. A. Haig, M. C. Clarke, Does the agent of scrapie replicate without nucleic acid? *Nature* **214**, 764–766 (1967). doi: 10.1038/214764a0; pmid: 4963878
24. D. C. Bolton, M. P. McKinley, S. B. Prusiner, Identification of a protein that purifies with the scrapie prion. *Science* **218**, 1309–1311 (1982). doi: 10.1126/science.6815801; pmid: 6815801
25. S. B. Prusiner, Novel proteinaceous infectious particles cause scrapie. *Science* **216**, 136–144 (1982). doi: 10.1126/science.6801762; pmid: 6801762
26. M. S. Palmer, A. J. Dryden, J. T. Hughes, J. Collinge, Homozygous prion protein genotype predisposes to sporadic Creutzfeldt-Jakob disease. *Nature* **352**, 340–342 (1991). doi: 10.1038/352340a0; pmid: 1677164
27. D. Kaski *et al*., Variant CJD in an individual heterozygous for PRNP codon 129. *Lancet* **374**, 2128 (2009). doi: 10.1016/S0140-6736(09)61568-3; pmid: 20109837
28. F. Owen *et al*., Insertion in prion protein gene in familial Creutzfeldt-Jakob disease. *Lancet* **333**, 51–52 (1989). doi: 10.1016/S0140-6736(89)91713-3; pmid: 2563037
29. K. Hsiao *et al*., Linkage of a prion protein missense variant to Gerstmann-Sträussler syndrome. *Nature* **338**, 342–345 (1989). doi: 10.1038/338342a0; pmid: 2564168
30. S. B. Prusiner, Prions. *Proc. Natl. Acad. Sci. U.S.A.* **95**, 13363–13383 (1998). doi: 10.1073/pnas.95.23.13363; pmid: 9811807
31. W. Q. Zou *et al*., Variably protease-sensitive prionopathy: A new sporadic disease of the prion protein. *Ann. Neurol.* **68**, 162–172 (2010). pmid: 20695009
32. H. Fraser, Neuronal spread of scrapie agent and targeting of lesions within the retino-tectal pathway. *Nature* **295**, 149–150 (1982). doi: 10.1038/295149a0; pmid: 6173756
33. R. A. Bessen, R. F. Marsh, Biochemical and physical properties of the prion protein from two strains of the transmissible mink encephalopathy agent. *J. Virol.* **66**, 2096–2101 (1992). pmid: 1347795
34. M. Tanaka, S. R. Collins, B. H. Toyama, J. S. Weissman, The physical basis of how prion conformations determine strain phenotypes. *Nature* **442**, 585–589 (2006). doi: 10.1038/nature04922; pmid: 16810177
35. D. Vilchez, I. Saez, A. Dillin, The role of protein clearance mechanisms in organismal ageing and age-related diseases. *Nat. Commun.* **5**, 5659 (2014). doi: 10.1038/ncomms6659; pmid: 25482515
36. S. Mead *et al*., A novel protective prion protein variant that colocalizes with kuru exposure. *N. Engl. J. Med.* **361**, 2056–2065 (2009). doi: 10.1056/NEJMoa0809716; pmid: 19923577
37. E. A. Asante *et al*., A naturally occurring variant of the human prion protein completely prevents prion disease. *Nature* **522**, 478–481 (2015). doi: 10.1038/nature14510; pmid: 26061765
38. S. B. Prusiner *et al*., Scrapie prions aggregate to form amyloid-like birefringent rods. *Cell* **35**, 349–358 (1983). doi: 10.1016/0092-8674(83)90168-X; pmid: 6418385
39. S. B. Prusiner, S. P. Cochran, M. P. Alpers, Transmission of scrapie in hamsters. *J. Infect. Dis.* **152**, 971–978 (1985). doi: 10.1093/infdis/152.5.971; pmid: 3930630
40. G. A. H. Wells *et al*., Bovine spongiform encephalopathy: The effect of oral exposure dose on attack rate and incubation period in cattle. *J. Gen. Virol.* **88**, 1363–1373 (2007). doi: 10.1099/vir.0.82421-0; pmid: 17374783
41. E. Zobeley, E. Flechsig, A. Cozzio, M. Enari, C. Weissmann, Infectivity of scrapie prions bound to a stainless steel surface. *Mol. Med.* **5**, 240–243 (1999). pmid: 10448646
42. Y. S. Eisele *et al*., Induction of cerebral beta-amyloidosis: Intracerebral versus systemic Aβ inoculation. *Proc. Natl. Acad. Sci. U.S.A.* **106**, 12926–12931 (2009). doi: 10.1073/pnas.0903200106; pmid: 19622727
43. S. K. Fritschi *et al*., Aβ seeds resist inactivation by formaldehyde. *Acta Neuropathol.* **128**, 477–484 (2014). doi: 10.1007/s00401-014-1339-2; pmid: 25193240
44. M. Schweighauser *et al*., Formaldehyde-fixed brain tissue from spontaneously ill α-synuclein transgenic mice induces fatal α-synucleinopathy in transgenic hosts. *Acta Neuropathol.* **129**, 157–159 (2015). doi: 10.1007/s00401-014-1360-5; pmid: 25367384
45. R. S. Hegde *et al*., Transmissible and genetic prion diseases share a common pathway of neurodegeneration. *Nature* **402**, 822–826 (1999). doi: 10.1038/45574; pmid: 10617204

46. A. F. Hill *et al*., Species-barrier-independent prion replication in apparently resistant species. *Proc. Natl. Acad. Sci. U.S.A.* **97**, 10248–10253 (2000). doi: 10.1073/pnas.97.18.10248; pmid: 10963685
47. M. K. Sandberg *et al*., Prion neuropathology follows the accumulation of alternate prion protein isoforms after infective titre has peaked. *Nat. Commun.* **5**, 4347 (2014). doi: 10.1038/ncomms5347; pmid: 25005024
48. J. A. Moreno *et al*., Oral treatment targeting the unfolded protein response prevents neurodegeneration and clinical disease in prion-infected mice. *Sci. Transl. Med.* **5**, 206ra138 (2013). doi: 10.1126/scitranslmed.3006767; pmid: 24107777
49. J. Kang *et al*., The precursor of Alzheimer's disease amyloid A4 protein resembles a cell-surface receptor. *Nature* **325**, 733–736 (1987). doi: 10.1038/325733a0; pmid: 2881207
50. C. L. Masters, D. J. Selkoe, Biochemistry of amyloid β-protein and amyloid deposits in Alzheimer disease. *Cold Spring Harb. Perspect. Med.* **2**, a006262 (2012). doi: 10.1101/cshperspect.a006262; pmid: 22675658
51. P. Lu *et al*., Three-dimensional structure of human γ-secretase. *Nature* **512**, 166–170 (2014). doi: 10.1038/nature13567; pmid: 25043039
52. T. Xie *et al*., Crystal structure of the γ-secretase component nicastrin. *Proc. Natl. Acad. Sci. U.S.A.* **111**, 13349–13354 (2014). doi: 10.1073/pnas.1414837111; pmid: 25197054
53. H. Acx *et al*., Signature amyloid β profiles are produced by different γ-secretase complexes. *J. Biol. Chem.* **289**, 4346–4355 (2014). doi: 10.1074/jbc.M113.530907; pmid: 24338474
54. D. C. Gajdusek, C. J. Gibbs, M. Alpers, Experimental transmission of a Kuru-like syndrome to chimpanzees. *Nature* **209**, 794–796 (1966). doi: 10.1038/209794a0; pmid: 5922150
55. J. Goudsmit *et al*., Evidence for and against the transmissibility of Alzheimer disease. *Neurology* **30**, 945–950 (1980). doi: 10.1212/WNL.30.9.945; pmid: 6775247
56. H. F. Baker, R. M. Ridley, L. W. Duchen, T. J. Crow, C. J. Bruton, Evidence for the experimental transmission of cerebral β-amyloidosis to primates. *Int. J. Exp. Pathol.* **74**, 441–454 (1993). pmid: 8217779
57. M. D. Kane *et al*., Evidence for seeding of β-amyloid by intracerebral infusion of Alzheimer brain extracts in β-amyloid precursor protein-transgenic mice. *J. Neurosci.* **20**, 3606–3611 (2000). pmid: 10804202
58. M. Meyer-Luehmann *et al*., Exogenous induction of cerebral β-amyloidogenesis is governed by agent and host. *Science* **313**, 1781–1784 (2006). doi: 10.1126/science.1131864; pmid: 16990547
59. Y. S. Eisele *et al*., Peripherally applied Abeta-containing inoculates induce cerebral β-amyloidosis. *Science* **330**, 980–982 (2010). doi: 10.1126/science.1194516; pmid: 20966215
60. J. Stöhr *et al*., Purified and synthetic Alzheimer's amyloid β (Aβ) prions. *Proc. Natl. Acad. Sci. U.S.A.* **109**, 11025–11030 (2012). doi: 10.1073/pnas.1206555109; pmid: 22711819
61. R. Morales, C. Duran-Aniotz, J. Castilla, L. D. Estrada, C. Soto, De novo induction of amyloid-β deposition in vivo. *Mol. Psychiatry* **17**, 1347–1353 (2012). doi: 10.1038/mp.2011.120; pmid: 21968933
62. H. Braak, E. Braak, Neuropathological stageing of Alzheimer-related changes. *Acta Neuropathol.* **82**, 239–259 (1991). doi: 10.1007/BF00308809; pmid: 1759558
63. D. R. Thal, U. Rüb, M. Orantes, H. Braak, Phases of A β-deposition in the human brain and its relevance for the development of AD. *Neurology* **58**, 1791–1800 (2002). doi: 10.1212/WNL.58.12.1791; pmid: 12084879
64. H. Braak, K. Del Tredici, Neuroanatomy and pathology of sporadic Alzheimer's disease. *Adv. Anat. Embryol. Cell Biol.* **215**, 1–162 (2015). doi: 10.1007/978-3-319-12679-1_1; pmid: 25920101
65. J. Stöhr *et al*., Distinct synthetic Aβ prion strains producing different amyloid deposits in bigenic mice. *Proc. Natl. Acad. Sci. U.S.A.* **111**, 10329–10334 (2014). doi: 10.1073/pnas.1408968111; pmid: 24982137
66. J. C. Watts *et al*., Serial propagation of distinct strains of Aβ prions from Alzheimer's disease patients. *Proc. Natl. Acad. Sci. U.S.A.* **111**, 10323–10328 (2014). doi: 10.1073/pnas.1408900111; pmid: 24982139
67. P. T. Nelson *et al*., Correlation of Alzheimer disease neuropathologic changes with cognitive status: A review of the literature. *J. Neuropathol. Exp. Neurol.* **71**, 362–381 (2012). doi: 10.1097/NEN.0b013e31825018f7; pmid: 22487856
68. J. Lewis *et al*., Enhanced neurofibrillary degeneration in transgenic mice expressing mutant tau and APP. *Science* **293**, 1487–1491 (2001). doi: 10.1126/science.1058189; pmid: 11520987
69. S. H. Choi *et al*., A three-dimensional human neural cell culture model of Alzheimer's disease. *Nature* **515**, 274–278 (2014). doi: 10.1038/nature13800; pmid: 25307057
70. E. D. Roberson *et al*., Reducing endogenous tau ameliorates amyloid β-induced deficits in an Alzheimer's disease mouse model. *Science* **316**, 750–754 (2007). doi: 10.1126/science.1141736; pmid: 17478722
71. H. Stefansson *et al*., A common inversion under selection in Europeans. *Nat. Genet.* **37**, 129–137 (2005). doi: 10.1038/ng1508; pmid: 15654335
72. G. U. Höglinger *et al*., Identification of common variants influencing risk of the tauopathy progressive supranuclear palsy. *Nat. Genet.* **43**, 699–705 (2011). doi: 10.1038/ng.859; pmid: 21685912
73. H. Braak, K. Del Tredici, The pathological process underlying Alzheimer's disease in individuals under thirty. *Acta Neuropathol.* **121**, 171–181 (2011). doi: 10.1007/s00401-010-0789-4; pmid: 21170538
74. C. R. Jack Jr. *et al*., Tracking pathophysiological processes in Alzheimer's disease: An updated hypothetical model of dynamic biomarkers. *Lancet Neurol.* **12**, 207–216 (2013). doi: 10.1016/S1474-4422(12)70291-0; pmid: 23332364
75. J. F. Crary *et al*., Primary age-related tauopathy (PART): A common pathology associated with human aging. *Acta Neuropathol.* **128**, 755–766 (2014). doi: 10.1007/s00401-014-1349-0; pmid: 25348064
76. C. Duyckaerts *et al*., PART is part of Alzheimer disease. *Acta Neuropathol.* **129**, 749–756 (2015). doi: 10.1007/s00401-015-1390-7; pmid: 25628035
77. Y. Saito *et al*., Staging of argyrophilic grains: An age-associated tauopathy. *J. Neuropathol. Exp. Neurol.* **63**, 911–918 (2004). pmid: 15453090
78. A. C. McKee *et al*., The spectrum of disease in chronic traumatic encephalopathy. *Brain* **136**, 43–64 (2013). doi: 10.1093/brain/aws307; pmid: 23208308
79. F. Clavaguera *et al*., Transmission and spreading of tauopathy in transgenic mouse brain. *Nat. Cell Biol.* **11**, 909–913 (2009). doi: 10.1038/ncb1901; pmid: 19503072
80. Z. Ahmed *et al*., A novel in vivo model of tau propagation with rapid and progressive neurofibrillary tangle pathology: The pattern of spread is determined by connectivity, not proximity. *Acta Neuropathol.* **127**, 667–683 (2014). doi: 10.1007/s00401-014-1254-6; pmid: 24531916
81. F. Clavaguera *et al*., Brain homogenates from human tauopathies induce tau inclusions in mouse brain. *Proc. Natl. Acad. Sci. U.S.A.* **110**, 9535–9540 (2013). doi: 10.1073/pnas.1301175110; pmid: 23690619
82. L. Liu *et al*., Trans-synaptic spread of tau pathology in vivo. *PLOS ONE* **7**, e31302 (2012). doi: 10.1371/journal.pone.0031302; pmid: 22312444
83. A. de Calignon *et al*., Propagation of tau pathology in a model of early Alzheimer's disease. *Neuron* **73**, 685–697 (2012). doi: 10.1016/j.neuron.2011.11.033; pmid: 22365544
84. F. Clavaguera *et al*., Peripheral administration of tau aggregates triggers intracerebral tauopathy in transgenic mice. *Acta Neuropathol.* **127**, 299–301 (2014). doi: 10.1007/s00401-013-1231-5; pmid: 24362441
85. D. W. Sanders *et al*., Distinct tau prion strains propagate in cells and mice and define different tauopathies. *Neuron* **82**, 1271–1288 (2014). doi: 10.1016/j.neuron.2014.04.047; pmid: 24857020
86. B. Falcon *et al*., Conformation determines the seeding potencies of native and recombinant Tau aggregates. *J. Biol. Chem.* **290**, 1049–1065 (2015). doi: 10.1074/jbc.M114.589309; pmid: 25406315
87. S. Boluda *et al*., Differential induction and spread of tau pathology in young PS19 tau transgenic mice following intracerebral injections of pathological tau from Alzheimer's disease or corticobasal degeneration brains. *Acta Neuropathol.* **129**, 221–237 (2015). doi: 10.1007/s00401-014-1373-0; pmid: 25534024
88. R. A. Crowther, M. Goedert, Abnormal tau-containing filaments in neurodegenerative diseases. *J. Struct. Biol.* **130**, 271–279 (2000). doi: 10.1006/jsbi.2000.4270; pmid: 10940231
89. J. Zhou, E. D. Gennatas, J. H. Kramer, B. L. Miller, W. W. Seeley, Predicting regional neurodegeneration from the healthy brain functional connectome. *Neuron* **73**, 1216–1227 (2012). doi: 10.1016/j.neuron.2012.03.004; pmid: 22445348
90. F. Roselli, P. Caroni, From intrinsic firing properties to selective neuronal vulnerability in neurodegenerative diseases. *Neuron* **85**, 901–910 (2015). doi: 10.1016/j.neuron.2014.12.063; pmid: 25741719
91. B. Frost, R. L. Jacks, M. I. Diamond, Propagation of tau misfolding from the outside to the inside of a cell. *J. Biol. Chem.* **284**, 12845–12852 (2009). doi: 10.1074/jbc.M808759200; pmid: 19282288
92. T. Nonaka, S. T. Watanabe, T. Iwatsubo, M. Hasegawa, Seeded aggregation and toxicity of α-synuclein and tau: Cellular models of neurodegenerative diseases. *J. Biol. Chem.* **285**, 34885–34898 (2010). doi: 10.1074/jbc.M110.148460; pmid: 20805224
93. J. T. Bendor, T. P. Logan, R. H. Edwards, The function of α-synuclein. *Neuron* **79**, 1044–1066 (2013). doi: 10.1016/j.neuron.2013.09.004; pmid: 24050397
94. J. Burré, M. Sharma, T. C. Südhof, Definition of a molecular pathway mediating α-synuclein neurotoxicity. *J. Neurosci.* **35**, 5221–5232 (2015). doi: 10.1523/JNEUROSCI.4650-14.2015; pmid: 25834048
95. K. C. Luk *et al*., Exogenous α-synuclein fibrils seed the formation of Lewy body-like intracellular inclusions in cultured cells. *Proc. Natl. Acad. Sci. U.S.A.* **106**, 20051–20056 (2009). doi: 10.1073/pnas.0908005106; pmid: 19892735
96. H. Braak *et al*., Staging of brain pathology related to sporadic Parkinson's disease. *Neurobiol. Aging* **24**, 197–211 (2003). doi: 10.1016/S0197-4580(02)00065-9; pmid: 12498954
97. H. Braak, K. Del Tredici, Neuroanatomy and pathology of sporadic Parkinson's disease. *Adv. Anat. Embryol. Cell Biol.* **201**, 1–119 (2009). pmid: 19230552
98. E. Svensson *et al*., Vagotomy and subsequent risk of Parkinson's disease. *Ann. Neurol.* 10.1002/ana24448 (2015). doi: 10.1002/ana24448
99. J. Y. Li *et al*., Lewy bodies in grafted neurons in subjects with Parkinson's disease suggest host-to-graft disease propagation. *Nat. Med.* **14**, 501–503 (2008). doi: 10.1038/nm1746; pmid: 18391963
100. J. H. Kordower, Y. Chu, R. A. Hauser, T. B. Freeman, C. W. Olanow, Lewy body-like pathology in long-term embryonic nigral transplants in Parkinson's disease. *Nat. Med.* **14**, 504–506 (2008). doi: 10.1038/nm1747; pmid: 18391962
101. C. W. Olanow, S. B. Prusiner, Is Parkinson's disease a prion disorder? *Proc. Natl. Acad. Sci. U.S.A.* **106**, 12571–12572 (2009). doi: 10.1073/pnas.0906759106 pmid: 19666621
102. P. Desplats *et al*., Inclusion formation and neuronal cell death through neuron-to-neuron transmission of α-synuclein. *Proc. Natl. Acad. Sci. U.S.A.* **106**, 13010–13015 (2009). doi: 10.1073/pnas.0903691106; pmid: 19651612
103. A. L. Mougenot *et al*., Prion-like acceleration of a synucleinopathy in a transgenic mouse model. *Neurobiol. Aging* **33**, 2225–2228 (2012). doi: 10.1016/j.neurobiolaging.2011.06.022; pmid: 21813214
104. J. C. Watts *et al*., Transmission of multiple system atrophy prions to transgenic mice. *Proc. Natl. Acad. Sci. U.S.A.* **110**, 19555–19560 (2013). doi: 10.1073/pnas.1318268110; pmid: 24218576
105. A. N. Sacino *et al*., Intramuscular injection of α-synuclein induces CNS α-synuclein pathology and a rapid-onset motor phenotype in transgenic mice. *Proc. Natl. Acad. Sci. U.S.A.* **111**, 10732–10737 (2014). doi: 10.1073/pnas.1321785111; pmid: 25002524
106. S. Holmqvist *et al*., Direct evidence of Parkinson pathology spread from the gastrointestinal tract to the brain in rats. *Acta Neuropathol.* **128**, 805–820 (2014). doi: 10.1007/s00401-014-1343-6; pmid: 25296989
107. W. Peelaerts *et al*., α-Synuclein strains cause distinct synucleinopathies after local and systemic administration. *Nature* **522**, 340–344 (2015). doi: 10.1038/nature14547; pmid: 26061766
108. K. C. Luk *et al*., Pathological α-synuclein transmission initiates Parkinson-like neurodegeneration in nontransgenic mice. *Science* **338**, 949–953 (2012). doi: 10.1126/science.1227157; pmid: 23161999
109. M. Masuda-Suzukake *et al*., Prion-like spreading of pathological α-synuclein in brain. *Brain* **136**, 1128–1138 (2013). doi: 10.1093/brain/awt037; pmid: 23466394
110. L. Bousset *et al*., Structural and functional characterization of two α-synuclein strains. *Nat. Commun.* **4**, 2575 (2013). doi: 10.1038/ncomms3575; pmid: 24108358
111. J. L. Guo *et al*., Distinct α-synuclein strains differentially promote tau inclusions in neurons. *Cell* **154**, 103–117 (2013). doi: 10.1016/j.cell.2013.05.057; pmid: 23827677
112. I. Benilova, E. Karran, B. De Strooper, The toxic Aβ oligomer and Alzheimer's disease: An emperor in need of clothes. *Nat. Neurosci.* **15**, 349–357 (2012). doi: 10.1038/nn.3028; pmid: 22286176
113. R. Sherrington *et al*., Cloning of a gene bearing missense mutations in early-onset familial Alzheimer's disease. *Nature* **375**, 754–760 (1995). doi: 10.1038/375754a0; pmid: 7596406

114. E. Levy-Lahad *et al*., Candidate gene for the chromosome 1 familial Alzheimer's disease locus. *Science* **269**, 973–977 (1995). doi: 10.1126/science.7638622; pmid: 7638622
115. B. Wang *et al*., γ-Secretase gene mutations in familial acne inversa. *Science* **330**, 1065 (2010). doi: 10.1126/science.1196284; pmid: 20929727
116. T. Jonsson *et al*., A mutation in APP protects against Alzheimer's disease and age-related cognitive decline. *Nature* **488**, 96–99 (2012). doi: 10.1038/nature11283; pmid: 22801501
117. E. H. Corder *et al*., Gene dose of apolipoprotein E type 4 allele and the risk of Alzheimer's disease in late onset families. *Science* **261**, 921–923 (1993). doi: 10.1126/science.8346443; pmid: 8346443
118. R. W. Mahley, Y. Huang, Apolipoprotein E sets the stage: Response to injury triggers neuropathology. *Neuron* **76**, 871–885 (2012). doi: 10.1016/j.neuron.2012.11.020; pmid: 23217737
119. D. Harold *et al*., Genome-wide association study identifies variants at CLU and PICALM associated with Alzheimer's disease. *Nat. Genet.* **41**, 1088–1093 (2009). doi: 10.1038/ng.440; pmid: 19734902
120. J. C. Lambert *et al*., Genome-wide association study identifies variants at CLU and CR1 associated with Alzheimer's disease. *Nat. Genet.* **41**, 1094–1099 (2009). doi: 10.1038/ng.439; pmid: 19734903
121. T. Jonsson *et al*., Variant of TREM2 associated with the risk of Alzheimer's disease. *N. Engl. J. Med.* **368**, 107–116 (2013). doi: 10.1056/NEJMoa1211103; pmid: 23150908
122. R. Guerreiro *et al*., TREM2 variants in Alzheimer's disease. *N. Engl. J. Med.* **368**, 117–127 (2013). doi: 10.1056/NEJMoa1211851; pmid: 23150934
123. K. G. Mawuenyega *et al*., Decreased clearance of CNS β-amyloid in Alzheimer's disease. *Science* **330**, 1774 (2010). doi: 10.1126/science.1197623; pmid: 21148344
124. R. Potter *et al*., Increased in vivo amyloid-β42 production, exchange, and loss in presenilin mutation carriers. *Sci. Transl. Med.* **5**, 189ra77 (2013). doi: 10.1126/scitranslmed.3005615; pmid: 23761040
125. A. B. Singleton *et al*., α-Synuclein locus triplication causes Parkinson's disease. *Science* **302**, 841 (2003). doi: 10.1126/science.1090278; pmid: 14593171
126. A. P. Kiely *et al*., α-Synucleinopathy associated with G51D SNCA mutation: A link between Parkinson's disease and multiple system atrophy? *Acta Neuropathol.* **125**, 753–769 (2013). doi: 10.1007/s00401-013-1096-7; pmid: 23404372
127. P. Pasanen *et al*., Novel α-synuclein mutation A53E associated with atypical multiple system atrophy and Parkinson's disease-type pathology. *Neurobiol. Aging* **35**, 2180.e1–2180.e5 (2014). doi: 10.1016/j.neurobiolaging.2014.03.024; pmid: 24746362
128. C. Paisán-Ruíz *et al*., Cloning of the gene containing mutations that cause PARK8-linked Parkinson's disease. *Neuron* **44**, 595–600 (2004). doi: 10.1016/j.neuron.2004.10.023; pmid: 15541308
129. A. Zimprich *et al*., Mutations in LRRK2 cause autosomal-dominant parkinsonism with pleomorphic pathology. *Neuron* **44**, 601–607 (2004). doi: 10.1016/j.neuron.2004.11.005; pmid: 15541309
130. A. Gardet *et al*., LRRK2 is involved in the IFN-gamma response and host response to pathogens. *J. Immunol.* **185**, 5577–5585 (2010). doi: 10.4049/jimmunol.1000548; pmid: 20921534
131. O. Neudorfer *et al*., Occurrence of Parkinson's syndrome in type I Gaucher disease. *Q. J. Med.* **89**, 691–694 (1996). doi: 10.1093/qjmed/89.9.691; pmid: 8917744
132. W. Satake *et al*., Genome-wide association study identifies common variants at four loci as genetic risk factors for Parkinson's disease. *Nat. Genet.* **41**, 1303–1307 (2009). doi: 10.1038/ng.485; pmid: 19915576
133. J. Simón-Sánchez *et al*., Genome-wide association study reveals genetic risk underlying Parkinson's disease. *Nat. Genet.* **41**, 1308–1312 (2009). doi: 10.1038/ng.487; pmid: 19915575
134. C. Münch, J. O'Brien, A. Bertolotti, Prion-like propagation of mutant superoxide dismutase-1 misfolding in neuronal cells. *Proc. Natl. Acad. Sci. U.S.A.* **108**, 3548–3553 (2011). doi: 10.1073/pnas.1017275108; pmid: 21321227
135. T. Nonaka *et al*., Prion-like properties of pathological TDP-43 aggregates from diseased brains. *Cell Reports* **4**, 124–134 (2013). doi: 10.1016/j.celrep.2013.06.007; pmid: 23831027
136. J. Brettschneider *et al*., Stages of pTDP-43 pathology in amyotrophic lateral sclerosis. *Ann. Neurol.* **74**, 20–38 (2013). doi: 10.1002/ana.23937; pmid: 23686809
137. D. B. Berry *et al*., Drug resistance confounding prion therapeutics. *Proc. Natl. Acad. Sci. U.S.A.* **110**, E4160–E4169 (2013). doi: 10.1073/pnas.1317164110; pmid: 24128760
138. R. A. Crowther, M. Goedert, C. M. Wischik, The repeat region of microtubule-associated protein tau forms part of the core of the paired helical filament of Alzheimer's disease. *Ann. Med.* **21**, 127–132 (1989). doi: 10.3109/07853899809149199; pmid: 2504257
139. M. G. Spillantini *et al*., Alpha-synuclein in Lewy bodies. *Nature* **388**, 839–840 (1997). doi: 10.1038/42166; pmid: 9278044

ACKNOWLEDGMENTS

I am grateful to S. B. Prusiner for his input and to F. Clavaguera, R. A. Crowther, D. S. Eisenberg, B. Ghetti, S. H. W. Scheres, M. G. Spillantini, and M. Tolnay for helpful comments on the manuscript. H. Braak, R. A. Crowther, K. Del Tredici, D. Eisenberg, B. Ghetti, G. Lingley, M. R. Sawaya and M. G. Spillantini helped with the figures. Our work is supported by the UK Medical Research Council (U105184291) and the "Association pour la Recherche sur Alzheimer." I am an Honorary Professor in the Department of Clinical Neurosciences, University of Cambridge.

10.1126/science.1255555

RESEARCH ARTICLES

PALEOECOLOGY

Abrupt warming events drove Late Pleistocene Holarctic megafaunal turnover

Alan Cooper,[1]* Chris Turney,[2]* Konrad A. Hughen,[3] Barry W. Brook,[4,5] H. Gregory McDonald,[6] Corey J. A. Bradshaw[4]

The mechanisms of Late Pleistocene megafauna extinctions remain fiercely contested, with human impact or climate change cited as principal drivers. We compared ancient DNA and radiocarbon data from 31 detailed time series of regional megafaunal extinctions and replacements over the past 56,000 years with standard and new combined records of Northern Hemisphere climate in the Late Pleistocene. Unexpectedly, rapid climate changes associated with interstadial warming events are strongly associated with the regional replacement or extinction of major genetic clades or species of megafauna. The presence of many cryptic biotic transitions before the Pleistocene/Holocene boundary revealed by ancient DNA confirms the importance of climate change in megafaunal population extinctions and suggests that metapopulation structures necessary to survive such repeated and rapid climatic shifts were susceptible to human impacts.

The debate surrounding the causes of the extinctions of megafaunal species (terrestrial taxa with adults >45 kg), which occurred during the last glacial period (~110,000 to 11,650 calendar years ago; 110 to 11.65 ka) in the Late Pleistocene, has continued for over two centuries, since Cuvier first identified the mammoth and giant ground sloth (*1*–*5*). Although human activity as a result of hunting ("overkill") and/or habitat modification and fragmentation are often cited as the principal driving force (*1*, *6*–*8*), the diversity of extinction patterns observed on different continents has led to increasing recognition of the potential synergistic role of climate change (*1*–*4*, *9*). A major confounding factor in the debate has been the coincident Late Pleistocene increase in human population size and dispersal into previously uninhabited areas, such as the New World, potentially exacerbating other ecological impacts.

Traditionally, a key argument against the potential role of climate-change impacts has been the paucity of identified extinction events during either previous glacial cycles or the many well-defined, climatic shifts recorded during the last glacial period (*3*, *4*), including the Last Glacial Maximum (LGM; ~23 to 19 ka) (Fig. 1). However, the lack of suitably resolved records of climate change and radiocarbon calibration on a common time scale makes such interpretations particularly challenging. The debate has also been constrained by the heavy reliance on fossil morphological evidence, precluding the identification of major genetic transitions or population-level turnovers. Recent work using ancient DNA (aDNA) has shown that morphological analyses of the Pleistocene paleontological record can have limited power to resolve species-level mammalian taxonomy issues or detect broad-scale genetic transitions at the population level, even when species suffer major genetic losses or almost go extinct (*10*–*15*). Indeed, aDNA and genomic studies have revealed a far more dynamic picture of megafaunal population ecology, including repeated localized extinctions, migrations, and replacements (*10*, *12*–*15*).

The Late Pleistocene was characterized by a series of severe and rapid climate oscillations (regional temperature changes of up to 16°C) known as Dansgaard-Oeschger (D-O) interstadial (warming) events that have been identified in oceanic, ice, and terrestrial records throughout the Northern Hemisphere (*16*) (Fig. 1 and fig. S3). The millennial-length D-O events can be bundled into semi-regular cooling cycles with an asymmetrical saw-tooth pattern (Bond cycles) (*17*) that culminate in massive discharges of ice into the North Atlantic, known as Heinrich events. However, the precise timing, magnitude, and global extent of these events remain sufficiently uncertain to impair research into the effects of such rapid and extreme climate shifts on landscape and paleoecological change. In particular, there has been limited analysis of the potential relationship between rapid climate change and major genetic transitions in widespread populations, marked by local extirpations or global extinctions of species and genetic diversity.

Megafaunal data

To investigate this, we examined all available megafaunal species with comprehensive radiocarbon-dated series and plotted 31 calibrated major megafaunal transition events (defined as geographically widespread or global extinctions, or invasions, of species or major clades) that have been detected in either genetic (13 events) or paleontological (18 events) studies against the Greenland ice core record [on the Greenland Ice Core Chronology 2005 (GICC05) time scale] (*18*–*20*) (Fig. 1).

The genetic and radiocarbon data reveal a temporally staggered, long-term dynamic record of major megafaunal transitions across species with diverse ecologies and life histories. The events were widely distributed geographically across both Eurasia and the New World and included periods before human invasion. Multiple events appear to involve the rapid replacement of one species or population by a conspecific or congeneric across a broad area, often making the events undetectable in the fossil record on the basis of morphology, and potentially even in low-resolution genetic reconstructions of population paleodemography (*21*). These rapid replacements suggest that putative taphonomic biases (e.g., increased fossilization rates during either interstadials or stadials—cold periods) are not responsible for the apparent sudden disappearance or appearance of genetic diversity. Furthermore, common megafaunal fossils, such as mammoth, appear throughout the time period examined (Fig. 1). The apparent absence of extinctions during the cold conditions of the LGM, when Northern Hemisphere ice sheets reached their maximum volume, or to a lesser extent during the Younger Dryas stadial (11.7 to 12.7 kya; table S3) at the very end of the Pleistocene, is surprising, given that these events are commonly postulated as potential causes of megafaunal extinctions (*3*, *22*). Although paleontological studies record range contractions into glacial refugia for many species during this period (*4*), it appears that, in general, cold conditions were not an important driver for extinctions, even in the presence of anatomically modern humans in Europe.

The megafaunal transitions appear to be centered around D-O warming events leading up to and then after the LGM, including a marked cluster of events around interstadials 5 to 7 in northern Europe (~37 to 32 ka; Fig. 1). A further well-known cluster of extinction events occurs during the termination of the Pleistocene (~14 to 11 ka), which has often been linked to the initial entry of humans into the New World (~15 ka) (*6*–*8*). However, half of the 12 extinction events in this period occur in western Eurasia, where modern humans arrived at least ~44 kya. Indeed, several taxa (e.g., mammoth) go extinct on the mainland of Eurasia considerably later than that of the New World, despite a much longer exposure to human hunting (*3*, *4*) (Fig. 1).

[1]Australian Centre for Ancient DNA, School of Earth and Environmental Sciences, and Environment Institute, University of Adelaide, Adelaide, Australia. [2]Climate Change Research Centre and School of Biological, Earth, and Environmental Sciences, University of New South Wales, Sydney, Australia. [3]Woods Hole Oceanographic Institution, Woods Hole, MA 02543, USA. [4]Environment Institute and School of Biological Sciences, University of Adelaide, Adelaide, Australia. [5]School of Biological Sciences, University of Tasmania, Hobart, Australia. [6]Museum Management Program, National Parks Service, Fort Collins, CO 80525, USA.
*Corresponding author. E-mail: alan.cooper@adelaide.edu.au (A.C.); c.turney@unsw.edu.au (C.T.)

Greenland-Cariaco climate time scale

A major challenge for testing whether the genetic transitions were synchronous with D-O events is the placement of megafaunal and climate records on a common time scale (*23*). Although the Greenland ice cores (*18*, *19*) provide a detailed record of climate change for the North Atlantic, cumulative counting errors can exceed 2% (fig. S1) (*20*), resulting in calendar time scale offsets of up to 1000 years between Greenland D-O events and radiocarbon-calibrated megafaunal transitions (*23*, *24*). To enable detailed comparisons, the climate and radiocarbon records should be on the same absolute time scale, which requires the merging of different high-resolution data sets. Importantly, this also provides a means to improve the accuracy and the precision of the chronological framework and to assess the hemispheric nature of the climate shifts. One such approach is to use the abrupt shifts at the onset of D-O warming as tie points to correlate across multiple climate records (*25*), because these events caused widespread and rapid climate effects by decreasing the Northern Hemisphere temperature gradient (*26*), resulting in a poleward migration of the Intertropical Convergence Zone (ITCZ) and associated changes in tropical rainfall belts (*27*–*31*). In this regard, a key record is the Venezuelan Cariaco Basin marine sequence, which captures a climate record via shifts in the trade winds associated with northward migration of the ITCZ in the tropical Atlantic (*20*, *28*), alongside a comprehensive suite of radiocarbon ages from planktonic foraminifera in the sediment core. The Cariaco sediments are annually laminated during the Late Glacial and Holocene, providing independent age control from 14.7 ka (*32*), before which distinct millennial-scale variability in sedimentological and geochemical proxies has been robustly correlated with the uranium series–dated Hulu Cave oxygen isotope ratio ($\delta^{18}O$) speleothem record (with age uncertainties < 1%) (*33*).

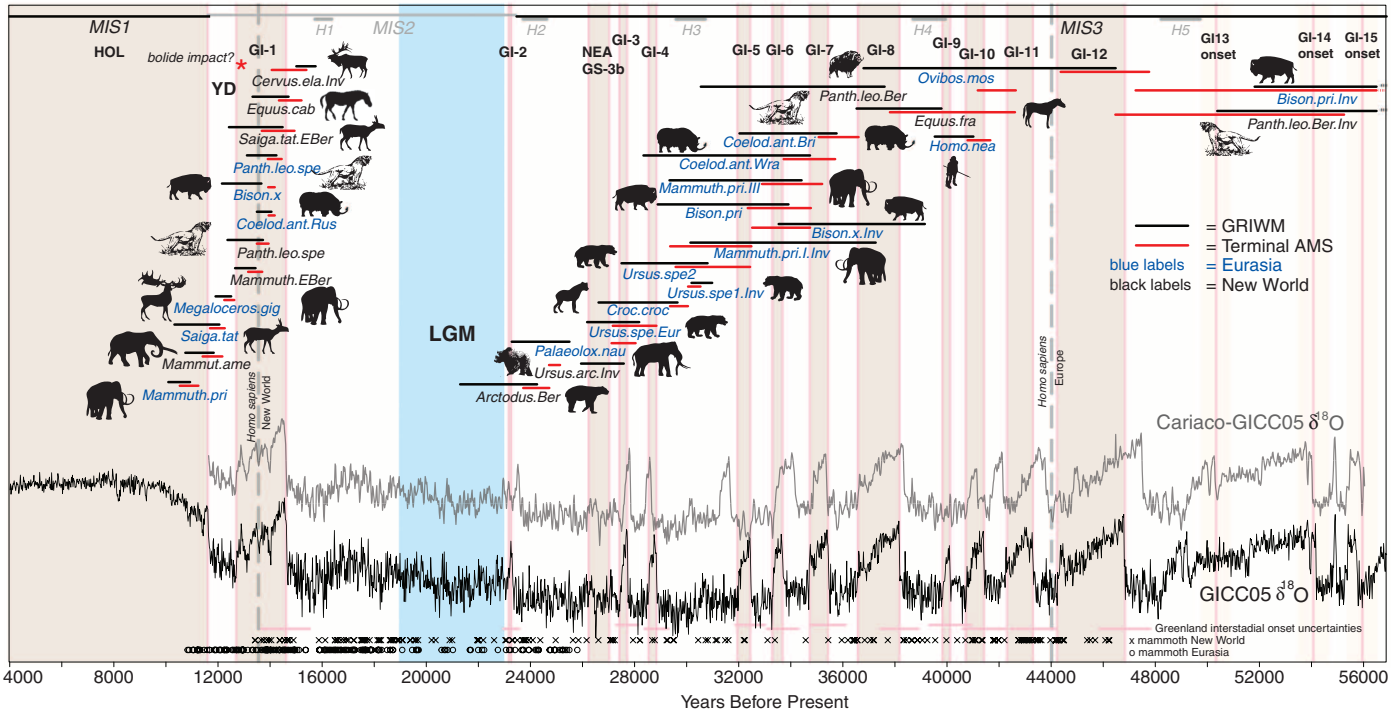

Fig. 1. Megafaunal transition events and Late Pleistocene climate records. Major megafaunal transition events (regionwide extirpations or global extinctions, or invasions, of species or major clades) identified in Late Pleistocene Holarctic megafaunal data sets through aDNA or paleontological studies, plotted on a reconstruction of Northern Hemisphere climate from the GICC05 $\delta^{18}O$ record (black wiggle curve). GICC05 interstadial warming events are shown with light gray boxes. There is an apparent absence of megafaunal events during the LGM (blue) and, to a lesser extent, the cold Younger Dryas stadial (YD) and a marked association with interstadials. Accelerator mass spectrometry (AMS) radiocarbon dates (red bar ± 2 SD, using *Phase* calibration in OxCal 4.1) calibrated by using the dendrodated IntCal <12,500-year data set (*36*) and Cariaco Basin (Hulu Cave) data set for older ages (*28*, *33*), or GRIWM-based estimates of ghost ranges (black bar, 95% confidence interval) are given for each event (*20*). Eurasian taxa are shown in blue and New World in black, with animals facing right representing extinctions and those facing left representing invasions (.Inv). The chronologically revised Greenland record, developed by combining the Cariaco Basin and Greenland ice core records, is also shown (dark gray wiggle curve) for the period >11.5 ka (because it is identical with GICC05 until this point) (*20*). Light pink bars (below) represent the error margins (1 SD) for the estimated onset of GI events in the published GICC05 chronology (*19*, *20*). Heinrich events (H*x*) are shown with marine isotope stages (MIS*x*) in light gray at top (*41*). NEA-GS-3b was identified via Atlantic marine sediment cores and radiocarbon dating (*42*). Calibrated radiocarbon ages (midpoints without laboratory dating errors) from mammoth remains in Eurasia (black circles) and New World (crosses) are plotted across the bottom of the figure to demonstrate the lack of obvious taphonomic hiatus during the time period analyzed (*20*). The approximate timing of the first presence of modern humans in North America (New World) and Europe are shown as vertical gray dashed lines. Abbreviated taxonomic names, with geographic area appended where necessary, are given: *Arctodus.Ber* (*Arctodus simus* East Beringia); *Bison.pri* (*Bison priscus* Europe); *Bison.x* (*Bison* n. sp. Europe); *Cervus.ela* (*Cervus elephas* New World); *Coelod.ant.Bri* (*Coelodonta antiquitatis* Britain); *Coelod.ant.Rus* (*C. antiquitatis* Russia); *Coelodonta.ant.Wra* (*C. antiquitatis* Wrangel Island); *Croc.croc* (*Crocuta crocuta spelaea* Europe); *Equus.cab* (*Equus caballus* East Beringia); *Equus.fra* (*E. francisci* East Beringia); *Homo.nea* (*Homo neanderthalensis* Europe); *Mammuth.pri* (*Mammuthus primigenius*); *Mammut.ame* (*Mammut americanum*); *Megaloceros.gig* (*Megaloceros giganteus* Western Europe); *Ovibos.mos* (*Ovibos moschatus* Beringia); *Palaeolox.nau* (*Palaeoloxodon naumanni* Japan); *Panth.leo.Ber* (*Panthera leo spelaea* Beringia); *Panth.leo.spe* (*P. leo spelaea* Eurasia); *Saiga.tat* (Saiga tatarica Eurasia); *Ursus.arc* (*Ursus arctos* East Beringia); *Ursus.spe1 and 2* (*U. spelaea* Germany); *Ursus.spe.Eur* (*U. spelaea* Europe). [Further details of the geographic region and nature of each megafaunal event are presented in tables S1 and S2.]

We therefore used a D-O event tie-point approach to combine the calendar-age estimates obtained from Cariaco Basin (*28*) with the same interstadial events recorded in Greenland to allow a direct comparison between radiocarbon dates and climate change, thereby allowing us to test the apparent association between megafaunal extinction or replacement with warming events (Fig. 1). We find the timing of onsets of interstadial warming events in the two records to be statistically identical (*20*), allowing us to use OxCal 4.1 (*34*) to combine the two chronologies, and merged the calendar-dated onset of each interstadial in Cariaco with the annual layer-counted interstadial onset and duration from Greenland to generate a new combined record of the timing and duration of abrupt and extreme swings of north Atlantic temperature during the past 56 thousand years (Fig. 1 and tables S3 and S4) (*20*). Our new reconstruction shows that, although all current estimates of the onset of interstadial events in the GICC05 $\delta^{18}O$ record are within the errors of our combined Cariaco-Greenland chronology, the uncertainty surrounding these transitions is greatly reduced (by 18 to 79%) (Fig. 1, table S3, and figs. S2 and S4).

Testing climate-extinction associations

We used statistical resampling to test the distribution of megafaunal transitions for randomness relative to extreme and abrupt climatic events (either stadials or interstadials), using both the existing GICC05 and our new Cariaco-Greenland chronology (Fig. 1 and table S4) (*20*). We calculated the probability that the observed overlap between climate events and extinction or invasion events might be nonrandom by repeatedly randomizing the temporal position (but not duration) of the former and, for each iteration, counting the number of times overlap was observed with the latter. To do this, we used the calibrated radiocarbon age of the terminal observation of a clade or taxon (youngest age for extinctions, oldest for invasions) but also inferred unobserved temporal (ghost) ranges using the Gaussian-resampled, inverse-weighted McInerney (GRIWM) method (*20*, *35*), which incorporates both sampling density and dating errors to estimate the most plausible temporal range of last or first occurrence. A nonrandom relationship was observed between interstadial events and megafaunal transitions for both the terminal observations and the GRIWM-based estimates, with statistical power depending on the number of transitions tested, but no such nonrandom overlap was detected for stadials (Fig. 2 and Table 1) (*20*). A nonrandom association is observed despite the uncertainties in the taphonomic, sampling, and dating processes involved in the data sets, and it is apparent with both the standard published GICC05 record and the new combined Cariaco-Greenland chronology (Table 1). A correlation can be seen even when terminal Pleistocene events are discarded to avoid the potential confounding impacts of human colonization (Fig. 2 and Table 1). The Younger Dryas stadial has also often been suggested as a prime climatic driver of extinctions (*3*, *4*, *22*), but even for this event, the observed extinction events are distributed much more toward the preceding interstadial warm period (Fig. 1 and fig. S7), despite the larger dating uncertainties caused by radiocarbon plateaus at this time (*36*).

Interstadial impacts

The onsets of interstadials represent the most rapid and extreme changes observed in the Late Pleistocene climate record (Fig. 1) (*20*), and these are likely to have caused abrupt shifts in temperature or precipitation (either wetter or drier depending on local environments) away from a previous relatively stable state. These factors would have promoted changes in species ranges and distributions, potentially resulting in regional turnover. The local or regional expression of global climate variation (such as D-O events) is highly variable (*37*), and this is consistent with the megafaunal transition events being distributed broadly in terms of geography, taxonomy, and age. This diffuse pattern, along with methodological limitations used in simple genetic paleodemographic reconstructions (*21*), might explain why correlations with climate events may have been difficult to detect previously. The lack of extinctions during the LGM is consistent with the stability of the climate during this period, albeit cold, in contrast with the large millennial-scale variability before and after, both of which coincide with high rates of extinctions.

The megafaunal taxa analyzed cover a wide range of life histories and ecological roles and include forest and steppe taxa. Many species have a broad niche (e.g., *Ursus arctos*, *Bison* spp., and Neandertals), making it difficult to classify taxa into cold- or warm-adapted groups as has previously been advocated (*3*, *4*, *38*). Furthermore, the rapid and drastic climate changes associated with both the onset and the end of interstadials, followed by new climate regimes, are potentially sufficient to disrupt populations of taxa across a

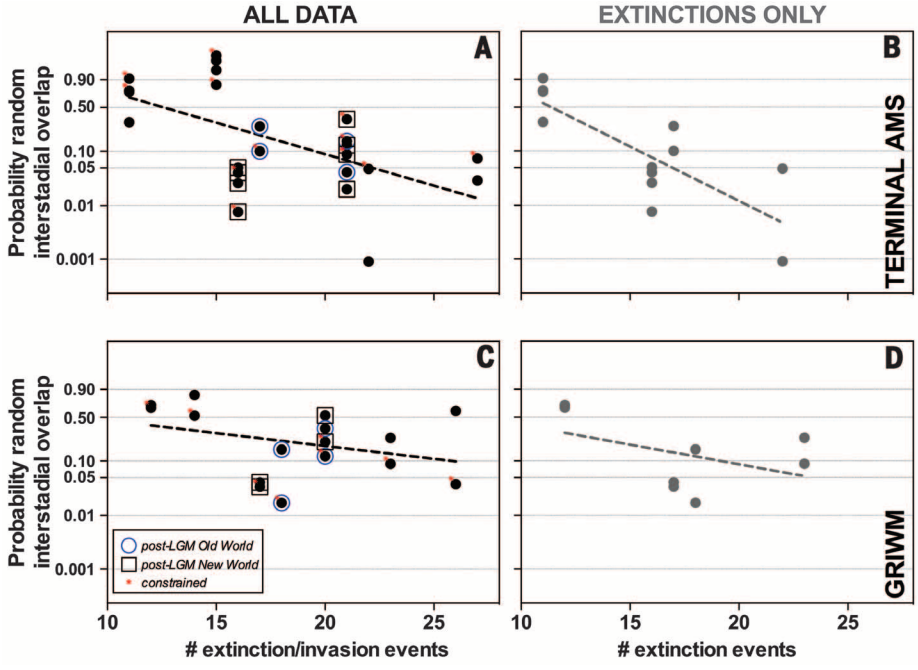

Fig. 2. Randomization tests of the timing of megafaunal transitions with interstadial events. Graphical representation of the simulation results presented in Table 1. The trend lines (dashed lines) show that the probability of generating the observed overlaps of megafaunal transition events with interstadials randomly (*P*) is inversely related to the number of events examined, whereas, in contrast, the probabilities for stadials were all > 0.60 (Table 1) (*20*). A strong correlation (steep gradient) was observed between megafaunal transitions (extinctions or invasion events) and interstadials using both: (**A** and **B**) terminal AMS ^{14}C dates and (**C** and **D**) GRIWM estimates (which use a statistical model of extinction times based on a time series of records). The correlation was observed by using either the GICC05 (shown) or new combined Cariaco-Greenland (Table 1 and fig. S6) chronologies. The plotted data are from simulations excluding events with wide confidence intervals, because inclusion nearly always resulted in a greater chance of overlap being random [i.e., higher *P* values; see (*20*)]. To explore the effect of different combinations of megafaunal-transition events, we removed certain subsets and repeated the simulations: (i) excluding invasion events [(B) and (D)]—resulting in lower *P* of randomness; (ii) with a constrained-range overlap (red *) applied to reduce error margins around an event where a rapid replacement by a congener or conspecific was observed (*20*)—producing little difference in the results; and (iii) with post-LGM events from either the New World (○) or Eurasia (□) only (to remove the potential effects of terminal Pleistocene human-associated impacts)—where low *P* were observed, but sample-size constraints limited the number of simulations able to detect nonrandom interstadial overlap (*20*). The results of these additional simulations are distributed along most of the power relationship, suggesting the correlations are not driven by any particular grouped subset of the data.

wide range of niches. The effects of high-amplitude climate change, followed by either stadial or interstadial conditions, are potentially compatible with previous suggestions that the extirpation of cold- or open-adapted taxa, such as woolly rhino and mammoth, occurred during interstadials and warm-adapted taxa, such as the giant deer, during stadials like the Younger Dryas (*38*). However, the widely dispersed temporal record of the megafaunal transitions suggests a markedly individualistic species response (*39*), presumably exaggerated by the localized environmental responses to climatic shifts (*37*). Simulations of paleovegetation patterns in the late Pleistocene have emphasized the importance of the duration and nature of interstadial events and their impact on the growth of factors, such as forests (*40*). In contrast, we observe a more pronounced relationship between short interstadials (IS 3 to 7) and megafaunal events, rather than with the longer interstadials, such as 8 and 12, which might have been expected to allow larger-scale changes in the extent and nature of forest cover.

Our results lend strong empirical support to the hypothesis that environmental changes associated with rapid climatic shifts were important factors in the extinction of many megafaunal lineages. Indeed, the rapid replacement of local genetic populations by congeners or conspecifics (e.g., cave bears, bison, and mammoth) revealed by aDNA suggests that broader-scale metapopulation structures or processes (e.g., long-distance dispersal, refugia, and rescue effects across spatially distributed subpopulations) were involved in maintaining ecosystem stability during the repeated phases of sudden climate change in the Pleistocene Holarctic. If so, human presence could have had a major and negative impact on megafaunal metapopulations by interrupting subpopulation connectivity, especially by concentrating on regular pathways between resource-rich zones (*1*), potentially leaving minimal signs of direct hunting. By interrupting metapopulation processes (e.g., dispersal and recolonization), humans could have both exacerbated regional extinctions brought

Table 1. Randomization tests of the timing of megafaunal transitions with major climate events. Randomization tests of the timing of major megafaunal transitions with either interstadial or stadial events on the existing GICC05 and new combined Cariaco-Greenland time scales (*20*). The probabilities of generating the observed overlaps of extinction or invasion events at random with interstadials [P(rand) interstadials] and stadials [P(rand) stadials] are shown for both GRIWM and the phase-calibrated terminal AMS dates, along with probabilities expressed on the complementary log-log scale. The correlation tests revealed nonrandom overlap relationships between the number of events, *n*, and interstadials for both GICC05 and Cariaco-Greenland time scales. In contrast, probabilities for overlaps at random with stadial events were >0.6 for both GRIWM and terminal AMS dates. Simulations producing low probabilities of generating the pattern of overlaps at random are cumulatively highlighted with asterisks ($P < 0.1$), in blue ($P < 0.05$), and in red ($P < 0.01$). The power relationships for correlations with the GICC05 time scale are shown in Fig. 2. Simulations including terminal Pleistocene events from only the New World (NW) or Eurasia (Eur.) or neither (Pre-LGM) were used to explore the potentially confounding influences of human impact. Simulations using extinctions only (Extns) are indicated. The GICC05 time scale did not include interstadial NEA-GS-3b (table S3) because it is not detected in ice core records (*41*). CI, confidence interval.

Events (Eurasia, New World)	Extinctions / Invasions	Muskox	Wide-CI species	Constrained range overlaps	Number of events (*n*) GRIWM	Number of events (*n*) Terminal AMS	Interstad P(random) GRIWM	Interstad P(random) Terminal AMS	Stadial P(random) GRIWM	Stadial P(random) Terminal AMS	Interstad P(random) GRIWM	Interstad P(random) Terminal AMS	Stadial P(random) GRIWM	Stadial P(random) Terminal AMS
							GICC05 chronology (19, 20)				*Cariaco-Greenland chronology*			
All	All	✓	✓	✓	28	29	0.031*	0.228	0.801	0.999	0.126	0.220	0.998	0.998
All	All	✓	✓	✗	28	29	0.109	0.009*	0.995	0.999	0.470	0.082*	0.989	0.999
All	All	✗	✓	✓	27	28	0.024*	0.020*	0.974	0.997	0.066*	0.091*	0.983	0.996
All	All	✗	✗	✓	21	27	0.038*	0.075*	0.994	0.975	0.252	0.117	0.998	0.995
All	All	✗	✗	✗	21	27	0.600	0.030*	0.992	0.999	0.487	0.037*	0.988	0.999
All	Extns	✓	✓	✗	24	23	0.296	0.005*	0.999	0.992	0.396	0.023*	0.999	0.999
All	Extns	✗	✓	✗	22	22	0.097*	0.026*	0.994	0.974	0.302	0.031*	0.999	0.999
All	Extns	✗	✓	✓	22	22	0.107	0.001*	0.965	0.999	0.023*	0.069*	0.999	0.997
All	Extns	✗	✗	✓	18	21	0.089*	0.048*	0.999	0.999	0.131	0.087*	0.994	0.999
All	Extns	✗	✗	✗	18	21	0.249	0.001*	0.999	0.999	0.287	0.007*	0.999	0.999
Eur.	All	✓	✓	✓	22	24	0.018*	0.230	0.985	0.897	0.414	0.529	0.998	0.914
Eur.	All	✓	✓	✗	23	24	0.453	0.046*	0.977	0.999	0.425	0.161	0.996	0.950
Eur.	All	✗	✓	✗	22	23	0.227	0.088*	0.962	0.822	0.250	0.164	0.994	0.980
Eur.	All	✗	✓	✓	22	23	0.040*	0.105	0.958	0.864	0.019*	0.245	0.982	0.958
Eur.	All	✗	✗	✓	16	22	0.122	0.150	0.997	0.855	0.125	0.324	0.981	0.971
Eur.	All	✗	✗	✗	16	22	0.347	0.042*	0.996	0.958	0.137	0.022*	0.986	0.987
Eur.	Extns	✗	✓	✓	17	17	0.283	0.160	0.999	0.964	0.252	0.116	0.998	0.977
Eur.	Extns	✗	✗	✓	13	16	0.017*	0.100*	0.985	0.991	0.073*	0.424	0.997	0.959
Eur.	Extns	✗	✗	✗	13	16	0.159	0.265	0.999	0.987	0.221	0.044*	0.992	0.997
NW	All	✓	✓	✗	23	25	0.335	0.060*	0.385	0.996	0.354	0.075*	0.975	0.830
NW	All	✗	✓	✗	23	24	0.377	0.014*	0.977	0.996	0.283	0.099*	0.621	0.840
NW	All	✗	✗	✓	16	27	0.215	0.088*	0.943	0.960	0.382	0.231	0.775	0.865
NW	All	✗	✗	✗	16	27	0.528	0.128	0.919	0.608	0.347	0.055*	0.883	0.899
NW	Extns	✗	✗	✓	13	17	0.034*	0.041*	0.848	0.929	0.111	0.124	0.943	0.956
NW	Extns	✗	✗	✗	13	17	0.041*	0.026*	0.636	0.967	0.094*	0.061*	0.986	0.952
Pre- LGM	All	✓	✓	✗	18	20	0.432	0.993	0.987	0.977	0.958	0.942	0.990	0.682
Pre- LGM	All	✗	✓	✗	17	19	0.918	0.966	0.999	0.611	0.961	0.879	0.999	0.818
Pre- LGM	Extns	✗	✗	✓	8	12	0.648	0.763	0.918	0.790	0.641	0.902	0.964	0.679
Pre- LGM	Extns	✗	✗	✗	8	12	0.688	0.743	0.999	0.641	0.999	0.944	0.999	0.842

on by climate changes and allowed them to coalesce, potentially leading to the eventual regime shifts and collapses observed in megafaunal ecosystems. The lack of evidence for larger-scale ecological regime shifts during earlier periods of the Glacial (i.e., >45 ka) when interstadial events were common, but modern humans were not, supports a synergistic role for humans in exacerbating the impacts of climate change and extinction in the terminal Pleistocene events.

REFERENCES AND NOTES

1. G. Haynes, *Quat. Int.* **285**, 89–98 (2013).
2. R. D. Guthrie, *Nature* **441**, 207–209 (2006).
3. P. L. Koch, A. D. Barnosky, *Annu. Rev. Ecol. Evol. Syst.* **37**, 215–250 (2006).
4. A. J. Stuart, A. M. Lister, *Quat. Sci. Rev.* **51**, 1–17 (2012).
5. G. Cuvier, Notice sur le squellette d'une très grande espèce de quadrupède inconnue jusqu'à présent, trouvé au Paraguay, et déposé au cabinet d'histoire naturelle de Madrid. *Magasin* encyclopédique, ou *Journal des Sciences, des Lettres et des Arts*, vol. 1, pp. 303–310 and vol. 2, pp. 227–228 (1796).
6. P. S. Martin, in *Quaternary Extinctions: A Prehistoric Revolution*, P. S. Martin, R. D. Klein, Eds. (Univ. of Arizona Press, Tucson, AZ, 1984).
7. J. Diamond, *J. Archaeol. Sci.* **16**, 167–175 (1989).
8. J. Alroy, *Science* **292**, 1893–1896 (2001).
9. E. D. Lorenzen *et al.*, *Nature* **479**, 359–364 (2011).
10. I. Barnes, P. Matheus, B. Shapiro, D. Jensen, A. Cooper, *Science* **295**, 2267–2270 (2002).
11. M. Bunce *et al.*, *Nature* **425**, 172–175 (2003).
12. B. Shapiro *et al.*, *Science* **306**, 1561–1565 (2004).
13. M. Hofreiter, J. Stewart, *Curr. Biol.* **19**, R584–R594 (2009).
14. W. Miller *et al.*, *Proc. Natl. Acad. Sci. U.S.A.* **109**, E2382–E2390 (2012).
15. S. Brace *et al.*, *Proc. Natl. Acad. Sci. U.S.A.* **109**, 20532–20536 (2012).
16. E. W. Wolff, J. Chappellaz, T. Blunier, S. O. Rasmussen, A. Svensson, *Quat. Sci. Rev.* **29**, 2828–2838 (2010).
17. G. Bond *et al.*, *Nature* **365**, 143–147 (1993).
18. S. O. Rasmussen *et al.*, *J. Geophys. Res.* **111**, D06102 (2006).
19. A. Svensson *et al.*, *Clim. Past* **4**, 47–57 (2008).
20. See supplementary materials available on *Science* Online.
21. T. Mourier, S. Y. Ho, M. T. Gilbert, E. Willerslev, L. Orlando, *Mol. Biol. Evol.* **29**, 2241–2251 (2012).
22. G. M. MacDonald *et al.*, *Nat. Commun.* **3**, 893 (2012).
23. R. Muscheler, F. Adolphi, A. Svensson, *Earth Planet. Sci. Lett.* **394**, 209–215 (2014).
24. C. Buizert *et al.*, *Clim. Past* **11**, 153–173 (2015).
25. N. J. Shackleton, R. G. Fairbanks, T. C. Chiu, F. Parrenin, *Quat. Sci. Rev.* **23**, 1513–1522 (2004).
26. J. T. Overpeck, L. C. Peterson, N. Kipp, J. Imbrie, D. Rind, *Nature* **338**, 553–557 (1989).
27. K. A. Hughen, J. T. Overpeck, L. C. Peterson, S. Trumbore, *Nature* **380**, 51–54 (1996).
28. K. Hughen, J. Southon, S. Lehman, C. Bertrand, J. Turnbull, *Quat. Sci. Rev.* **25**, 3216–3227 (2006).
29. L. C. Peterson, G. H. Haug, K. A. Hughen, U. Röhl, *Science* **290**, 1947–1951 (2000).
30. S. C. Porter, A. Zhisheng, *Nature* **375**, 305–308 (1995).
31. Y. Wang *et al.*, *Nature* **451**, 1090–1093 (2008).
32. K. A. Hughen, J. R. Southon, C. J. H. Bertrand, B. Frantz, P. Zermeño, *Radiocarbon* **46**, 1161–1187 (2004).
33. T. J. Heaton, E. Bard, K. Hughen, *Radiocarbon* **55**, 1975–1997 (2013).
34. C. B. Ramsey, *Radiocarbon* **51**, 337–360 (2009).
35. C. J. A. Bradshaw, A. Cooper, C. S. M. Turney, B. W. Brook, *Quat. Sci. Rev.* **33**, 14–19 (2012).
36. P. J. Reimer *et al.*, *Radiocarbon* **55**, 1869–1887 (2013).
37. X. A. S. Wang *et al.*, *Geophys. Res. Lett.* **34**, L23701 (2007).
38. A. J. Stuart, P. A. Kosintsev, T. F. G. Higham, A. M. Lister, *Nature* **431**, 684–689 (2004).
39. J. R. Stewart, *J. Evol. Biol.* **22**, 2363–2375 (2009).
40. B. Huntley *et al.*, *PLOS ONE* **8**, e61963 (2013).
41. P. C. Tzedakis, K. A. Hughen, I. Cacho, K. Harvati, *Nature* **449**, 206–208 (2007).
42. W. E. N. Austin *et al.*, *Quat. Sci. Rev.* **36**, 154–163 (2012).

ACKNOWLEDGMENTS

We thank the following museums and curators for their generous assistance with samples, advice and encouragement: Canadian Museum of Nature (R. Harington); American Museum of Natural History (R. Tedford); Natural History Museum London (A. Currant); Yukon Heritage Centre (J. Storer and G. Zazula); University of Alaska, Fairbanks (D. Guthrie, C. Gerlach, and P. Matheus), Royal Alberta Museum (J. Burns); Institute of Plant and Animal Ecology, RAS Yekaterinburg (P. Kosintsev and A. Vorobiev); Laboratory of Prehistory, St. Petersburg (V. Doronichev and L. Golovanova); D. Froese; T. Higham; A. Sher; J. Glimmerveen; B. Shapiro; T. Gilbert; E. Willerslev; R. Barnett; Yukon miners (B. and R. Johnson, the Christie family, K. Tatlow, S. and N. Schmidt); L. Dalen and J. Soubrier for data and assistance. This work was supported by NSF NESCENT workshop "Integrating datasets to investigate megafaunal extinction in the late Quaternary." A.C., C.T., B.W.B., and C.J.A.B. were supported by Australian Research Council Federation, Laureate and Future Fellowships. The new GICCO5-Cariaco Basin $\delta^{18}O$ record is provided in (*20*) and also lodged on the Paleoclimatology Database (National Oceanic and Atmospheric Administration dataset ID: noaa-icecore-19015). The previously published radiocarbon data, with original references, is presented in (*20*). A.C. and C.T. conceived and performed research; A.C., C.J.A.B., C.T., and B.W.B. designed methods and performed analysis; A.C. and C.T. wrote the paper with input from all authors.

SUPPLEMENTARY MATERIALS

www.sciencemag.org/content/349/6248/602/suppl/DC1
Materials and Methods
Supplementary Text
Figs. S1 to S8
Tables S1 to S4
References (*43*–*54*)

27 April 2015; accepted 3 July 2015
Published online 23 July 2015
10.1126/science.aac4315

IMMUNODEFICIENCIES

Impairment of immunity to *Candida* and *Mycobacterium* in humans with bi-allelic *RORC* mutations

Satoshi Okada,[1,2]* Janet G. Markle,[1]*† Elissa K. Deenick,[3,4]‡ Federico Mele,[5]‡ Dina Averbuch,[6]‡ Macarena Lagos,[7,8]‡ Mohammed Alzahrani,[9]‡ Saleh Al-Muhsen,[9,10]‡ Rabih Halwani,[10] Cindy S. Ma,[3,4] Natalie Wong,[3] Claire Soudais,[11] Lauren A. Henderson,[12] Hiyam Marzouqa,[13] Jamal Shamma,[13] Marcela Gonzalez,[7] Rubén Martinez-Barricarte,[1] Chizuru Okada,[1] Danielle T. Avery,[3] Daniela Latorre,[5] Caroline Deswarte,[14,15] Fabienne Jabot-Hanin,[14,15] Egidio Torrado,[16]§ Jeffrey Fountain,[16]|| Aziz Belkadi,[14,15] Yuval Itan,[1] Bertrand Boisson,[1] Mélanie Migaud,[14,15] Cecilia S. Lindestam Arlehamn,[17] Alessandro Sette,[17] Sylvain Breton,[18] James McCluskey,[19] Jamie Rossjohn,[20,21,22] Jean-Pierre de Villartay,[23] Despina Moshous,[23,24] Sophie Hambleton,[25] Sylvain Latour,[26] Peter D. Arkwright,[27] Capucine Picard,[1,14,15,24,28] Olivier Lantz,[11] Dan Engelhard,[6] Masao Kobayashi,[2] Laurent Abel,[1,14,15] Andrea M. Cooper,[16]¶ Luigi D. Notarangelo,[12,29]¶ Stéphanie Boisson-Dupuis,[1,14,15]¶ Anne Puel,[1,14,15]¶ Federica Sallusto,[5,30]# Jacinta Bustamante,[1,14,15,28]# Stuart G. Tangye,[3,4]# Jean-Laurent Casanova[1,14,15,24,31]†

Human inborn errors of immunity mediated by the cytokines interleukin-17A and interleukin-17F (IL-17A/F) underlie mucocutaneous candidiasis, whereas inborn errors of interferon-γ (IFN-γ) immunity underlie mycobacterial disease. We report the discovery of bi-allelic *RORC* loss-of-function mutations in seven individuals from three kindreds of different ethnic origins with both candidiasis and mycobacteriosis. The lack of functional RORγ and RORγT isoforms resulted in the absence of IL-17A/F–producing T cells in these individuals, probably accounting for their chronic candidiasis. Unexpectedly, leukocytes from RORγ- and RORγT-deficient individuals also displayed an impaired IFN-γ response to *Mycobacterium*. This principally reflected profoundly defective IFN-γ production by circulating γδ T cells and $CD4^+CCR6^+CXCR3^+$ αβ T cells. In humans, both mucocutaneous immunity to *Candida* and systemic immunity to *Mycobacterium* require RORγ, RORγT, or both.

Inborn errors of human interleukin-17A and interleukin-17F (IL-17A/F) or interferon-γ (IFN-γ) immunity are each associated with a specific set of infections. Inborn errors of IL-17A/F underlie chronic mucocutaneous candidiasis (CMC), which is characterized by infections of the skin, nails, and oral and genital mucosae with *Candida albicans*, typically in the absence of other infections. Five genetic etiologies of CMC have been reported, with mutations in five genes (*1*, *2*). Inborn errors of IFN-γ underlie Mendelian susceptibility to mycobacterial disease (MSMD), which is characterized by selective susceptibility to weakly pathogenic mycobacteria, such as *Mycobacterium bovis* Bacille Calmette-Guérin (BCG) vaccines and environmental mycobacteria. Eighteen genetic etiologies of MSMD have been reported, involving mutations of nine genes (*3*, *4*). Only a few patients display both candidiasis and mycobacteriosis, including some

patients with IL-12p40 and IL-12Rβ1 deficiencies, which impair IFN-γ immunity in all patients and IL-17A/F immunity in some patients (*4*). We studied seven patients from three unrelated consanguineous families with this unusual combination of infectious diseases but no known genetic disorder. A Palestinian child (Fig. 1A, Kindred A, patient P1; see also supplementary text) died at the age of 6 years from disseminated BCG disease. Two other children (P2 and P3) in Kindred A had similar clinical presentations but survived and are now 7 and 4 years old, respectively. A 6-year-old Chilean child (Fig. 1A, Kindred B, P4; see also supplementary text) had disseminated BCG infection at age 16 months. Finally, three siblings from Saudi Arabia (Fig. 1A, Kindred C, P5, P6, and P7; see also supplementary text), ages 9, 6, and 3 years, had mycobacterial diseases caused by BCG in two children and by *M. tuberculosis* in the third. Six of the seven patients also had mucocutaneous candidiasis of varying severity (table S1).

Bi-allelic *RORC* mutations

We combined whole-exome sequencing and genome-wide linkage (GWL) analysis to search for homozygous genetic lesions in the three probands (P1, P4, and P6) (fig. S1). We identified a homozygous C/T mutation in the *RORC* gene in P1, P2, and P3, resulting in a missense Ser^{38}→Leu^{38} (S38L) substitution in the RORγ isoform or a S17L substitution in the RORγT isoform (Fig. 1, A and B, and fig. S2). In P4, we identified a homozygous *RORC* C/T mutation converting the Gln^{329} (Q329) residue of RORγ (or Q308 in RORγT) into a stop codon (Fig. 1, A and B, and fig. S2). In P5, P6, and P7, we identified a homozygous C/T mutation converting the Q441 residue of RORγ (or Q420 in RORγT) into a stop codon (Fig. 1, A and B, and fig. S2). In each kindred, all unaffected family members were either heterozygous or homozygous for the wild-type (WT) allele (Fig. 1A and fig. S2). The familial segregation of these mutant *RORC* alleles was therefore consistent with an autosomal recessive (AR) pattern of inheritance. There were no other genes mutated in the three kindreds among the 173 genes on the 6.87-Mb interval linked with disease (maximum LOD score 6.35). The S17L mutation affects a strictly conserved residue of the DNA binding domain of RORγT (Fig. 1B) and is predicted to be damaging by multiple software algorithms (*5*). The Q308X and Q420X (X signifies a stop codon) nonsense mutations are predicted to result in truncated proteins lacking part of the ligand-binding domain (Fig. 1B). The Q308X and Q420X alleles were not found in the National Center for Biotechnology Information, Ensembl, Exome Aggregation Consortium (ExAC), and dbSNP databases; in our own in-house database of more than 3000 exomes; or in 1052 controls from 52 ethnic groups in the CEPH-HGD panel, indicating that they were very rare variants, possibly exclusive to these two kindreds. There were no nonsense or frameshift mutations affecting isoform 2 (RORγT) in these databases. The S17L allele was found in one heterozygous individual of the ExAC database, indicating that its frequency is less than 10^{-5}. We therefore hypothesized that the bi-allelic *RORC* mutations found in these three kindreds were disease-causing.

Complete RORγ and RORγT deficiency

In mice and humans, the RORγ and RORγT isoforms are generated by transcription from different start sites (*6*–*10*) (Fig. 1B). Both molecules are transcription factors, but they have different expression patterns in inbred mice: RORγ is ubiquitous, whereas RORγT is restricted to leukocytes (*10*). RORγT plays an important role in T cell development and function in mice (*11*, *12*). Animals lacking only RORγT apparently have the same immunological phenotype as those lacking both isoforms (*10*). We first assessed the effect of *RORC* mutations by transiently expressing WT and mutant RORγT and RORγ in human embryonic kidney 293T (HEK293T) cells in the presence and absence of stimulation with phorbol 12-myristate 13-acetate (PMA) and ionomycin. We detected both the WT and S17L RORγT proteins at the expected molecular mass of 56 kD (Fig. 1C). The Q308X and Q420X RORγT mutant proteins had molecular weights consistent with truncation at residues 308 and 420, respectively (Fig. 1C). Similar results were obtained upon expression of RORγ (fig. S3). We then performed an electrophoretic mobility shift assay (EMSA) to assess the ability of the mutant RORγT and RORγ isoforms to respectively bind to RORE-2 and RORE-1, the consensus binding sites in the promoter of *IL17A* (fig. S3). The three mutations abolished DNA binding of RORγT to RORE-2 (Fig. 1C) and of RORγ to RORE-1 (fig. S3), but not by disrupting the nuclear localization of the protein (fig. S3). Each mutation resulted in the loss of *IL17A* promoter activation by RORγT (Fig. 1D) or RORγ (fig. S4). Thus, each mutant allele was associated with a complete loss of function of the two encoded protein isoforms, identifying these patients as cases of human AR complete RORγ/RORγT deficiency (hereafter referred to as RORγT deficiency).

Broad immunological phenotype

Mouse RORγT is expressed in lymphoid tissue inducer (LTi) cells, type 3 innate lymphoid cells (ILC3), type 1 natural killer T (NKT) cells, some γδ T cells, immature $CD4^+CD8^+$ αβ thymocytes, and IL-17A/F–producing $CD4^+$ αβ T cells [T helper 17 (T_H17) cells] (*7*, *11*, *13*–*16*). LTi, ILC3, type 1 NKT, and T_H17 cells fail to develop in $Rorc^{-/-}$ mice, and $CD4^+CD8^+$ αβ thymocytes have a reduced life span (*11*, *14*, *17*). $RORC^{-/-}$ patients displayed clinical signs consistent with LTi deficiency, including absence of palpable axillary and cervical lymph nodes (despite visible tonsils), and had reduced thymus size (Fig. 2A). As in $Rorc^{-/-}$ mice, ILC3 were barely detectable in the patients' blood (fig. S5). In $Rorc^{-/-}$ mice, the short life span of $CD4^+CD8^+$ αβ thymocytes results in an inability to use the most 5′ segments of the T cell receptor (TCR) Vα array (*12*), including those encoding the Vα chains of mucosal associated invariant T (MAIT) (*12*) and type 1 NKT cells (*18*). High-throughput sequencing of the *TRA/TRD* and *TRG* loci revealed that 5′ Vα gene segment use had decreased, whereas Vδ and Vγ usage was normal in $RORC^{-/-}$ T cell clonotypes (fig. S6). Further, these patients lacked *TRA* clonotypes using 5′ Vα and distal 3′ Jα pairings (fig. S6). In total $RORC^{-/-}$ T cell clonotypes, the usage of Vγ9 was elevated (fig. S6), consistent with antigen-driven peripheral expansion of this subset, perhaps driven by mycobacteria (*19*). Abolished use of the Vα segments *TRAV10* (encoding Vα24) and *TRAV1.2* (encoding Vα7.2) was confirmed by quantitative polymerase chain reaction

[1]St. Giles Laboratory of Human Genetics of Infectious Diseases, Rockefeller Branch, The Rockefeller University, New York, NY 10065, USA. [2]Department of Pediatrics, Hiroshima University Graduate School of Biomedical and Health Sciences, Hiroshima, Japan. [3]Immunology Division, Garvan Institute of Medical Research, Darlinghurst, New South Wales, Australia. [4]St Vincent's Clinical School, University of New South Wales, Sydney, New South Wales, Australia. [5]Institute for Research in Biomedicine, University of Italian Switzerland, Bellinzona, Switzerland. [6]Department of Pediatrics, Hadassah University Hospital, Jerusalem, Israel. [7]Department of Immunology, School of Medicine, Universidad de Valparaíso, Santiago, Chile. [8]Department of Pediatrics, Padre Hurtado Hospital and Clinica Alemana, Santiago, Chile. [9]Department of Pediatrics, King Faisal Specialist Hospital and Research Center, Riyadh, Saudi Arabia. [10]Department of Pediatrics, Prince Naif Center for Immunology Research, College of Medicine, King Saud University, Riyadh, Saudi Arabia. [11]Institut Curie, INSERM U932, Paris, France. [12]Division of Immunology, Boston Children's Hospital, Boston, MA 02115, USA. [13]Caritas Baby Hospital, Post Office Box 11535, Jerusalem, Israel. [14]Laboratory of Human Genetics of Infectious Diseases, Necker Branch, INSERM UMR 1163, Paris, France. [15]Paris Descartes University, Imagine Institute, Paris, France. [16]Trudeau Institute, Saranac Lake, NY 12983, USA. [17]La Jolla Institute for Allergy and Immunology, La Jolla, CA 92037, USA. [18]Department of Radiology, Assistance Publique–Hôpitaux de Paris (AP-HP), Necker Hospital for Sick Children, Paris, France. [19]Department of Microbiology and Immunology, Peter Doherty Institute for Infection and Immunity, University of Melbourne, Parkville, Victoria, Australia. [20]Department of Biochemistry and Molecular Biology, School of Biomedical Sciences, Monash University, Clayton, Victoria, Australia. [21]Australian Research Council Centre of Excellence for Advanced Molecular Imaging, Monash University, Clayton, Victoria, Australia. [22]Institute of Infection and Immunity, Cardiff University, School of Medicine, Heath Park, Cardiff CF14 4XN, UK. [23]Laboratoire Dynamique du Génome et Système Immunitaire, INSERM UMR 1163, Université Paris Descartes–Sorbonne Paris Cité, Imagine Institute, Paris, France. [24]Pediatric Hematology-Immunology Unit, AP-HP, Necker Hospital for Sick Children, Paris, France. [25]Institute of Cellular Medicine, Newcastle University and Great North Children's Hospital, Newcastle upon Tyne NE4 6BE, UK. [26]Laboratory of Lymphocyte Activation and Susceptibility to EBV Infection, INSERM UMR 1163, Université Paris Descartes–Sorbonne Paris Cité, Imagine Institute, Paris, France. [27]Department of Paediatric Allergy Immunology, University of Manchester, Royal Manchester Children's Hospital, Manchester, UK. [28]Center for the Study of Primary Immunodeficiencies, AP-HP, Necker Hospital for Sick Children, Paris, France. [29]Manton Center for Orphan Disease Research, Children's Hospital, Boston, MA 02115, USA. [30]Center of Medical Immunology, Institute for Research in Biomedicine, University of Italian Switzerland, Bellinzona, Switzerland. [31]Howard Hughes Medical Institute, New York, NY 10065, USA.

*These authors contributed equally to this work. **†Corresponding author. E-mail: jmarkle@rockefeller.edu (J.G.M.); jean-laurent.casanova@rockefeller.edu (J.-L.C.)** ‡These authors contributed equally to this work. §Present address: Life and Health Sciences Research Institute (ICVS), School of Health Sciences, University of Minho, Braga, Portugal. ||Present address: National Center for HIV/AIDS, Viral Hepatitis, STD, and TB Prevention, Office of Infectious Diseases, Centers for Disease Control and Prevention, Atlanta, GA 30329, USA. ¶These authors contributed equally to this work. #These authors contributed equally to this work.

(fig. S7) and resulted in a lack of both CD161$^+$Vα7.2$^+$ MAIT cells and Vα24$^+$Vβ11$^+$ type 1 NKT cells (Fig. 2, B and C, and fig. S7). Some Vα7.2$^+$ cells other than MAIT cells have recently been shown to recognize *Mycobacterium*-derived mycolyl lipids (*20*); they were also missing in *RORC*$^{-/-}$ patients. Nevertheless, *RORC*$^{-/-}$ patients displayed only mild CD4$^+$ and CD8$^+$ αβ T cell lymphopenia, with normal B and NK cell counts (Fig. 2D and table S2). These patients did not, therefore, have T cell deficiency [also known as "combined" immunodeficiency (CID)], consistent with their lack of broad infectious and autoimmune phenotypes (*21*). Finally, the frequencies of circulating γδ T cells were normal (table S2). Overall, these *RORC*$^{-/-}$ patients displayed the general immunological features characteristic of *Rorc*$^{-/-}$ mice (*11*, *12*, *14*, *22*, *23*). These studies also revealed that the development of MAIT and other Vα7.2$^+$ T cells is critically dependent on RORγT, which had been predicted but not shown in mice. No infectious phenotype can be unambiguously assigned to any of these individual immunological anomalies.

Abolished production of IL-17A/F

Given the critical role of murine RORγT in generating IL-17A/F– and IL-22–producing lymphocytes [including ILC3, γδ T cells, and T_H17 cells (*11*, *13*, *24*)] and the finding that patients with compromised IL-17A/F immunity are susceptible to mucocutaneous candidiasis (*1*), we assessed the development and function of IL-17A/F–producing lymphocytes in the patients. Circulating ILC3 were too few to assess their production of IL-17. CD3$^+$ T cells from *RORC*$^{-/-}$ patients displayed a severe impairment in the production of IL-17A, IL-17F, and IL-22, at both the mRNA (fig. S8) and the protein level (Fig. 3A), after polyclonal stimulation. CD4$^+$ αβ T cells are a major source of IL-17A/F (*9*). Memory (CD45RA$^-$) CD4$^+$ T cells from *RORC*$^{-/-}$ patients produced much less IL-17A, IL-17F, and IL-22 than WT and heterozygous controls (Fig. 3B).

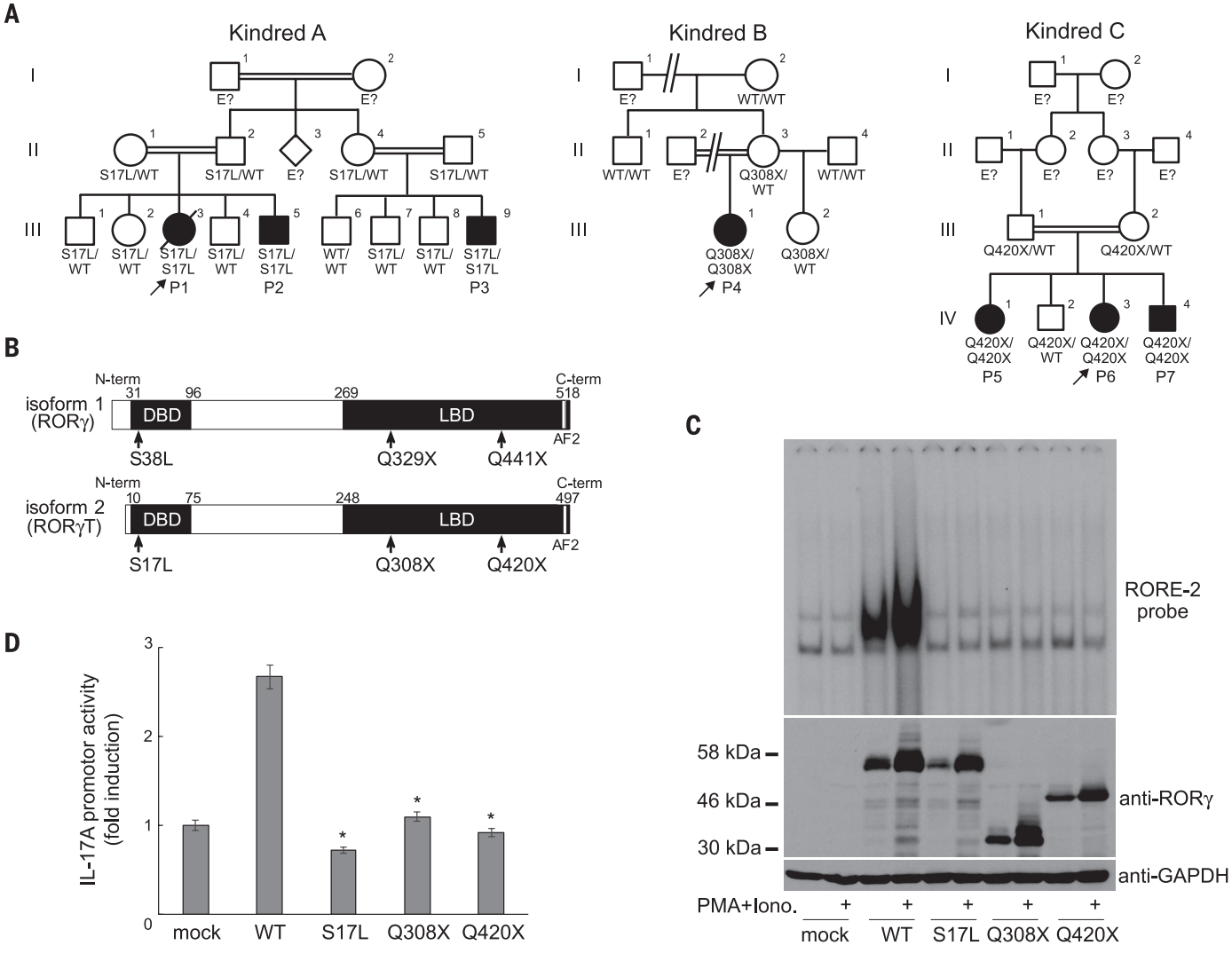

Fig. 1. Identification of homozygous loss-of-function mutations affecting the human RORγT protein. (**A**) Sanger sequencing results and familial segregation of previously unidentified homozygous *RORC* mutations in three unrelated consanguineous families, indicating an AR pattern of inheritance, with complete clinical penetrance. P1, patient 1; P2, patient 2; etc. (**B**) Graphical representation of the RORγ and RORγT proteins, encoded by *RORC* isoforms 1 and 2, respectively. AF2, activation function 2 domain. Arrows indicate the location of the sites affected by the *RORC* mutations found in the families. DBD, DNA binding domain; LBD, ligand-binding domain. (**C**) HEK293T cells were either mock-transfected or transfected with the indicated plasmids. After 24 hours, cells were either left untreated or stimulated with PMA and ionomycin. Whole-cell lysates were obtained and subjected to Western blotting (lower panel), and nuclear lysates were subjected to EMSA with a ^{32}P-labeled RORE-2 probe derived from the *IL17A* promoter sequence (upper panel). GAPDH, glyceraldehyde-3-phosphate dehydrogenase. (**D**) *IL17A* reporter plasmids, the pRL-SV40 vector, and WT or mutant *RORC* plasmid were used to transfect HEK293T cells. After 24 hours, cells were stimulated with PMA and ionomycin as in (C) and then subjected to luciferase assays. Experiments were performed in triplicate, and *IL17A* promoter activity is expressed as fold induction relative to mock-transfected cells. *P < 0.05 versus WT controls; two-tailed Mann-Whitney tests with Bonferroni correction. Error bars denote SEM.

In contrast, the memory CD4$^+$ T cells from these patients produced large amounts of IL-4, IL-5, and IL-13 (fig. S8). In separate experiments, naïve (CD45RA$^+$CCR7$^+$) CD4$^+$ T cells from *RORC*$^{-/-}$ patients cultured under T_H17-polarizing conditions secreted less IL-17A and IL-17F than cells from healthy donors or heterozygous relatives (Fig. 3C). We next assessed the proliferation and cytokine secretion of highly purified WT, heterozygous, and *RORC*$^{-/-}$ CD4$^+$CCR6$^+$ memory αβ T cells (fig. S9), a population enriched in IL-17A/F–secreting cells (T_H17 cells, which express CCR4), as well as cells secreting IL-17A/F and IFN-γ (herein designated as T_H1* cells, which express CXCR3) (*25*), after stimulation with *C. albicans* lysate. By monitoring the incorporation of a radioactive label, we found that CD4$^+$CCR6$^+$ T cells from *RORC*$^{-/-}$ patients had normal frequencies of antigen-specific cells recognizing *C. albicans* (Fig. 3D). However, these cells [including both T_H17 and T_H1* cells, whose proportions were normal (fig. S9)] secreted much lower amounts of IL-17A and IL-22 than did control cells (Fig. 3E). IFN-γ was also reduced, but large amounts of IL-4 were secreted, serving as a control (Fig. 3E). Finally, *Herpesvirus saimiri*–transformed CD4$^+$ αβ T cells from *RORC*$^{-/-}$ patients showed abolished induction of *RORC* (Fig. 4A) and *IL17A* (Fig. 4B), but not *IFNG* serving as a control (fig. S10). The defect in *IL17A* induction could be rescued by retroviral transduction with WT *RORC* (Fig. 4B). Collectively, these data demonstrate a profound diminution of IL-17A/F and IL-22 production by all leukocytes tested in *RORC*$^{-/-}$ patients. As CMC-causing germline mutations have previously been identified in *IL17F*, *IL17RA*, *IL17RC*, and *ACT1* (*1*, *2*, *26*), we conclude that impaired IL-17A/F immunity in *RORC*$^{-/-}$ patients accounts for their development of CMC. Human IL-17A/F–producing ILC3, γδ T cells, and αβ T cells, or any of their subsets, may individually or collectively confer protection against *Candida*.

Selective defect in IFN-γ production

We then investigated the cellular mechanism underlying the patients' surprising susceptibility to mycobacteria. The patients did not display chronic granulomatous disease or severe CID, which can underlie BCG disease (*4*). The CD3$^+$ T cells (including both γδ and αβ T cells) from *RORC*$^{-/-}$ patients produced IFN-γ normally, after the stimulation of whole blood or peripheral blood mononuclear cells (PBMCs) with PMA and ionomycin (fig. S10). Likewise, total CD4$^+$ αβ T cells, memory (CD45RA$^-$) CD4$^+$ T cells, naïve CD4$^+$ T cells cultured under T_H1-polarizing conditions, and *Herpesvirus saimiri*–transformed T cells from

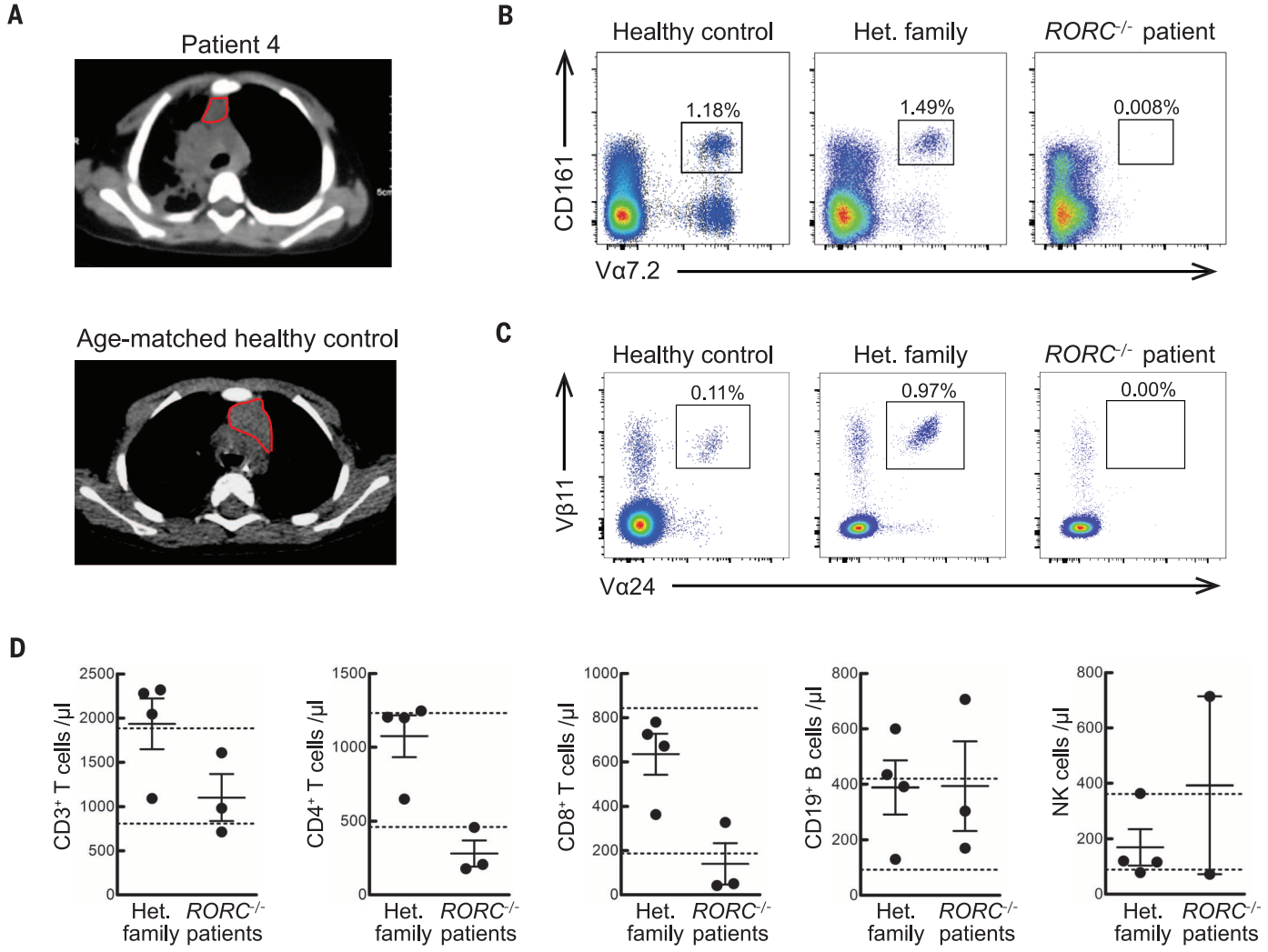

Fig. 2. *RORC*$^{-/-}$ patients display abnormal thymus size and TCRα rearrangement in line with their mild T cell lymphopenia with a complete absence of MAIT and type 1 NKT cells. (**A**) Computed tomography (CT) scan of P4's chest at the age of 16 months compared with a CT scan of a healthy control. P4's scan reveals right lung infiltrate and thymic hypoplasia. (**B** and **C**) PBMCs from WT controls, heterozygous family members, or *RORC*$^{-/-}$ patients were analyzed for MAIT (B) and type 1 NKT (C) cell frequencies by flow cytometry. Each plot is representative of $n = 3$ experiments. (**D**) Cell counts were performed on fresh blood samples from heterozygous family members ($n = 4$) and *RORC*$^{-/-}$ patients ($n = 3$). Dotted lines indicate the normal ranges for each lymphocyte population per microliter of blood, based on the results for healthy individuals tested at the Necker Hospital for Sick Children (Paris, France).

the patients produced IFN-γ normally (fig. S10). Overall, and in contrast to the IL-17A/F defect, RORγT deficiency does not impair IFN-γ secretion in conditions of polyclonal stimulation. We next assessed *Mycobacterium*-specific IFN-γ responses from whole blood (Fig. 5A) or PBMCs (Fig. 5B) of *RORC*$^{-/-}$ patients, heterozygous family members, and healthy controls. The patients' cells produced very little IFN-γ in response to treatment with BCG plus IL-12 (Fig. 5, A and B). This defect was as profound as that seen in patients with IL-12Rβ1 deficiency (*27*). The production of IL-12p40 by *RORC*$^{-/-}$ cells was normal (fig. S11). Impaired IFN-γ production may account for mycobacterial diseases in *RORC*$^{-/-}$ patients. This IFN-γ defect was not secondary to excessive IL-4, IL-5, or IL-13 production (fig. S11) or to the IL-17A/F defect (fig. S12). Many single-gene immunodeficiencies do not predispose to BCG disease despite impaired or abolished development or function of various αβ T cell subsets, including CD4$^+$ T cells (*28*), CD8$^+$ T cells (*29*), type 1 NKT cells (*30*, *31*), and MAIT cells (*31*). Even rare patients deficient in total αβ T cell function [*ZAP70*$^{-/-}$ (*32*), *TRAC*$^{-/-}$ (*33*)] have not been reported to develop BCG disease. Whole blood or PBMCs from such patients responded normally to treatment with BCG plus IL-12, except for patients lacking all functional αβ T cells (fig. S12). As MAIT cells were shown to respond to mycobacteria (*34*), we purified these

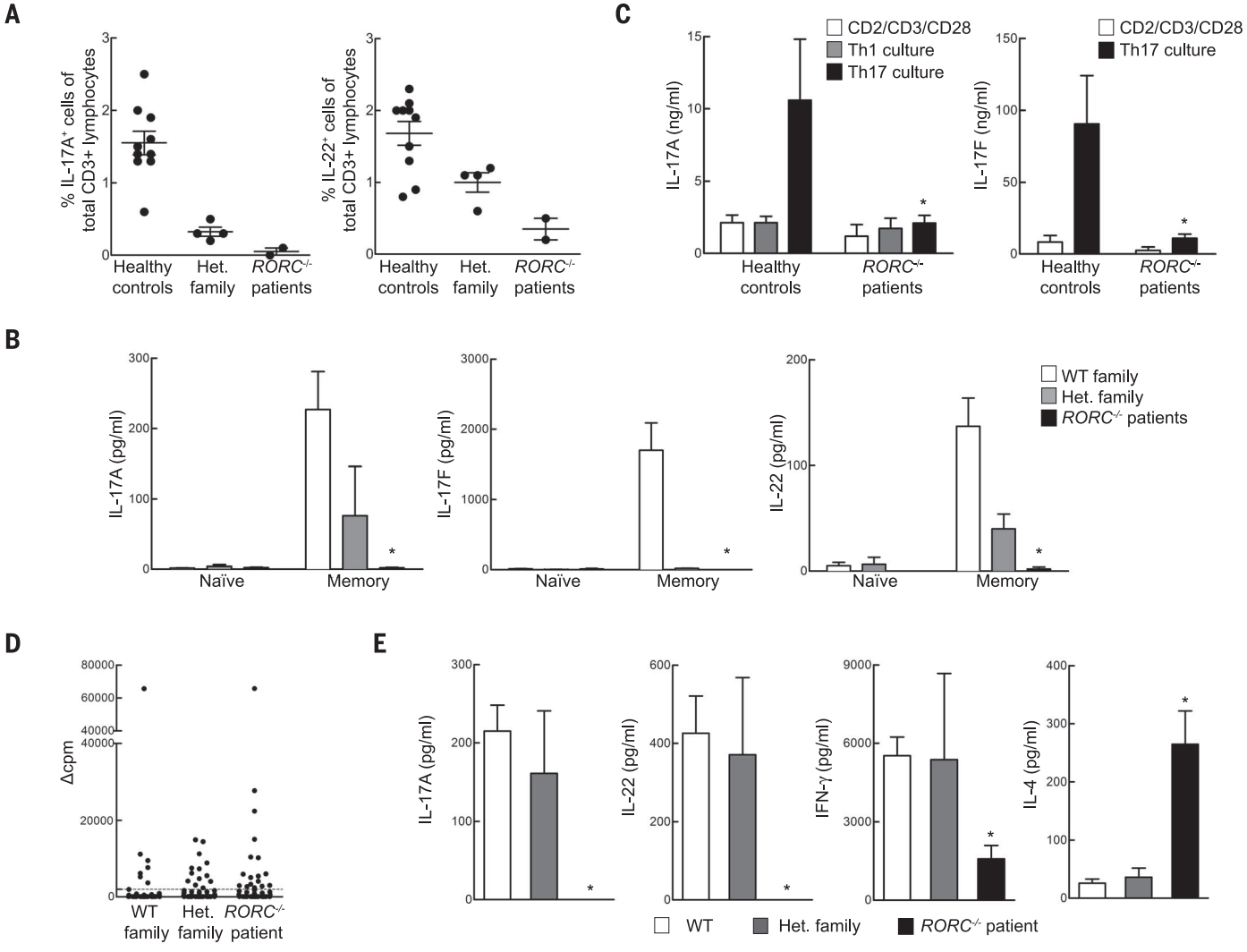

Fig. 3. Cellular mechanisms of compromised IL-17 immunity and CMC in *RORC*$^{-/-}$ patients. (**A**) Whole blood from healthy WT donors, heterozygous family members, or *RORC*$^{-/-}$ patients was activated by PMA and ionomycin in the presence of brefeldin A, then assessed by intracellular flow cytometry for the production of IL-17A and IL-22. (**B**) Naïve and memory CD4$^+$ T cells from WT controls (n = 7), heterozygous family members (n = 2), and *RORC*$^{-/-}$ patients (n = 3) were cultured with T cell activation and expansion (TAE) beads, and the culture supernatants were then assessed for secretion of the cytokine indicated (*37*). (**C**) Cytokine production by in vitro–differentiated CD4$^+$ T cells from control donors and *RORC*$^{-/-}$ patients. Naïve (CD45RA$^+$CCR7$^+$) CD4$^+$ T cells were purified from the PBMCs of WT controls (n = 6) or *RORC*$^{-/-}$ patients (n = 3), then cultured in the presence of TAE beads alone or TAE beads together with polarizing stimuli to induce the differentiation of T_H1- or T_H17-type cells (*37*). After 5 days, culture supernatants were assessed for the secretion of the cytokines indicated. (**D**) Sorted CCR6$^+$ memory CD4$^+$ T cells from WT controls, heterozygous family members, and *RORC*$^{-/-}$ patients were initially polyclonally stimulated to generate T cell libraries, then cultured with autologous irradiated B cells, with or without a 3-hour pulse with *C. albicans* lysate (5 μg/ml) (*37*). Proliferation was assessed by evaluating radiolabel incorporation on day 4 and is expressed as Δcpm values (cpm, counts per minute) (*37*). Dotted lines represent the cutoff values. The frequencies of specific T cells using the Poisson distribution were 315/10^6, 631/10^6, and 874/10^6 in WT control, heterozygous family member, and *RORC*$^{-/-}$ patient, respectively. (**E**) Concentrations of the indicated cytokines were measured in the supernatants from positive cultures (Δcpm values above the cut-off value) from experiments performed as in (D) with cells from WT controls, heterozygous family members, and *RORC*$^{-/-}$ patients (n = 2 each). Number of wells: n = 45 to 64 for WT controls, n = 4 to 10 for heterozygous family members, and n = 14 to 23 for *RORC*$^{-/-}$ patients. *P < 0.05 versus WT controls; in two-tailed Mann-Whitney tests with Bonferroni correction. Error bars in (B), (C), and (E) indicate SEM.

cells from WT donor PBMCs and added them to PBMCs from *RORC*$^{-/-}$ patients before BCG stimulation. The lack of MAIT cells in *RORC*$^{-/-}$ patients did not account for their impaired IFN-γ production (fig. S13). Overall, the absence of type 1 NKT and MAIT cells, the mild T cell lymphopenia, and the poor development of IL-17A/F T cells may contribute marginally to mycobacterial susceptibility but do not account for the low level of IFN-γ production by *RORC*$^{-/-}$ leukocytes stimulated with BCG and IL-12, and probably not for the patients' mycobacterial disease.

Impaired IFN-γ production by γδ T cells

We thus systematically characterized the consequences of leukocyte population depletions on BCG-dependent IFN-γ production by PBMCs in healthy controls. We found no overt IFN-γ defect as a consequence of depleting NK cells, CD14$^+$ cells, or CD4$^+$ or CD8$^+$ T cells. Depletion of αβ T cells, γδ T cells, or both resulted in diminished IFN-γ production (fig. S14). To probe the kinetics of this phenotype, a similar experiment was repeated and supernatant was assessed at 6, 12, 18, 24, and 48 hours poststimulation (fig. S14). The effect of γδ T cell depletion was most apparent at 24 hours (fig. S14). We observed high expression of *RORC* isoform 2 mRNA in both αβ and γδ T cells of healthy donors (fig. S15), prompting further analyses of γδ T cell function. Flow cytometry analyses revealed that the TCR^{high} γδ T cells from *RORC*$^{-/-}$ patients could not secrete IFN-γ in response to stimulation with PMA and ionomycin, unlike TCR^{low} γδ T cells (fig. S15). TCR Vδ2$^+$ cells have been reported as the predominant cells responding to human BCG vaccination (*19*). *RORC*$^{-/-}$ patients had normal frequencies of TCR Vδ2$^+$ cells, but these cells were unable to secrete IFN-γ when stimulated with PMA and ionomycin (fig. S15), suggesting a possible contribution of this γδ T cell subset defect to mycobacterial susceptibility in *RORC*$^{-/-}$ patients. Overall, RORγT deficiency diminishes the IFN-γ–producing capacity of γδ T cells, which normally produce this cytokine in response to *Mycobacterium* stimulation.

The patients' CD4$^+$CCR6$^+$ αβ T cells produce little IFN-γ in response to BCG

Previous studies have demonstrated that the T-bet– and RORγT-expressing, IFN-γ and IL-17A/F–producing CCR6$^+$CXCR3$^+$ T$_H$1* subset is strongly enriched for *Mycobacterium*-responsive CD4$^+$ αβ T cells, unlike the CCR6$^+$CCR4$^+$ T$_H$17 cells that only express RORγT and produce IL-17A/F and are enriched for *Candida*-responsive T cells (*25*). We therefore purified memory (CD45RA$^-$) αβ T cell subsets (fig. S9) and assessed their proliferation and cytokine production in response to a pool of BCG peptides. CD4$^+$CCR6$^+$ αβ T cells from *RORC*$^{-/-}$ patients had a normal or high frequency of antigen-specific cells recognizing BCG peptides, as demonstrated by the induction of proliferation (Fig. 5C and fig. S16). However, although CD4$^+$CCR6$^+$ T cells from *RORC*$^{-/-}$ patients responded to mycobacterial antigens, they secreted much less IFN-γ than CD4$^+$CCR6$^+$ αβ T cells from normal donors (Fig. 5D). The normal proliferation and cytokine production of other CD4$^+$ memory T cell subsets in response to *Candida* and *Mycobacterium* (fig. S17) and to irrelevant viral stimuli (fig. S18) indicate a selective RORγT-dependent functional defect in *Mycobacterium*-specific CD4$^+$CCR6$^+$ αβ T cells. Although we did not purify and test T$_H$1* cells, they were present in normal proportions in the patients (fig. S9), implying that they are functionally defective for IFN-γ production upon *Mycobacterium* stimulation. Collectively, these data suggest that mycobacterial diseases in *RORC*$^{-/-}$ patients may result from the poor production of IFN-γ by γδ T cells, CCR6$^+$CXCR3$^+$CD4$^+$ αβ T$_H$1* cells, or both in response to mycobacteria. IFN-γ treatment may therefore be beneficial for *RORC*$^{-/-}$ patients. This combined defect probably also accounts for mycobacterial disease in severe combined immunodeficient patients, as patients with various forms of CID are normally resistant to BCG (*27*, *33*). Finally, the lack of MAIT and type 1 NKT cells, reduction in ILC3, and possibly the absence of other lymphocytes not analyzed using blood samples (e.g., LTi) may aggravate the mycobacterial phenotype of *RORC*$^{-/-}$ patients.

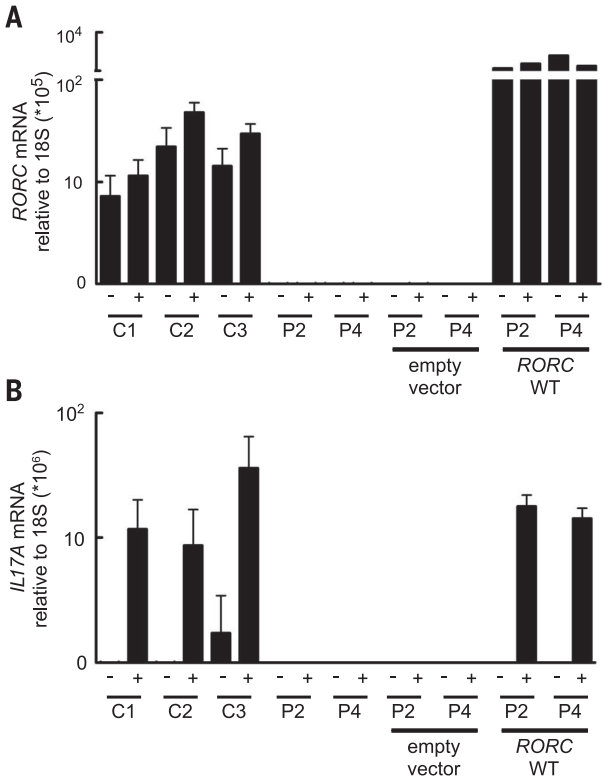

Fig. 4. T cell lines from *RORC*$^{-/-}$ patients fail to induce *IL17A* after mitogen stimulation. (**A**) *Herpesvirus saimiri*–transformed T cells from healthy donors (C1, C2, C3) or *RORC*$^{-/-}$ patients (P2, P4) were cultured in the presence (+) or absence (–) of PMA and ionomycin, and then total RNA was extracted and used for quantitative reverse transcription polymerase chain reaction for total *RORC*. T cell lines from *RORC*$^{-/-}$ patients were transduced with retrovirus encoding either a tag only (empty vector) or tagged WT *RORC* isoform 2. (**B**) *IL17A* expression was assessed in the same RNA samples presented in (A). *n* = 3 replicates; error bars represent SEM.

Conclusion

Collectively, these data demonstrate that human *RORC* plays a surprising dual role in host defense. These findings are clinically, immunologically, and genetically robust, as they were consistent in seven patients from three ethnic groups, homozygous for three different *RORC* mutations that are loss-of-function for both isoforms. Although the two infectious phenotypes are purely recessive, some immunological phenotypes showed codominant or dominant inheritance. The mild T cell lymphopenia, small thymus, lack of palpable axillary and cervical lymph nodes, and absence of MAIT and type 1 NKT cells in *RORC*$^{-/-}$ patients were consistent with the phenotype of *Rorc*$^{-/-}$ mice (table S3). Likewise, impaired IL-17A/F immunity was predicted to account for impaired protection against *Candida albicans* (*35*), as *Rorc* is the master gene controlling T$_H$17 differentiation in inbred mice (*11*), and mutations affecting human IL-17A/F immunity underlie isolated CMC (*1*, *26*, *36*). The IL-17A/F defect therefore underlies CMC in RORγT-deficient patients, probably but not necessarily because of T cells, as other cells can produce these cytokines in healthy individuals. We expected these patients to be susceptible to candidiasis, but their susceptibility to mycobacterial disease and its severity were unanticipated. This phenotype does not seem to be human-specific, as we also found that mice deficient for *Rorc* (*14*) are susceptible to mycobacterial infection (fig. S19). Our data conclusively demonstrate that human *RORC* plays an indispensable role in the induction of IFN-γ–dependent antimycobacterial systemic immunity. The mechanism underlying disease in these patients probably involves an impairment of the induction of IFN-γ production by γδ T cells, CCR6$^+$CXCR3$^+$CD4$^+$ αβ T$_H$1* cells, or both in response to mycobacteria. Other mechanisms may also be at work. Human *RORC* is essential not only for the development of IL-17A/F–producing lymphocytes protecting the mucocutaneous barriers against *Candida* but also for the activation of IFN-γ–producing T cells and for systemic protection against *Mycobacterium*.

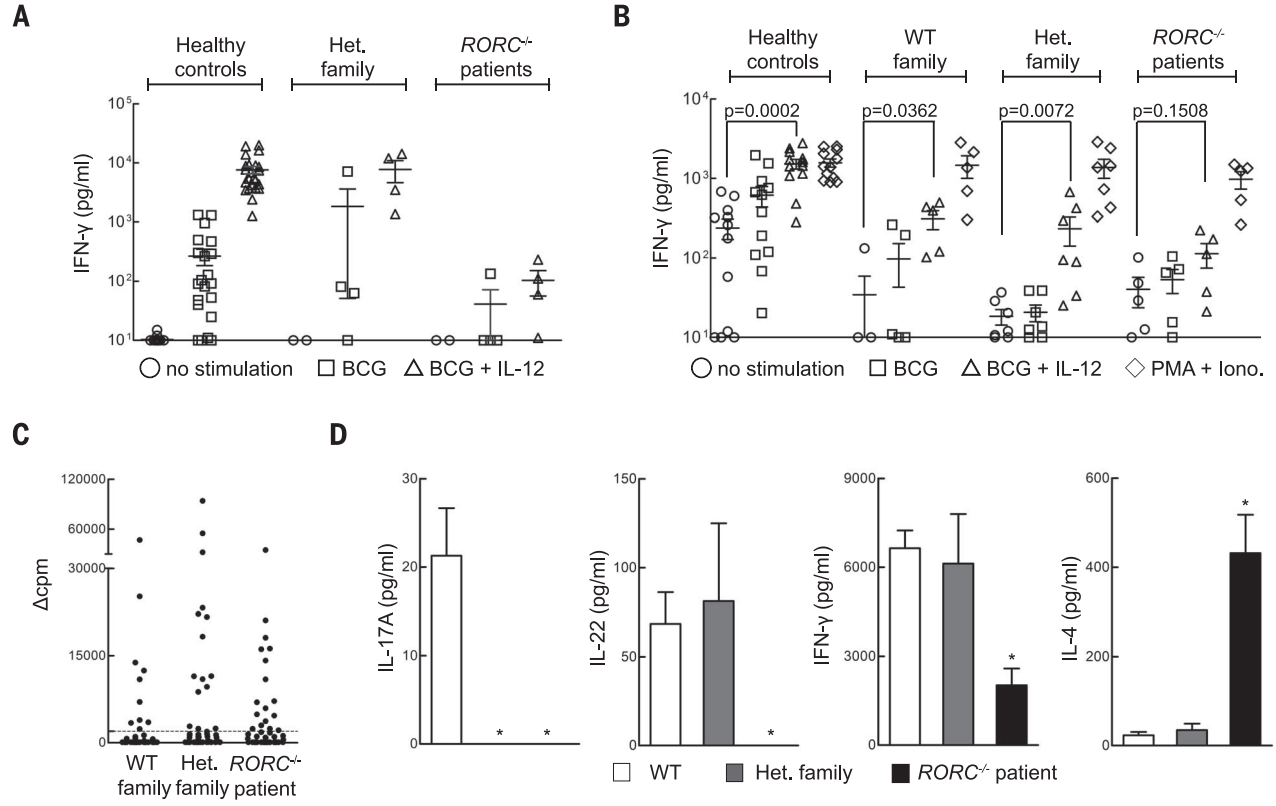

Fig. 5. Cellular mechanisms of impaired IFN-γ immunity to *Mycobacterium* in *RORC*$^{-/-}$ patients. (**A**) Whole-blood samples from healthy controls (n = 23), heterozygous family members (n = 4), or *RORC*$^{-/-}$ patients (n = 4) were incubated for 48 hours under three different sets of activation conditions: (i) medium alone, (ii) live *M. bovis*–BCG (BCG) at a multiplicity of infection of 20 BCG cells per leukocyte, and (iii) BCG plus 20 ng/ml IL-12. The IFN-γ levels of culture supernatants were determined by enzyme-linked immunosorbent assay (ELISA). (**B**) Equal numbers of live PBMCs from healthy controls, WT family members, heterozygous family members, or *RORC*$^{-/-}$ patients were cultured in the presence of live BCG, BCG and IL-12, or PMA/ionomycin for 48 hours. IFN-γ concentration in the culture supernatant was assessed by ELISA. (**C**) Sorted CCR6^{+} memory CD4^{+} T cells were polyclonally stimulated with PHA in the presence of irradiated allogeneic feeder cells and IL-2 to generate T cell libraries, as in Fig. 3D. Library screening was performed 14 to 21 days after initial stimulation by culturing thoroughly washed T cells with autologous irradiated B cells, with or without a 3-hour pulse with *M. bovis*–BCG peptide pools. Proliferation was measured by radiolabel incorporation on day 4 and is expressed as Δcpm values. Each symbol illustrates one culture. Dotted lines represent the cutoff value. The frequencies of specific T cells calculated using the Poisson distribution were 467/10^{6}, 749/10^{6}, and 875/10^{6} in WT control, heterozygous family member, and *RORC*$^{-/-}$ patient, respectively. (**D**) The cytokines indicated were determined in the culture supernatants from (C) for wells with Δcpm values above the cutoff value. Number of wells: n = 45 to 64 for WT controls, n = 4 to 10 for heterozygous family members, and n = 14 to 23 for *RORC*$^{-/-}$ patients. *P < 0.05 versus WT controls; in two-tailed Mann-Whitney tests with Bonferroni correction. Error bars in (D) indicate SEM.

REFERENCES AND NOTES

1. A. Puel *et al.*, *Science* **332**, 65–68 (2011).
2. Y. Ling *et al.*, *J. Exp. Med.* **212**, 619–631 (2015).
3. D. Bogunovic *et al.*, *Science* **337**, 1684–1688 (2012).
4. J. Bustamante, S. Boisson-Dupuis, L. Abel, J.-L. Casanova, *Semin. Immunol.* **26**, 454–470 (2014).
5. M. Kircher *et al.*, *Nat. Genet.* **46**, 310–315 (2014).
6. A. Medvedev, A. Chistokhina, T. Hirose, A. M. Jetten, *Genomics* **46**, 93–102 (1997).
7. I. Villey, R. de Chasseval, J. P. de Villartay, *Eur. J. Immunol.* **29**, 4072–4080 (1999).
8. Y. W. He, M. L. Deftos, E. W. Ojala, M. J. Bevan, *Immunity* **9**, 797–806 (1998).
9. Q. Ruan *et al.*, *J. Exp. Med.* **208**, 2321–2333 (2011).
10. G. Eberl, D. R. Littman, *Immunol. Rev.* **195**, 81–90 (2003).
11. I. I. Ivanov *et al.*, *Cell* **126**, 1121–1133 (2006).
12. J. Guo *et al.*, *Nat. Immunol.* **3**, 469–476 (2002).
13. X. O. Yang *et al.*, *Immunity* **28**, 29–39 (2008).
14. G. Eberl *et al.*, *Nat. Immunol.* **5**, 64–73 (2004).
15. C. E. Sutton *et al.*, *Immunity* **31**, 331–341 (2009).
16. M. L. Robinette *et al.*, *Nat. Immunol.* **16**, 306–317 (2015).
17. M. L. Michel *et al.*, *Proc. Natl. Acad. Sci. U.S.A.* **105**, 19845–19850 (2008).
18. T. Egawa *et al.*, *Immunity* **22**, 705–716 (2005).
19. D. F. Hoft, R. M. Brown, S. T. Roodman, *J. Immunol.* **161**, 1045–1054 (1998).
20. I. Van Rhijn *et al.*, *Nat. Immunol.* **14**, 706–713 (2013).
21. L. D. Notarangelo, *Annu. Rev. Immunol.* **31**, 195–225 (2013).
22. Z. Sun *et al.*, *Science* **288**, 2369–2373 (2000).
23. G. Eberl, D. R. Littman, *Science* **305**, 248–251 (2004).
24. H. Takatori *et al.*, *J. Exp. Med.* **206**, 35–41 (2009).
25. E. V. Acosta-Rodriguez *et al.*, *Nat. Immunol.* **8**, 639–646 (2007).
26. B. Boisson *et al.*, *Immunity* **39**, 676–686 (2013).
27. J. Feinberg *et al.*, *Eur. J. Immunol.* **34**, 3276–3284 (2004).
28. M. Ouederni *et al.*, *Blood* **118**, 5108–5118 (2011).
29. O. de la Calle-Martin *et al.*, *J. Clin. Invest.* **108**, 117–123 (2001).
30. B. Pasquier *et al.*, *J. Exp. Med.* **201**, 695–701 (2005).
31. E. Martin *et al.*, *Nature* **510**, 288–292 (2014).
32. A. C. Chan *et al.*, *Science* **264**, 1599–1601 (1994).
33. N. V. Morgan *et al.*, *J. Clin. Invest.* **121**, 695–702 (2011).
34. L. Le Bourhis *et al.*, *Nat. Immunol.* **11**, 701–708 (2010).
35. H. R. Conti *et al.*, *J. Exp. Med.* **206**, 299–311 (2009).
36. L. Liu *et al.*, *J. Exp. Med.* **208**, 1635–1648 (2011).
37. Materials and methods are available as supplementary materials on *Science* Online.

ACKNOWLEDGMENTS

We thank the patients and their families for their collaboration; both branches of the Laboratory of Human Genetics of Infectious Diseases for helpful discussions and support; M. Hindiyeh for expert clinical care of the patients from Kindred A; G. C. Tsokos for providing the *IL17A* reporter luciferase plasmid; E. Van de Vosse for providing the pLZRS-IRES-ΔNGFR vector; D. Littman for helpful discussions; B. Fleckenstein and M. Schmidt for the generation of patient-derived T cell lines; and Y. Nemirovskaya, L. Amar, E. Anderson, M. Courat, and T. Nivare for administrative support. The data presented in the manuscript are tabulated in the main paper and in the supplementary materials. The sequence data are available in the Sequence Read Archive (www.ncbi.nlm.nih.gov/sra) with accession numbers SRS964935, SRS965039, SRS965040, and SRS965042. J.Mc. and The University of Melbourne filed Australian provisional patent application numbers 2014901185 and 2014901 that relate to ligands that bind MR1 and stimulate MAIT cells. The Laboratory of Human Genetics of Infectious Diseases is supported by grants from the National Center for Research Resources and the National Center for Advancing Sciences,

NIH (8UL1TR000043); the French National Research Agency (ANR) under the "Investments for the Future" program (grant ANR-10-IAHU-01), grant IFNGPHOX (13-ISV3-0001-01 to J.B.), and grant GENCMCD (11-BSV3-005-01 to A.P); Laboratoire d'Excellence Integrative Biology of Emerging Infectious Diseases (ANR-10-LABX-62-IBEID); the National Health and Medical Research Council (NHMRC) (to E.K.D., C.S.M., S.G.T, and J.Mc.); the Rockefeller University; INSERM; Université Paris Descartes; the St. Giles Foundation; the National Institute of Allergy and Infectious Diseases (R37AI095983 to J.-L.C.); and the NIH (contract HHSN272200900044C to A.S.). S.O. was supported by Grants-in-Aid for Scientific Research from the Japan Society for the Promotion of Science (25713039 and 25670477), J.G.M. by the Canadian Institutes of Health Research, R.M.-B. by the European Molecular Biology Organization, Y.I. by the AXA Research Fund, L.A.H. by the Rheumatology Research Foundation's Scientist Development Award, and F.S. by grants from the European Research Council (323183 PREDICT) and the Swiss National Science Foundation (149475). The Institute for Research in Biomedicine and the Center of Medical Immunology are supported by the Helmut Horten Foundation. S.A.-M. is the bronchial asthma research chair of the Prince Naif Center for Immunology Research.

SUPPLEMENTARY MATERIALS

www.sciencemag.org/content/349/6248/606/suppl/DC1
Materials and Methods
Supplementary Text
Figs. S1 to S19
Tables S1 to S3
References (*38*–*67*)

7 December 2014; accepted 29 June 2015
Published online 9 July 2015
10.1126/science.aaa4282

TOPOLOGICAL MATTER

Discovery of a Weyl fermion semimetal and topological Fermi arcs

Su-Yang Xu,[1,2]* Ilya Belopolski,[1]* Nasser Alidoust,[1,2]* Madhab Neupane,[1,3]* Guang Bian,[1] Chenglong Zhang,[4] Raman Sankar,[5] Guoqing Chang,[6,7] Zhujun Yuan,[4] Chi-Cheng Lee,[6,7] Shin-Ming Huang,[6,7] Hao Zheng,[1] Jie Ma,[8] Daniel S. Sanchez,[1] BaoKai Wang,[6,7,9] Arun Bansil,[9] Fangcheng Chou,[5] Pavel P. Shibayev,[1,10] Hsin Lin,[6,7] Shuang Jia,[4,11] M. Zahid Hasan[1,2]†

A Weyl semimetal is a new state of matter that hosts Weyl fermions as emergent quasiparticles and admits a topological classification that protects Fermi arc surface states on the boundary of a bulk sample. This unusual electronic structure has deep analogies with particle physics and leads to unique topological properties. We report the experimental discovery of a Weyl semimetal, tantalum arsenide (TaAs). Using photoemission spectroscopy, we directly observe Fermi arcs on the surface, as well as the Weyl fermion cones and Weyl nodes in the bulk of TaAs single crystals. We find that Fermi arcs terminate on the Weyl fermion nodes, consistent with their topological character. Our work opens the field for the experimental study of Weyl fermions in physics and materials science.

Weyl fermions have long been known in quantum field theory, but have not been observed as a fundamental particle in nature (*1*–*3*). Recently, it was understood that a Weyl fermion can emerge as a quasiparticle in certain crystals, Weyl fermion semimetals (*1*–*22*). Despite being a gapless metal, a Weyl semimetal is characterized by topological invariants, broadening the classification of topological phases of matter beyond insulators. Specifically, Weyl fermions at zero energy correspond to points of bulk band degeneracy, Weyl nodes, which are associated with a chiral charge that protects gapless surface states on the boundary of a bulk sample. These surface states take the form of Fermi arcs connecting the projection of bulk Weyl nodes in the surface Brillouin zone (BZ) (*6*). A band structure like the Fermi arc surface states would violate basic band theory in an isolated two-dimensional (2D) system and can only arise on the boundary of a 3D sample, providing a dramatic example of the bulk-boundary correspondence in a topological phase. In contrast to topological insulators where only the surface states are interesting (*21*, *22*), a Weyl semimetal features unusual band structure in the bulk and on the surface. The Weyl fermions in the bulk are predicted to provide a condensed-matter realization of the chiral anomaly, giving rise to a negative magnetoresistance under parallel electric and magnetic fields, unusual optical conductivity, nonlocal transport, and local nonconservation of ordinary current (*5*, *12*–*16*). At the same time, the Fermi arc surface states are predicted to show unconventional quantum oscillations in magneto-transport, as well as unusual quantum interference effects in tunneling spectroscopy (*17*–*19*). The prospect of the realization of these phenomena has inspired much experimental and theoretical work (*1*–*22*).

Here we report the experimental realization of a Weyl semimetal in a single crystalline material, tantalum arsenide (TaAs). Using the combination of the vacuum ultraviolet (low–photon-energy) and soft x-ray (SX) angle-resolved photoemission spectroscopy (ARPES), we systematically and differentially study the surface and bulk electronic structure of TaAs. Our ultraviolet (low–photon-energy) ARPES measurements, which are highly surface sensitive, demonstrate the existence of the Fermi arc surface states, consistent with our band calculations presented here. Moreover, our SX-ARPES measurements, which are reasonably bulk sensitive, reveal the 3D linearly dispersive bulk Weyl cones and Weyl nodes. Furthermore, by combining the low–photon-energy and SX-ARPES data, we show that the locations of the projected bulk Weyl nodes correspond to the terminations of the Fermi arcs within our experimental resolution. These systematic measurements demonstrate TaAs as a Weyl semimetal.

The material system and theoretical considerations

Tantalum arsenide is a semimetallic material that crystallizes in a body-centered tetragonal lattice system (Fig. 1A) (*23*). The lattice constants are a = 3.437 Å and c = 11.656 Å, and the space group is $I4_1md$ (#109, C_{4v}), as consistently reported in previous structural studies (*23*–*25*). The crystal consists of interpenetrating Ta and As sublattices, where the two sublattices are shifted by $(\frac{a}{2}, \frac{a}{2}, \delta)$, $\delta \approx \frac{c}{12}$. Our diffraction data match well with the lattice parameters and the space group $I4_1md$ (*26*). The scanning tunneling microscopic (STM) topography (Fig. 1B) clearly resolves the (001) square lattice without any obvious defect. From the topography, we obtain a lattice constant a = 3.45 Å. Electrical transport measurements on TaAs confirmed its semimetallic transport properties and reported negative magnetoresistance, suggesting the anomalies due to Weyl fermions (*23*).

We discuss the essential aspects of the theoretically calculated bulk band structure (*9*, *10*) that predicts TaAs as a Weyl semimetal candidate. Without spin-orbit coupling, calculations (*9*, *10*) show that the conduction and valence bands interpenetrate (dip into) each other to form four 1D line nodes (closed loops) located on the k_x and k_y planes (shaded blue in Fig. 1, C and E). Upon the inclusion of spin-orbit coupling, each line node loop is gapped out and shrinks into six Weyl nodes that are away from the $k_x = 0$ and $k_y = 0$ mirror planes (Fig. 1E, small filled circles). In our calculation, in total there are 24 bulk Weyl cones (*9*, *10*), all of which are linearly dispersive and are associated

[1]Laboratory for Topological Quantum Matter and Spectroscopy (B7), Department of Physics, Princeton University, Princeton, NJ 08544, USA. [2]Princeton Center for Complex Materials, Princeton Institute for Science and Technology of Materials, Princeton University, Princeton, NJ 08544, USA. [3]Condensed Matter and Magnet Science Group, Los Alamos National Laboratory, Los Alamos, NM 87545, USA. [4]International Center for Quantum Materials, School of Physics, Peking University, China. [5]Center for Condensed Matter Sciences, National Taiwan University, Taipei 10617, Taiwan. [6]Centre for Advanced 2D Materials and Graphene Research Centre National University of Singapore, 6 Science Drive 2, Singapore 117546. [7]Department of Physics, National University of Singapore, 2 Science Drive 3, Singapore 117542. [8]Quantum Condensed Matter Division, Oak Ridge National Laboratory, Oak Ridge, TN 37831, USA. [9]Department of Physics, Northeastern University, Boston, MA 02115, USA. [10]Princeton Institute for Science and Technology of Materials, Princeton University, Princeton, NJ 08544, USA. [11]Collaborative Innovation Center of Quantum Matter, Beijing, 100871, China.
*These authors contributed equally to this work. †Corresponding author. E-mail: mzhasan@princeton.edu

with a single chiral charge of ±1 (Fig. 1E). We denote the 8 Weyl nodes that are located on the brown plane ($k_z = \frac{2\pi}{c}$) as W1 and the other 16 nodes that are away from this plane as W2. At the (001) surface BZ (Fig. 1F), the eight W1 Weyl nodes are projected in the vicinity of the surface BZ edges, $\overline{X}$ and $\overline{Y}$. More interestingly, pairs of W2 Weyl nodes with the same chiral charge are projected onto the same point on the surface BZ. Therefore, in total there are eight projected W2 Weyl nodes with a projected chiral charge of ±2, which are located near the midpoints of the $\overline{\Gamma} - \overline{X}$ and the $\overline{\Gamma} - \overline{Y}$ lines. Because the ±2 chiral charge is a projected value, the Weyl cone is still linear (*9*). The number of Fermi arcs terminating on a projected Weyl node must equal its projected chiral charge. Therefore, in TaAs, two Fermi arc surface states must terminate on each projected W2 Weyl node.

Surface electronic structure of TaAs

We carried out low–photon-energy ARPES measurements to explore the surface electronic structure of TaAs. Figure 1H presents an overview of the (001) Fermi surface map. We observe three types of dominant features, namely a crescent-shaped feature in the vicinity of the midpoint of each $\overline{\Gamma} - \overline{X}$ or $\overline{\Gamma} - \overline{Y}$ line, a bowtie-like feature centered at the $\overline{X}$ point, and an extended feature centered at the $\overline{Y}$ point. We find that the Fermi surface and the constant-energy contours at shallow binding energies (Fig. 2A) violate the C_4 symmetry, considering the features at $\overline{X}$ and $\overline{Y}$ points. In the crystal structure of TaAs, where the rotational symmetry is implemented as a screw axis that sends the crystal back into itself after a C_4 rotation and a translation by $\frac{c}{2}$ along the rotation axis, such an asymmetry is expected in calculation. The crystallinity of the (001) surface in fact breaks the rotational symmetry. We now focus on the crescent-shaped features. Their peculiar shape suggests the existence of two arcs, and their termination points in k-space seem to coincide with the surface projection of the W2 Weyl nodes. Because the crescent feature consists of two nonclosed curves, it can either arise from two Fermi arcs or a closed contour; however, the decisive property that clearly distinguishes one case from the other is the way in which the constant-energy contour evolves as a function of energy. As shown in Fig. 2F, in order for the crescent feature to be Fermi arcs, the two nonclosed curves have to move (disperse) in the same direction as one varies the energy (*26*). We now provide ARPES data to show that the crescent features in TaAs indeed exhibit this "copropagating" property. To do so, we single out a crescent feature, as shown in Fig. 2, B and E, and show the band dispersions at representative momentum space cuts, cut I and cut II, as defined in Fig. 2E. The corresponding E–k dispersions are shown in Fig. 2, C and D. The evolution (dispersive "movement") of the bands as a function of binding energy can be clearly read from the slope of the bands in the dispersion maps and is indicated in Fig. 2E by the white arrows. It can be seen that the evolution of the two nonclosed curves is consistent with the copropagating property. To further visualize the evolution of the constant-energy contour throughout k_x, k_y space, we use surface state constant-energy contours at two slightly different binding energies, namely $E_B = 0 = E_F$ and $E_B = 20$ meV. Figure 2G shows the difference between these two constant-energy contours, namely $\Delta I(k_x, k_y) = I(E_B = 20\ \text{meV}, k_x, k_y) - I(E_B = 0\ \text{meV}, k_x, k_y)$, where I is the ARPES intensity. The k-space regions in Fig. 2G that have negative spectral weight (red) correspond to the constant-energy contour at $E_B = 0$ meV, whereas those regions with positive spectral weight (blue) correspond to the contour at $E_B = 20$ meV. Thus, one can visualize the two contours in a single k_x, k_y map. The alternating "red-blue-red-blue" sequence for each crescent feature in Fig. 2G shows the copropagating property, consistent with Fig. 2F. Furthermore, we note that there are two crescent features, one located near the $k_x = 0$ axis and the other near the $k_y = 0$ axis, in Fig. 2G. The fact that we observe the copropagating property for two independent crescent features that are 90° rotated with respect to each other further shows that this observation is not due to artifacts, such as a k misalignment while performing the subtraction. The above systematic data reveal the existence of Fermi arcs on the (001) surface of TaAs. Just as one can identify a crystal as a topological insulator by observing an odd number of Dirac cone surface states, we emphasize that our data here are sufficient to identify TaAs as a Weyl semimetal because of bulk-boundary correspondence in topology.

Theoretically, the copropagating property of the Fermi arcs is unique to Weyl semimetals

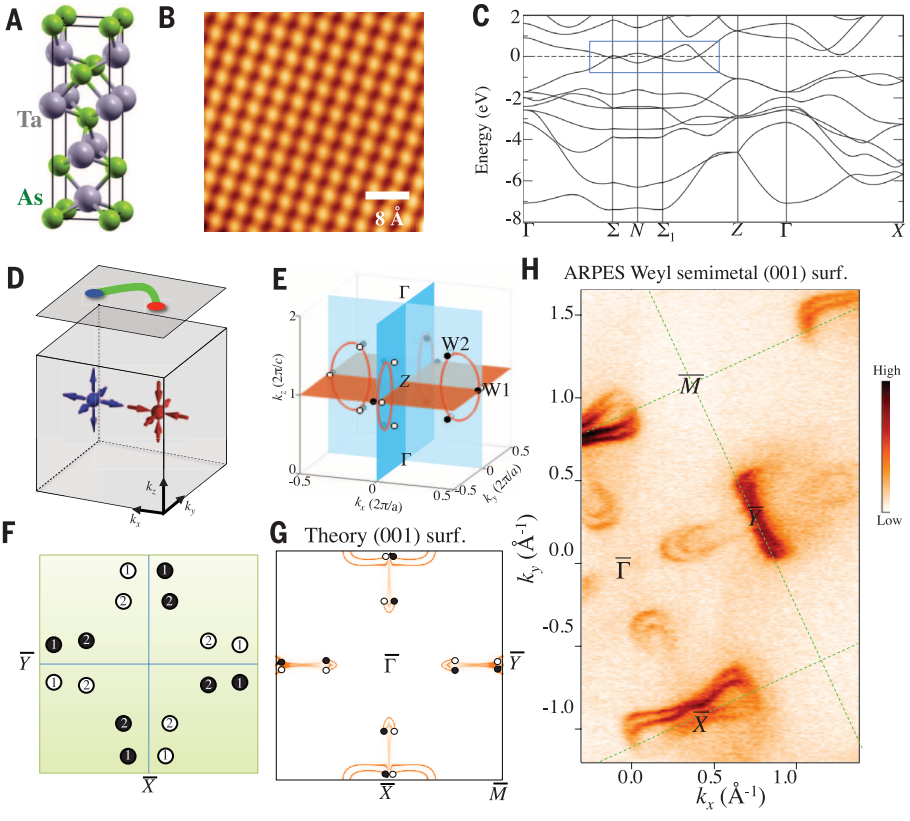

Fig. 1. Topology and electronic structure of TaAs. (**A**) Body-centered tetragonal structure of TaAs, shown as stacked Ta and As layers. The lattice of TaAs does not have space inversion symmetry. (**B**) STM topographic image of TaAs's (001) surface taken at the bias voltage −300 mV, revealing the surface lattice constant. (**C**) First-principles band structure calculations of TaAs without spin-orbit coupling. The blue box highlights the locations where bulk bands touch in the BZ. (**D**) Illustration of the simplest Weyl semimetal state that has two single Weyl nodes with the opposite (±1) chiral charges in the bulk. (**E**) In the absence of spin-orbit coupling, there are two line nodes on the k_x mirror plane and two line nodes on the k_y mirror plane (red loops). In the presence of spin-orbit coupling, each line node reduces into six Weyl nodes (small black and white circles). Black and white show the opposite chiral charges of the Weyl nodes. (**F**) A schematic (not to scale) showing the projected Weyl nodes and their projected chiral charges. (**G**) Theoretically calculated band structure (*26*) of the Fermi surface on the (001) surface of TaAs. (**H**) The ARPES-measured Fermi surface of the (001) cleaving plane of TaAs. The high-symmetry points of the surface BZ are noted.

because it arises from the nonzero chiral charge of the projected bulk Weyl nodes (*26*), which in this case is ±2. Therefore, this property distinguishes the crescent Fermi arcs not only from any closed contour but also from the double Fermi arcs in Dirac semimetals (*27*, *28*), because the bulk Dirac nodes do not carry any net chiral charges (*26*). After observing the surface electronic structure containing Fermi arcs in our ARPES data, we are able to slightly tune the free parameters of our surface calculation and obtain a calculated surface Fermi surface that reproduces and explains our ARPES data (Fig. 1G). This serves as an important cross-check that our data and interpretation are self-consistent. Specifically, our surface calculation indeed also reveals the crescent Fermi arcs that connect the projected W2 Weyl nodes near the midpoints of each $\overline{\Gamma}-\overline{X}$ or $\overline{\Gamma}-\overline{Y}$ line (Fig. 1G). In addition, our calculation shows the bowtie surface states centered at the $\overline{X}$ point, also consistent with our ARPES data. According to our calculation, these bowtie surface states are in fact Fermi arcs (*26*) associated with the W1 Weyl nodes near the BZ boundaries. However, our ARPES data cannot resolve the arc character because the W1 Weyl nodes are too close to each other in momentum space compared to the experimental resolution. Additionally, we note that the agreement between the ARPES data and the surface calculation upon the contour at the $\overline{Y}$ point can be further improved by fine-optimizing the surface parameters. To establish the topology, it is not necessary for the data to have a perfect correspondence with the details of calculation because some changes in the choice of the surface potential allowed by the free parameters do not change the topology of the materials, as is the case in topological insulators (*21*, *22*). In principle, Fermi arcs can coexist with additional closed contours in a Weyl semimetal (*6*, *9*), just as Dirac cones can coexist with additional trivial surface states in a topological insulator (*21*, *22*). Particularly, establishing one set of Weyl Fermi arcs is sufficient to prove a Weyl semimetal (*6*). This is achieved by observing the crescent Fermi arcs as we show here by our ARPES data in Fig. 2, which is further consistent with our surface calculations.

Bulk measurements

We now present bulk-sensitive SX-ARPES (*29*) data, which reveal the existence of bulk Weyl cones and Weyl nodes. This serves as an independent proof of the Weyl semimetal state in TaAs. Figure 3B shows the SX-ARPES measured k_x-k_z Fermi surface at $k_y=0$ (note that none of the Weyl nodes are located on the $k_y=0$ plane). We emphasize that the clear dispersion along the k_z direction (Fig. 3B) firmly shows that our SX-ARPES predominantly images the bulk bands. SX-ARPES boosts the bulk-surface contrast in favor of the bulk band structure, which can be further tested by measuring the band dispersion along the k_z axis in the SX-ARPES setting. This is confirmed by the agreement between the ARPES data (Fig. 3B) and the corresponding bulk band calculation (Fig. 3A). We now choose an incident photon energy (i.e., a k_z value) that corresponds to the k-space location of W2 Weyl nodes and map the corresponding k_x-k_y Fermi surface. As shown in Fig. 3C, the Fermi points that are located away from the k_x or k_y axes are the W2 Weyl nodes. In Fig. 3D, we clearly observe two linearly dispersive cones that correspond to the two nearby W2 Weyl nodes along cut 1. The k-space separation between the two W2 Weyl nodes is measured to be 0.08 Å^{-1}, which is consistent with both the bulk calculation and the separation of the two terminations of the crescent Fermi arcs measured in Fig. 2. The linear dispersion along the out-of-plane direction for the W2 Weyl nodes is shown by our data in Fig. 3E. Additionally, we also observe the W1 Weyl cones in Fig. 3, G to I. Notably, our data show that the energy of the bulk W1 Weyl nodes is lower than that of the bulk W2 Weyl nodes, which agrees well with our calculation shown in Fig. 3J and an independent modeling of the bulk transport data on TaAs (*23*).

In general, in a spin-orbit–coupled bulk crystal, point-like linear band crossings can either be Weyl cones or Dirac cones. Because the observed bulk

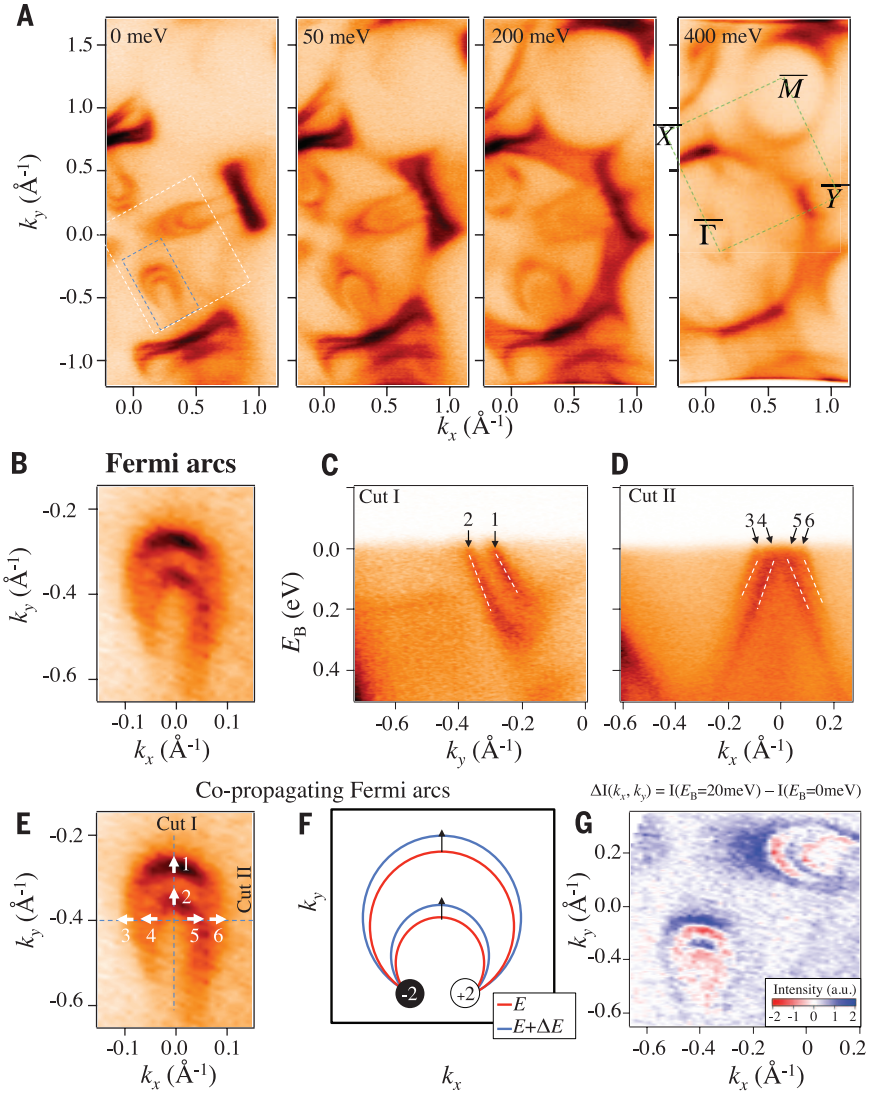

Fig. 2. Observation of topological Fermi arc surface states on the (001) surface of TaAs. (**A**) ARPES Fermi surface map and constant–binding energy contours measured with incident photon energy of 90 eV. (**B**) High-resolution ARPES Fermi surface map of the crescent Fermi arcs. The k-space range of this map is defined by the blue box in (A). (**C** and **D**) Energy dispersion maps along cuts I and II. (**E**) Same Fermi surface map as in (B). The dotted lines define the k-space direction for cuts I and II. The numbers 1 to 6 denote the Fermi crossings that are located on cuts I and II. The white arrows show the evolution of the constant-energy contours as one varies the binding energy, which is obtained from the dispersion maps in (C) and (D). (**F**) A schematic showing the evolution of the Fermi arcs as a function of energy, which clearly distinguishes between two Fermi arcs and a closed contour. (**G**) The difference between the constant-energy contours at the binding energy $E_B=20$ meV and the binding energy $E_B=0$ meV, from which one can visualize the evolution of the constant-energy contours through k_x-k_y space. The range of this map is shown by the white dotted box in (A).

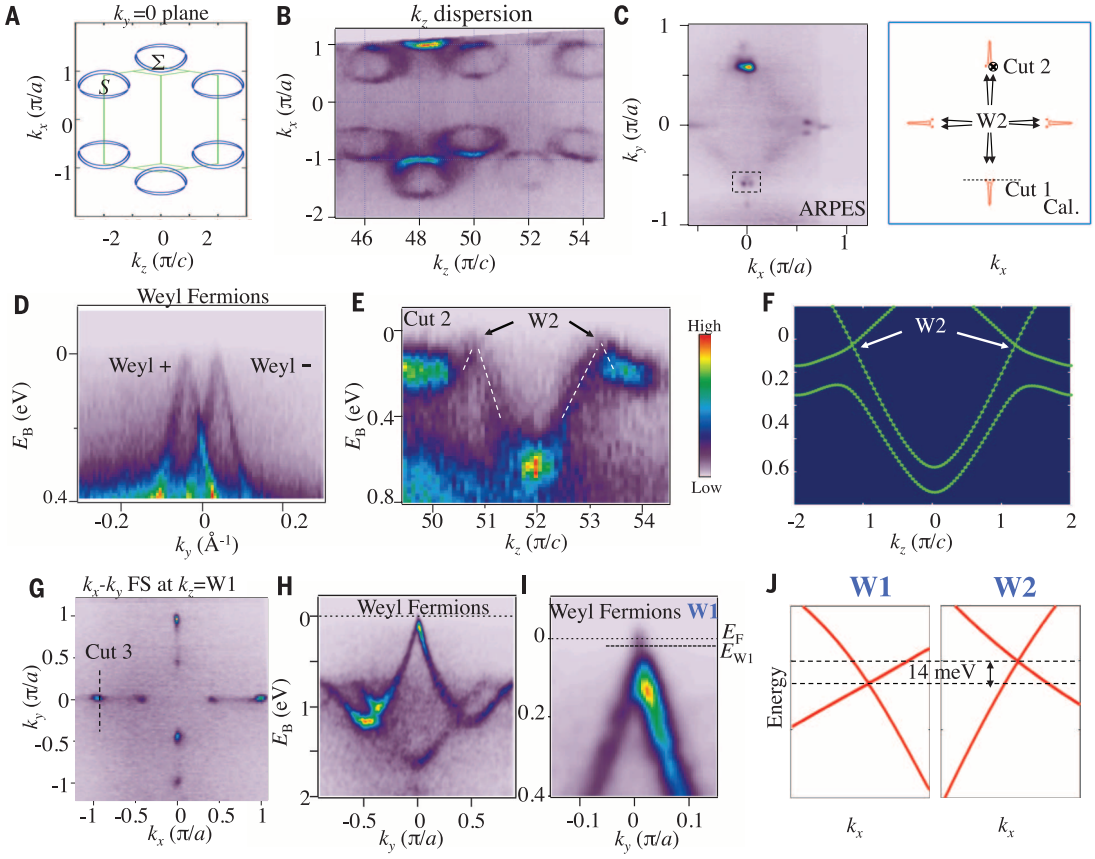

Fig. 3. Observation of bulk Weyl fermion cones and Weyl nodes in TaAs. (**A** and **B**) First-principles calculated and ARPES-measured $k_z - k_x$ Fermi surface maps at $k_y = 0$, respectively. (**C**) ARPES-measured and first-principles calculated $k_x - k_y$ Fermi surface maps at the k_z value that corresponds to the W2 Weyl nodes. The dotted line defines the k-space cut direction for cut 1, which goes through two nearby W2 Weyl nodes along the k_y direction. The black cross defines cut 2, which means that the k_x, k_y values are fixed at the location of a W2 Weyl node and one varies the k_z value. (**D**) ARPES $E - k_y$ dispersion map along the cut 1 direction, which clearly shows the two linearly dispersive W2 Weyl cones. (**E**) ARPES $E - k_z$ dispersion map along the cut 2 direction, showing that the W2 Weyl cone also disperses linearly along the out-of-plane k_z direction. (**F**) First-principles calculated $E - k_z$ dispersion that corresponds to the cut 2 shown in (E). (**G**) ARPES measured $k_x - k_y$ Fermi surface maps at the k_z value that corresponds to the W1 Weyl nodes. The dotted line defines the k-space cut direction for cut 3, which goes through the W1 Weyl nodes along the k_y direction. (**H** and **I**) ARPES $E - k_y$ dispersion map and its zoomed-in version along the cut 3 direction, revealing the linearly dispersive W1 Weyl cone. (**J**) First-principles calculation shows a 14-meV energy difference between the W1 and W2 Weyl nodes.

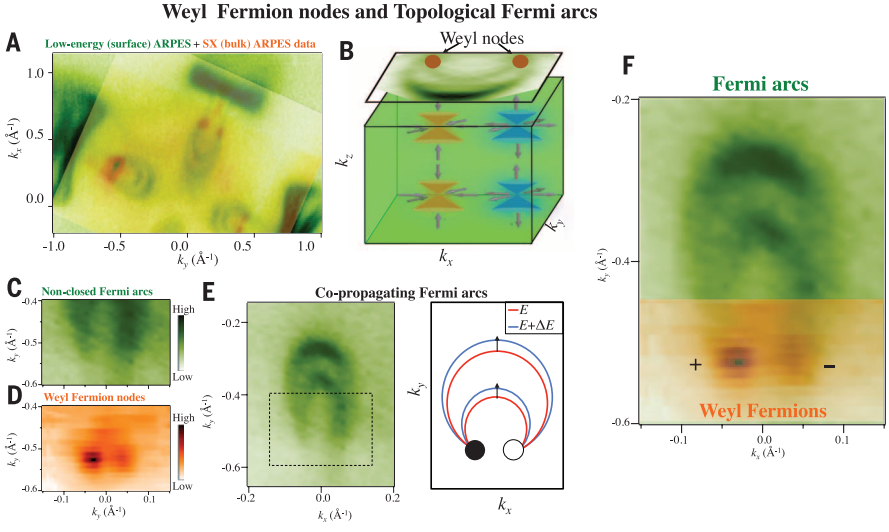

Fig. 4. Surface-bulk correspondence and the topologically nontrivial state in TaAs. (**A**) Low–photon-energy ARPES Fermi surface map ($h\upsilon = 90$ eV) from Fig. 2A, with the SX-ARPES map ($h\upsilon = 650$ eV) from Fig. 3C overlaid on top of it to scale, showing that the locations of the projected bulk Weyl nodes correspond to the terminations of the surface Fermi arcs. (**B**) The bottom shows a rectangular tube in the bulk BZ that encloses four W2 Weyl nodes. These four W2 Weyl nodes project onto two points at the (001) surface BZ with projected chiral charges of ±2, shown by the brown circles. The top surface shows the ARPES measured crescent surface Fermi arcs that connect these two projected Weyl nodes. (**C**) Surface state Fermi surface map at the k-space region corresponding to the terminations of the crescent Fermi arcs. The k-space region is defined by the black dotted box in (E). (**D**) Bulk Fermi surface map at the k-space region corresponding to the W2 Weyl nodes. The k-space region is defined by the black dotted box in Fig. 3C. (**E**) ARPES and schematic of the crescent-shaped co-propagating Fermi arcs. (**F**) High resolution ARPES maps of the Fermi arcs and the Weyl fermion nodes.

cones in Fig. 3, C and D, are located neither at Kramers' points nor on a rotational axis, they cannot be identified as bulk Dirac cones and have to be Weyl cones according to topological theories (*6*, *28*). Therefore, our SX-ARPES data alone prove the existence of bulk Weyl nodes. The agreement between the SX-ARPES data and our bulk calculation, which only requires the crystal structure and the lattice constants as inputs, provides a further cross-check.

Bulk-surface correspondence

Finally, we show that the k-space locations of the surface Fermi arc terminations match with the projection of the bulk Weyl nodes on the surface BZ. We superimpose the SX-ARPES measured bulk Fermi surface containing W2 Weyl nodes (Fig. 3C) onto the low–photon-energy ARPES Fermi surface containing the surface Fermi arcs (Fig. 2A) to scale. From Fig. 4A we see that all the arc terminations and projected Weyl nodes match with each other within the k-space region that is covered in our measurements. To establish this point quantitatively, in Fig. 4C, we show the zoomed-in map near the crescent Fermi arc terminations, from which we obtain the k-space location of the terminations to be at $\vec{k}_{\mathrm{arc}} = (0.04 \pm 0.01\,\text{Å}^{-1}, 0.51 \pm 0.01\,\text{Å}^{-1})$. Figure 4D shows the zoomed-in map of two nearby W2 Weyl nodes, from which we obtain the k-space location of the W2 Weyl nodes to be at $\vec{k}_{\mathrm{W2}} = (0.04 \pm 0.015\,\text{Å}^{-1}, 0.53 \pm 0.015\,\text{Å}^{-1})$. In our bulk calculation, the k-space location of the W2 Weyl nodes is found to be at $(0.035\,\text{Å}^{-1}, 0.518\,\text{Å}^{-1})$. Because the SX-ARPES bulk data and the low–photon-energy ARPES surface data are completely independent measurements obtained with two different beamlines, the fact that they match well provides another piece of evidence of the topological nature (the surface-bulk correspondence) of the Weyl semimetal state in TaAs. In figs. S5 to S7, we further show that the bulk Weyl cones can also be observed in our low–photon-energy ARPES data, although their spectral weight is much lower than the surface state intensities that dominate the data. Our demonstration of the Weyl fermion semimetal state in and Fermi arc surface metals paves the way (*30*) for the realization of many fascinating topological quantum phenomena.

REFERENCES AND NOTES

1. H. Weyl, *Z. Phys.* **56**, 330–352 (1929).
2. L. Balents, *Physics* **4**, 36 (2011).
3. F. Wilczek, *Phys. Today* **51**, 11 (1998).
4. M. Z. Hasan, S.-Y. Xu, M. Neupane, in *Topological Insulators: Fundamentals and Perspectives*, F. Ortmann, S. Roche, S. O. Valenzuela, Eds. (Wiley, New York, 2015).
5. H. B. Nielsen, M. Ninomiya, *Phys. Lett. B* **130**, 389–396 (1983).
6. X. Wan, A. M. Turner, A. Vishwanath, S. Y. Savrasov, *Phys. Rev. B* **83**, 205101 (2011).
7. B. Singh *et al.*, *Phys. Rev. B* **86**, 115208 (2012).
8. S.-Y. Xu *et al.*, *Science* **332**, 560–564 (2011).
9. S.-M. Huang *et al.*, *Nat. Commun.* **6**, 7373 (2015).
10. H. Weng, C. Fang, Z. Fang, F. B. Andrei Bernevig, X. Dai, *Phys. Rev. X* **5**, 011029 (2015).
11. J. Liu, D. Vanderbilt, *Phys. Rev. B* **90**, 155316 (2014).
12. A. A. Zyuzin, A. A. Burkov, *Phys. Rev. B* **86**, 115133 (2012).
13. D. T. Son, B. Z. Spivak, *Phys. Rev. B* **88**, 104412 (2013).
14. C.-X. Liu, P. Ye, X.-L. Qi, *Phys. Rev. B* **87**, 235306 (2013).
15. H. Wei, S.-P. Chao, V. Aji, *Phys. Rev. Lett.* **109**, 196403 (2012).
16. P. E. C. Ashby, J. P. Carbotte, *Phys. Rev. B* **87**, 245131 (2013).
17. P. Hosur, *Phys. Rev. B* **86**, 195102 (2012).
18. T. Ojanen, *Phys. Rev. B* **87**, 245112 (2013).
19. A. C. Potter, I. Kimchi, A. Vishwanath, *Nat. Commun.* **5**, 5161 (2014).
20. S. Murakami, *New J. Phys.* **9**, 356 (2007).
21. M. Z. Hasan, C. L. Kane, *Rev. Mod. Phys.* **82**, 3045–3067 (2010).
22. X.-L. Qi, S.-C. Zhang, *Rev. Mod. Phys.* **83**, 1057–1110 (2011).
23. C.-L. Zhang *et al.*, Observation of the Adler-Bell-Jackiw chiral anomaly in a Weyl semimetal. http://arxiv.org/abs/1503.02630 (2015).
24. J. J. Murray *et al.*, *J. Less Common Met.* **46**, 311–320 (1976).
25. S. Furuseth *et al.*, *Acta Chem. Scand.* **19**, 95–106 (1965).
26. Materials and methods are available as supplementary materials on *Science* Online.
27. S.-Y. Xu *et al.*, *Science* **347**, 294–298 (2015).
28. B.-J. Yang, N. Nagaosa, *Nat. Commun.* **5**, 4898 (2014).
29. V. N. Strocov *et al.*, *J. Synchrotron Radiat.* **21**, 32–44 (2014).
30. M. Z. Hasan, "Topological Insulators: A New Form of Quantum Matter," presentation at 2014 Nobel Symposium on New Forms of Matter, www.fysik.su.se/~ardonne/nobel/ns156-program.pdf (2014).

ACKNOWLEDGMENTS

Work at Princeton University and Princeton-led synchrotron-based ARPES measurements were supported by the Gordon and Betty Moore Foundations EPiQS Initiative through grant GBMF4547 (Hasan). First-principles band structure calculations at National University of Singapore were supported by the National Research Foundation, Prime Minister's Office, Singapore, under its NRF fellowship (NRF Award no. NRF-NRFF2013-03). Single-crystal growth was supported by National Basic Research Program of China (grant nos. 2013CB921901 and 2014CB239302) and characterization by U.S. Department of Energy DE-FG-02-05ER46200. F.C. acknowledges the support provided by MOST-Taiwan under project no. 102-2119-M-002-004. We gratefully acknowledge J. D. Denlinger, S. K. Mo, A. V. Fedorov, M. Hashimoto, M. Hoesch, T. Kim, and V. N. Strocov for their beamline assistance at the Advanced Light Source, the Stanford Synchrotron Radiation Lightsource, the Diamond Light Source, and the Swiss Light Source under their external user programs. Part of the work was carried out at the Swiss Light Source through the external/international facility user program. We thank T.-R. Chang for help on theoretical band structure calculations. We also thank L. Balents, D. Huse, I. Klebanov, T. Neupert, A. Polyakov, P. Steinhardt, H. Verlinde, and A. Vishwanath for discussions. R.S. and H.L. acknowledge visiting scientist support from Princeton University. M.Z.H. acknowledges hospitality of the Lawrence Berkeley National Laboratory and Aspen Center for Physics as a visiting scientist. A patent application is being prepared on behalf of the authors on the discovery of a Weyl semimetal.

SUPPLEMENTARY MATERIALS

www.sciencemag.org/content/349/6248/613/suppl/DC1
Materials and Methods
Supplementary Text
Figs. S1 to S10
References (*31*, *32*)

15 February 2015; accepted 6 July 2015
Published online 16 July 2015
10.1126/science.aaa9297

REPORTS

ROCK PHYSICS

Rock physics of fibrous rocks akin to Roman concrete explains uplifts at Campi Flegrei Caldera

Tiziana Vanorio* and Waruntorn Kanitpanyacharoen†

Uplifts in the Campi Flegrei caldera reach values unsurpassed anywhere in the world (~2 meters). Despite the marked deformation, the release of strain appears delayed. The rock physics analysis of well cores highlights the presence of two horizons, above and below the seismogenic area, underlying a coupled process. The basement is a calc-silicate rock housing hydrothermal decarbonation reactions, which provide lime-rich fluids. The caprock above the seismogenic area has a pozzolanic composition and a fibril-rich matrix that results from lime-pozzolanic reactions. These findings provide evidence for a natural process reflecting that characterizing the cementitious pastes in modern and Roman concrete. The formation of fibrous minerals by intertwining filaments confers shear and tensile strength to the caprock, contributing to its ductility and increased resistance to fracture.

The caldera of Campi Flegrei (fig. S1) is one of the active hydrothermal systems of the Mediterranean region experiencing notable unrest episodes in a densely populated area. During the last crisis of 1982 to 1984, nearly 40,000 people were evacuated for almost 2 years from the main town of Pozzuoli, the Roman Puteoli, owing to the large uplifts (~2 m over 2 years) and the persistent seismic activity (*1*). The evacuation severely hampered the economy and the social make-up of the community, which included the relocation of schools and commercial shops, as well as the harbor being rendered useless for docking. Despite the large uplifts, the release of strain appears delayed (*2*, *3*). Seismicity reaches a magnitude of 4.0 only upon relatively

Stanford Rock Physics Laboratory, Department of Geophysics, Stanford University, Stanford, CA 94305, USA.
***Corresponding author. E-mail: tvanorio@stanford.edu** †Present address: Department of Geology, Faculty of Science, Chulalongkorn University, Thailand.

large uplifts (~70 to 80 cm), contrary to what is generally observed for calderas exhibiting much lower deformation levels (*4*–*6*). Over and above the specific mechanism causing the unrest (*7*, *8*) and the lack of identification of a shallow magmatic reservoir (<4 km) by seismic data (*9*–*11*), there is a core question of how the subsurface rocks of Campi Flegrei withstand a large strain and have high strength. We combine high-resolution microstructural and mineralogical analyses with the elastic and mechanical properties of well cores (fig. S2) from the deep wells of San Vito (SV1 and SV2) and Mofete (MF1, MF2, and MF5) that were drilled in the area right before the unrest of 1982 to 1984 (*12*) (fig. S1). The rock physics analysis provides evidence for a natural, coupled process that by releasing lime-rich fluids from the deeper basement through decarbonation reactions triggers pozzolanic activity in the shallower caprock. The fibril-rich matrix characterizing the caprock is responsible for an improved resistance to fracture.

The submersion below sea level of part of Pozzuoli due to the slow sinking of the ground and the difficulty of the local economy in buffering the adverse impacts of ground deformations have been known since Roman time (*13*). Because of the ancient civilization of Puteoli (~600 BCE), there is a richness of historical resources as well as an unprecedented record of data (~2000 years) of the gradual uplift and subsidence of the town (*14*) (Fig. 1). The phenomenon is referenced in the literature as the Bradyseism, which slowly affected the area over time, leading to the existence of numerous Roman sites below sea level (e.g., the Roman harbor of Portus Julius, Claudius' Villa, spas, and fishponds). A key feature of the secular displacement is that it is at times interrupted by short-term, high-rate uplift episodes (e.g., 1538, 1970 to 1972, 1982 to 1984). Among these, only the episode on the secular uplift characterizing the period from 1000 to 1500 (Fig. 1A) led to an eruption in 1538. The most recent, large uplift episodes (1970 to 1972, 1982 to 1984; Fig. 1B), which instead occurred on a long-term descending phase (Fig. 1A), did not culminate in an eruption despite the large magnitude of the deformations. These latter examples are three to six times as large as those observed at Yellowstone and Long Valley caldera (*15*).

The starting points of this study are two of the features identified through the three-dimensional (3D) tomographic reconstruction of the Campi Flegrei caldera from passive data (*11*). The seismogenic area (fig. S3) lies between a higher-velocity basement (depth ~3.0 km) and a caprock whose existence and morphology are traced by the inversion of *P*- and *S*-wave velocities (1.0 km < depth < 2.0 km) (*11*). The caprock (fig. S3) corresponds to a seismic horizon that bends upward in an arch shape underneath the town of Pozzuoli, overtopping the seismo-active area. Starting from these premises, we characterize the microstructure and the rock physics properties of the caprock along with the microstructural composition of the basement rock by selecting well-core samples from a depth of 1.0 to 2.0 km and 2.0 to 2.8 km, respectively.

The rock samples selected from the deeper basement are siltstones and marls (*16*). Compositionally, the samples range from a calc-silicate (calcite <5%) to carbonate-silicate rock (calcite ~26%) as depth increases. In addition, they contain phlogopite (10 to 19%), K-feldspar (22 to 48%), diopside (0 to 36%, in SV wells), calc-analbite (30 to 45%), and quartz (0 to 27%, in MF wells). We conducted additional imaging analyses to complement the mineralogical ones and to observe the nature of the rock microstructure, identifying the smallest minerals and examining the distribution of these within the pore space (*17*). At high magnification, the microstructure of the rock reveals the presence of porous rims containing a well-aligned, needly crystalline phase that grows in between calcite grains and the quartz- and feldspar-rich matrix (Fig. 2, A, B, D, and E). Synchrotron x-ray diffraction

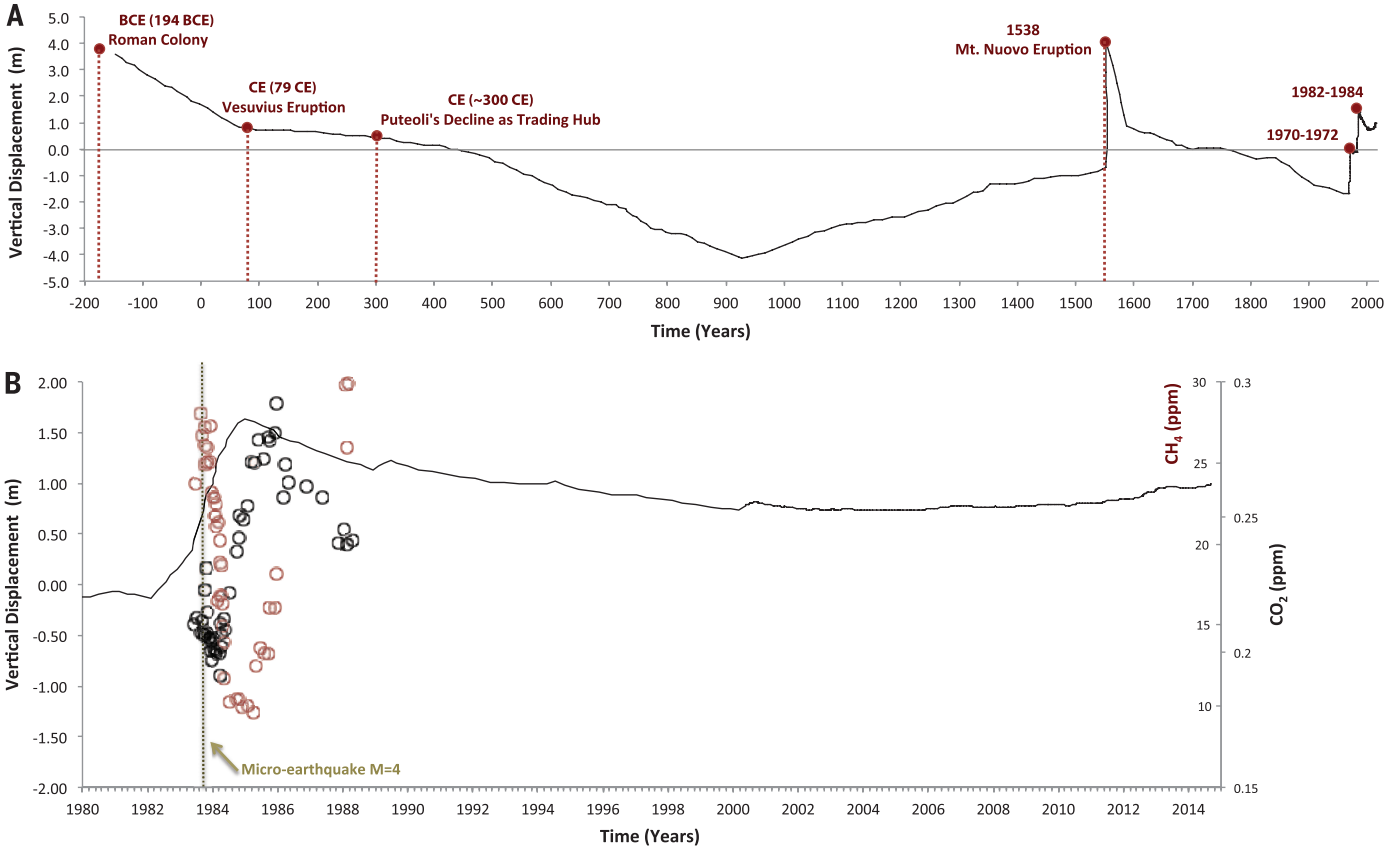

Fig. 1. Vertical displacement and geochemical variations as functions of time. (**A**) Vertical displacement measured in Pozzuoli over the last 2000 years (*2*, *16*). The figure highlights main historical and volcanological events concerning the Roman Puteoli and the Neapolitan area. (**B**) Magnified scale of the vertical displacement over the last 34 years (*2*), along with the measured variations of CO_2 (open black circles) and CH_4 (open red circles) (*33*).

(XRD) analysis identified this phase as actinolite (Fig. 2, C and F), in the amount of 4% (*17*). A closer analysis of the images revealed the presence of clusters of spherules about 10 μm in size (Fig. 2, G and H), which are nested in between the needle structure of actinolite. We performed scanning electron microscopy–energy-dispersive x-ray spectroscopy (SEM-EDS) analysis for elemental concentration, which identified the spherules to be pure graphite (Fig. 2I).

Of particular interest is the microstructural and elastic characterization of the rocks from the tuffite formation between 1.3- and 1.7-km depth (*16*), as it corresponds to the caprock that overtops the seismogenic area. The samples exhibit a fine microcrystalline structure (Fig. 3, A and B) that XRD analysis shows to be constituted by K-feldspar, albite, and fine crystals of calcite. The microcrystalline matrix is interspersed with inclusions of calcium carbonate (Fig. 3C) and secondary porosity (Fig. 3A) likely due to the enhancement of the pore space by dissolution of relict Ca-rich inclusions. Most interesting is the presence of platy and fibrous minerals (Fig. 3, D to F) finely interwoven with the matrix. XRD analysis revealed the presence of about 11% of hydrated mineral phases (calcium-alumino-sulfate and calcium-alumino-silicate phases) such as ettringite and tobermorite (table S1). The rocks from this horizon also exhibit considerably higher elastic moduli—Young's (E), bulk (K), and shear moduli (μ)—with respect to the main pyroclastic deposits outcropping in the caldera [i.e., Neapolitan Yellow Tuff (NYT) and Campanian Ignimbrite (CI)]. Figure 4A simultaneously displays the variation of Young's modulus (*E*) as a function of bulk (*K*) and shear moduli (μ). Elastic moduli are derived from *P*- and *S*-wave velocity measured under stress conditions (up to 50 MPa) (Fig. 4) and show ranges of values that are noticeably higher than the dynamic moduli measured on NYT and CI under the same conditions of stress (*18*). Particularly interesting is the enhancement in the shear moduli of the caprock samples (Fig. 4A), which reach values close to those of the bulk moduli. The difference between bulk and shear moduli decreases going from NYT and CI to the caprock samples. That is likely due to both compaction and the ability of the fibrous network of tobermorite and ettringite to withstand shear stress.

The compositional, microstructural, and elastic characterization of the caprock and basement rocks suggests a system having tightly coupled functions. At depths greater than 2.0 km, the profuse occurrence of needle-shaped actinolite along with epigenetic graphite spherules within the basement rocks suggests the occurrence of hydrothermal decarbonation reactions in impure siliceous-carbonate systems (marlstones) (*16*) in the presence of silica-rich fluids and K-feldspar–rich rocks (*19*). Decarbonation reactions (reactions S1 to S5) (*17*) release CO_2, which can be reduced to graphite in the presence of either H_2 (reaction S6) (*19*) forming through high-temperature (steam) electrolysis (HTE) or metallic Fe (*20*). In the presence of calcium-bearing formations, the volatile reaction (reaction S6) (*17*) leads to the formation of calcium hydroxide, graphite, and methane. The metamorphic decarbonation of marine sediments helps explain the puzzling origin of CO_2 in Campi Flegrei arising from (i) the constant ^{13}C values over the period 1970 to 1988 (*21*), suggesting a stable source of carbon over time, and (ii) its enriched isotopic signature of up to −1.6 ± 0.2‰. This value is higher than those typically obtained

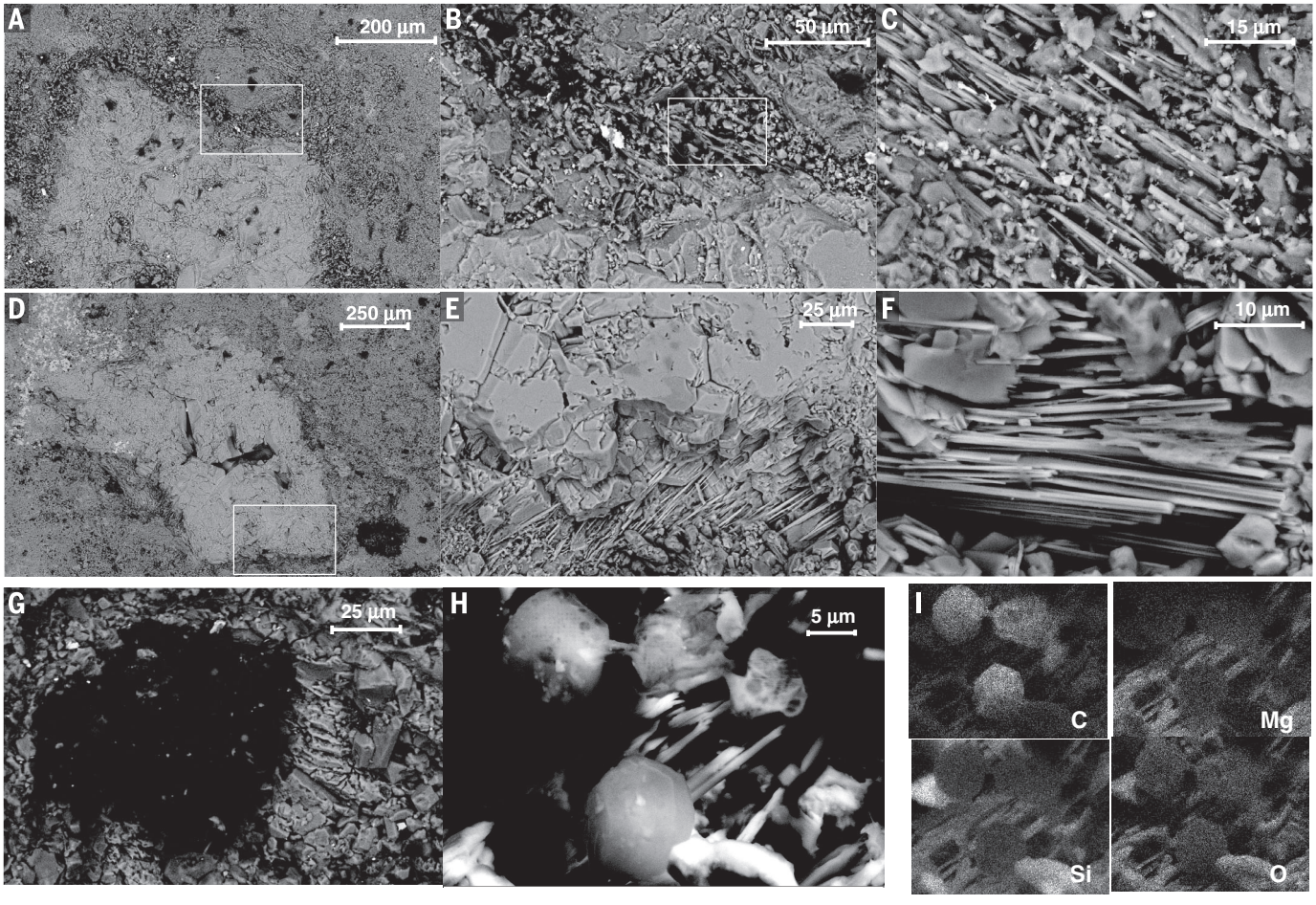

Fig. 2. High-resolution SEM images of the basement rocks. Different magnifications of the rock microstructure reveal the presence of porous rims (**A**, **B**, **D**, and **E**) containing well-aligned, needly actinolite (**C** and **F**) that grows in between calcite grains and the quartz- and feldspar-rich matrix (A and D). Clusters of carbon spherules (graphite) (**G** and **H**) about 10 μm in size are nested in between the needly structure of actinolite. Sometimes this phase appears to be enriched in elemental Na, probably as a result of cation substitution, leading to a stoichiometric composition that is similar to that of richterite and edenite. (**I**) EDS elemental composition of the carbon spherules showed in (H).

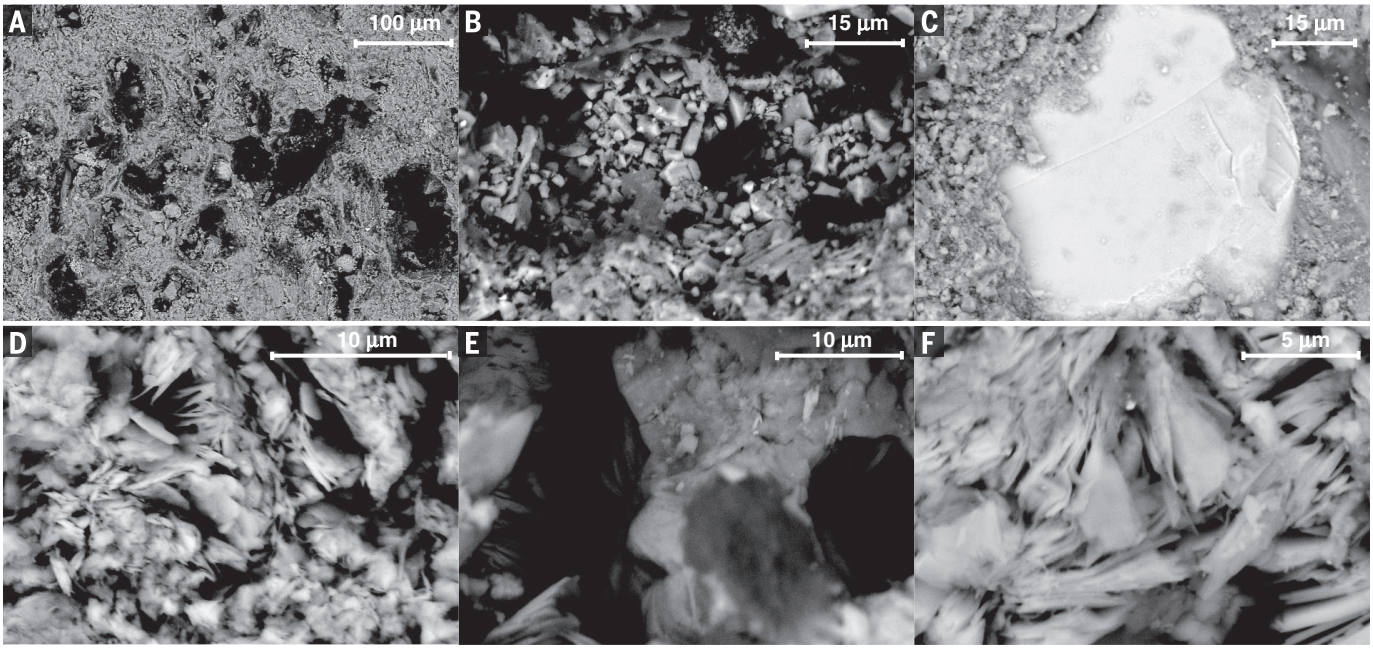

Fig. 3. High-resolution SEM images of the caprock. Different magnifications of sample microstructure reveal a fine microcrystalline matrix (**A** and **B**), which is interspersed with inclusions of calcite (**C**) and secondary porosity (A). The sample microstructure also shows the presence of platy and fibrous tobermorite (**D** to **F**) finely interwoven with the matrix.

for mantle-magmatic origin and plots within the ^{13}C range of marine carbonates (*21*). At shallower depth (1.0 to 2.0 km), the presence of tobermorite and ettringite within the caprock suggests limewater-pozzolana reactions. These minerals, besides being found in nature as alteration minerals in metamorphically altered limestones and skarns, also form from the curing and hardening of hydrated cement paste. The latter is the product of the reaction between seawater, lime, and pozzolana—the pyroclastic product of Campi Flegrei. Specifically, ettringite is related to the reaction of Ca-aluminates and ion sulfates (SO_4^{2-}) (*22*), whereas tobermorite is a phase that, even though predominantly associated with high temperature and pressure, has also been found in a block of Roman concrete from the harbor of Portus Julius, now submerged in the Bay of Pozzuoli (*23*). The XRF analysis (fig. S5) shows the composition of the caprock to be the same as that of the pozzolanic ash (Baia Ash) used for Roman concrete formulation (*23*–*25*).

The special binding properties that result from the chemical interaction between the Ca-rich mineral waters and the local pyroclastic rock are very well documented in the Roman literature to describe both the in situ processes from the hills surrounding the Solfatara crater (*26*, *27*) and the engineering of pozzolanic mortar (*28*). It was, in fact, in the Roman Puteoli that ancient Roman builders made the remarkable technological breakthrough of how to make a resilient, impermeable mortar that would set and cure underwater by mixing slaked lime with the local volcanic ash, called Pulvis Puteolanus (*28*) and pozzolana today. The widespread use of this highly reactive volcanic ash owes its efficacy to the Roman Puteoli serving, until the submersion of the harbor in 4 CE (Fig. 1A), as the military and major commercial harbor of the Roman Empire. The special ties to the eastern Mediterranean for the trade of grain and pozzolana (*29*) have led to the construction of several harbor structures within the Mediterranean (*25*) by using this volcanic ash for the mortar formulation.

The finding of tobermorite and ettringite in the pozzolana-rich caprock from the well cores in Campi Flegrei, along with the evidence of decarbonation products such as actinolite and graphite in the basement rock, suggests the existence of a natural process in the Campi Flegrei subsurface reflecting that of the engineering of the mortar of the Roman concrete. Such a process involves the reaction between the calcium oxide from the decarbonating basement (reaction S6), the pozzolana-rich formation at depths between 1.0 and 1.5 km, and the potassium- and calcium-rich seawater dominating the composition of the connate fluids in the geothermal reservoirs of Campi Flegrei (*30*). The resulting product of this natural pozzolanic activity with lime is the fiber-reinforced caprock whose intertwining filaments of ettringite and tobemorite help confer an enhanced shear and tensile strength to the rock, similar to cementitious infill in the concrete (*24*). Analogous to the recognized ability of fibers to improve the ductility of concrete, the fibrous microstrostructure of the caprock is thus responsible for the increased toughness (resistance to fracture) and strains at peak stress (table S2) that are higher than at NYT and CI (*18*, *31*). The specific curing conditions within the Campi Flegrei subsurface, such as the presence of steam favoring hydration and sulfate ions (*22*, *32*), can greatly help to enhance the microstructure and setting strength of the caprock. Specifically, the presence of sulfate ions helps retard the hydration of the aluminate and ferrite minerals (C_4AF), allowing hydration to proceed at a controlled rate and the fibers of ettringite to grow and stabilize (*22*). Hydration at a controlled rate avoids the undesirable condition known as flash set of the cementitious paste (*22*, *32*), which would add stiffness rather than toughness to the matrix. Figure 4B compares the compressive strength and the Young's modulus of concrete as a function of curing age (*32*) to those of the caprock samples, NYT and CI samples (*18*), and the Roman concrete from submerged harbors in the Mediterranean (*25*). The samples from the caprock show ranges of Young's modulus and compressive strength that are typical of later-stage, well-cured modern concrete. Therefore, this low permeability ($k = 10^{-18}$ to 10^{-17} m^2 at P_c = 40 MPa) and fiber-reinforced caprock are capable of holding the overpressured gas-bearing formation lying underneath (*11*), as well as accommodating larger strain as fluids accumulate and pore fluid pressure builds up.

The existence of a natural process similar to that used for concrete, involving lime-bearing and calc-alumino-silica formations in the subsurface of Campi Flegrei, opens a different path to understanding the cascading sequence of events that underlie the large strain setting off seismicity and, in turn, the release of fluids such as CO_2, CH_4, and steam (Fig. 1B). The importance of the findings reported in this study lies specifically in the nature of the caprock and hence, its possible physicochemical deterioration. Specific conditions may lead to its mechanical failure over time, after having reached the setting strength that results from the pozzolanic activity with lime. The loss of load-carrying capacity of a material can be mechanistically formulated as either a

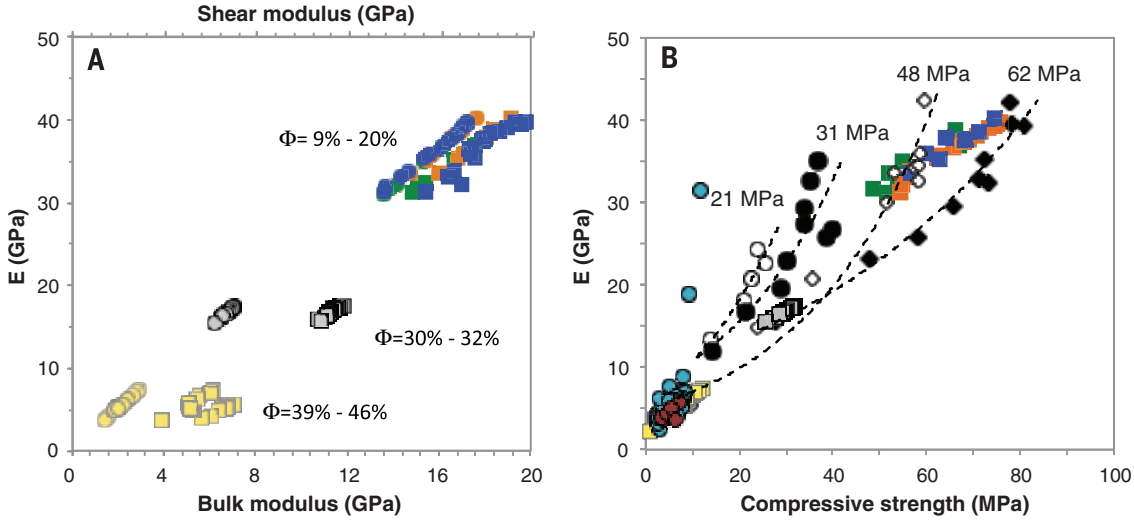

Fig. 4. Elastic moduli and strength of the caprock. (**A**) Variation of Young's modulus (*E*) as a function of bulk (*K*, squares) and shear moduli (μ, circles). Moduli are derived from *P*- and *S*-wave velocity measured on the samples from the caprock (green, orange, and blue symbols) under stress conditions. Values are noticeably higher than those measured on the pyroclastic counterpart (i.e., Neapolitan Yellow Tuff and Campanian Ignimbrite; yellow and gray symbols, respectively) outcropping in the area, under the same conditions of stress (*18*). (**B**) Compressive strength and Young's modulus of concrete as functions of curing age. Curing age increases going from open circles to black diamonds (*32*). The samples from the caprock of Campi Flegrei show ranges of Young modulus and compressive strength that are similar to those of later-stage, well-cured concrete. Neapolitan Yellow Tuff (yellow squares) and Campanian Ignimbrite (gray squares) exhibit much lower elastic modulus and compressive strength. Cyan and brown circles refer to Young's modulus and compressive strength measured on Roman concrete cored from submerged harbors in the Mediterranean (*25*).

decrease in the effective stress (i.e., an increase in pore pressure) on a time-invariant material or as a deterioration of its physical and mechanical properties under a constant stress. In the context of an internally buffered decarbonating system (reaction S6 reached equilibrium), the additional pore pressure on the caprock may come from an increase in mass (and by proxy volume) of CO_2. Given the *P-T-*X_{CO2} conditions regulating the reaction (fig. S4) (*17*), the formation of additional CO_2 is prompted by the arrival of new fluid, which by diluting the carbon dioxide in the system lowers the temperature of the decarbonation reaction (fig. S4). Brine not in thermodynamic equilibrium with the host rock can be in the form of fluid transferred from deep regions (*2*, *33*) or even seawater intrusion, which can result either from fluid withdrawal due to pumping or by the rise in seawater levels (*7*). Conversely, under the hypothesis of an unaltered effective stress, the instability of the calcium- alumino-silicate hydrates composing the matrix of the caprock occurs as the pH of the fluid falls below 12.5 (*32*). Indeed, the two processes described above can interact and feed back upon each other. That is, the enrichment of CO_2 in the subsurface can both decrease the effective stress and lower the pH of the connate reservoir fluids, thus favoring the chemical instability of the calcium-alumino-silicate hydrates in a cracking (higher surface area) caprock.

The change in mechanical properties by rock-fluid interactions under Campi Flegrei requires consideration of similar processes in other volcanic systems. A deeper understanding of natural conditions leading to the relationship between rock-fluid interactions, microstructure, and the change in mechanical properties also has important consequences for devising geomaterials that require an enhanced performance. This may be particularly useful in environments experiencing harsh conditions such as large changes in stress (e.g., concrete around well casing), high tensile and shear strain (e.g., construction materials in areas with high seismic hazard), and self-healing properties (e.g., geological storage of waste).

REFERENCES AND NOTES

1. F. Barberi, D. P. Hill, F. Innocenti, G. Luongo, M. Treuil, *Bull. Volcanol.* **47**, 173 (1984).
2. L. D'Auria *et al.*, *J. Geophys. Res.* **116** (B4), B04313 (2011).
3. G. Berrino, G. Corrado, G. Luongo, B. Toro, *Bull. Volcanol.* **47**, 187–200 (1984).
4. D. P. Hill, J. O. Langbein, S. Prejean, *J. Volcanol. Geotherm. Res.* **127**, 175–193 (2003).
5. D. R., *J. Geophys. Res. Solid Earth* **118**, 1–15 (2013).
6. J. Farrell, R. B. Smith, S. Husen, T. Diehl, *Geophys. Res. Lett.* **41**, 3068–3073 (2014).
7. L. Casertano, A. Oliveri del Castillo, M. T. Quagliariello, *Nature* **264**, 161–164 (1976).
8. R. Bianchi *et al.*, *J. Geophys. Res.* **92**, 14,139–14,150 (1987).
9. R. C. Aster, R. P. Meyer, *Tectonophysics* **149**, 195–218 (1988).
10. A. Zollo *et al.*, *Geophys. Res. Lett.* **30**, 2002 (2003).
11. T. Vanorio, J. Virieux, P. Capuano, G. Russo, *J. Geophys. Res.* **110**, B03201 (2005).
12. Agip, Modello Geotermico del Sistema Flegreo Internal Report, AGIP SERG-MESG, Milan, Italy (1987).
13. G. Camodeca, Ricerche su Puteoli tardo-romana (fine III-IV secolo), in *Puteoli* **4–5**, 59–126 (1980).
14. A. Parascandola, *I Fenomeni Bradisismici del Serapeo di Pozzuoli* (republished by Guida Editori, Napoli, 1983).
15. M. Battaglia, C. Roberts, P. Segall, *Science* **285**, 2119–2122 (1999).
16. M. Rosi, A. Sbrana, Eds., Phlegraean Fields, **114**, *CNR Quad. Ric. Sci.*, Roma (1987).
17. Materials and methods are available as supplementary materials on *Science* Online.
18. T. Vanorio, M. Prasad, D. Patella, A. Nur, *Geophys. J. Int.* **149**, 22–36 (2002).
19. A. A. Giardini, C. A. Salotti, J. F. Lakner, *Science* **159**, 317–319 (1968).
20. K. Silva, *Econ. Geol.* **82**, 1710–1722 (1987).
21. P. Allard, A. Maiorani, A. Tedesco, G. Cortecci, B. Turi, *J. Volcanol. Geotherm. Res.* **48**, 139–159 (1991).
22. H. Lechtman, L. Hobbs, in *High-Technology Ceramics: Past, Present, Future*, W.D. Kingery, Ed. (American Ceramics Society, Westerville, OH, 1986).
23. M. D. Jackson *et al.*, *Am. Mineral.* **98**, 1669–1687 (2013).
24. L. W. Hobbs, R. Siddall, in *Building Roma Aeterna: Current Research on Roman Mortar and Concrete*, Å. Ringbom, R. L. Hohlfelder, Eds. (Finnish Society of Sciences and Letters, Helsinki, 2011), pp. 35–60.
25. C. Brandon, R. L. Hohlfelder, M. D. Jackson, J. P. Oleson, *Building for Eternity* (Oxbow Books, Oxford, UK, 2014).
26. Pliny, *Natural History*, Book 35–47.
27. Seneca, *Questions About Nature*, Book 3.20.3.
28. Vitruvius, *De Architectura*, 2.6.1; 5.12.2-3.
29. D. Jones, *The Bankers of Puteoli: Finance, Trade, and Industry in the Roman World* (Tempus, Stroud, UK, 2006).
30. R. Carella, M. Guglielminetti, Proceedings 9th Workshop on Geothermal Reservoir Engineering, Stanford University, Stanford, California, 13 to 15 December 1983.
31. M. J. Heap, P. Baud, P. G. Meredith, S. Vinciguerra, T. Reuschlé, *Solid Earth* **5**, 25–44 (2014).
32. P. K. Mehta, P. J. M. Monteiro, *Concrete: Microstructure, Properties, and Materials* (McGraw-Hill Education, New York, ed. 4, 2014).
33. G. Chiodini, *Geophys. Res. Lett.* **36**, L02302 (2009).

ACKNOWLEDGMENTS

We are grateful to A. Nur and H.-R. Wenk for discussions and valuable feedback. We also thank the anonymous reviewers for their comments and contributions that improved the manuscript. We greatly appreciated the access to beamlime 11-ID-C of the Advanced Photon Source, Argonne National Laboratory, and thank Y. Ren for technical help. We thank L.-M. Joubert for assistance with SEM imaging at the Cell Sciences Imaging Facility, Stanford University. Part of this work was supported by the NSF CAREER Award (EAR-1451345 to T.V.) and by the startup fund to T.V. of the School of Earth, Energy, and Environmental Sciences at Stanford University. Data are available in the supplementary materials.

SUPPLEMENTARY MATERIALS

www.sciencemag.org/content/349/6248/617/suppl/DC1
Materials and Methods
Supplementary Text
Figs. S1 to S5
Tables S1 and S2
References (*34*–*44*)

16 March 2015; accepted 17 June 2015
Published online 9 July 2015
10.1126/science.aab1292

TOPOLOGICAL MATTER

Experimental observation of Weyl points

Ling Lu,[1]* Zhiyu Wang,[2] Dexin Ye,[2] Lixin Ran,[2] Liang Fu,[1]
John D. Joannopoulos,[1] Marin Soljačić[1]

The massless solutions to the Dirac equation are described by the so-called Weyl Hamiltonian. The Weyl equation requires a particle to have linear dispersion in all three dimensions while being doubly degenerate at a single momentum point. These Weyl points are topological monopoles of quantized Berry flux exhibiting numerous unusual properties. We performed angle-resolved microwave transmission measurements through a double-gyroid photonic crystal with inversion-breaking where Weyl points have been theoretically predicted to occur. The excited bulk states show two linear dispersion bands touching at four isolated points in the three-dimensional Brillouin zone, indicating the observation of Weyl points. This work paves the way to a variety of photonic topological phenomena in three dimensions.

In 1929, Hermann Weyl derived (*1*) the massless solutions to the Dirac equation—the relativistic wave equation for electrons. Neutrinos were thought, for decades, to be Weyl fermions until the discovery of the neutrino mass. Moreover, it has been suggested that low-energy excitations in condensed matter (*2*–*12*) can be the solutions to the Weyl Hamiltonian $H(k) = v_x k_x \sigma_x + v_y k_y \sigma_y + v_z k_z \sigma_z$, where v_i and k_i are the group velocities and momenta and σ_i are the Pauli matrices. Recently, photons have also been proposed to emerge as Weyl particles inside photonic crystals (*13*). In all cases, two linear dispersion bands in three-dimensional (3D) momentum space intersect at a single degenerate point—the Weyl point. Weyl points are 3D extensions of the 2D Dirac cones, as in graphene, possessing unique density of states and transport properties (*14*). Notably, Weyl points are monopoles of Berry flux with topological charges defined by the Chern numbers (*4*, *5*). These topological invariants enable materials containing Weyl points to exhibit a variety of unusual phenomena, including topological surface states (*15*), chiral anomaly (*16*), quantum anomalous Hall effect (*17*), and others (*18*, *19*). Furthermore, Weyl points are the intermediate topological gapless phases between topologically distinct bandgap materials (*20*), facilitating the search for other topological phases in 3D. In this work, we report on the observation of Weyl points in an inversion-breaking 3D double-gyroid (DG) photonic crystal without breaking time-reversal symmetry.

Weyl points are sources of quantized Berry flux in the momentum space (see the supplementary text). Their charges can be defined by the corresponding Chern numbers of ±1 (Fig. 1A). So, Weyl points robustly appear in pairs and can only be removed through pair annihilation. Because the Berry curvature is strictly zero under $\mathcal{PT}$ symmetry—the product of parity ($\mathcal{P}$, inversion) and time-reversal symmetry ($\mathcal{T}$)—isolated Weyl points only exist when at least one of $\mathcal{P}$ or $\mathcal{T}$ is broken. In (*13*), frequency-isolated Weyl points were predicted in $\mathcal{PT}$-breaking DG photonic crystals. In our experiment, we chose to break $\mathcal{P}$ instead of $\mathcal{T}$ to avoid using lossy magnetic materials and external magnetic fields. This choice also allows our approach to be directly extended to photonic crystals at optical wavelengths.

In Fig. 1B, we plotted the body-centered-cubic (bcc) Brillouin zone (BZ) of the $\mathcal{P}$-breaking DG shown in Fig. 1C. When $\mathcal{T}$ is preserved, there must exist even pairs of Weyl points (*13*). The two pairs of Weyl points illustrated in the (101) plane of the BZ, in Fig. 1B, are thus the minimum number of Weyl points possible. The band structure plotted in Fig. 1D shows two linear band crossings along $\Gamma - N$ and $\Gamma - H$; the other two Weyl points have identical dispersions due to $\mathcal{T}$. The four Weyl points are isolated in frequency and well separated in the momentum space, making their characterization easier.

We work at the microwave frequencies around 10 GHz, where fabrication of 3D photonic crystals is more accessible. Additive processes such as 3D printing cannot yet fulfill the material requirement of having low-loss dielectrics with high-dielectric constants. To fabricate two interpenetrating gyroids with a subtractive fabrication process, we open up each gyroid network by layers along the [101] direction with equal thickness of $a/\sqrt{2}$. Here, a is the cubic lattice constant. The cylindrical defects are introduced in each layer of the red gyroid in Fig. 1C.

We approximate each gyroid network by three sets of hole drillings, as illustrated in Fig. 2A. Similar methods of drilling and angled etching have been used in the fabrication of 3D photonic crystals in the microwave (*21*) and near-infrared wavelengths (*22*). The three cylindrical air holes of the blue gyroid, along x, y, and z, go through $(0,1/4,0)a$, $(0,0,1/4)a$, and $(1/4,0,0)a$, respectively. All air holes have a diameter of $0.54a$. Gyroids approximated by this drilling approach have almost identical band structures as those defined by the level-set isosurfaces in (*13*).

The second (red) gyroid is the inversion counterpart of the blue gyroid. To break $\mathcal{P}$, we shrink the red gyroid at $(1/4,-1/8,1/2)a$ to be a cylinder oriented along [101]. Shown in Fig. 2B, the defect cylinder has a diameter of $0.1a$ and height of $0.2a$. We separate the red gyroid by cutting (101) planes at the centers of the defect cylinders. The blue gyroid, without introduced defects, is separated at the corresponding position of $(-1/4,1/8,-1/2)a$. Each layer is $a/\sqrt{2}$ thick. The separated layers of each gyroid are identical up to translations of $\mathbf{a}_2$ (the bcc lattice vector in Fig. 1C). One unit vertical period of DG consists of two layers from each gyroid (Fig. 2B).

The materials of choice are slabs of ceramic-filled plastics (C-STOCK AK, Cuming Microwave Corp., MA) of dielectric constant 16 and loss tangent 0.01. Each slab has a thickness of 9.5 mm ($= a/\sqrt{2}$). Both the width and the length of the slabs are 304 mm (~12 inches). The material hardness is adjusted between 80 and 90 on a Shore D gauge to be machined by carbide tools without cracking. Each layer experienced around 700 drillings along ±45° away from its surface normal (in x and z) and about 40 ball-end millings in-plane (in y) on both top and bottom surfaces. These operations were performed using a computer-numerical-controlled three-axis vertical milling machine (fig. S1A). Although all slabs of the same gyroid can in principle be machined together, we processed no more than two layers at the same time to leave a solid frame for handling. About 20 mm were left undrilled from each of the four edges of the slabs. We subsequently cut two sides of the frames of each gyroid for their assembly (fig. S1B). Figure 2B illustrates that the layers of the two gyroids were offset vertically by half of the slab thickness (4.25 mm). A picture of the assembled sample is shown in Fig. 2C (more pictures are in fig. S1, C and D). The final sample in measurements consists of a total of 20 layers, with 10 layers from each gyroid stacked in alternating order (*23*).

We performed angle-resolved transmission measurements on the photonic crystal sample to probe the dispersions of the 3D bulk states (*24*–*26*). The schematic of the experimental setup is shown in Fig. 3A (also see fig. S1E). A pair of lens antennas were placed on the two sides of the sample. Transmission amplitudes (S-parameter S21) were recorded by the network analyzer. The half-power beam widths (divergent angles) of the lens antennas were 9°. The collimated beam impinged on the sample (101) surface, in which the incident angle is varied by rotating the sample around the vertical axis. As illustrated in Fig. 3B, the component of the incident wave vector parallel to the sample surface $[k_0 \sin(\theta)]$ is conserved up to a reciprocal lattice vector of the sample surface, due to the discrete

[1]Department of Physics, Massachusetts Institute of Technology (MIT), Cambridge, MA 02139, USA. [2]Laboratory of Applied Research on Electromagnetics (ARE), Zhejiang University, Hangzhou, Zhejiang 310027, China.
*Corresponding author. E-mail: linglu@mit.edu

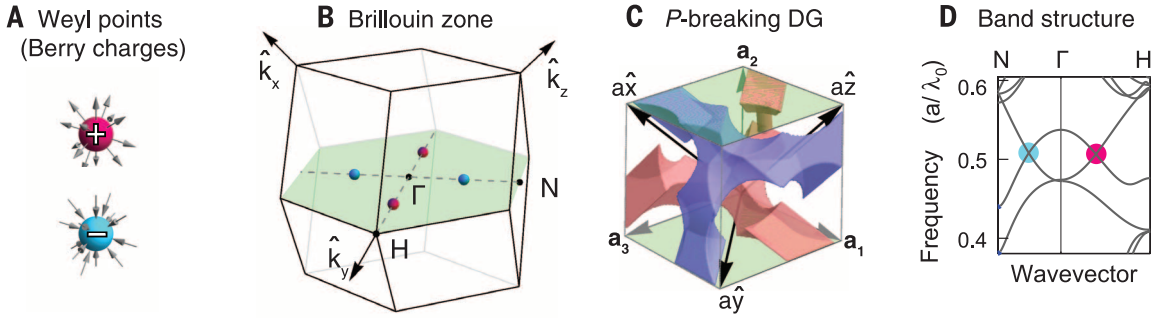

Fig. 1. Weyl points in the BZ of a $\mathcal{P}$-breaking gyroid photonic crystal. (**A**) Weyl points are monopoles of Berry flux in the momentum space. (**B**) The BZ of the DG photonic crystal in (C). The (101) surfaces are highlighted in green. Four Weyl points are illustrated on the green (101) plane along $\Gamma - H$ and $\Gamma - N$, where $H = (0,1,0)2\pi/a$ and $N = (-1/2,0,1/2)2\pi/a$. (**C**) The bcc cell of the DG with a $\mathcal{P}$-breaking cylindrical defect on the red gyroid, where $\mathbf{a}_1 = (-1,1,1)a/2$, $\mathbf{a}_2 = (1,-1,1)a/2$, and $\mathbf{a}_3 = (1,1,-1)a/2$. (**D**) The photon dispersions are plotted along $N - \Gamma - H$. The Weyl points are the linear band touchings between the fourth and fifth bands.

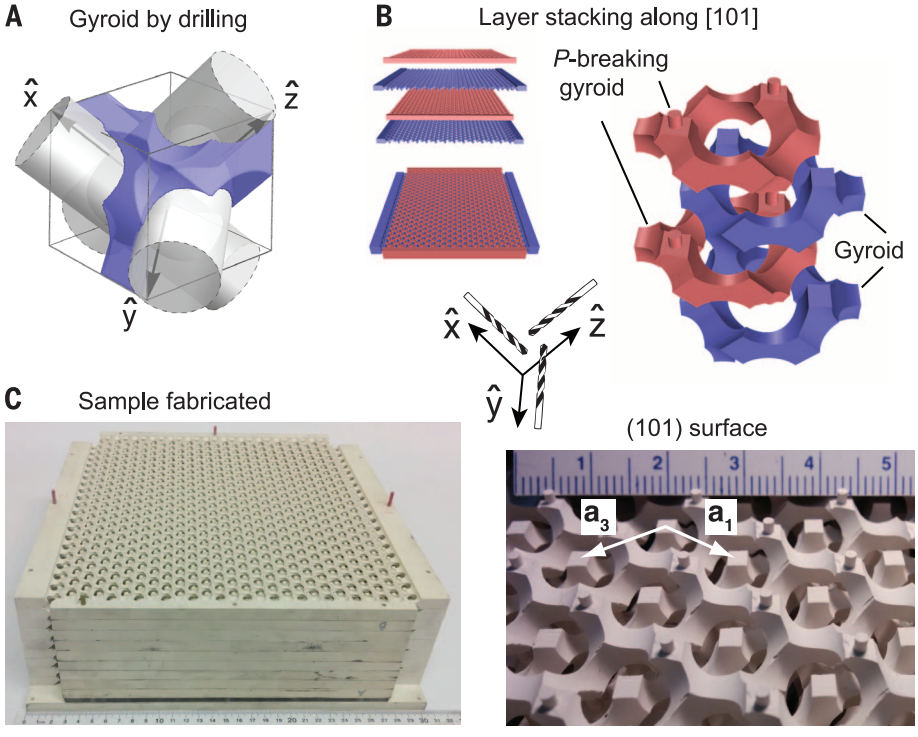

Fig. 2. Fabrication of gyroids by drilling and stacking layers. (**A**) Illustration in a bcc unit cell that a single gyroid structure can be approximated by drilling periodic air holes along the *x*, *y*, and *z* directions. (**B**) The DG structure can be made by stacking layers along the [101] direction. The red and blue gyroids, being inversion counterparts, interpenetrate each other. We shrink the vertical connections of the red gyroid to thin cylinders in order to break $\mathcal{P}$. (**C**) (Left) A total of 20 layers were stacked. (Right) A zoom-in view from the top, with a ruler (in centimeters) in the background.

translational symmetry. All the bulk states of the same wave-vector projection (dashed line in Fig. 3B) and frequency could be excited in the bulk and exit the sample in the same direction as the incident beam. The exiting signal was collected by the antenna at the opposite side. A pair of prisms was used to increase the magnitudes of the incident wave vectors for sampling a larger volume in the BZ. We placed the angled prisms (12.4°) in contact with the opposite surfaces of the sample (Fig. 3A); the prisms are made of the same material as the sample ($\varepsilon = 16$).

Both the source and receiving antennas were linearly polarized. To account for the complex polarization response in the 3D $\mathcal{P}$-breaking photonic crystal, we summed up the transmitted power of different polarizations to resolve more bulk states in the sample. Illustrated in Fig. 3A, the electric-field directions of the *s* and *p* polarizations are vertical and parallel to the incident plane, respectively. We first set the source antenna to be in one of the polarization states (e.g., *s*) and measured the transmitted power twice by setting the receiving antenna to be *s* and *p* polarized, respectively. The sum of the two transmitted signals was normalized to the transmission signal without the sample. Second, we set the source antenna to be the other polarization (e.g., *p*) and repeated the above procedure. Last, we summed the transmission power for both polarizations and plotted it in Fig. 3C. For details, see figs. S2 and S3.

We mapped out all 3D bulk states, projected along [101], by varying θ and α as shown in Fig. 3, A and B. Six sets of transmission data of representative directions are plotted in Fig. 3C. The transmission data stop on the right slanted boundary, which corresponds to the maximum rotation angle in θ. Close to this boundary, the transmission intensity is low due to the smaller effective cross section of the samples at large angles. For comparison, the corresponding band structures (projected along the transmission direction [101]) are plotted as figure insets. In principle, all states in the projected band structure can be observed in the transmission data, where the transmission amplitudes are proportional to the bulk density of states. However, the coupling and transmission efficiencies depend on the details of the Bloch mode polarizations, modal symmetries, radiation lifetimes, finite size effects, group velocities, and Berry-curvature-induced anomalous velocities. Although the signal strength varies in some areas in the experimental data, all the transmission responses (Fig. 3C) compare very well and are consistent with the theoretical band structures in the insets.

When $\alpha = 90°$ (in Fig. 3), the beam scans through the upper Weyl point along $\Gamma - H$, represented by a magenta sphere in Fig. 3B. The outline of the transmission intensity in Fig. 3C clearly shows a linear point crossing around 11.3 GHz in frequency and close to $0.45(2\pi/a)$ in wave vector. As α increases from 90° to 105° and 120°, we are moving off the Weyl point and observe the opening of a small gap. This gap opening is expected for a point degeneracy and excludes the possibility of the state being associated with a line degeneracy [line node (*13*)]. Because photons do not have spin or polarization degeneracies in our crystal, every band dispersion represents a single state, excluding the possibility of being a four-fold 3D Dirac degeneracy (*27*). Due to the aspect ratio of our sample, we were unable to scan the dispersions

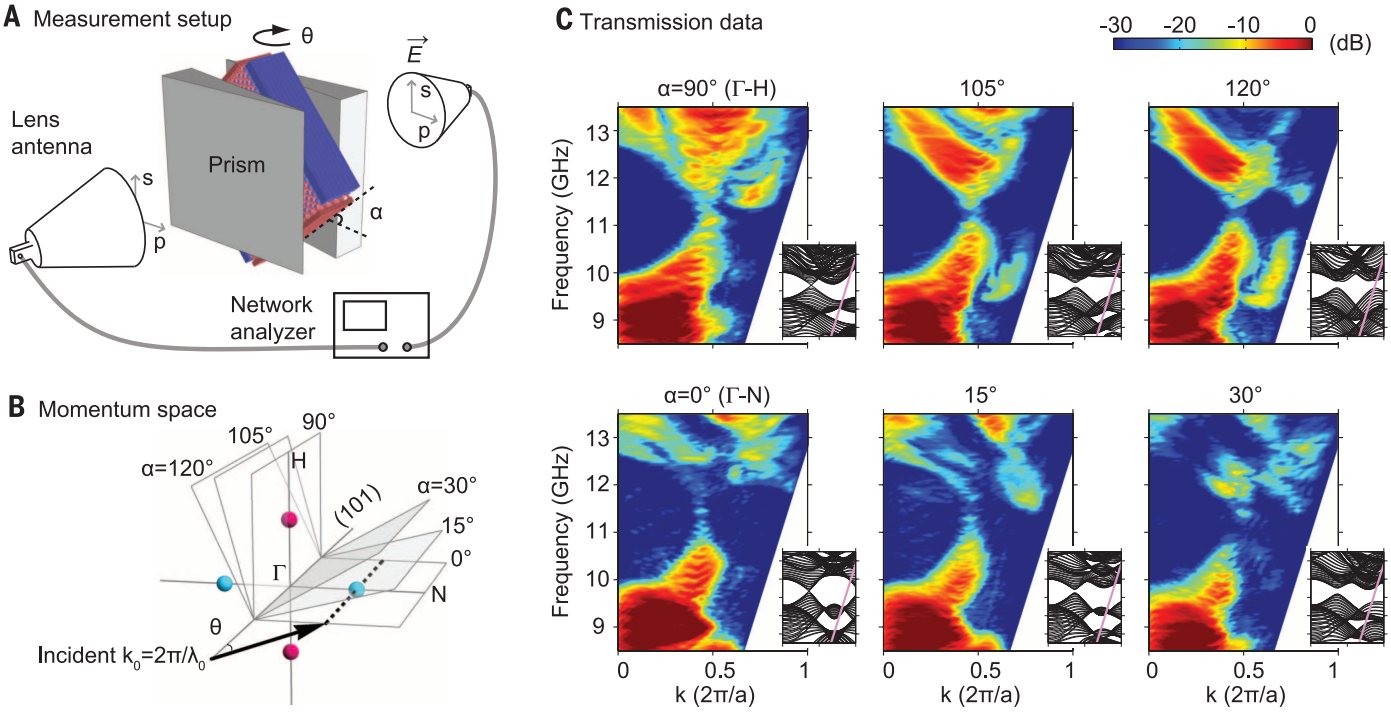

Fig. 3. Angle-resolved transmission measurements. (**A**) Schematic of the microwave transmission setup. (**B**) The bulk states of the **k** vectors on the dashed line can be excited by the incident wave at incidence angle θ. (**C**) Transmission data, summed over both *s* and *p* polarizations, as the sample is rotated along the [101] axis by the angle α. The insets show the calculated band structures projected along [101]; they are scaled to the same range and ratio as the measured data.

along the [101] transmission direction. However, our transmission data do contain all the contributions from those dispersions projected together. For example, the resonance lines below and above the Weyl point, in Fig. 3C (α = 90°), indicate the gap opening along the [101] direction as well. Similarly, the other Weyl point, in cyan, on the right of the Γ – *N* axis, is studied by orienting α to be 0°, 15°, and 30°. Although the transmission intensity of the upper bulk bands is not as prominent, the Weyl point dispersions can still be inferred. The remaining two Weyl points, at the opposite **k** locations, relate to the two measured Weyl points by $\mathcal{T}$. They have the same projected band dispersions and the same transmission pattern as the data shown in Fig. 3C.

The photonic Weyl points observed in our experiment pave the way to topological photonics (*28*–*31*) in 3D, where 3D Dirac points (*27*, *32*) and various gapped topological phases (*33*, *34*) can be accessed. Similar approaches can be readily adopted to observe Weyl points at optical frequencies using 3D nanofabrication (*35*–*37*). The surface states, not seen in our transmission experiments, could potentially be characterized through reflection spectra or evanescent-wave measurements. Close to the Weyl-point frequencies, photonic Weyl materials provide angular selectivity (*38*) for filtering light from any 3D incident angle. The unique density of states at the Weyl point can potentially enable devices such as high-power single-mode lasers (*39*).

REFERENCES AND NOTES

1. H. Weyl, *Z. Phys.* **56**, 330–352 (1929).
2. C. Herring, *Phys. Rev.* **52**, 365–373 (1937).
3. A. Abrikosov, S. Beneslavskii, *Sov. Phys. JETP* **32**, 699 (1971).
4. G. E. Volovik, *The Universe in a Helium Droplet* (Oxford Univ. Press, Oxford, 2009).
5. X. Wan, A. M. Turner, A. Vishwanath, S. Y. Savrasov, *Phys. Rev. B* **83**, 205101 (2011).
6. A. A. Burkov, L. Balents, *Phys. Rev. Lett.* **107**, 127205 (2011).
7. G. Xu, H. Weng, Z. Wang, X. Dai, Z. Fang, *Phys. Rev. Lett.* **107**, 186806 (2011).
8. J. Liu, D. Vanderbilt, *Phys. Rev. B* **90**, 155316 (2014).
9. D. Bulmash, C.-X. Liu, X.-L. Qi, *Phys. Rev. B* **89**, 081106 (2014).
10. M. Hirayama, R. Okugawa, S. Ishibashi, S. Murakami, T. Miyake, *Phys. Rev. Lett.* **114**, 206401 (2015).
11. H. Weng, C. Fang, Z. Fang, B. A. Bernevig, X. Dai, *Phys. Rev. X* **5**, 011029 (2015).
12. S.-M. Huang *et al.*, *Nat. Commun.* **6**, 7373 (2015).
13. L. Lu, L. Fu, J. D. Joannopoulos, M. Soljačić, *Nat. Photonics* **7**, 294–299 (2013).
14. P. Hosur, S. A. Parameswaran, A. Vishwanath, *Phys. Rev. Lett.* **108**, 046602 (2012).
15. A. C. Potter, I. Kimchi, A. Vishwanath, *Nat. Commun.* **5**, 5161 (2014).
16. H. Nielsen, M. Ninomiya, *Phys. Lett. B* **130**, 389–396 (1983).
17. K.-Y. Yang, Y.-M. Lu, Y. Ran, *Phys. Rev. B* **84**, 075129 (2011).
18. A. M. Turner, A. Vishwanath, *Topological Insulators* **6**, 293–324 (2013).
19. P. Hosur, X. Qi, *C. R. Phys.* **14**, 857–870 (2013).
20. S. Murakami, *New J. Phys.* **9**, 356 (2007).
21. E. Yablonovitch, T. J. Gmitter, K. M. Leung, *Phys. Rev. Lett.* **67**, 2295–2298 (1991).
22. S. Takahashi *et al.*, *Nat. Mater.* **8**, 721–725 (2009).
23. L. Lu *et al.*, *Opt. Lett.* **37**, 4726–4728 (2012).
24. W. M. Robertson *et al.*, *Phys. Rev. Lett.* **68**, 2023–2026 (1992).
25. E. Özbay *et al.*, *Phys. Rev. B* **50**, 1945–1948 (1994).
26. C. Pouya, P. Vukusic, *Interface Focus* **2**, 645–650 (2012).
27. S. M. Young *et al.*, *Phys. Rev. Lett.* **108**, 140405 (2012).
28. L. Lu, J. D. Joannopoulos, M. Soljačić, *Nat. Photonics* **8**, 821–829 (2014).
29. Z. Wang, Y. Chong, J. D. Joannopoulos, M. Soljacić, *Nature* **461**, 772–775 (2009).
30. M. Hafezi, S. Mittal, J. Fan, A. Migdall, J. Taylor, *Nat. Photonics* **7**, 1001–1005 (2013).
31. M. C. Rechtsman *et al.*, *Nature* **496**, 196–200 (2013).
32. Z. K. Liu *et al.*, *Science* **343**, 864–867 (2014).
33. L. Fu, *Phys. Rev. Lett.* **106**, 106802 (2011).
34. L. Lu, C. Fang, S. G. Johnson, J D. Joannopoulos, M. Soljačić, arXiv 1507.00337 (2015).
35. E. J. Crossland *et al.*, *Nano Lett.* **9**, 2807–2812 (2009).
36. M. D. Turner, G. E. Schröder-Turk, M. Gu, *Opt. Express* **19**, 10001–10008 (2011).
37. M. D. Turner *et al.*, *Nat. Photonics* **7**, 801–805 (2013).
38. Y. Shen *et al.*, *Science* **343**, 1499–1501 (2014).
39. S.-L. Chua, L. Lu, J. Bravo-Abad, J. D. Joannopoulos, M. Soljačić, *Opt. Lett.* **39**, 2072–2075 (2014).

ACKNOWLEDGMENTS

We thank A. Gallant and E. Johnson at the MIT central machine shop for machining the gyroid layers; Y. Shen, B. Zhang, J. Liu, B. Zhen, B. Wang, A. Vishwanath, H. Chen, Q. Yan, and C. Fang for discussions; and P. Rebusco for critical reading and editing of the manuscript. J.D.J. was supported in part by the U.S. Army Research Office through the Institute for Soldier Nanotechnologies under contract W911NF-13-D-0001. L.F. was supported by the U.S. Department of Energy (DOE) Office of Basic Energy Sciences, Division of Materials Sciences and Engineering, under award DE-SC0010526. L.L. was supported in part by the Materials Research Science and Engineering Center Program of the NSF under award DMR-1419807. M.S. and L.L. (analysis and reading of the manuscript) were supported in part by the MIT Solid-State Solar-Thermal Energy Conversion Center and Energy Frontier Research Center of DOE under grant DE-SC0001299. Z.W, D.Y., and L.R. were supported by the Chinese National Science Foundation (CNSF) under grants 61401395, 61401393, and 61131002, respectively.

SUPPLEMENTARY MATERIALS

www.sciencemag.org/content/349/6248/622/suppl/DC1
Supplementary Text
Figs. S1 to S3

15 February 2015; accepted 6 July 2015
Published online 16 July 2015
10.1126/science.aaa9273

DEVICE TECHNOLOGY

Phase patterning for ohmic homojunction contact in $MoTe_2$

Suyeon Cho,[1] Sera Kim,[1,2] Jung Ho Kim,[1,2] Jiong Zhao,[1] Jinbong Seok,[1,2] Dong Hoon Keum,[1,2] Jaeyoon Baik,[3] Duk-Hyun Choe,[4] K. J. Chang,[4] Kazu Suenaga,[5] Sung Wng Kim,[2]* Young Hee Lee,[1,2]* Heejun Yang[2]*

Artificial van der Waals heterostructures with two-dimensional (2D) atomic crystals are promising as an active channel or as a buffer contact layer for next-generation devices. However, genuine 2D heterostructure devices remain limited because of impurity-involved transfer process and metastable and inhomogeneous heterostructure formation. We used laser-induced phase patterning, a polymorph engineering, to fabricate an ohmic heterophase homojunction between semiconducting hexagonal (2H) and metallic monoclinic (1T′) molybdenum ditelluride ($MoTe_2$) that is stable up to 300°C and increases the carrier mobility of the $MoTe_2$ transistor by a factor of about 50, while retaining a high on/off current ratio of 10^6. In situ scanning transmission electron microscopy results combined with theoretical calculations reveal that the Te vacancy triggers the local phase transition in $MoTe_2$, achieving a true 2D device with an ohmic contact.

Despite the promise of using two-dimensional (2D) atomic crystals in device applications (*1*, *2*), the issue of Schottky contact between the semiconducting 2D channel material and the metal electrode has been studied extensively without being resolved. The solution to the Schottky contact issue for silicon is local doping near silicon-metal junctions to reduce the depletion region width and to decrease the contact resistance (*3*). The 3D doping method used in silicon technology is unavailable in 2D devices, and previous efforts, such as aligning the metal work function with the conduction/valence band edge of 2D semiconductors (*4*), inserting graphene in the junction by the transfer method (*5*, *6*), and MoS_2 phase-engineering by chemical doping (*7*), showed inherent limitations in the processes. These limitations include a lack of true ohmic contact caused by a large interface resistance between the 2D semiconductor and the metal, and the formation of metastable and inhomogeneous junctions between 1T-MoS_2 and the metal.

Global structural phase transition in transition metal dichalcogenides (TMDs) has been related to diverse areas of physics, such as metal/band insulators (*2*), superconductors (*8*–*10*), charge density waves (*11*), spintronics, and valley optoelectronics (*12*). Recently, considerable academic interest has focused on atomic-scale observations of local phase transitions in TMDs by using transmission electron microscopy (TEM), highlighting the potential engineering of local material properties (*13*, *14*). However, the electrical and chemical properties of a phase-modified area, or a phase interface between intrinsic and modified areas in TMDs, have not yet been clearly verified because of instrumental limitations (*14*) or inhomogeneous metastable junctions (*7*).

Local phase transitions in 2D TMDs enable the fabrication of high-quality heterophase structures that are promising as a buffer contact layer to construct an ohmic contact. If the work function match between semiconducting and metallic phases in a TMD material guarantees the band alignment of ohmic contact (*4*), then the metal-semiconductor homojunction would be an ideal contact for 2D devices. Previous studies revealed that the energy difference between semiconducting hexagonal (2H) and metallic distorted octahedral (1T′) structures in $MoTe_2$ is substantially smaller (~35 meV) than the comparable energy differences in other TMD materials (*15*, *16*). In this respect, $MoTe_2$ offers the opportunity for creating stable homojunction contacts by phase transition, in contrast to its MoS_2 counterpart, which has a metastable metallic 1T phase (*7*). In addition to the feasibility of phase transition, a band gap of ~1.0 eV in 2H-$MoTe_2$, which is similar

[1]IBS Center for Integrated Nanostructure Physics (CINAP), Institute for Basic Science, Sungkyunkwan University, Suwon 440-746, Korea. [2]Department of Energy Science, Sungkyunkwan University, Suwon 440-746, Korea. [3]Pohang Accelerator Laboratory, Pohang University of Science and Technology, Pohang 790-784, Korea. [4]Department of Physics, Korea Advanced Institute of Science and Technology, Daejeon 305-701, Korea. [5]National Institute of Advanced Industrial Science and Technology (AIST), Tsukuba 305-8565, Japan.
*Corresponding author. E-mail: kimsungwng@skku.edu (S.W.K.); leeyoung@skku.edu (Y.H.L.); h.yang@skku.edu (H.Y.)

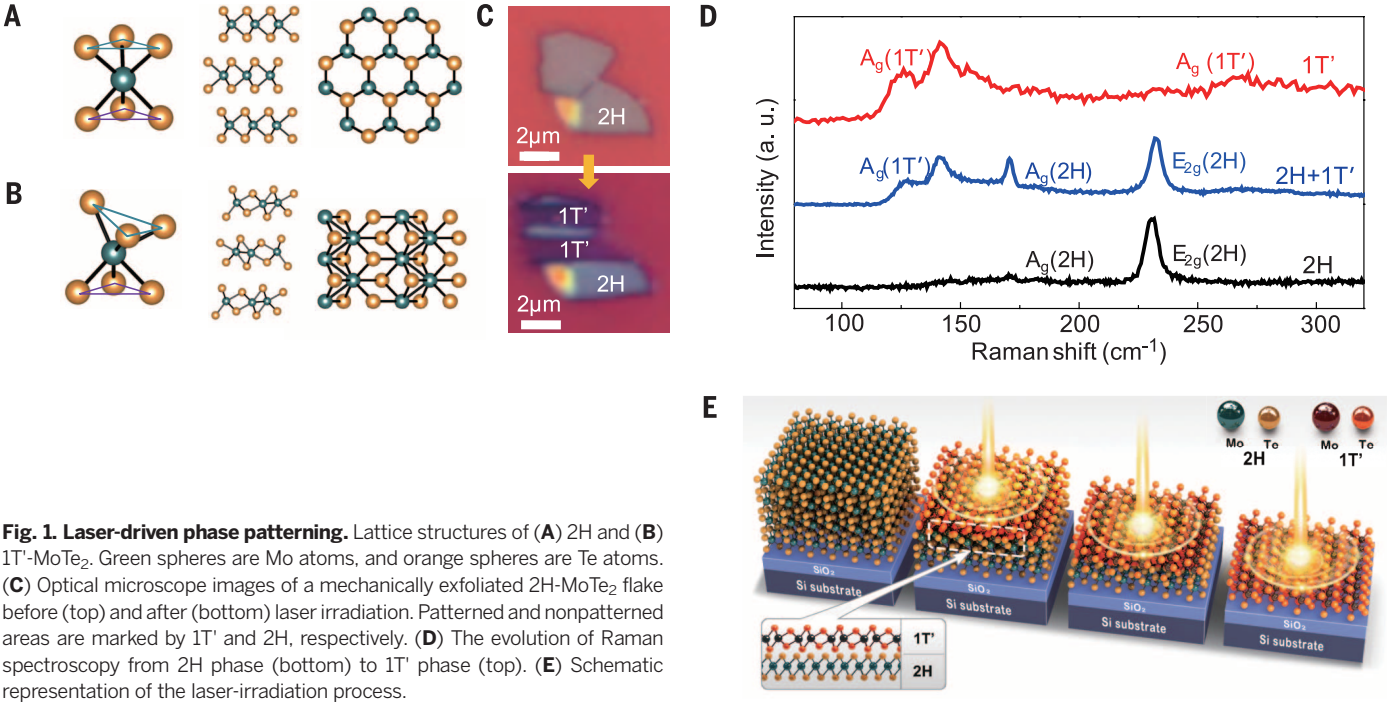

Fig. 1. Laser-driven phase patterning. Lattice structures of (**A**) 2H and (**B**) 1T′-$MoTe_2$. Green spheres are Mo atoms, and orange spheres are Te atoms. (**C**) Optical microscope images of a mechanically exfoliated 2H-$MoTe_2$ flake before (top) and after (bottom) laser irradiation. Patterned and nonpatterned areas are marked by 1T′ and 2H, respectively. (**D**) The evolution of Raman spectroscopy from 2H phase (bottom) to 1T′ phase (top). (**E**) Schematic representation of the laser-irradiation process.

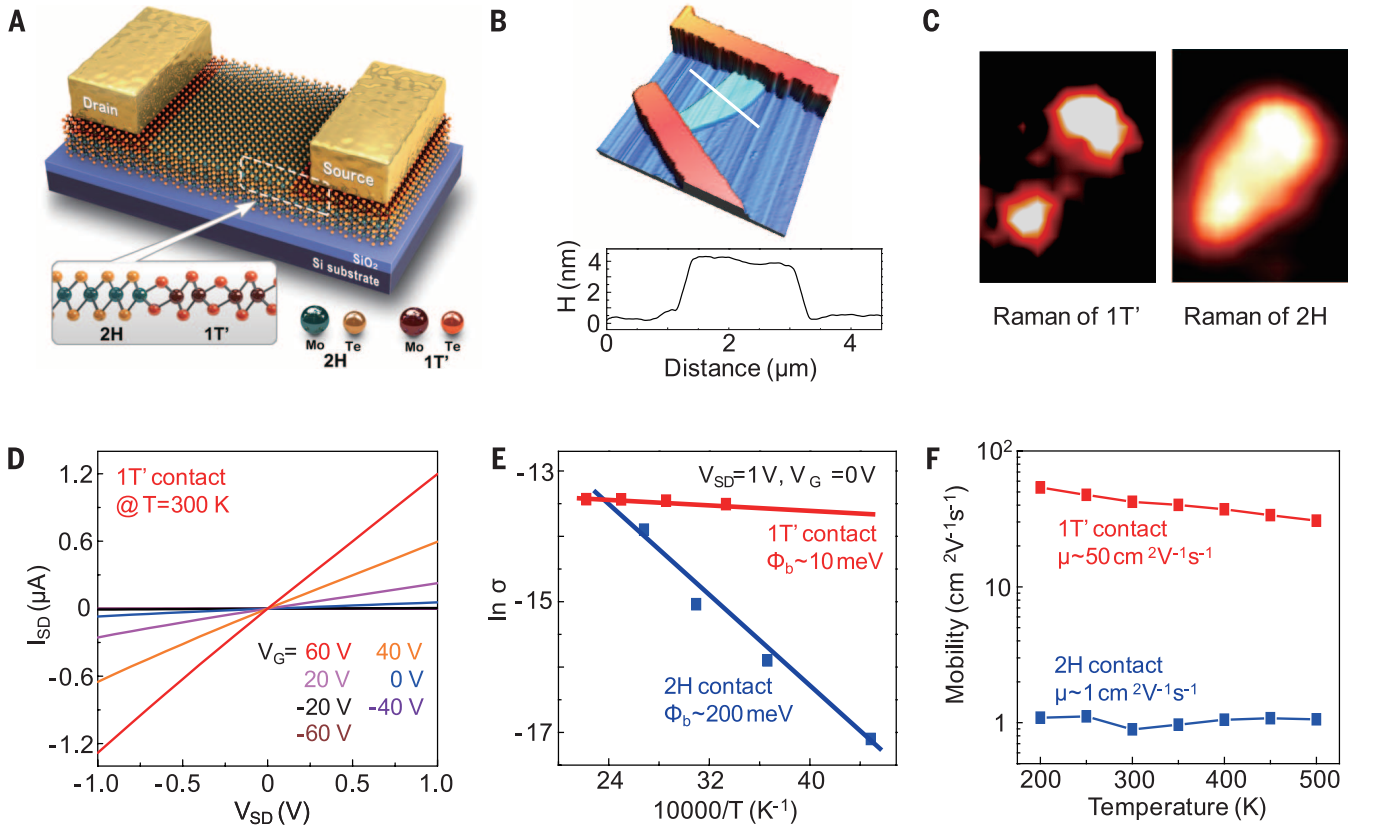

Fig. 2. Transport through a heterophase homojunction structure in $MoTe_2$. (**A**) Schematic diagrams of a device with a 1T′/2H phase homojunction. (**B**) AFM image of a device with the 1T′/2H phase homojunction in $MoTe_2$. (**C**) Raman mapping images of 1T′ (A_g) and 2H (E_{2g}) vibrational modes in the device channel in (B). (**D**) Source-drain current I_{SD} characteristics for gate voltage V_G ranging from −60 V to 60 V. (**E**) Arrhenius plots of the conductance. (**F**) Field-effect mobility as a function of temperature.

to that of bulk silicon, is appealing for 2D electronics (*17*, *18*).

We report laser-driven phase patterning, which is a type of local polymorph engineering, in $MoTe_2$ to realize a heterophase homojunction that shows ohmic contact in $MoTe_2$ transistors. The phase transition from the 2H to 1T′ phase in $MoTe_2$ is driven by laser irradiation in a desired area. We named this robust design of heterophase structures "phase patterning." We verified that the lattice vibration modes and chemical states of the phase-patterned areas correspond to those of single-crystalline 1T′-$MoTe_2$. The heterophase homojunction between 2H- and 1T′-$MoTe_2$ is stable up to 300°C, indicating that this phase patterning should be compatible with most semiconductor manufacturing processes. We also identified that the formation of the Te vacancy is the key origin of the unidirectional phase transition from 2H to 1T′ phase via laser irradiation.

We synthesized 2H- and 1T′-$MoTe_2$ single crystals by the flux method, as previously reported (*16*). The two structures (2H and 1T′) of $MoTe_2$ are schematically described in Fig. 1, A and B, in which six Te atoms constitute two triangles in the same orientation (2H) and in the opposite orientation (1T′) around the centered Mo atom. Mechanically exfoliated flakes of multilayer (~30 layers in Fig. 1C) 2H-$MoTe_2$ were used for the laser-irradiation–driven phase patterning in the desired area [figs. S1 and S2 (*19*)]. The optical images in Fig. 1C and the Raman spectra in Fig. 1D revealed the effect of the laser irradiation with a spatial resolution of less than 1 μm. The laser irradiation decreased the flake thickness and led to a new structural phase evolution in the irradiated region. The initial 2H-$MoTe_2$ flakes exhibited two distinct Raman modes, an in-plane E_{2g} mode near 235 cm^{-1} and an out-of-plane A_g mode near 174 cm^{-1} (*20*), whereas the laser-irradiated areas showed new peaks near 124, 138, and 272 cm^{-1}, corresponding to the A_g mode of 1T′-$MoTe_2$ (*16*). The evolution of Raman modes at the representative stages shown in Fig. 1D, from the 2H phase (bottom) to the 1T′ phase (top), manifests the local phase transition in $MoTe_2$. Other possible origins for the Raman mode changes were excluded by a comparison experiment with hexagonal boron nitride (*h*-BN)-covered $MoTe_2$ [figs. S3 and S4 (*19*)].

Figure 1E shows a schematic of the laser-irradiation process. Although the confocal Raman spectroscopy cannot provide information about the vertical location of the 1T′ phase in the $MoTe_2$ flake, we verified from surface-sensitive x-ray photoemission spectroscopy that the phase transition initially occurs at the top layer, and the thinning effect follows the phase transition in the flake, as represented in Fig. 1E. The phase transition begins around a temperature of 400°C, estimated by the 2H-$MoTe_2$ Raman peak shift [fig. S5 (*19*)]. The irradiated region in the 2H-$MoTe_2$ flake continued to thin during the laser irradiation until the flake thickness reached a few layers of the transformed 1T′ phase. We deduce that these few layers remained because of the heat-sink effect toward the bottom of the SiO_2 substrate during the irradiation process (*19*, *21*).

The phase patterning can resolve the Schottky contact issue in 2D transistors (Fig. 2). Before depositing a metal electrode in the fabrication process of the 2H-$MoTe_2$ transistor, the 1T′ phase was patterned only near the area where metal electrodes would be located (Fig. 2A). To demonstrate the effect of the heterophase homojunction in Fig. 2A, adjacent 2H-$MoTe_2$ flakes on the same SiO_2 substrate were used to fabricate transistors without the 1T′ buffer layer. Figure 2, B and C, show the geometry of a device in which we conducted phase patterning and the evidence of the phase change from 2H to 1T′ in the desired areas by 2D confocal Raman mapping. The two circled areas in the Raman 1T′ map are located at the deposition sites of the metal electrodes.

The consequences of this new homojunction in the $MoTe_2$ transistor are summarized in Fig. 2, D to F. The n-type transistor characteristics (Fig. 2D) showed ohmic contact behavior with current I_{on}/I_{off} of 10^6 (fig. S6). Furthermore, the robust heterophase homojunction structure in the $MoTe_2$ transistor allows a high-temperature transport

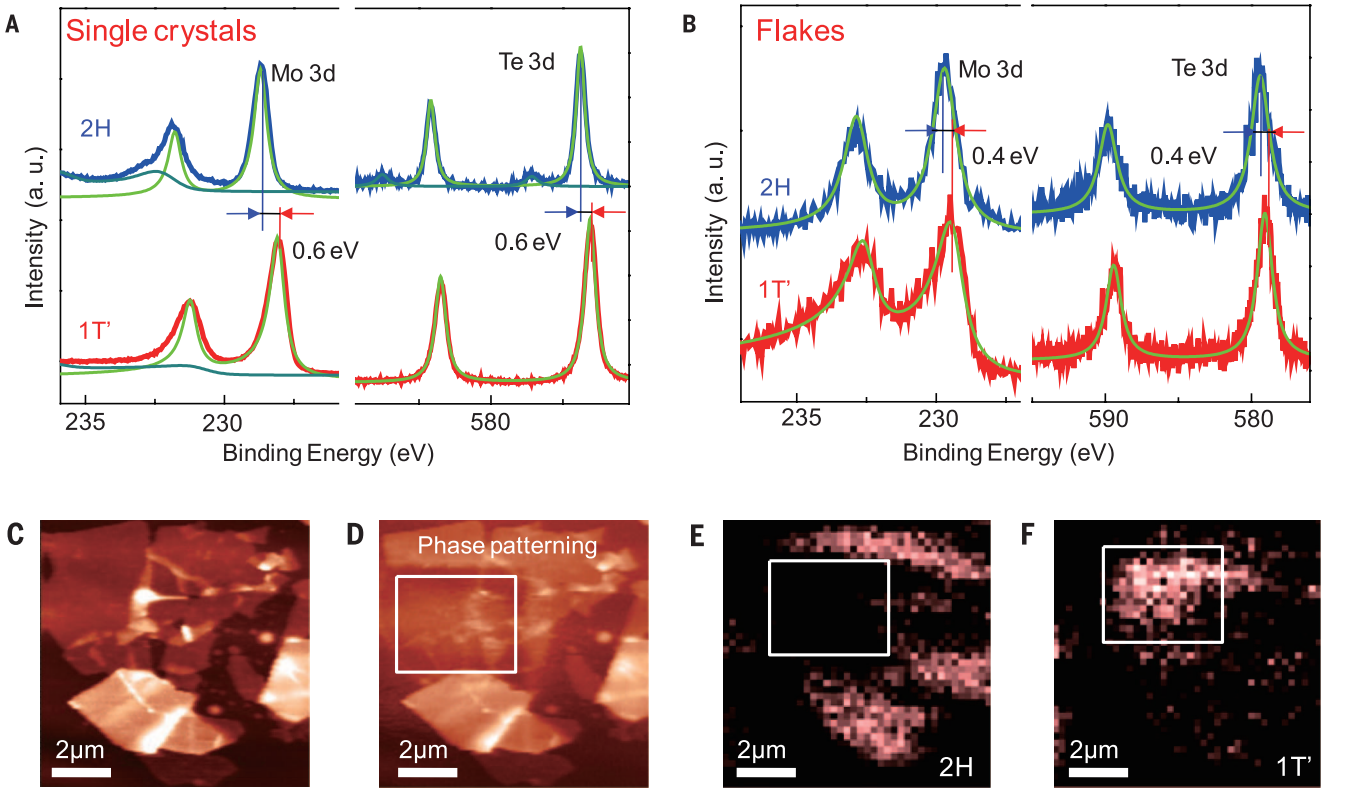

Fig. 3. SPEM study of phase-patterned $MoTe_2$. (**A**) Photoemission spectra of Mo 3d and Te 3d electrons in single-crystalline 1T'- (red) and 2H-$MoTe_2$ (blue). Green and dark cyan curves are $MoTe_2$ and MoO_3 (or TeO_2) fitting, respectively. (**B**) Photoemission spectra of Mo 3d and Te 3d electrons in patterned (1T', red) and nonpatterned (2H, blue) areas. AFM images (**C**) before and (**D**) after laser irradiation, with a white rectangle indicating the illuminated region. Binding energy map of Mo 3d electrons for the (**E**) 2H phase and (**F**) 1T' phase in the same region as (D).

up to 300°C, where operation is still stable. The Arrhenius plots reveal the substantially decreased energy barrier height in the phase-patterned device (1T' contact in Fig. 2E). The energy barrier extraction from the Arrhenius plot provides direct evidence of the true ohmic contact, negligible energy barrier height, in phase-patterned devices. Accordingly, the carrier field-effect mobility is enhanced by a factor of ~50 compared with that of the device with a conventional 2H-$MoTe_2$/metal contact [Fig. 2F, fig. S7, and table S3 (19)].

The chemical states of the Mo and Te atoms in the phase-patterned $MoTe_2$ were investigated by scanning photoelectron microscopy (SPEM) with a spatial resolution of 200 nm. The binding energies of the Mo and Te 3d electrons measured in 2H- and 1T'-$MoTe_2$ single crystals (Fig. 3A) revealed an energy shift of 0.6 eV between the 2H- and 1T'-$MoTe_2$ samples that can be explained by the different lattice symmetry of 2H and 1T'-$MoTe_2$. A similar energy shift, 0.4 eV, was seen between patterned and nonpatterned areas (Fig. 3B). Thus, the phase-patterned area has chemical states of Mo and Te atoms similar to the 1T'-$MoTe_2$ single crystal.

Atomic force microscopy (AFM) images with a rectangle indicating the laser-irradiated area (Fig. 3, C and D) show a thinning effect after laser irradiation. The sample shown in Fig. 3D was used for the SPEM study. The SPEM mapping images in Fig. 3, E and F, were obtained with photoelectron counts in a selective window of binding energies for each phase, which reveal the spatial distribution of the 2H (Fig. 3E) and 1T' (Fig. 3F) phases, respectively. The surface-sensitive SPEM shows only the 1T' phase in the patterned area. By noting that Raman spectroscopy shows a mixed phase of 2H and 1T', we support the

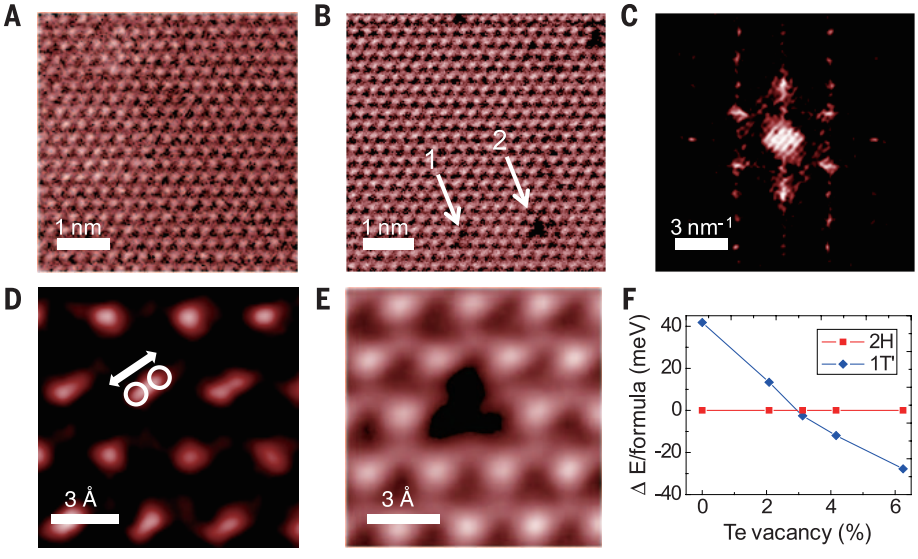

Fig. 4. In situ STEM observation of Te-defect–driven structural phase transition in a monolayer of $MoTe_2$ (T = 400°C). (**A**) Atomic image of a monolayer of 2H-$MoTe_2$. Bright spheres are Te atoms with hexagonal symmetry. (**B**) Atomic Te vacancies created artificially. Te single vacancy and divacancy are visible and marked by 1 and 2, respectively. (**C**) FFT image of (B). (**D**) Filtered high-resolution image near a Te vacancy showing the splitting of the Te atoms. (**E**) Atomic resolution image of a Te divacancy defect. (**F**) The energy differences between the 2H and 1T' phases as a function of the Te vacancy concentration from the DFT calculation.

argument that the 1T' phase is located in the upper layer (Fig. 1E). Furthermore, no MoO_3, TeO_2, or other elements were observed in the SPEM results [figs. S8 and S9 (*19*)], which is consistent with the Raman spectroscopy results in Fig. 1. This demonstrates a clean heterophase homojunction structure without oxides or other elements by our phase patterning, which is an advantage compared with the precedent of metastable phase engineering with MoS_2 by a chemical method (*7*).

The structural transformation process during phase patterning was clarified by in situ scanning transmission electron microscopy (STEM) with a monolayer of 2H-$MoTe_2$ (Fig. 4). Of the two major physical processes, local heating and valence electron excitation related to laser irradiation, we explored the former on the atomic scale. In Fig. 4A, the atomic images obtained at T = 400°C, similar to the estimated temperature during laser irradiation, primarily show Te atoms of 2H-$MoTe_2$. Although Te atoms can be sublimated at T = ~400°C (*16*), the monolayer 2H phase region remained robust without generating Te vacancies (Fig. 4A). To slightly stimulate the temperature effect, we used a scanning electron beam irradiation (with a beam size of 1 Å and a beam current of 20 pA). Then, low-density atomic Te defects were created (Fig. 4B), and, more important, a clear sign of the structural phase transition from the 2H to 1T' phases was observed in Fig. 4C, which is a fast Fourier-transform (FFT) image of Fig. 4B. Although the hexagonal symmetry remains, as shown by the lattice symmetry of 2H-$MoTe_2$, extra periodic spots with a rectangular symmetry appear in Fig. 4C. The rectangular lattice symmetry is a feature of distorted octahedral (1T') $MoTe_2$ (*16*, *22*).

In contrast to 2H-$MoTe_2$, in which two Te atoms completely overlap in the top view of the crystal in the STEM images, 1T'-$MoTe_2$ should show split Te positions in the top view STEM image (Fig. 1A). The initial stage of splitting the Te atom positions is captured in Fig. 4D, which is a filtered STEM image to clearly show the Te atoms. As marked by two circles and an arrow, the Te atoms start splitting but do not yet completely reach the 1T' phase over the entire area. No such split or rectangular symmetry in FFT was observed without Te vacancies in the monolayer of 2H-$MoTe_2$. This result indicates that the phase transition originates from the Te vacancies at an elevated temperature, either by laser irradiation or by a heating stage. An atomic vacancy is shown in Fig. 4E.

Our density functional theory (DFT) calculations that explain the phase transition by the Te vacancy are shown in Fig. 4F. To select the most stable phase at a low temperature, the relative binding energy per unit formula between the 2H and 1T' phases is plotted as a function of Te vacancy concentration in Fig. 4F. It is clear that a Te monovacancy concentration exceeding 3% causes the 1T' phase to be more stable than the 2H phase, which is qualitatively consistent with our experimental results. Furthermore, the band alignment of ohmic contact at the homojunction of the 2H and the 1T' phases of $MoTe_2$ was verified by our DFT calculations (*19*). Compared with the Schottky contact between 2H-$MoTe_2$ and the Au electrode, the interlayer charge transfer across the homojunction in $MoTe_2$ causes only a slight energy difference between the electron affinity of 2H-$MoTe_2$ and the work function of atomically thin 1T'-$MoTe_2$.

The reverse phase transition from the 1T' to the 2H phase was not observed by laser irradiation, even with a higher energy or intensity of the laser. In previous studies (*23*, *24*), temperature has been considered as the primary origin of the phase transition, but the irreversible phase change from the 2H to 1T' phase cannot be explained simply by the thermodynamic reaction in the phase diagram. Moreover, the estimated temperature by laser irradiation (~400°C) is markedly lower than the reported temperature (880°C) for the phase transition. A possible scenario for the one-way phase transition is the strain effect originating from thermal expansion, but the expected thermal coefficient (~10^{-6} K^{-1}) produces substantially less lattice strain (~0.05%) than the required amount of strain (~5%) for the phase transition (*15*). Thus, the driving force for the phase patterning is the irreversible Te vacancy created by laser irradiation, as verified in the STEM experiment.

REFERENCES AND NOTES

1. Q. H. Wang, K. Kalantar-Zadeh, A. Kis, J. N. Coleman, M. S. Strano, *Nat. Nanotechnol.* **7**, 699–712 (2012).
2. M. Chhowalla *et al.*, *Nat. Chem.* **5**, 263–275 (2013).
3. A. Y. C. Yu, *Solid-State Electron.* **13**, 239–247 (1970).
4. S. Das, H.-Y. Chen, A. V. Penumatcha, J. Appenzeller, *Nano Lett.* **13**, 100–105 (2013).
5. K.-E. Byun *et al.*, *Nano Lett.* **13**, 4001–4005 (2013).
6. W. S. Leong *et al.*, *ACS Nano* **9**, 869–877 (2015).
7. R. Kappera *et al.*, *Nat. Mater.* **13**, 1128–1134 (2014).
8. E. Morosan *et al.*, *Nat. Phys.* **2**, 544–550 (2006).
9. B. Sipos *et al.*, *Nat. Mater.* **7**, 960–965 (2008).
10. J. T. Ye *et al.*, *Science* **338**, 1193–1196 (2012).
11. D. W. Shen *et al.*, *Phys. Rev. Lett.* **99**, 216404 (2007).
12. Y. J. Zhang, T. Oka, R. Suzuki, J. T. Ye, Y. Iwasa, *Science* **344**, 725–728 (2014).
13. G. Eda *et al.*, *ACS Nano* **6**, 7311–7317 (2012).
14. Y.-C. Lin, D. O. Dumcenco, Y.-S. Huang, K. Suenaga, *Nat. Nanotechnol.* **9**, 391–396 (2014).
15. K.-A. N. Duerloo, Y. Li, E. J. Reed, *Nat. Commun.* **5**, 4214 (2014).
16. D. H. Keum *et al.*, *Nat. Phys.* **11**, 482–486 (2015).
17. Y.-F. Lin *et al.*, *Adv. Mater.* **26**, 3263–3269 (2014).
18. N. R. Pradhan *et al.*, *ACS Nano* **8**, 5911–5920 (2014).
19. Supplementary materials are available on *Science* Online.
20. M. Yamamoto *et al.*, *ACS Nano* **8**, 3895–3903 (2014).
21. G. H. Han *et al.*, *ACS Nano* **5**, 263–268 (2011).
22. J. Heising, M. G. Kanatzidis, *J. Am. Chem. Soc.* **121**, 638–643 (1999).
23. M. B. Vellinga, R. de Jonge, C. Haas, *J. Solid State Chem.* **2**, 299–302 (1970).
24. A. Conan, A. Bonnet, A. Amrouche, M. Spiesser, *J. Phys.* **45**, 459–465 (1984).

ACKNOWLEDGMENTS

We acknowledge support from the Institute for Basic Science (IBS-R011-D1), the National Research Foundation of Korea (NRF) under grant NRF-2014R1A1A2056386 (H. Y.), the NRF under grant 2013R1A1A1008025 (S.W.K.), and the NRF under grant NRF-2005-0093845 (D.H.C. and K.J.C.). All data described are presented in the supplementary materials.

SUPPLEMENTARY MATERIALS

www.sciencemag.org/content/349/6248/625/suppl/DC1
Materials and Methods
Figs. S1 to S15
Tables S1 to S3
References (*25*–*39*)

9 April 2015; accepted 29 June 2015
10.1126/science.aab3175

BIOLOGICAL ADHESIVES

Adaptive synergy between catechol and lysine promotes wet adhesion by surface salt displacement

Greg P. Maier,[1]* Michael V. Rapp,[2]* J. Herbert Waite,[3]† Jacob N. Israelachvili,[2,4]† Alison Butler[1]†

In physiological fluids and seawater, adhesion of synthetic polymers to solid surfaces is severely limited by high salt, pH, and hydration, yet these conditions have not deterred the evolution of effective adhesion by mussels. Mussel foot proteins provide insights about adhesive adaptations: Notably, the abundance and proximity of catecholic Dopa (3,4-dihydroxyphenylalanine) and lysine residues hint at a synergistic interplay in adhesion. Certain siderophores—bacterial iron chelators—consist of paired catechol and lysine functionalities, thereby providing a convenient experimental platform to explore molecular synergies in bioadhesion. These siderophores and synthetic analogs exhibit robust adhesion energies (E_{ad} ≥ −15 millijoules per square meter) to mica in saline pH 3.5 to 7.5 and resist oxidation. The adjacent catechol-lysine placement provides a "one-two punch," whereby lysine evicts hydrated cations from the mineral surface, allowing catechol binding to underlying oxides.

Water disrupts adhesion on polar surfaces by forming hydration layers that impede intimate contact between adhesive polymers and surfaces. Sessile marine organisms, including barnacles, kelps, and mussels, routinely adhere to wet saline surfaces, suggesting that successful adaptations for removing weak boundary layers have evolved. Identifying these adaptations holds great promise for adhesion science and technology. The mussel holdfast or

byssus contains ~15 adhesive mussel foot proteins (mfps), two of which, mfp-3 and mfp-5, are deposited first as a primer to condition the target surface and enable other mfps to adhere (*1*) and are peculiar in containing between 20 and 30 mole percent (mol %) Dopa (3,4-dihydroxyphenylalanine). Demonstration by atomic force microscopy of wet adhesion to titania by a single Dopa (*2*) sparked functionalization of synthetic polymeric adhesives and self-healing hydrogels with catechol (*3*–*8*), but wet adhesion of these polymers to oxides and minerals remains controversial (*9*, *10*). In actuality, mfp-3 and -5 are rich in Lys as well as Dopa, which are frequently in adjacent positions along the protein backbone (*1*). The surface forces apparatus (SFA) has measured impressive wet adhesion of these proteins to mineral, oxide, and organic surfaces (*11*). Dopa residues in mfp-3 and -5 form bidentate coordination and hydrogen bonds to mineral and oxide surfaces and hydrophobic interactions on polymeric surfaces (*11*), but only if protected from oxidation by low pH and antioxidants during deposition (*12*, *13*). Several mimics of mfps have been synthesized, most notably Dopa-Lys copolymers by Yamamoto (*14*) and Deming (*15*) using N-carboxyanhydride ring-opening polymerization, as well as the polymer brush anchors developed by Messersmith (*6*). However, the role of Lys in both the mussel surface primers and in synthetic wet adhesives remains poorly understood.

Many marine and pathogenic bacteria have evolved an adaptive iron-sequestration pathway that is based on catechol-containing siderophores, including enterobactin, the lactone of *tris*-2,3-dihydroxybenzoyl-L-Ser (2,3-DHBA-L-Ser) (*16*). The plant pathogen *Dickeya chrysanthemi* produces the siderophore, cyclic trichrysobactin (CTC), the lactone of *tris*-2,3-DHBA-D-Lys-L-Ser (Fig. 1A), in which Lys is present adjacent to each catechol (*17*). The prominence and proximity of catechol and Lys in CTC resemble the interfacial adhesive proteins mfp-3 and mfp-5. However, the mass of CTC (1053 g/mol) is a fraction of the mfp-3 and -5 masses (6 kD and 10 kD, respectively). As such, the siderophore has relaxed steric constraints when adsorbed to a surface, and the simpler siderophore structure allows for more straightforward interpretation of the adhesive mechanisms. In addition, the autoxidation of 2,3-DHBA is much slower than 4-methylcatechol, a proxy for the 3,4-dihydroxy substituents in the Dopa catechol, at pH 7.5 and 10 (fig. S1 and supplementary text), reflecting intramolecular H-bonding between the ortho-OH and the carbonyl oxygen and the electron-withdrawing nature of the carboxylate substituent (Fig. 1B), both of which stabilize CTC against oxidation compared with Dopa in mfps. Ultimately, subtle molecular differences in 2,3-DHBA contribute to the oxidation resistance in siderophores and enlarge the pH range over which these compounds bind to target surfaces.

A SFA was used to measure the normalized force (F/R)–distance (D) profiles of two molecularly smooth mica surfaces (of radius R) during their approach and separation in buffered solutions of CTC (*18*). In these SFA measurements, the surfaces are first slowly brought into contact and compressed. The thickness of the intervening compressed film between the surfaces is measured as D_T. The surfaces are then slowly separated, and the adhesion force (F_{ad}/R) is measured at the force minimum, at a point just before the surfaces rapidly jump apart.

Mica is an anionic and molecularly smooth aluminosilicate mineral that allows for Å-level mechanistic insight during adhesion measurements. In saline solutions, mica adsorbs cations (particularly K^+) to form a tightly bound hydration layer at the solid-liquid interface (*19*, *20*). These hydration layers, present at virtually all marine and physiological interfaces, impose a substantial molecular barrier to coatings and high-performance adhesives for wet surfaces (*21*). The effects of these hydration layers between mica surfaces in buffered solution without any added siderophores (Fig. 1C, black circles) are seen in the SFA measurements: When compressed to 10 mN m^{-1}, hydrated K^+ ions form a D_T = 13 ± 1 Å–thick layer between the mica surfaces, and only a weak adhesion force is measured on separation. However, nanomole amounts of CTC form a single monolayer "molecular bridge" that results in a large adhesion force between the micas, presumably by displacing the hydrated salt ions from the mica surface (Fig. 1C, red circles). After injecting 10 nanomoles of CTC into the buffered gap solution between the mica surfaces (~50 μL total volume, 200 μM bulk concentration), the compressed film thins to 11 ± 1 Å, indicating that the hydrated salt ions have been

[1]Department of Chemistry and Biochemistry, University of California, Santa Barbara, CA 93106, USA. [2]Department of Chemical Engineering, University of California, Santa Barbara, CA 93106, USA. [3]Molecular, Cellular, and Developmental Biology, University of California, Santa Barbara, CA 93106, USA. [4]Materials Department, University of California, Santa Barbara, CA 93106, USA.
*These authors contributed equally to this work.
†Corresponding author. E-mail: herbert.waite@lifesci.ucsb.edu (J.H.W.); jacob@engineering.ucsb.edu (J.N.I.); butler@chem.ucsb.edu (A.B.)

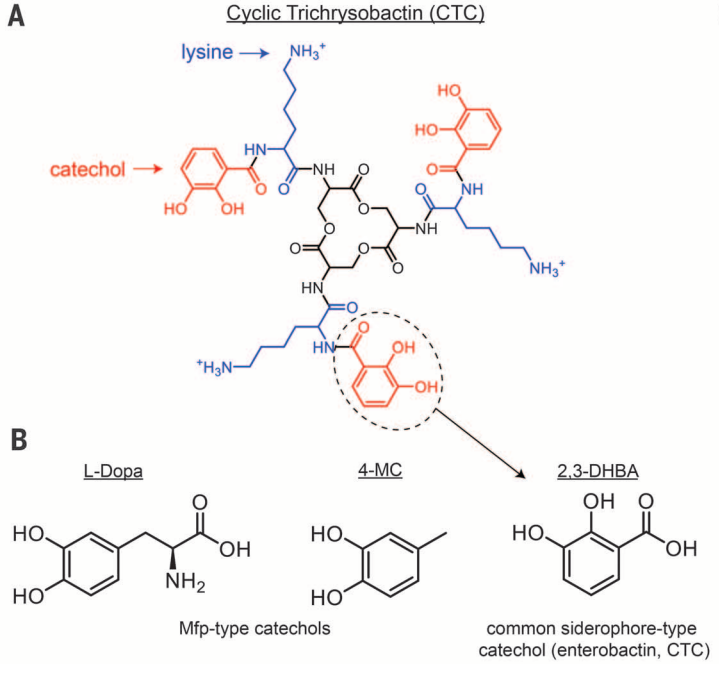

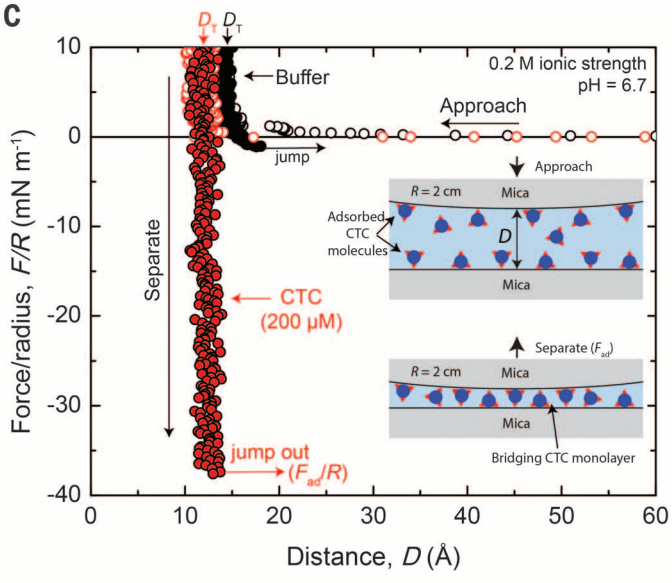

Fig. 1. Adhesion of a natural bacterial catechol siderophore. (**A**) Structure of CTC. (**B**) Structures of catechols illustrating the difference between 3,4-dihydroxy catechol, as in Dopa or 4-methylcatechol (4-MC), and 2,3-dihydroxy catechol, as commonly present in DHBA-containing-siderophores. (**C**) SFA force-distance interaction for CTC-mediated adhesion between two mica surfaces in buffer (50 mM phosphate buffer + 150 mM KNO_3) at pH 6.7. The surfaces were left in contact for 30 min before separation. The open and solid circles are for data measured on approach and separation, respectively, of the mica surfaces. The inset displays a schematic of the interacting surfaces throughout the SFA experiments.

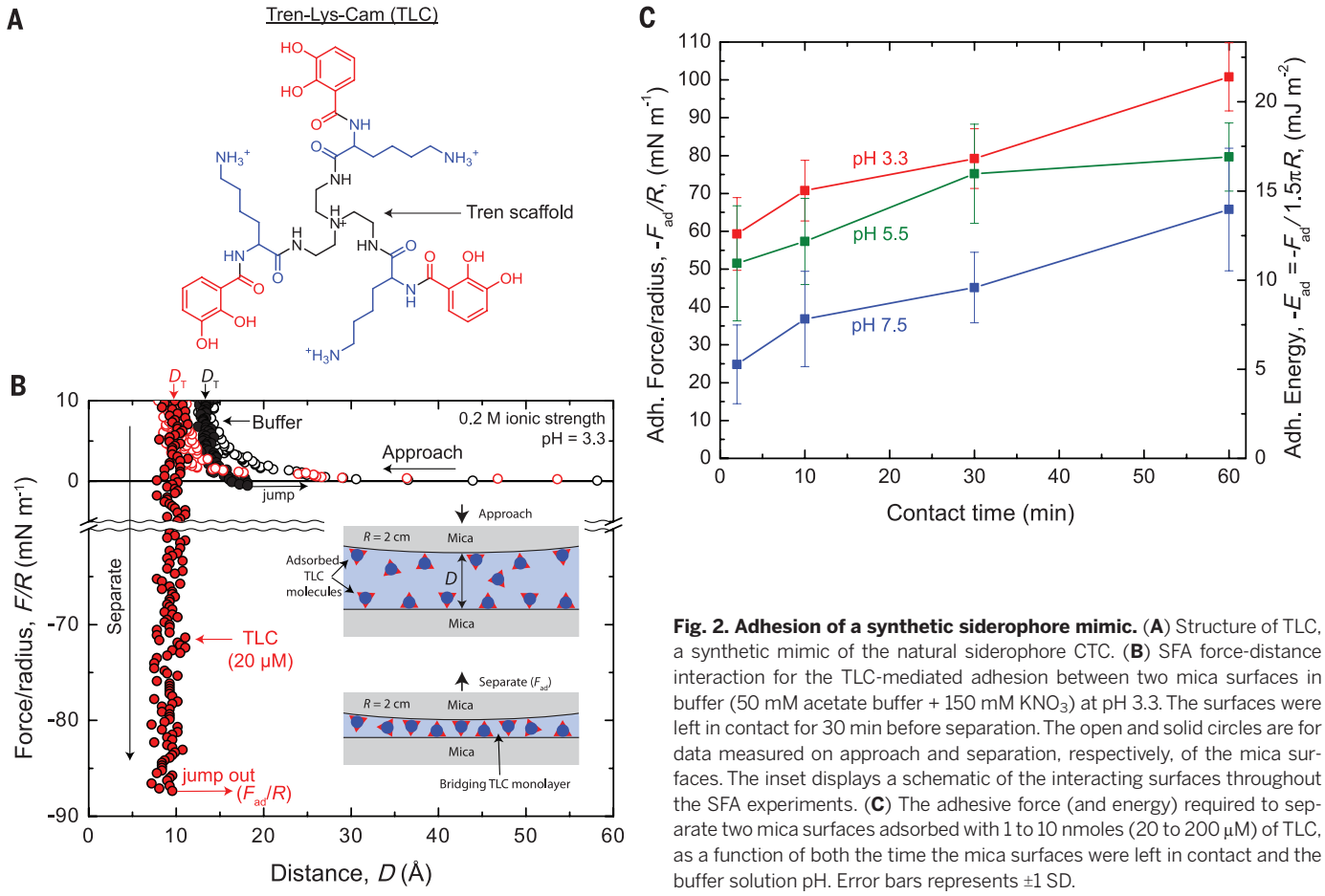

Fig. 2. Adhesion of a synthetic siderophore mimic. (**A**) Structure of TLC, a synthetic mimic of the natural siderophore CTC. (**B**) SFA force-distance interaction for the TLC-mediated adhesion between two mica surfaces in buffer (50 mM acetate buffer + 150 mM KNO_3) at pH 3.3. The surfaces were left in contact for 30 min before separation. The open and solid circles are for data measured on approach and separation, respectively, of the mica surfaces. The inset displays a schematic of the interacting surfaces throughout the SFA experiments. (**C**) The adhesive force (and energy) required to separate two mica surfaces adsorbed with 1 to 10 nmoles (20 to 200 μM) of TLC, as a function of both the time the mica surfaces were left in contact and the buffer solution pH. Error bars represents ±1 SD.

replaced with CTC at the surface, and the adhesion force between the surfaces increases by a factor of approximately 30-fold to −30 ± 10 mN m^{-1}. As the surfaces are separated, the sharply vertical shape of the separation force curve does not exhibit any observable bridging (i.e., an increase in the separation distance), indicating that the physical bonds supporting adhesion are specific and short-ranged (effective only over several Å), such as a hydrogen bond or specific Coulombic interaction (*20*).

The natural 2,3-DHBA–containing CTC siderophore promotes adhesion at near-neutral pH (pH 6.7), a solution condition that rapidly oxidizes Dopa in mfps leading to reduced adhesion (*12*). Yet, the triserine lactone scaffold of CTC hydrolyses under acidic conditions, limiting its usefulness as an adhesive primer over a wide range of pH. To circumvent this limitation, we synthesized a mimic of CTC, Tren-Lys-Cam (TLC) (Fig. 2A) built on the robust tris(2-aminoethyl)amine (Tren) scaffold that retains integrity over a wide pH range (fig. S2) (*22*). TLC exhibits nearly identical adsorption and adhesion behavior to the natural CTC siderophore. In parallel SFA experiments at pH 3.3 (Fig. 2B), TLC molecules displace hydrated salt ions at the mica surface and, after compression of the surfaces, form a 9 ± 1 Å–thick monolayer that bridges between the two surfaces. The thickness of the TLC film, the shape of the force-distance profile (narrow adhesion well), and dramatically increased adhesion all indicate that the synthetic TLC performs similarly to CTC at mineral surfaces.

TLC mediates adhesion between mineral surfaces in saline solution from pH 3.3 to 7.5 (Fig. 2C). The TLC peak adhesion concentration is ~20 μM (fig. S3). Adhesion forces measured in SFA experiments are converted to adhesion energies through the Johnson-Kendal-Roberts theory of adhesive surfaces ($E_{ad} = F_{ad}/1.5\pi R$) (*23*). Adhesion is strongest at pH 3.3 and is not statistically different from pH 5.5 for $P \leq 0.05$ (table S1). At pH 7.5, adhesion decreases ($P \leq 0.05$), yet TLC still maintains ~65% of the peak adhesion. The cause for the decrease in adhesion at pH 7.5 is under investigation; we speculate that either slow TLC oxidation or subtle interfacial pH changes reduce the number of bridging hydrogen bonds at pH 7.5. Moreover, adhesion energy increases with contact time before separation, a common trait among adhesives. As longer contact allows for better interfacial equilibration, more siderophore molecules are able to rearrange and maximize the number of bridging bonds (*20*).

To ascertain specific contributions made by catechol and Lys in the siderophore adhesive platform, we synthesized a suite of five additional Tren-based homologs, varying properties of the amine and the aromatic functionalities (Fig. 3, A to G; figs. S4 to S13; and tables S2 to S4). Group I homologs retain both catechol and amine functionalities (Fig. 3, B and C), group II retains Lys but removes the catechol functionality (Figs. 3D and 3E), and group III retains catechol but removes the amine functionality (Figs. 3F and 3G). Collectively, the results of the six synthetic homologs reveal a requirement for catechol and an alkylamine cation (e.g., Lys and Dab) for appreciable surface binding and adhesion.

Group I includes TLC and Tren-Dab-Cam (TDC), with the Lys chain shortened by two methylene units to diaminobutyric acid (Dab). Group I assesses whether the length or flexibility of the amine is critical to adsorption and adhesion. The length of the amine chain between 2 and 4 carbons does not alter the homolog's behavior, because both TLC and TDC displace salt on the mica surface and promote large adhesion energies (Fig. 3, H and I, and fig. S14C).

Group II homologs test the effect of removing catechol, while maintaining the 4+ cationic charge: Tren-Lys-Pam (TLC) retains one hydroxyl group, whereas Tren-Lys-Bam (TLB) removes both hydroxyls. Without catechol, the group II homologs exhibit comparatively weak adhesion between mica surfaces—i.e., ~15% of the group I homologs with both Lys and catechol. Contrary to the narrow adhesion wells of the group I homologs, the separation force curves of group II homologs display weak bridging (~5 to 10 Å) before the surfaces jump apart (fig. S14, A and B), suggesting that the adhesion may be due to nonspecific interactions

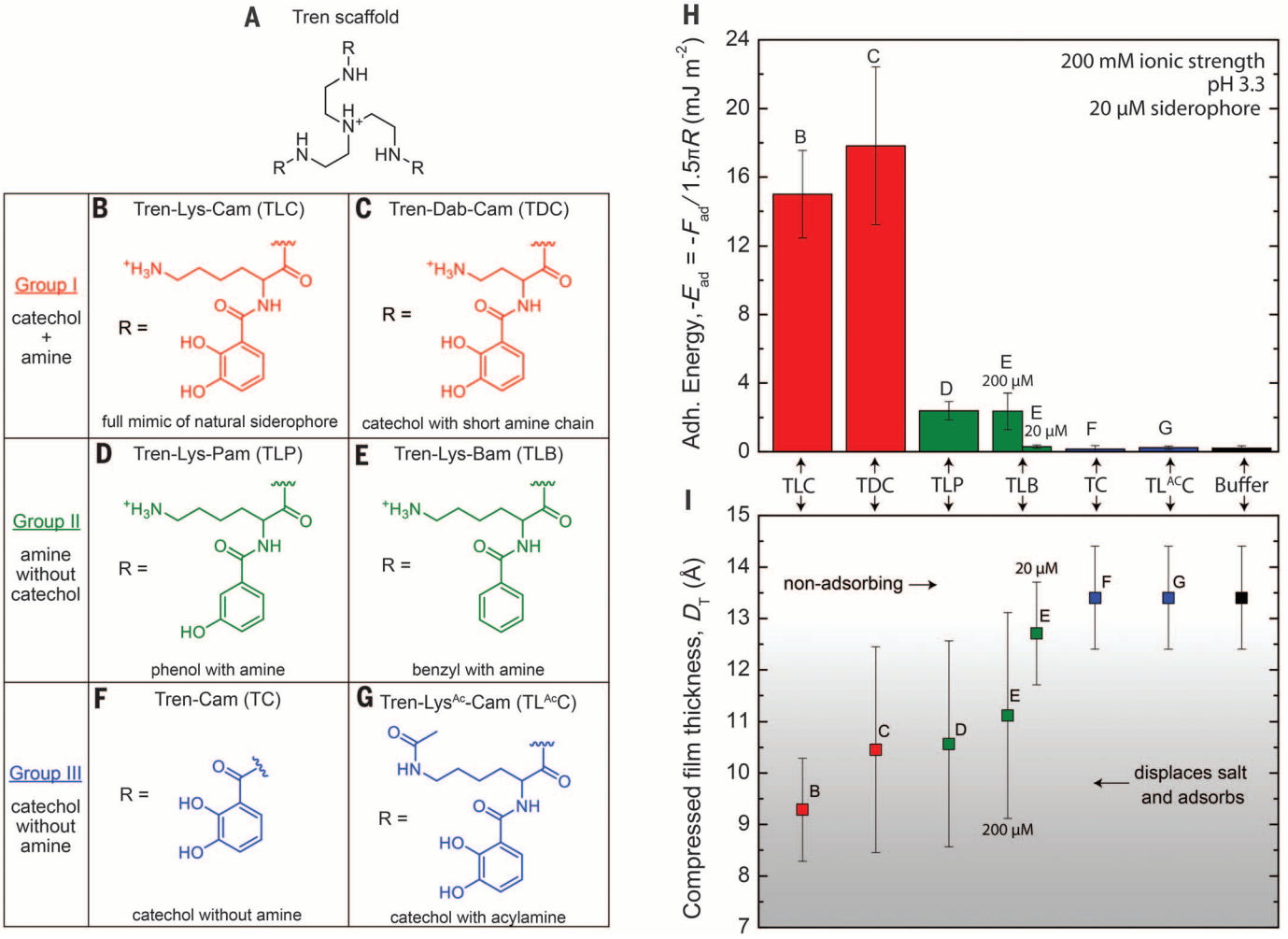

Fig. 3. The synergy of catechol and Lys in siderophore adhesion. (**A**) Structure of the Tren scaffold. (**B** to **G**) The R groups appended to Tren. (**H**) The average adhesion energy required to separate two mica surfaces adsorbed with 1 nmole (20 μM, except where indicated at 200 μM) of the homolog in buffer (50 mM acetate + 150 mM KNO_3) at pH 3.3 after 10 min of contact. (**I**) D_T of the siderophore monolayer between two mica surfaces at 10 mN/m of compressive load. The film thicknesses correspond with the adhesion energy displayed in (H). A decreased film thickness (<12 Å) indicates that homologs B, C, D, and E (200 μM) adsorb, displace hydrated salt at the mica surface, and mediate adhesion between two mica surfaces. SFA force-distance measurements for each molecule are shown in figs. S14 and S15.

between two or more homologs (such as hydrophobic interactions or π-cation interactions) (*24*). TLB is unable to donate H bonds and has increased hydrophobicity; hence, it has an increased energy barrier for adsorption. TLP adsorbs to the mica surface at 20 μM (the same as the TLC critical aggregation concentration), yet TLB requires an elevated bulk concentration of 200 μM before adsorption begins.

Group III homologs compromise the amine functionality through acetylation [Tren-Lys^{Ac}-Cam (TL^{Ac}C)] or by omission of Lys [Tren-Cam (TC)], while maintaining the catechol presence. Over the concentration range of 2 to 200 μM, group III homologs do not adsorb on the mica surface at high salt (μ = 200 mM) and provide no adhesion (fig. S15, A and B). In pure water, TC adsorbs as a multilayer on mica and demonstrates modest cohesion (fig. S15C).

In sum, the amine and catechol moieties interact synergistically to mediate surface priming by the catechol alkylamine compounds to mineral surfaces. Bidentate catechol-mediated H-bonding is necessary for robust bridging attachments between surfaces; however, catechols alone are insufficient to breach the hydrated salt layer on mica, which is typical of a wide variety of aluminosilicate minerals in its cation binding properties (*25*). The amines in CTC and TLC may serve as molecular vanguards to displace hydrated salt ions and ready the surface for bidentate catechol binding (*26*).

The discovery that 2,3-dihydroxycatechol and alkyl ammonium (e.g., Lys and Dab) functionalities limit oxidation and promote adhesion has relevance to other adhesive platforms in providing a compelling rationale for the >20 mol % of cationic residues in Dopa-rich mfps (*1*) and establishing a set of design parameters for future bio-inspired synthetic polymers. Because many synthetic adhesives are functionalized with catechols and amines (*27*) for improved solubility (*10*) or cross-linking effects (*28*, *29*), our results highlight the need to couple catechol and cationic functionalities to displace surface salts.

REFERENCES AND NOTES

1. B. P. Lee, P. B. Messersmith, J. N. Israelachvili, J. H. Waite, *Annu. Rev. Mater. Res.* **41**, 99–132 (2011).
2. H. Lee, N. F. Scherer, P. B. Messersmith, *Proc. Natl. Acad. Sci. U.S.A.* **103**, 12999–13003 (2006).
3. M. Krogsgaard, M. A. Behrens, J. S. Pedersen, H. Birkedal, *Biomacromolecules* **14**, 297–301 (2013).
4. H. Shao, R. J. Stewart, *Adv. Mater.* **22**, 729–733 (2010).
5. C. J. Kastrup *et al.*, *Proc. Natl. Acad. Sci. U.S.A.* **109**, 21444–21449 (2012).
6. A. R. Statz, R. J. Meagher, A. E. Barron, P. B. Messersmith, *J. Am. Chem. Soc.* **127**, 7972–7973 (2005).
7. J. Ryu, S. H. Ku, H. Lee, C. B. Park, *Adv. Funct. Mater.* **20**, 2132–2139 (2010).
8. J. D. White, J. J. Wilker, *Macromolecules* **44**, 5085–5088 (2011).
9. Y. Li, M. Qin, Y. Li, Y. Cao, W. Wang, *Langmuir* **30**, 4358–4366 (2014).
10. J. Wang *et al.*, *Adv. Mater.* **20**, 3872–3876 (2008).
11. J. Yu *et al.*, *Proc. Natl. Acad. Sci. U.S.A.* **110**, 15680–15685 (2013).
12. J. Yu *et al.*, *Nat. Chem. Biol.* **7**, 588–590 (2011).
13. N. R. Martinez Rodriguez, S. Das, Y. Kaufman, J. N. Israelachvili, J. H. Waite, *Biofouling* **31**, 221–227 (2015).
14. H. Yamamoto, *J. Chem. Soc., Perkin Trans. 1* 613–618 (1987).
15. M. Yu, J. Hwang, T. Deming, *J. Am. Chem. Soc.* **121**, 5825–5826 (1999).

16. K. N. Raymond, E. A. Dertz, S. S. Kim, *Proc. Natl. Acad. Sci. U.S.A.* **100**, 3584–3588 (2003).
17. M. Sandy, A. Butler, *J. Nat. Prod.* **74**, 1207–1212 (2011).
18. J. Israelachvili *et al.*, *Rep. Prog. Phys.* **73**, 036601 (2010).
19. R. M. Pashley, *Adv. Colloid Interface Sci.* **16**, 57–62 (1982).
20. J. N. Israelachvili, *Intermolecular and Surface Forces: Revised Third Edition* (Academic Press, 2011).
21. J. Israelachvili, H. Wennerström, *Nature* **379**, 219–225 (1996).
22. S. J. Rodgers, C. W. Lee, C. Y. Ng, K. N. Raymond, *Inorg. Chem.* **26**, 1622–1625 (1987).
23. K. L. Johnson, K. Kendall, A. D. Roberts, *Proc. R. Soc. A Math. Phys. Eng. Sci.* **324**, 301–313 (1971).
24. S. Kim *et al.*, *J. Mater. Chem. B* **3**, 738–743 (2015).
25. W. Stumm, J. J. Morgan, *Aquatic Chemistry: Chemical Equilibria and Rates in Natural Waters, 3rd Edition* (Wiley, New York, 1996).
26. Y. Akdogan *et al.*, *Angew. Chem.* **53**, 11253–11256 (2014).
27. P. Podsiadlo, Z. Liu, D. Paterson, P. B. Messersmith, N. A. Kotov, *Adv. Mater.* **19**, 949–955 (2007).
28. F. Zhang, S. Liu, Y. Zhang, Y. Wei, J. Xu, *RSC Adv.* **2**, 8919–8921 (2012).
29. Q. Wei *et al.*, *Angew. Chem. Int. Ed. Engl.* **53**, 11650–11655 (2014).

ACKNOWLEDGMENTS

We are grateful for support from the Materials Research and Science Engineering Centers Program of the National Science Foundation under award DMR 1121053, NSF CHE-1411942 (A.B.), and NSF GRFP (M.R.).

SUPPLEMENTARY MATERIALS

www.sciencemag.org/content/349/6248/628/suppl/DC1
Materials and Methods
Supplementary Text
Figs. S1 to S15
Tables S1 to S4
Reference (*30*)

4 March 2015; accepted 15 June 2015
10.1126/science.aab0556

CHARGE TRANSFER

Efficient hot-electron transfer by a plasmon-induced interfacial charge-transfer transition

K. Wu,[1] J. Chen,[1] J. R. McBride,[2] T. Lian[1]*

Plasmon-induced hot-electron transfer from metal nanostructures is a potential new paradigm for solar energy conversion; however, the reported efficiencies of devices based on this concept are often low because of the loss of hot electrons via ultrafast electron-electron scattering. We propose a pathway, called the plasmon-induced interfacial charge-transfer transition (PICTT), that enables the decay of a plasmon by directly exciting an electron from the metal to a strongly coupled acceptor. We demonstrated this concept in cadmium selenide nanorods with gold tips, in which the gold plasmon was strongly damped by cadmium selenide through interfacial electron transfer. The quantum efficiency of the PICTT process was high (>24%), independent of excitation photon energy over a ~1–electron volt range, and dependent on the excitation polarization.

The surface plasmon resonance (SPR) of metallic nanostructures has been widely used to improve the efficiency of photovoltaics (*1*–*5*), photocatalysis (*6*, *7*), and photodetectors (*8*, *9*), either by increasing light absorption through enhanced local fields near the metal nanostructures (*10*) or by plasmon-induced charge transfer from the excited metal (*11*–*13*). The latter enhancement mechanism suggests the possibility of using plasmonic metal nanostructures as light absorbers with broad spectral tunability, large absorption cross sections, superior long-term stability, and low-cost colloidal synthesis (*14*, *15*). Thus far, all reported plasmon-induced charge-separation processes have been believed to occur through a conventional plasmon-induced hot-electron transfer (PHET) mechanism (Fig. 1A). During PHET, a plasmon decays into a hot electron–hole pair within the metal via Landau damping on time scales of a few to tens of femtoseconds (*16*–*18*); this is followed by the transfer of the hot electron into adjacent semiconductors or molecules. Hot-electron transfer competes with electron relaxation through rapid electron-electron scattering in the metal's conduction band (CB) on time scales of hundreds of femtoseconds (*18*–*20*). Efficient PHET requires interfacial charge separation on an even faster time scale, which is difficult to realize in many semiconductor-metal hybrid materials. Thus, the reported efficiencies for devices based on plasmon-induced charge-separation concepts are too low for practical applications (*6*–*8*).

Metal-to-semiconductor hot-electron transfer efficiencies can be enhanced if the competition with ultrafast electron-electron scattering in the metal can be avoided. One approach is to create a direct metal-to-semiconductor interfacial charge-transfer transition (DICTT) that can be directly excited to promote an electron from the metal into the semiconductor CB (Fig. 1B). Such transitions between metal adatoms and semiconductor electrodes have been reported (*21*), as have metal-to-adsorbate resonances for CO adsorbed on Pt nanoparticles (NPs) (*22*, *23*) and Cs atoms adsorbed on Cu(111) (*24*, *25*). However, these interfacial transitions are often too weak as compared with bulk metal transitions or plasmon bands (*22*–*25*) and cannot serve as efficient light-harvesting pathways. Ideally, a desirable photoinduced hot-electron transfer pathway would combine the strong light-absorbing power of plasmonic transitions with the superior charge-separation properties of the DICTT mechanism (Fig. 1C). In this plasmon-induced metal-to-semiconductor interfacial charge-transfer transition (PICTT) pathway, the metal plasmon serves as a light absorber, but strong interdomain coupling and mixing of the metal and semiconductor levels lead to a new plasmon

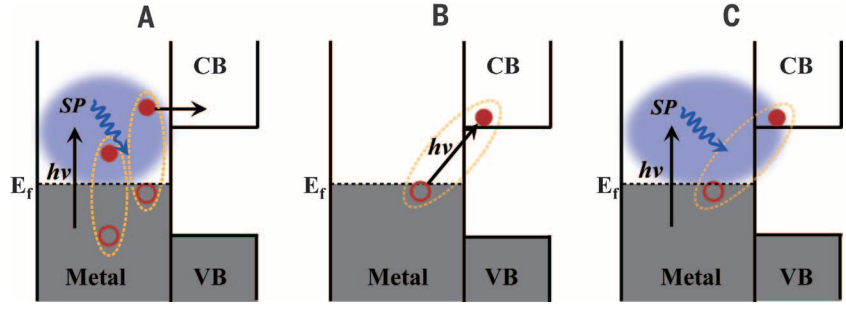

Fig. 1. Metal-to-semiconductor charge-separation pathways. (**A**) Conventional PHET mechanism, in which a photoexcited plasmon (SP, blue ellipsoid) in the metal decays into a hot electron–hole pair (solid and open red circles in the dotted ellipsoids) through Landau damping, followed by injection of the hot electron into the CB of the semiconductor. The electron-hole pair has a broad distribution of initial electron and hole energies; only two are shown for clarity. (**B**) Optical excitation of an electron in the metal directly into the CB of the semiconductor through the DICTT pathway. (**C**) The newly demonstrated PICTT pathway, where the plasmon decays by directly creating an electron in the CB of the semiconductor and a hole in the metal. VB is the semiconductor valence band and *hv* indicates the excitation photons.

[1]Department of Chemistry, Emory University, 1515 Dickey Drive, Atlanta, GA 30322, USA. [2]Department of Chemistry, The Vanderbilt Institute of Nanoscale Science and Engineering, Vanderbilt University, Nashville, TN 37235, USA.
***Corresponding author. E-mail: tlian@emory.edu (T.L.)**

decay pathway: the direct generation of an electron in the semiconductor and an electron hole in the metal. This model is an extension of the chemical interface damping model that has been proposed to account for adsorbate-induced broadening of the plasmon bands of metal NPs (*26*–*28*).

We proposed and experimentally demonstrated the PICCT pathway in colloidal quantum-confined CdSe-Au nanorod (NR) heterostructures. Strong Au-CdSe interactions led to strong damping of the plasmon band in the Au tip. The proposed pathway was verified by observing highly efficient plasmon-induced Au-to-CdSe charge separation with >24% quantum efficiencies upon excitation of the Au tip. Measurements of transient absorption anisotropy showed more efficient Au-to-CdSe charge transfer when the plasmon was excited along the NR axis, consistent with the PICTT mechanism. The charge-separation efficiencies were independent of excitation photon energy, a result that is inconsistent with the conventional PHET mechanism and supports the proposed PICTT pathway.

Colloidal CdSe-Au NRs were synthesized according to a published procedure (*29*, *30*). Representative transmission electron microscope (TEM) images of CdSe and CdSe-Au NRs (Fig. 2A and figs. S1 and S3) showed well-defined dumbbell-like morphologies for CdSe-Au, with two Au NPs at both ends of a single-crystalline CdSe NR. Static absorption spectra of CdSe and CdSe-Au NRs dispersed in chloroform are shown in Fig. 2B. The discrete absorption peaks of CdSe NRs at ~480 and ~582 nm are attributed to the 1Π and 1Σ exciton bands, respectively, arising from quantum confinement in the radial direction (*31*).

Compared with free Au NPs, the SPR band of the Au tips (diameter, ~4.1 nm) was strongly damped and showed a continuous absorption feature extending to the near-infrared (IR) spectrum, consistent with previous observations (*29*, *32*). It has been suggested that such an extreme change in the SPR band cannot be accounted for by dielectric effects alone; rather, it requires strong electronic interactions between the CdSe and Au domains through some mechanism that is yet to be understood (*32*). We observed ultrafast quenching (<100 fs) of excitons in the CdSe NR by the Au tips (fig. S5), consistent with previous results for related CdSe-Au NRs (*33*). In contrast to the pronounced broadening of the Au plasmon band, changes in the CdSe exciton bands were not apparent (Fig. 2B). The CdSe NR was much longer than the strongly interacting metal/semiconductor interface region; the ends of the CdSe NR (at the CdSe/Au interface) were probably strongly perturbed, whereas the center was relatively unperturbed (*34*).

To mimic the tip region of the CdSe-Au NRs, we synthesized CdSe quantum dot (QD)–Au dimers using CdSe QDs with a lowest-energy exciton band similar to that of the CdSe NRs (fig. S2). In these dimers, the excitonic peaks of the QDs and the Au plasmon band were completely damped (Fig. 2B), showing a continuous absorption feature that closely matched the feature observed in the CdSe-Au NRs. Subtracting this feature from the CdSe-Au NR absorption spectrum revealed slightly blue-shifted exciton bands relative to free CdSe NRs (Fig. 2B), which can be attributed to NR etching during the growth of the Au tips (*29*). Thus, the electronic structure of CdSe-Au NRs can be viewed as a combination of the strongly

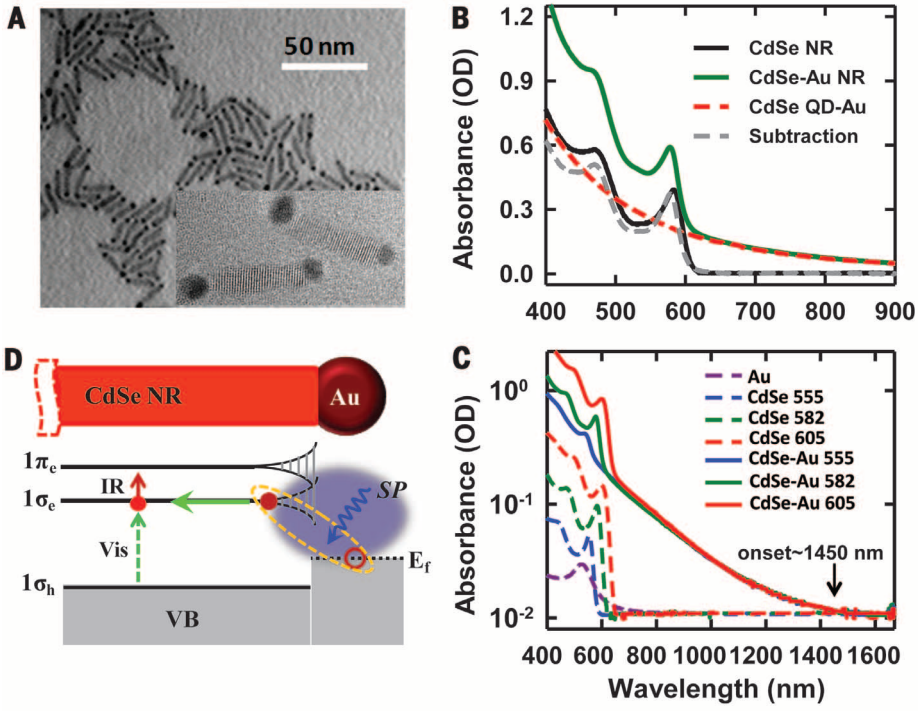

Fig. 2. Plasmon-induced metal-to-semiconductor charge-transfer transition in CdSe-Au NRs. (**A**) A representative TEM image of CdSe-Au NRs (inset: a representative high-resolution TEM image). (**B**) Absorption spectra of CdSe NRs, CdSe-Au NRs, and CdSe QD-Au dimers dispersed in chloroform. The gray dashed line is the difference spectrum between the absorptions of the CdSe-Au NRs and the CdSe QD-Au dimers. (**C**) Absorption spectra (with the *y* axis plotted on a logarithmic scale and shifted by +0.01 to avoid negative values) of (i) isolated Au NPs and (ii) CdSe and CdSe-Au NRs with their first excitonic peak positions at 555, 582, and 605 nm. The absorption spectra of CdSe-Au NRs show an onset at ~1450 nm (0.85 eV). (**D**) Schematic electronic structure of a CdSe-Au NR, composed of a strongly damped Au tip with broadened electronic levels and a central region with relatively unperturbed discrete levels ($1\sigma_e$, $1\pi_e$, $1\sigma_h$). The green dashed arrow indicates the interband transition in the visible (Vis) spectrum, the red arrow indicates the intraband transition in the IR spectrum, and the green solid arrow indicates electron transport in the NR.

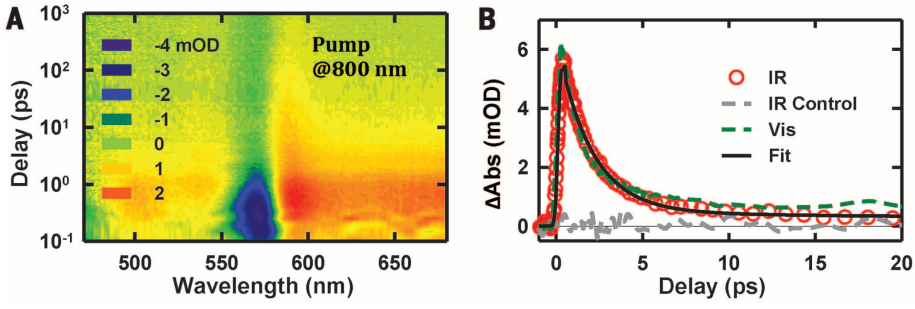

Fig. 3. Plasmon-induced charge separation in CdSe-Au NRs. (**A**) Two-dimensional pseudo-color plot of TA spectra for CdSe-Au NRs at 800-nm excitation [*x* axis, probe wavelength; *y* axis, pump-probe delay; colors, change in absorbance (ΔAbs), shown in milli–optical density units (mOD)]. (**B**) Intraband absorption (probed at ~3000 nm, red circles) and 1Σ-exciton-bleach (~580 nm, green dashed line) kinetics of CdSe-Au NRs after 800-nm excitation. A negligible intraband absorption signal is apparent in a control sample of a mixture of CdSe NRs and Au nanoparticles (gray dashed line). The black solid line is a multiexponential fit of the kinetics.

interacting tip region, which resembles the CdSe QD-Au dimers (with strongly damped plasmon and exciton bands), and the center part, which is similar to the unperturbed CdSe NRs (Fig. 2D).

The broad, featureless, near-IR absorption spectra of the CdSe-Au NRs showed an onset at ~1450 nm (0.85 eV) for three NRs with 1Σ exciton bands at 555, 582, and 605 nm (with a corresponding shift of ~150 meV in the CB-edge position) (Fig. 2C). This suggests that the transition cannot be attributed to the DICTT mechanism (Fig. 1B), which should have an onset wavelength that shifts with the CdSe CB edge. Instead, we attribute the broad near-IR absorption feature to a strongly damped Au plasmon caused by the strong mixing of Au and CdSe electronic levels. Such strong interaction activates the PICTT plasmon decay pathway (Fig. 1C), which is not possible in isolated Au NPs.

In the PICTT pathway, the damped plasmon decays via direct excitation of an interfacial electron-hole pair (with an electron in CdSe and a hole in Au). Direct evidence to support this proposed mechanism was obtained through ultrafast transient absorption (TA) studies. In these studies, a pump laser with a photon energy below the CdSe band gap was used to excite the Au tip, and the electron transferred to the CdSe domain was probed through the bleaching of the 1Σ exciton band in the visible spectrum (caused by state filling of the $1\sigma_e$ level) and/or the $1\sigma_e$ to $1\pi_e$ intraband absorption in the mid-IR spectrum (Fig. 2D) (*35*). The assignment of these spectral signatures was confirmed by comparing transient spectra of CdSe NRs and CdSe-benzoquinone (electron-acceptor) complexes.

The kinetics of the 1Σ exciton bleach at ~580 nm and the intraband absorption at ~3000 nm matched closely in free CdSe NRs, and electron transfer from CdSe to adsorbed electron acceptors led to a faster decay of both spectral features in the NR electron-acceptor complexes (fig. S4). The TA spectra of CdSe-Au NRs (Fig. 3A) showed a pronounced 1Σ-exciton-bleach feature at ~575 nm, indicating the formation of CdSe CB electrons through the excitation of the damped Au plasmon band at 800 nm. The bleach overlapped with a broad positive TA feature that was also present in the TA spectra of CdSe QD-Au dimers (fig. S6). This broad feature was subtracted from the total TA signal to obtain the TA spectra (fig. S8) and the kinetics of the 1Σ exciton bleach (Fig. 3C and fig. S8). Excitation at 800 nm also generated an intraband absorption feature at 3000 nm. The formation and decay kinetics of this signal and the 1Σ-exciton-bleach signal agreed well (Fig. 3B), further confirming the presence of CB electrons in CdSe.

These intra- and interband signals were absent in control samples composed of a mixture of CdSe NRs and Au NPs (Fig. 3B and fig. S7). Fitting these kinetics yielded a formation time of ~20 ± 10 fs and a biexponential decay with a half-life of ~1.45 ± 0.15 ps, which corresponded to plasmon-induced hot-electron transfer and charge-recombination times, respectively (*35*). Such an ultrafast charge-separation time is consistent with the PICTT mechanism, in which the decay of a plasmon instantaneously generates an electron in CdSe (giving rise to the observed inter- and intraband features) and a hole in Au near the CdSe/Au interface. The injected electron quickly relaxes back to the Au with a recombination time of 1.45 ps, which indicates a negligible band-bending–induced recombination barrier at the CdSe/Au interface.

The transient quantum yields (*QY*) of Au-to-CdSe charge separation as a function of excitation wavelength are shown in Fig. 4. These *QY* values were determined by the peak amplitude of the CdSe intraband absorption signal (which averaged between 0.2 and 0.4 ps; see the supplementary materials for details). The pump wavelength (energy) was tuned over a >1-eV range below the band gap of CdSe NRs: 670 nm (1.85 eV), 710 nm (1.75 eV), 750 nm (1.65 eV), 800 nm (1.55 eV), 1160 nm (1.07 eV), 1340 nm (0.92 eV), and 1550 nm (0.80 eV). Within experimental errors, the measured *QY* values were constant (~24%) above ~0.85 eV (Fig. 4), the onset of the near-IR absorption feature shown in Fig. 2B. Below the onset, no measurable electron signals were observed because of a lack of photon absorption.

In the conventional PHET mechanism (Fig. 1A), the excitation energy dependence of the charge-separation *QY* has been shown to follow Fowler's equation (*36*)

$$QY(\omega) = (\hbar\omega - E_B)^2/(4E_F\hbar\omega) \qquad (1)$$

where $\hbar\omega$ is the energy of the excitation photon, E_B is the barrier height between the metal and the semiconductor, and E_F is the Fermi energy of the metal. Most devices based on hot-electron transfer reported to date have been shown to follow this model (*8*, *37*–*39*). For small NPs, *QY* values of metal-to-semiconductor photoemission generally follow the same functional form, but they can be enhanced by a factor *C* through a geometric effect (*40*, *41*) and a lowering of the escape barrier (*42*)

$$QY(\omega) = C(\hbar\omega - E_B)^2/(4E_F\hbar\omega) \qquad (2)$$

Recently, it has also been found that the momentum conservation requirement can be relaxed if electrons only scatter at the semiconductor/metal interface (*43*). Under this condition, *QY* is determined by

$$QY(\omega) = (\hbar\omega - E_B)/(2\hbar\omega) \qquad (3)$$

The predicted *QY* values according to Eqs. 1 to 3 are shown in Fig. 4. For Eq. 2, we chose the value of *C* so that the predicted *QY* at 1.85 eV agreed with the experimental results. The estimated value of E_B was 0.7 to 1.4 V because of uncertainty in the reported band-edge positions (*30*). We used a value of 0.85 V to allow more convenient comparison with the experimental results. The Fowler-type conventional hot-electron transfer models predict an increasing *QY* at higher excitation energies (because of the increase in hot

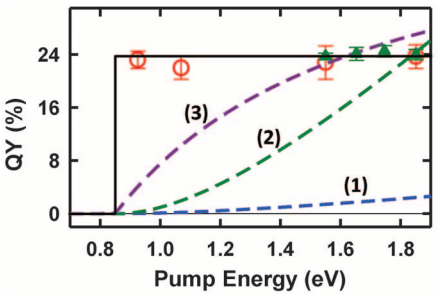

Fig. 4. Quantum yield of wavelength-independent hot-electron transfer. *QY* values of plasmon-induced charge separation as a function of excitation photon energies are shown (red open circles and green solid triangles, measured with PbS and Cd_3P_2 QDs as calibration samples, respectively; see the supplementary materials for details), with predictions according to various Fowler models: Eq. 1(blue dashed line), Eq. 2 (green dashed line), and Eq. 3 (purple dashed line). The black solid line is a step function with an onset at ~0.85 eV.

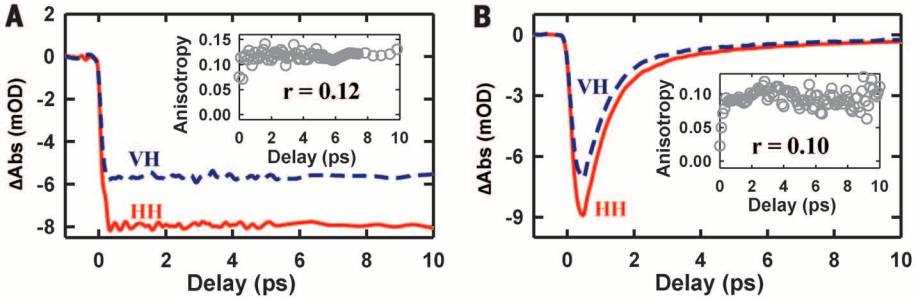

Fig. 5. Transient absorption anisotropy of CdSe and CdSe-Au NRs. (**A**) 1Σ-exciton-bleach kinetics (probed at ~580 nm) in free CdSe NRs after band-edge (590-nm) excitation, with pump and probe beams with parallel (HH, horizontal pump and horizontal probe, red solid line) and perpendicular (VH, vertical pump and horizontal probe, blue dashed line) polarizations. Calculated anisotropy, *r*, is shown in the inset as a function of pump-probe delay. (**B**) 1Σ-exciton-bleach kinetics (probed at ~575 nm) in CdSe-Au NRs after 800-nm excitation, with pump and probe beams with parallel (HH, red solid line) and perpendicular (VH, blue dashed line) polarizations. *r* is shown in the inset.

electrons with energies above the semiconductor CB edge) and are inconsistent with our experimental data.

The measured *QY* values are consistent with the PICTT pathway. In this pathway, the plasmon decays by direct excitation of an electron from Au to CdSe, and the *QY* is independent of the excess energy of the electron above the CB edge. The strongly damped plasmon bandwidth is probably dominated by homogeneous broadening: As long as the excitation energy is above the absorption threshold (~0.85 eV), the same plasmon is excited, and therefore the charge-separation *QY* is independent of excitation energy. The estimated full width at half maximum of the damped plasmon band, ~1.6 eV (fig. S11), corresponds to a plasmon dephasing time of ~0.8 fs, which is consistent with the observed fast hot-electron transfer time. Furthermore, the observed *QY* is about an order of magnitude higher than the reported value for CdS-Au NRs (2.75%) (*35*). In CdS-Au NRs, the Au plasmon band is weakly perturbed, and the plasmon-induced hot-electron transfer occurs through the conventional PHET mechanism (Fig. 1A), where the competition of hot-electron transfer with ultrafast relaxation reduces its efficiency. Compared with CdSe-Au NRs, the hot-electron transfer time in CdS-Au NRs is noticeably slower (90 ± 20 fs) (fig. S9). The microscopic origin of the dramatic differences in plasmon damping and hot-electron transfer between CdS-Au and CdSe-Au NRs remains unclear and will be examined in future studies.

The observed *QY* values in CdSe-Au NRs are less than unity for at least two reasons. First, PICTT is probably not the exclusive decay channel for the strongly damped plasmon. The plasmon could also be damped in the Au domain, thereby proceeding via the less efficient conventional PHET pathway (*35*). Second, the electron generated in CdSe could either quickly relax back into the Au or escape into the center of the CdSe NR (and recombine on the 1.4-ps time scale); only the latter process was detected in our measurements. Thus, the measured *QY* values represent a lower limit of plasmon-induced electron transfer in this system.

Further insight into the nature of the PICTT pathway can also be obtained through polarization-dependent TA studies. Plasmons polarized in the direction parallel to the NR may be more strongly coupled to the CdSe than those polarized in the direction perpendicular to the NR. Because the optical transition in the CdSe NRs is strongly polarized (*31*, *44*), the TA signal should depend on the relative polarization of the pump and the probe beams. This polarization dependence can be quantified by the anisotropy (r) of the TA signals, so that $r = (SHH - SVH) / (SHH + 2SVH)$, where *SHH* and *SVH* are TA signals with the polarizations of the pump and probe beams parallel (*SHH*) or perpendicular (*SVH*) to each other. For band-edge (590-nm) excitation of free CdSe NRs (without Au tips), the 1Σ-exciton-bleach signal amplitude for *SHH* was larger than for *SVH* (Fig. 5A). The calculated anisotropy was 0.12 and showed negligible decay over 10 ps (Fig. 5A, inset), which indicates that the band-edge–absorption transition dipole has 70% axial and 30% radial components (fig. S12; see the supplementary materials for details), consistent with previous reports (*45*). The intraband transition between $1\sigma_e$ and $1\pi_e$ showed negligible anisotropy (fig. S13). Thus, we used the 1Σ exciton bleach to probe anisotropy in CdSe-Au NRs. For 800-nm excitation of CdSe-Au NRs, the resulting 1Σ-exciton-bleach signal amplitude for *SHH* was larger than for *SVH*, with an anisotropy value of 0.10 (Fig. 5B). This result suggests a more efficient hot-electron transfer by plasmons polarized parallel to the NR axis, consistent with the PICTT mechanism. In contrast, in CdS-Au NRs where the conventional PHET mechanism dominates (*35*), we detected negligible anisotropy in the CdS 1Σ-exciton-bleach signal generated by exciting the Au plasmon band (fig. S15).

Finally, we showed that in the presence of sacrificial electron donors (S^{2-}), the electrons injected into CdSe could be used to reduce methyl viologen, a well-known redox mediator for solar fuel generation (*46*), with a steady-state *QY* of >0.75% (fig. S18; see the supplementary materials for details). In light of the high *QY* values measured for transient charge separation (>24%), the relatively low steady-state *QY* can be attributed to ultrafast charge recombination. Charge recombination can be retarded by creating a built-in electric field at the semiconductor/metal interface using longer NRs (>100s nm) or by applying a large external bias (*8*).

Strong mixing of Au and TiO_2 electronic levels has been reported in a recent computational study of Au-cluster–sensitized TiO_2 NPs (*47*). Strongly broadened Au plasmon bands and efficient plasmon-induced hot-electron transfer were also observed in Au-NP–sensitized TiO_2 nanocrystalline thin films (*11*). Thus, the PICTT mechanism reported here is potentially a general phenomenon at metal/semiconductor and/or metal/molecule interfaces. PICTT may present a new opportunity to circumvent energy-loss channels in metal nanostructures and greatly increase the efficiencies of devices based on plasmonic light-absorption materials.

REFERENCES AND NOTES

1. H. A. Atwater, A. Polman, *Nat. Mater.* **9**, 205–213 (2010).
2. C. Clavero, *Nat. Photonics* **8**, 95–103 (2014).
3. S. Linic, P. Christopher, D. B. Ingram, *Nat. Mater.* **10**, 911–921 (2011).
4. S. Mubeen *et al.*, *Nat. Nano.* **8**, 247–251 (2013).
5. I. Thomann *et al.*, *Nano Lett.* **11**, 3440–3446 (2011).
6. P. Christopher, H. Xin, S. Linic, *Nat. Chem.* **3**, 467–472 (2011).
7. A. Marimuthu, J. Zhang, S. Linic, *Science* **339**, 1590–1593 (2013).
8. M. W. Knight, H. Sobhani, P. Nordlander, N. J. Halas, *Science* **332**, 702–704 (2011).
9. M. L. Brongersma, N. J. Halas, P. Nordlander, *Nat. Nano.* **10**, 25–34 (2015).
10. J. A. Schuller *et al.*, *Nat. Mater.* **9**, 193–204 (2010).
11. A. Furube, L. Du, K. Hara, R. Katoh, M. Tachiya, *J. Am. Chem. Soc.* **129**, 14852–14853 (2007).
12. J. Li *et al.*, *J. Am. Chem. Soc.* **136**, 8438–8449 (2014).
13. Y. Tian, T. Tatsuma, *J. Am. Chem. Soc.* **127**, 7632–7637 (2005).
14. P. K. Jain, K. S. Lee, I. H. El-Sayed, M. A. El-Sayed, *J. Phys. Chem. B* **110**, 7238–7248 (2006).
15. K. L. Kelly, E. Coronado, L. L. Zhao, G. C. Schatz, *J. Phys. Chem. B* **107**, 668–677 (2002).
16. A. O. Govorov, H. Zhang, Y. K. Gun'ko, *J. Phys. Chem. C* **117**, 16616–16631 (2013).
17. C. Sönnichsen *et al.*, *Phys. Rev. Lett.* **88**, 077402 (2002).
18. G. V. Hartland, *Chem. Rev.* **111**, 3858–3887 (2011).
19. W. S. Fann, R. Storz, H. W. K. Tom, J. Bokor, *Phys. Rev. B* **46**, 13592–13595 (1992).
20. C. Voisin, N. Del Fatti, D. Christofilos, F. Vallée, *J. Phys. Chem. B* **105**, 2264–2280 (2001).
21. D. Kolb, M. Przasnyski, H. Gerischer, *Z. Phys. Chem.* **93**, 1–14 (1974).
22. K. C. Chou, S. Westerberg, Y. R. Shen, P. N. Ross, G. A. Somorjai, *Phys. Rev. B* **69**, 153413 (2004).
23. M. J. Kale, T. Avanesian, H. Xin, J. Yan, P. Christopher, *Nano Lett.* **14**, 5405–5412 (2014).
24. H. Petek, M. J. Weida, H. Nagano, S. Ogawa, *Science* **288**, 1402–1404 (2000).
25. H. Petek, *J. Chem. Phys.* **137**, 091704 (2012).
26. B. N. J. Persson, *Surf. Sci.* **281**, 153–162 (1993).
27. A. Iline, M. Simon, F. Stietz, F. Träger, *Surf. Sci.* **436**, 51–62 (1999).
28. H. Hövel, S. Fritz, A. Hilger, U. Kreibig, M. Vollmer, *Phys. Rev. B* **48**, 18178–18188 (1993).
29. T. Mokari, E. Rothenberg, I. Popov, R. Costi, U. Banin, *Science* **304**, 1787–1790 (2004).
30. Materials and methods are available as supplementary materials on *Science* Online.
31. A. Shabaev, A. L. Efros, *Nano Lett.* **4**, 1821–1825 (2004).
32. E. Shaviv *et al.*, *ACS Nano* **5**, 4712–4719 (2011).
33. P. Yu *et al.*, *J. Phys. Chem. Lett.* **4**, 3596–3601 (2013).
34. D. Steiner, T. Mokari, U. Banin, O. Millo, *Phys. Rev. Lett.* **95**, 056805 (2005).
35. K. Wu, W. E. Rodríguez-Córdoba, Y. Yang, T. Lian, *Nano Lett.* **13**, 5255–5263 (2013).
36. R. H. Fowler, *Phys. Rev.* **38**, 45–56 (1931).
37. H. M. Chen *et al.*, *ACS Nano* **6**, 7362–7372 (2012).
38. W. Li, J. Valentine, *Nano Lett.* **14**, 3510–3514 (2014).
39. Y. K. Lee *et al.*, *Nano Lett.* **11**, 4251–4255 (2011).
40. Q. Y. Chen, C. W. Bates Jr., *Phys. Rev. Lett.* **57**, 2737–2740 (1986).
41. A. Schmidt-Ott, P. Schurtenberger, H. C. Siegmann, *Phys. Rev. Lett.* **45**, 1284–1287 (1980).
42. U. Müller, H. Burtscher, A. Schmidt-Ott, *Phys. Rev. B* **38**, 7814–7816 (1988).
43. A. Giugni *et al.*, *Nat. Nano.* **8**, 845–852 (2013).
44. J. Hu *et al.*, *Science* **292**, 2060–2063 (2001).
45. D. B. Tice, D. J. Weinberg, N. Mathew, R. P. H. Chang, E. A. Weiss, *J. Phys. Chem. C* **117**, 13289–13296 (2013).
46. J. Kiwi, M. Gratzel, *Nature* **281**, 657–658 (1979).
47. R. Long, O. V. Prezhdo, *J. Am. Chem. Soc.* **136**, 4343–4354 (2014).

ACKNOWLEDGMENTS

This work was funded by the U.S. Department of Energy, Office of Basic Energy Sciences, Solar Photochemistry Program (grant DE-FG02-12ER16347). J.R.M. acknowledges financial support from NSF (grant CHE-1213758). Scanning transmission electron microscope and energy-dispersive x-ray spectroscope images were acquired using an FEI Tecnai Osiris electron microscope purchased with support from NSF (grant EPS-1004083).

SUPPLEMENTARY MATERIALS

www.sciencemag.org/content/349/6248/632/suppl/DC1
Materials and Methods
Supplementary Text
Figs. S1 to S18
Tables S1 to S5
References (*48*–*72*)

9 May 2015; accepted 6 July 2015
10.1126/science.aac5443

STATISTICS

The reusable holdout: Preserving validity in adaptive data analysis

Cynthia Dwork,[1]* Vitaly Feldman,[2]* Moritz Hardt,[3]* Toniann Pitassi,[4]* Omer Reingold,[5]* Aaron Roth[6]*

Misapplication of statistical data analysis is a common cause of spurious discoveries in scientific research. Existing approaches to ensuring the validity of inferences drawn from data assume a fixed procedure to be performed, selected before the data are examined. In common practice, however, data analysis is an intrinsically adaptive process, with new analyses generated on the basis of data exploration, as well as the results of previous analyses on the same data. We demonstrate a new approach for addressing the challenges of adaptivity based on insights from privacy-preserving data analysis. As an application, we show how to safely reuse a holdout data set many times to validate the results of adaptively chosen analyses.

Throughout the scientific community there is a growing recognition that claims of statistical significance in published research are frequently invalid. There has been a great deal of effort to understand and propose mitigations for this problem, largely focusing on statistical methods for controlling the false discovery rate in multiple hypothesis testing (*1*). However, the statistical inference theory surrounding this body of work assumes that a fixed procedure is performed, selected before the data are gathered. In contrast, the practice of data analysis in scientific research is, by nature, an adaptive process in which new analyses are chosen on the basis of data exploration and previous analyses of the same data.

It is now well understood that adapting the analysis to data results in an implicit multiple comparisons problem that is not captured in the reported significance levels of standard statistical procedures or by existing techniques for controlling the false discovery rate. This problem, in some contexts referred to as "p-hacking" or "researcher degrees of freedom," is one of the primary explanations as to why research findings are frequently false (*2*–*4*).

The traditional perspective on adaptivity makes it necessary to explicitly account for all of the possible ways to perform the analysis to provide validity guarantees for the adaptive analysis. Although this approach might be possible in simpler studies, it is technically challenging and often impractical in more complicated analyses (*4*). Numerous techniques have been developed by statisticians to address common special cases of adaptive data analysis. Most of these methods focus on a single round of adaptivity—such as variable selection followed by regression on selected variables or model selection followed by testing—and are optimized for specific inference procedures [the literature is too vast to adequately cover here, but see chapter 7 in (*5*) for a starting point]. There are also procedures for controlling false discovery in a sequential setting where tests arrive one-by-one (*6*–*8*). However, these results crucially depend on all tests maintaining their statistical properties despite being sequentially chosen—an assumption that is often difficult to justify in a complex adaptive analysis.

One proposed approach for avoiding the issue of adaptivity is preregistration; that is, defining the entire data analysis protocol ahead of time, thus forcing the analysis to be nonadaptive. A recent open letter (*9*) with more than 80 signatories calls for preregistration in science. Although safe, this proposal can be burdensome on the researcher and may limit the kind of analysis he or she can perform (*4*). As a result, this method has had difficulty gaining momentum in practice. A more popular approach for avoiding problems of this type is to validate data-dependent hypotheses or statistics on a holdout set. The data analyst starts by partitioning data samples randomly into training data and holdout data. The analyst interacts with the training set to obtain a data statistic of interest: for example, correlation between certain traits or the accuracy of a predictive model. The statistic is then validated by computing its value on the holdout set. Because the holdout was drawn from the same data distribution independently of the statistic, standard statistical inference procedures can safely be used.

A major drawback of this basic approach is that the holdout set, in general, is not reusable. If the analyst uses the outcome of the validation to select an additional data statistic, that statistic is no longer independent of the holdout data, and further use of the holdout set for validation can lead to incorrect statistical inference. To preserve statistical validity, the only known safe approach is to collect new data for a fresh holdout set. This conservative approach is very costly and thus is frequently abused, resulting in overfitting to the holdout set (*10*–*12*).

In this work we describe a general method, together with a specific instantiation for reusing a holdout set while maintaining the statistical guarantees of fresh data. The analyst is given unfettered access to the training data set but can only access the holdout set via an algorithm (equivalently, a mechanism) that allows the analyst to validate statistics on the holdout set. Armed with such a mechanism, the analyst is free to explore the (training) data ad libitum, generating and computing statistics, validating them on the holdout, and repeating this procedure, as well as sharing outcomes with other analysts who may also use the same holdout set.

The crucial idea behind our reusable holdout method comes from differential privacy—a notion of privacy preservation in data analysis introduced in computer science (*13*). Roughly speaking, differential privacy ensures that the probability of observing any outcome from an analysis is essentially unchanged by modifying any single data set element. Such a condition is often called a stability guarantee. An important line of work establishes connections between the stability of a learning algorithm and its ability to generalize (*14*–*16*). It is known that certain stability notions are necessary and sufficient for generalization. Unfortunately, the stability notions considered in these prior works do not compose in the sense that running multiple stable algorithms sequentially and adaptively may result in a procedure that is not stable. Differential privacy is stronger than these previously studied notions of stability and, in particular, possesses strong adaptive composition guarantees.

In a nutshell, the reusable holdout mechanism is simply this: access the holdout set only via a differentially private mechanism. The intuition is that if we can learn about the data set in aggregate while provably learning very little about any individual data element, then we can control the information leaked and thus prevent overfitting. More specifically, we introduce a new notion of maximum information that controls overfitting and can be bounded using differential privacy [for an overview, see section 1 of (*17*)]. We present an implementation of the reusable holdout, called Thresholdout, and show that it provably validates a large number of adaptively chosen statistics. We then use a simple classification algorithm on synthetic data to illustrate the properties of Thresholdout. The classifier produced by the algorithm overfits the data when the holdout set is reused naively but does not overfit if used with our reusable holdout.

We operate in a standard setting: an analyst is given a data set $S = (x_1, \ldots, x_n)$ of n samples drawn randomly and independently from some unknown distribution P over a discrete universe X of possible data points. Although our approach can be applied more generally, we focus here on validating statistics that can be expressed as the mean of some arbitrary function $\phi : X \to [0, 1]$ on the data set $E_S[\phi] = \frac{1}{n}\sum_{i=1}^{n}\phi(x_i)$ [for additional details, see section 1.1 of (*17*)]. Such statistics are

[1]Microsoft Research, Mountain View, CA 94043, USA. [2]IBM Almaden Research Center, San Jose, CA 95120, USA. [3]Google Research, Mountain View, CA 94043, USA. [4]Department of Computer Science, University of Toronto, Toronto, Ontario M5S 3G4, Canada. [5]Samsung Research America, Mountain View, CA 94043, USA. [6]Department of Computer and Information Science, University of Pennsylvania, Philadelphia, PA 19104, USA.
*Corresponding author. E-mail: dwork@microsoft.com (C.D.); vitaly@post.harvard.edu (V.F.); m@mrtz.org (M.H.); toni@cs.toronto.edu (T.P.); omer.reingold@gmail.com (O.R.); aaroth@cis.upenn.edu (A.R.)

used to estimate the expected value of ϕ on a sample drawn randomly from the distribution P or $P[\phi] = \mathbf{E}_{x\sim P}[\phi(x)]$. A variety of quantities of interest in data analysis can be expressed as the expectation $\mathbf{E}_{x\sim P}[\phi(x)]$ of some function ϕ on P. Examples include true means and moments of individual attributes, correlations between attributes and the generalization error of a predictive model. Moreover, sufficiently precise estimates of these expectations suffice for model selection and assessment.

The data set S is randomly partitioned into training and holdout sets (S_t and S_h, respectively), and the data analyst is allowed to explore the training set without restrictions and generate functions ϕ to estimate the expectation on P. The analyst may access S_h only through Thresholdout. Thresholdout takes the holdout and training sets as input and, for all functions given by the analyst, provides statistically valid estimates of each function's expectation on P. Specifically, for a sufficiently large holdout set, Thresholdout guarantees that for every function $\phi : X \to [0,1]$ generated by the analyst, it will return a value v_ϕ such that $|v_\phi - P[\phi]| \leq \tau$, with probability at least $1 - \beta$, for analyst's choice of error τ and confidence β. The probability space is over the random choice of the data elements in S_h and S_t and the randomness introduced by the mechanism. We emphasize that the estimates are guaranteed to be accurate with respect to the true distribution, even when the functions are generated sequentially and adaptively by the analyst, up to a large number of functions. Our algorithm can equivalently be viewed as producing conservative confidence intervals on adaptively chosen sequences of linear functionals [for the formal connection to confidence intervals, see section 4 of (*17*)].

Given a function ϕ, the algorithm first checks if the difference between the average value of ϕ on the training set S_t (denoted by $E_{S_t}[\phi]$) and the average value of ϕ on the holdout set S_h (denoted by $E_{S_h}[\phi]$) is below a certain threshold $T + \eta$. Here, T is a fixed number such as 0.01, and η is a Laplace noise variable of standard deviation smaller than T by a small factor such as 4. [The Laplace distribution is a symmetric exponential distribution. Adding Laplace noise is one of the most basic operations in differential privacy (*13*).] If the difference is below the threshold, then the algorithm returns $E_{S_t}[\phi]$; that is, the value of ϕ on the training set. If the difference is above the threshold, then the algorithm returns the average value of the function on the holdout after adding Laplacian noise; that is, $E_{S_h}[\phi] + \xi$ (where ξ is a random variable distributed according to the Laplace distribution).

Though it is very simple, Thresholdout gives a surprisingly strong guarantee. Informally, the guarantee is that for any fixed accuracy parameter τ, Thresholdout can continue validating the estimates on the training sets until either the total number of functions asked becomes exponentially large in the size of S_h or the number of functions that fail the validation (meaning average values on S_h and S_t differ by more than the noisy threshold) becomes quadratically large in the size of S_h. Our guarantee can therefore be interpreted as saying that Thresholdout detects a quadratic number of functions that overfit to the training set (or false discoveries) and arise due to adaptivity; additionally, Thresholdout provides a correct estimate of the expectation for those functions. We describe further details of the implementation of Thresholdout and the formal guarantees it satisfies in section 2 of (*17*).

We describe a simple experiment on synthetic data that illustrates the danger of reusing a standard holdout set and how this issue can be resolved by our reusable holdout. The design of this experiment is inspired by Freedman's classical experiment, which demonstrated the dangers of performing variable selection and regression on the same data (*18*). The experiment is commonly referred to as "Freedman's paradox" due to the surprisingly strong effect on the validity of the results.

In our experiment, the analyst wants to build a classifier via the following common strategy. First, the analyst finds a set of single attributes that are correlated with the class label. Then he or she aggregates the correlated variables into a single model of higher accuracy (for example, using boosting or bagging methods). More formally, the analyst is given a d-dimensional labeled data set S of size $2n$ and splits it randomly into a training set S_t and a holdout set S_h of equal size. We denote an element of S by a tuple (x,y), where x is a d-dimensional vector and $y \in \{-1, 1\}$ is the corresponding class label. The analyst wishes to select variables to be included in the classifier. For various values k of the number of variables to select, the analyst picks k variables with the

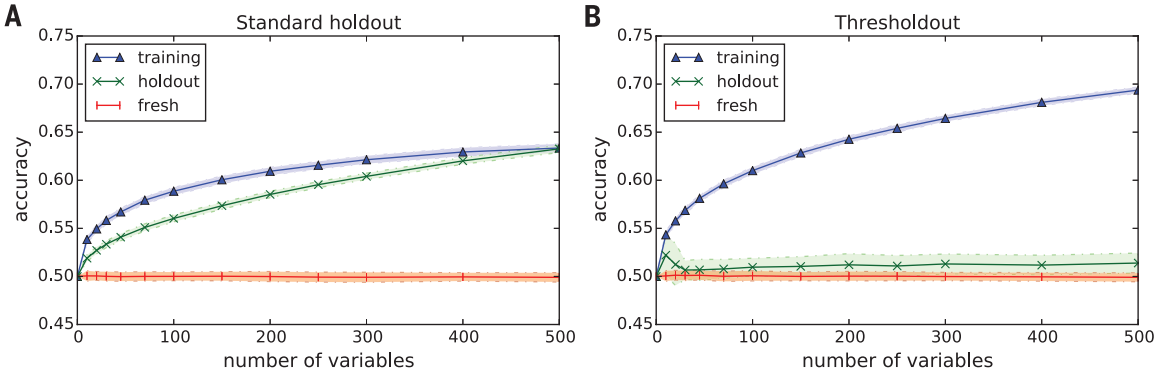

Fig. 1. Learning uncorrelated label. (**A**) Using the standard holdout. (**B**) Using Thresholdout. Vertical axes indicates average classification accuracy over 100 executions (margins are SD) of the classifier on training, holdout, and fresh sets. Horizontal axes show the number of variables selected for the classifier.

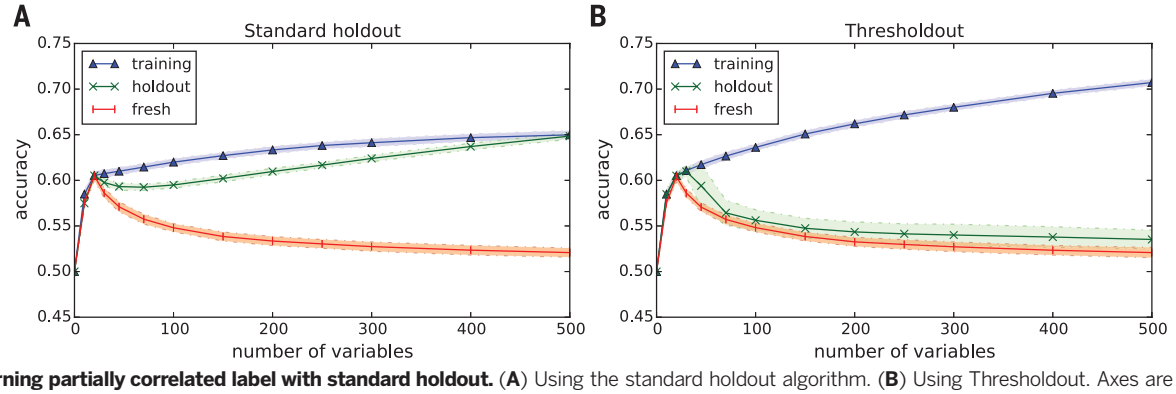

Fig. 2. Learning partially correlated label with standard holdout. (**A**) Using the standard holdout algorithm. (**B**) Using Thresholdout. Axes are as in Fig. 1.

largest absolute correlations with the label. However, he or she verifies the correlations (with the label) on the holdout set and uses only those variables whose correlation agrees in sign with the correlation on the training set and for which both correlations are larger than some threshold in absolute value. The analyst then creates a simple linear threshold classifier on the selected variables using only the signs of the correlations of the selected variables. A final test evaluates the classification accuracy of the classifier on the holdout set. Full details of the analyst's algorithm can be found in section 3 of (*17*).

In our first experiment, each attribute is drawn independently from the normal distribution $N(0,1)$, and we choose the class label $y \in \{-1, 1\}$ uniformly at random so that there is no correlation between the data point and its label. We chose $n = 10{,}000$ and $d = 10{,}000$ and varied the number of selected variables k. In this scenario no classifier can achieve true accuracy better than 50%. Nevertheless, reusing a standard holdout results in reported accuracy of $>63 \pm 0.4\%$ for $k = 500$ on both the training set and the holdout set. The average and standard deviation of results obtained from 100 independent executions of the experiment are plotted in Fig. 1A, which also includes the accuracy of the classifier on another fresh data set of size n drawn from the same distribution. We then executed the same algorithm with our reusable holdout. The algorithm Thresholdout was invoked with $T = 0.04$ and $\tau = 0.01$, which explains why the accuracy of the classifier reported by Thresholdout is off by up to 0.04 whenever the accuracy on the holdout set is within 0.04 of the accuracy on the training set. Thresholdout prevents the algorithm from overfitting to the holdout set and gives a valid estimate of classifier accuracy. In Fig. 1B, we plot the accuracy of the classifier as reported by Thresholdout. In addition, in fig. S2 we include a plot of the actual accuracy of the produced classifier on the holdout set.

In our second experiment, the class labels are correlated with some of the variables. As before, the label is randomly chosen from {–1,1} and each of the attributes is drawn from $N(0,1)$, aside from 20 attributes drawn from $N(y \cdot 0.06, 1)$, where y is the class label. We execute the same algorithm on this data with both the standard holdout and Thresholdout and plot the results in Fig. 2. Our experiment shows that when using the reusable holdout, the algorithm still finds a good classifier while preventing overfitting.

Overfitting to the standard holdout set arises in our experiment because the analyst reuses the holdout after using it to measure the correlation of single attributes. We first note that neither cross-validation nor bootstrap resolve this issue. If we used either of these methods to validate the correlations, overfitting would still arise as a result of using the same data for training and validation (of the final classifier). It is tempting to recommend other solutions to the specific problem on which we based our experiment. Indeed, a substantial number of methods in the statistics literature deal with inference for fixed two-step procedures in which the first step is variable selection [see (*5*) for examples]. Our experiment demonstrates that even in such simple and standard settings, our method avoids false discovery without the need to use a specialized procedure and, of course, extends more broadly. More importantly, the reusable holdout gives the analyst a general and principled method to perform multiple validation steps where previously the only known safe approach was to collect a fresh holdout set each time a function depends on the outcomes of previous validations.

REFERENCES AND NOTES

1. Y. Benjamini, Y. Hochberg, *J. R. Stat. Soc. B* **57**, 289–300 (1995).
2. J. P. A. Ioannidis, *PLOS Med.* **2**, e124 (2005).
3. J. P. Simmons, L. D. Nelson, U. Simonsohn, *Psychol. Sci.* **22**, 1359–1366 (2011).
4. A. Gelman, E. Loken, *Am. Stat.* **102**, 460 (2014).
5. T. Hastie, R. Tibshirani, J. H. Friedman, *The Elements of Statistical Learning: Data Mining, Inference, and Prediction* (Springer Series in Statistics, Springer, New York, ed. 2, 2009).
6. D. Foster, R. Stine, *J. R. Stat. Soc. B* **70**, 429–444 (2008).
7. E. Aharoni, H. Neuvirth, S. Rosset, *IEEE/ACM Trans. Comput. Biol. Bioinform.* **8**, 1431–1437 (2011).
8. A. Javanmard, A. Montanari, On online control of false discovery rate. http://arxiv.org/abs/1502.06197 (2015).
9. C. Chambers, M. Munafo, "Trust in science would be improved by study pre-registration," *Guardian US*, 5 June 2013; www.theguardian.com/science/blog/2013/jun/05/trust-in-science-study-pre-registration.
10. J. Reunanen, *J. Mach. Learn. Res.* **3**, 1371–1382 (2003).
11. R. B. Rao, G. Fung, in *Proceedings of the SIAM International Conference on Data Mining 2008* (Society for Industrial and Applied Mathematics, Philadelphia, PA, 2008), pp. 588–596.
12. G. C. Cawley, N. L. C. Talbot, *J. Mach. Learn. Res.* **11**, 2079–2107 (2010).
13. C. Dwork, F. McSherry, K. Nissim, A. Smith, in *Theory of Cryptography* (Lecture Notes in Computer Science Series, Springer, Berlin, 2006), pp. 265–284.
14. O. Bousquet, A. Elisseeff, *J. Mach. Learn. Res.* **2**, 499–526 (2002).
15. T. Poggio, R. Rifkin, S. Mukherjee, P. Niyogi, *Nature* **428**, 419–422 (2004).
16. S. Shalev-Shwartz, O. Shamir, N. Srebro, K. Sridharan, *J. Mach. Learn. Res.* **11**, 2635–2670 (2010).
17. Supplementary materials are available on *Science* Online.
18. D. A. Freedman, *Am. Stat.* **37**, 152–155 (1983).

ACKNOWLEDGMENTS

Authors are listed in alphabetical order. A.R. was supported in part by an NSF CAREER grant (CNS 1253345), NSF grant CCF 1101389, and the Alfred P. Sloan Foundation. T.P. was supported in part by grants from the Natural Sciences and Engineering Research Council of Canada. We thank S. Arora, M. F. Balcan, A. Blum, D. Foster, M. Kearns, J. Kleinberg, A. Rakhlin, P. Rigollet, W. Su, and J. Ullman for enlightening discussions about this work. We also thank the Simons Institute for the Theory of Computing at the University of California Berkeley, where part of this research was done.

SUPPLEMENTARY MATERIALS

www.sciencemag.org/content/349/6248/636/suppl/DC1
Supplementary Text
Figs. S1 and S2
References (*19*–*25*)
Data S1

17 February 2015; accepted 15 June 2015
10.1126/science.aaa9375

ENVIRONMENTAL SCIENCE

Profiling risk and sustainability in coastal deltas of the world

Z. D. Tessler,[1]* C. J. Vörösmarty,[1,2] M. Grossberg,[3] I. Gladkova,[3] H. Aizenman,[3] J. P. M. Syvitski,[4] E. Foufoula-Georgiou[5]

Deltas are highly sensitive to increasing risks arising from local human activities, land subsidence, regional water management, global sea-level rise, and climate extremes. We quantified changing flood risk due to extreme events using an integrated set of global environmental, geophysical, and social indicators. Although risks are distributed across all levels of economic development, wealthy countries effectively limit their present-day threat by gross domestic product–enabled infrastructure and coastal defense investments. In an energy-constrained future, such protections will probably prove to be unsustainable, raising relative risks by four to eight times in the Mississippi and Rhine deltas and by one-and-a-half to four times in the Chao Phraya and Yangtze deltas. The current emphasis on short-term solutions for the world's deltas will greatly constrain options for designing sustainable solutions in the long term.

Deltas present a quintessential challenge for humans amid global environmental change. Home to some of the world's largest urban areas, deltas are also highly dynamic landforms shaped by fluvial and coastal flooding (*1*–*3*). Human activities at the local and regional scales can perturb the water and sedimentary dynamics necessary to maintain a delta's integrity, increasing the rate of relative sea-level rise (RSLR, the combination of land subsidence and offshore sea-level rise) and increasing flood risk (*4*, *5*).

Delta sediments naturally compact over time, requiring new sediment fluxes from the upstream river network and deposition on the delta surface

[1]Environmental CrossRoads Initiative, City University of New York, NY 10031, USA. [2]Department of Civil Engineering, City College of New York, NY 10031, USA. [3]Department of Computer Science, City College of New York, NY 10031, USA. [4]Department of Geological Sciences, University of Colorado–Boulder, Boulder, CO 80309, USA. [5]Department of Civil, Environmental, and Geo- Engineering, University of Minnesota, Minneapolis, MN 55455, USA.
***Corresponding author. E-mail: ztessler@ccny.cuny.edu**

to maintain land elevation (*4*). Upstream dams and reservoirs trap sediment (*6*), and soil conservation practices can reduce the mobilization of sediment (*7*). River channelization on deltas inhibits depositional processes (*8*), whereas urban construction and groundwater extraction can accelerate sediment compaction (*9*, *10*). Land subsidence is compounded by rising sea levels and the changing intensity and distribution of extreme events related to climate change (*11*, *12*). Policies aimed at reducing the apparent levels of risk often employ costly engineering solutions that may be inherently unsustainable (*13*–*15*). A framework to enable comparative risk assessment for deltas across the globe that specifically accounts for the dual natural and anthropogenic forces shaping these systems is a necessary precursor for strategies to improve their long-term resilience (*16*).

We present a systematic global-scale assessment of the changing risk profiles of coastal deltas. Most manifestations of risk are the immediate

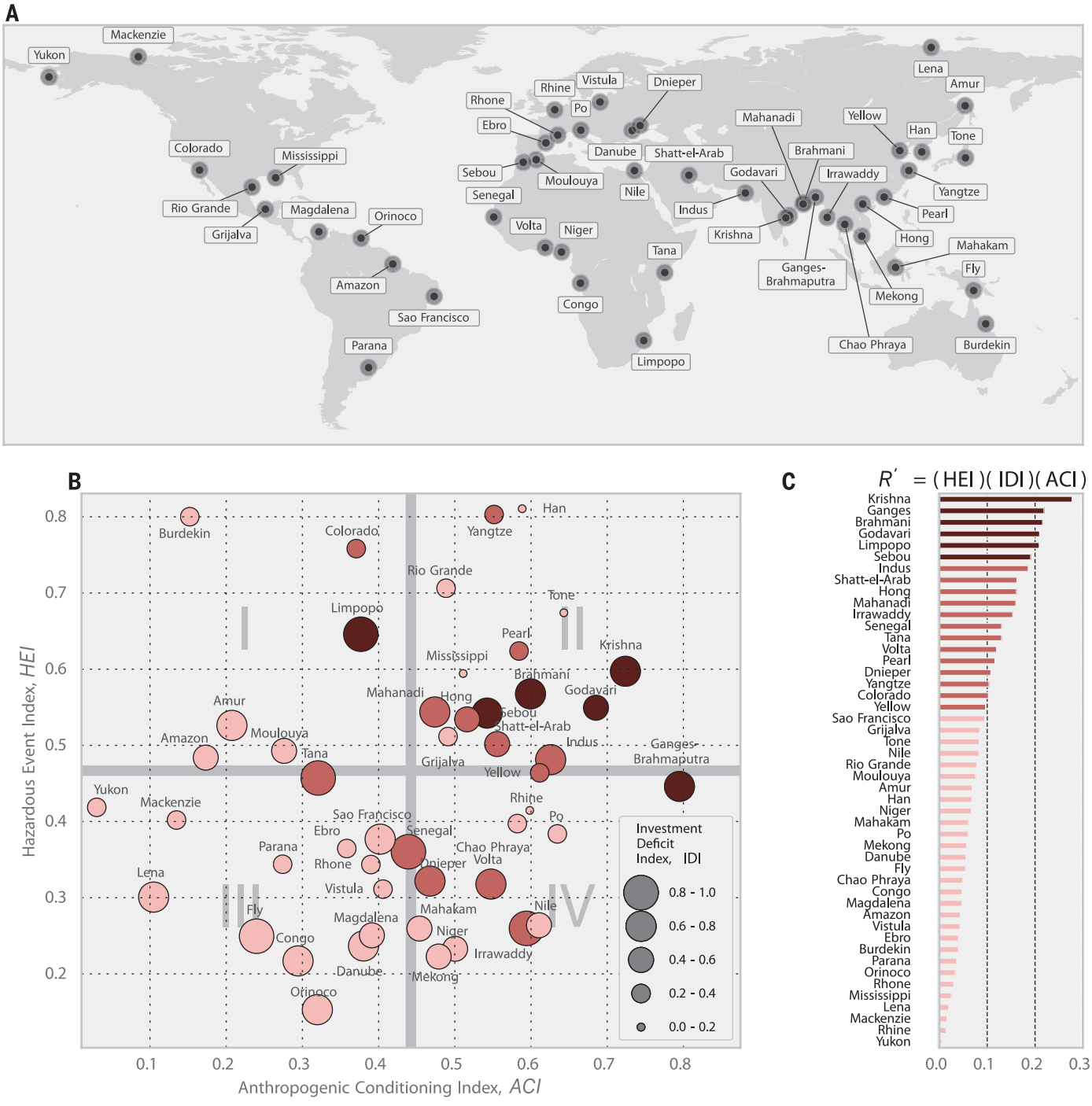

Fig. 1. Risk trends for deltas worldwide. (**A**) Map showing the 48 deltas included in this study. (**B**) Phase diagram of contemporary risk assessment results, showing the three component proxy indices used to estimate per-capita *R*′. Color density represents a delta's overall risk trend. Quadrant III deltas have predominantly low *R*′, whereas quadrant II deltas have high *R*′. (**C**) Estimates of the relative rate of change in risk, or risk trend, for each delta due to increasing exposure associated with RSLR. The Krishna and Ganges-Brahmaputra deltas, despite being only moderately susceptible to short-term hazardous events, are increasingly at risk because of high rates of RSLR and high socioeconomic vulnerability. Ganges-Brahmaputra is abbreviated to "Ganges" in some panels for brevity.

consequences of extreme events (*3*), such as fluvial and coastal flooding, that act over short time scales. Overall risk, however, is conditioned over longer periods by anthropogenically modified geomorphic processes such as changes in sediment supply, deposition, and compaction—which increase land subsidence and RSLR—and by the socioeconomic capability to prepare for and mitigate exposure to hazardous conditions (*17*). Focusing on interdelta differences in risk, we used sufficiently mature global data sets that depict factors with well-documented impacts on delta conditions, together with established methods for spatial integration of qualitatively distinct data types (*18*–*20*). We focused on 48 major coastal deltas across a wide range of climate, biome, and socioeconomic contexts (Fig. 1A), with an estimated current combined population of over 340 million (*21*) (see the supplementary materials). At less direct risk are an additional 140 million people living within 25 km of these deltas, who, together with 3.5 billion people in upstream catchment basins, produce additional human impacts. We defined risk (R), or expected loss, to a delta population as a product of hazard (H), exposure (E), and vulnerability (V): $R = HEV$ (*17*, *22*, *23*). Hazard is the probability of a damage-producing event, defined as fluvial or coastal flooding. Exposure is the expected number of people exposed to hazardous conditions for a given event, and vulnerability is the harm or loss caused by the exposure (eq. S1).

Previous direct estimates of H, E, and V have been carried out in a number of local and regional studies (*23*–*25*) using high-resolution data sets that are not currently available at the global scale. Exposure data at the necessary scales exist for select deltas; however, for global-scale analysis, the rate of change in exposure, E', is a more tractable measure for interdelta comparison. By reducing the relative elevation of a delta, RSLR results in increased population exposure to a given hazard and thus increased expected loss. The rate of change in expected loss (R') due to anthropogenic RSLR is termed the risk trend: $R' = HE'V$ (see the supplementary materials).

We estimated H, E', and V for each delta, using empirical indices derived from global data sets. The Hazardous Event Index (HEI) is a proxy for hazard, based on empirical indicators of the probability and intensity of delta flood events. E' was estimated using the Anthropogenic Conditioning Index (ACI), which is built from measures of long-term anthropogenic drivers of RSLR (fig. S1). Vulnerability, which is strongly dependent on socioeconomic conditions in the delta (*17*, *22*), was estimated as a function of per-capita gross domestic product (GDP), aggregate GDP, and government effectiveness. High GDP provides the financial capacity to make vulnerability-reducing investments from household to delta scales, when effective governments are present to leverage aggregate wealth to reduce vulnerability. An index representing the absence of this capacity, the Investment Deficit Index (IDI), was used as a proxy for V. The risk component estimates derived from the ACI, HEI, and IDI indices were used to estimate the risk trend resulting from RSLR (eq. S7).

We mapped the 48 deltas into a risk space defined by each delta's specific anthropogenic, geophysical, and socioeconomic characteristics (Fig. 1). These estimates were made in an index space, comparing delta systems with each other on a relative per-capita basis. In quadrant I, which contains deltas with low ACI and high HEI scores, the Limpopo delta stands out because of its high vulnerability associated with a lack of infrastructure investment capacity. Most of the high-R' deltas fell in quadrant II, including the Krishna delta, which had the highest R'. In quadrant IV, characterized by high ACI and low to moderate HEI scores, the Ganges-Brahmaputra delta had a high R' due to high vulnerability. In contrast, quadrant III contains deltas with low R' due to both low ACI and low HEI scores, including the high-latitude Yukon, Lena, and Mackenzie deltas.

The Mississippi, Rhine, and Tone deltas had ACI and HEI scores similar to those of the Brahmani and Godavari deltas (between 0.4 and 0.7), but they had far lower IDI scores (<0.2). Their resulting risk levels were much more stable, with risk trends among the lowest of all the deltas in the study. Although the results presented here

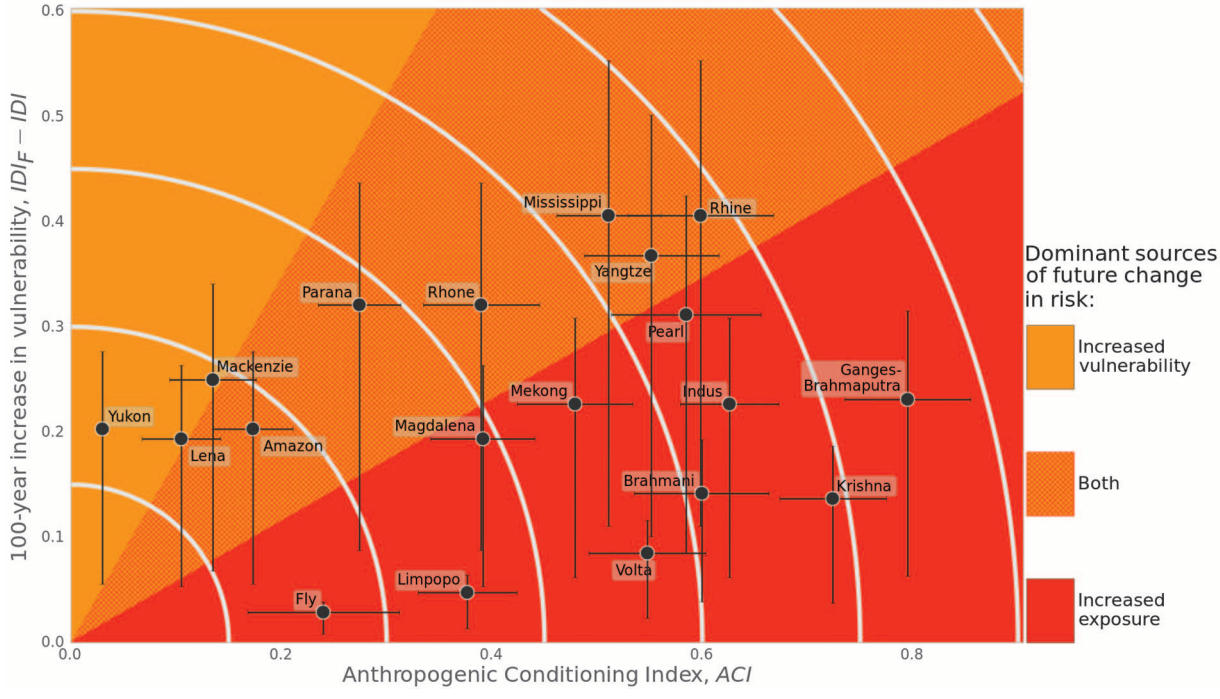

Fig. 2. Estimated future change in exposure and vulnerability for selected deltas. The vertical axis, showing one scenario of change in vulnerability, is the difference between the 100-year future Investment Deficit Index, IDI_F, and the current index, IDI. The origin represents current conditions. Both axes indicate a change over time for the two risk components: Increases in exposure are taken as proportional to the current rate of change, and increases in vulnerability are based on the difference between current and future estimates. Future change in risk is either associated predominately with increases in exposure (red) or increases in vulnerability (orange). Several delta systems (e.g., Mississippi, Rhine, and Yangtze) are at risk both from RSLR, leading to increased exposure to flooding, and from reduced effectiveness of risk reduction strategies that may not be sustainable on the century scale.

are for per-capita risk, the Ganges-Brahmaputra system had, by far, the greatest rate of change in risk when aggregating across delta populations. The Ganges-Brahmaputra had the second highest R' on a per-capita basis, and at more than 100 million people, it has more than twice the population of the Nile, the second most populous delta.

A low IDI, indicating a high capacity for investment in risk-reducing technologies, is the primary reason that several wealthy, developed deltas today have relatively low risk trends. For instance, after catastrophic flooding of the Rhine delta in 1953, the Dutch Delta Works were constructed to reduce future flood risk, using a network of storm-surge barriers, dams, levees, and other engineered structures. A long history of land subsidence, however, has left parts of this delta 6 m below sea level (*26*). Modernization and improvement costs across the Netherlands are projected to reach €1 billion to €2 billion per annum over the next century (*27*). The long-term sustainability of this and similar risk-reducing investments elsewhere has been called into question because of their heavy reliance on external financial and energy subsidies (*14*).

To examine the sensitivity of delta risk to reduced infrastructure investment benefits, we considered a future scenario in which infrastructure costs have increased. For our analysis, we used an increase in energy prices as a likely reason for a rise in the cost of infrastructure, but factors such as relative increases in the costs of labor and material or rising interest rates would have similar impacts on infrastructure cost. We modeled this scenario by adjusting IDI scores: We reduced GDP indicator weights based on 100-year projections of energy price growth in excess of GDP (*28*) (see the supplementary materials), reflecting expectations of higher costs for a given level of risk reduction. Estimates of future vulnerability increased for all deltas under this scenario (Fig. 2) but were greatest for systems with high GDP. The Mississippi, Rhine, Han, Chao Phraya, and Yangtze deltas had the greatest increases in vulnerability under this scenario, although others were also strongly affected, including the Parana, Rhone, and Pearl deltas. Deltas in low-GDP regions, such as the Irrawaddy, Tana, and Fly, were the least sensitive to these potential future changes. These and other less economically developed deltas were instead more sensitive to future risk increases stemming from increased exposure to hazardous events.

A given increase in vulnerability will not affect risk trends in all deltas equally; rather, its effect will be related to each delta's ACI and HEI scores. We started with each system's uncompensated R' based on anthropogenic and geophysical considerations alone (Fig. 3A). When considering contemporary vulnerability estimates (Fig. 3B), the wealthy but otherwise at-risk deltas such as the Rhine, Mississippi, and Han benefited

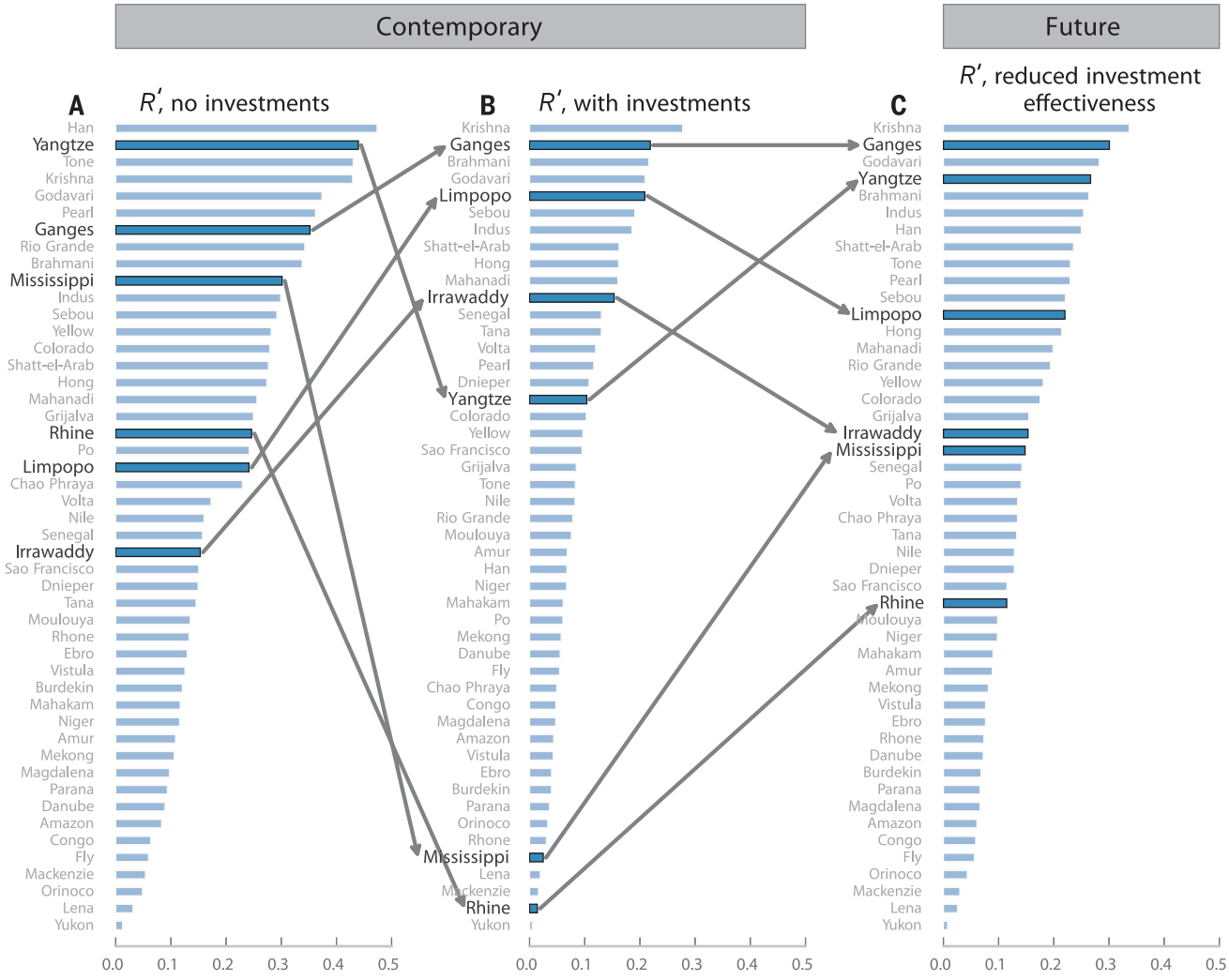

Fig. 3. Current and future investment impacts on risk-trend rankings. (**A**) Contemporary risk trend when considering only the anthropogenic and geophysical setting of each delta. (**B**) When also considering relative vulnerability, which is low for deltas that can make risk-reducing investments, the overall contemporary risk trend changes, in many cases dramatically. The Mississippi and Rhine deltas show substantially reduced risk. (**C**) Current risk-reduction strategies become more expensive and less sustainable in a more energy-constrained future scenario (*14*). In the long term, deltas that today are protected by substantial compensating infrastructure are likely to see their risk profiles approach those in (A).

substantially from their capacity to sustain engineering and infrastructure investments. Low-GDP deltas that are not able to make risk-reduction investments moved to higher risk rankings. The largest increases in R' ranks occurred for the Limpopo and Irrawaddy deltas. Improved economic development and associated vulnerability reductions would result in the largest decreases in risk in these deltas, akin to a transition from Fig. 3B to Fig. 3A. In the future vulnerability scenario (Fig. 3C), where investment capacity less effectively reduces risk trends, R' ranks for high-GDP deltas reverted back toward expectations based on geophysical hazards and anthropogenic change alone. Although contemporary estimates of risk trends were highest in South Asia (Fig. 4A), future increases in R', relative to current estimates, were greatest in the Rhine, Mississippi, Han, Tone, Chao Phraya, and Yangtze deltas (Fig. 4B). These systems are highly stressed by anthropogenic activities and regularly contend with hazardous events, so future increases in vulnerability will have a disproportionately large risk impact relative to other deltas. Management strategies that address the drivers of RSLR, particularly sediment supply and deposition, will be a core determinant of long-term sustainability over the next century.

Future changes in the intensity and distribution of hazardous events, which are highly uncertain at the local scale, are also an important driver of future risk trends. Broad evidence suggests that climate change is affecting tropical cyclone intensity and river flooding (*11*, *29*), global sea-level rise is accelerating (*12*, *30*), and local sea-level rise may be substantially different than the global mean in some coastal areas because of regional patterns of ocean heat uptake and glacial isostatic adjustment (*30*). Land subsidence, taken as constant over time in our study, is also likely to change as future global population growth occurs predominantly in urban areas (*31*), driving further anthropogenic change in already stressed deltas. Growth in population, urbanization, and economic development is leading to increased interest in expanding hydropower infrastructure, which is already proliferating across many river systems (*32*, *33*). Expanding hydropower infrastructure will reduce sediment transport and the discharge capacity of river systems that are essential for nourishing deltas (*6*). Delta shorelines, for instance, are highly sensitive to the balance between sediment supply and absolute wave energy (*4*).

Future environmental, geophysical, and societal changes will reposition, in many cases considerably, most of the world's deltas into a future space of elevated risk. Although potential geophysical changes require additional research at the regional and local scales, our study demonstrates that economic ability and decisions to deploy engineering solutions will be key factors in

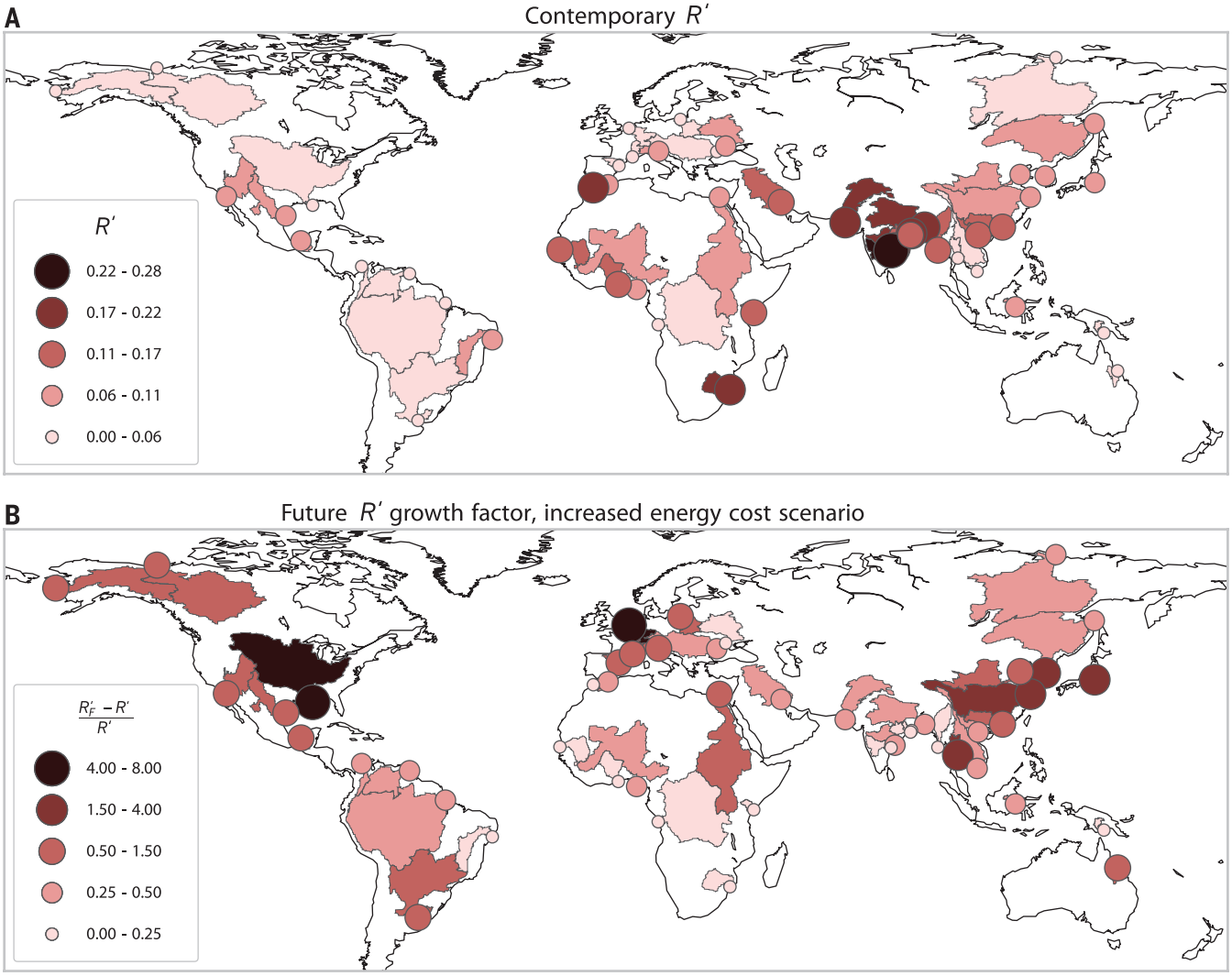

Fig. 4. Contemporary risk trend and future risk-trend growth. (**A**) High contemporary values of R' are distributed globally among the highly populated deltas of Southeast Asia and deltas in developing parts of Africa and the Middle East. (**B**) Estimated 50-year growth in the future risk trend, R'_F, relative to the current R'. The highest relative increases in R'_F are in the Rhine, Mississippi, Han, Tone, and Chao Phraya deltas, all systems where current risk is reduced through investments enabled by high GDP and energy costs that are affordable relative to the future scenario.

determining how sustainable deltas become in the long term. Investments that manage the drivers of RSLR, rather than its symptoms, will be necessary to sustain deltas. Although the time horizons are long, acting now is essential, given that rehabilitation will be difficult (if not impossible) to achieve once ground is lost to rising seas.

REFERENCES AND NOTES

1. C. D. Woodroffe, R. J. Nicholls, Y. Saito, Z. Chen, S. L. Goodbred, in *Global Change and Integrated Coastal Management*, N. Harvey, Ed. (Springer Science and Business Media, Dordrecht, Netherlands, 2006), pp. 277–314.
2. M. VanKoningsveld, J. P. M. Mulder, M. J. F. Stive, L. VanDerValk, A. W. VanDerWeck, *J. Coast. Res.* **242**, 367–379 (2008).
3. J. W. Day Jr. *et al.*, *Science* **315**, 1679–1684 (2007).
4. J. P. M. Syvitski, Y. Saito, *Global Planet. Change* **57**, 261–282 (2007).
5. J. P. Ericson, C. J. Vorosmarty, S. L. Dingman, L. G. Ward, M. Meybeck, *Global Planet. Change* **50**, 63–82 (2006).
6. C. J. Vörösmarty *et al.*, *Global Planet. Change* **39**, 169–190 (2003).
7. H. J. Wang *et al.*, *Global Planet. Change* **57**, 331–354 (2007).
8. J. P. M. Syvitski *et al.*, *Nat. Geosci.* **2**, 681–686 (2009).
9. S. Mazzotti, A. Lambert, M. Van der Kooij, A. Mainville, *Geology* **37**, 771–774 (2009).
10. S. Higgins, I. Overeem, A. Tanaka, J. P. M. Syvitski, *Geophys. Res. Lett.* **40**, 3898–3902 (2013).
11. T. R. Knutson *et al.*, *Nat. Geosci.* **3**, 157–163 (2010).
12. B. P. Horton, S. Rahmstorf, S. E. Engelhart, A. C. Kemp, *Quat. Sci. Rev.* **84**, 1–6 (2014).
13. F. G. Renaud *et al.*, *Curr. Opin. Environ. Sustain.* **5**, 644–654 (2013).
14. J. W. Day, M. Moerschbaecher, D. Pimentel, C. Hall, A. Yáñez-Arancibia, *Ecol. Eng.* **65**, 33–48 (2014).
15. S. Temmerman *et al.*, *Nature* **504**, 79–83 (2013).
16. National Research Council, *Landscapes on the Edge: New Horizons for Research on Earth's Surface* (National Academies Press, Washington, DC, 2010).
17. N. Brooks, W. N. Adger, P. M. Kelly, *Glob. Environ. Change* **15**, 151–163 (2005).
18. V. Gornitz, *Palaeogeogr. Palaeoclimatol. Palaeoecol.* **89**, 379–398 (1991).
19. B. S. Halpern *et al.*, *Science* **319**, 948–952 (2008).
20. C. J. Vörösmarty *et al.*, *Nature* **467**, 555–561 (2010).
21. D. L. Balk *et al.*, *Adv. Parasitol.* **62**, 119–156 (2006).
22. S. Cutter, *Prog. Hum. Geogr.* **20**, 529–539 (1996).
23. C. J. Vörösmarty, L. B. de Guenni, W. M. Wollheim, B. Pellerin, D. Bjerklie, M. Cardoso, C. D'Almeida, P. Green, L. Colon, *Philos. Trans. R. Soc. London Ser. A* **371** (2013); http://rsta.royalsocietypublishing.org/content/371/2002/20120408.
24. Y. Budiyono, J. Aerts, J. Brinkman, M. A. Marfai, P. Ward, *Nat. Hazards* **75**, 389–413 (2015).
25. Y. C. E. Yang, P. A. Ray, C. M. Brown, A. F. Khalil, W. H. Yu, *Nat. Hazards* **75**, 2773–2791 (2015).
26. T. Bucx, M. Marchand, B. Makaske, C. van de Guchte, *Comparative Assessment of the Vulnerability and Resilience of 10 Deltas – Synthesis Report* (Delta Alliance report number 1, Delta Alliance International, Delft-Wageningen, Netherlands, 2010).
27. P. Kabat *et al.*, *Nat. Geosci.* **2**, 450–452 (2009).
28. U.S. Energy Information Administration, *Annual Energy Outlook 2015* (DOE/EIA-0383, U.S. Department of Energy, Washington, DC, 2015).
29. R. Dankers *et al.*, *Proc. Natl. Acad. Sci. U.S.A.* **111**, 3257–3261 (2014).
30. S. Jevrejeva, J. C. Moore, A. Grinsted, A. P. Matthews, G. Spada, *Global Planet. Change* **113**, 11–22 (2014).
31. K. C. Seto, B. Güneralp, L. R. Hutyra, *Proc. Natl. Acad. Sci. U.S.A.* **109**, 16083–16088 (2012).
32. C. Kuenzer *et al.*, *Sustain. Sci.* **8**, 565–584 (2013).
33. C. Zarfl, A. E. Lumsdon, J. Berlekamp, L. Tydecks, K. Tockner, *Aquat. Sci.* **77**, 161–170 (2015).

ACKNOWLEDGMENTS

Data are available as supplementary materials on *Science* Online. This work was supported by NASA (Land Cover/Land Use Change Program grant NNX12AD28G) and NSF (Belmont Forum Coastal Vulnerability awards 1343458 and 1342944, and Dynamics of Coupled Natural and Human Systems award 1115025). The authors report no conflicts of interest. The authors thank B. Fekete and P. Green for helpful comments on the manuscript.

SUPPLEMENTARY MATERIALS

www.sciencemag.org/content/349/6248/638/suppl/DC1
Materials and Methods
Figs. S1 to S4
Tables S1 to S3
References (*34*–*52*)

15 April 2015; accepted 30 June 2015
10.1126/science.aab3574

HUMORAL IMMUNITY

T cell help controls the speed of the cell cycle in germinal center B cells

Alexander D. Gitlin,[1] Christian T. Mayer,[1] Thiago Y. Oliveira,[1] Ziv Shulman,[1] Mathew J. K. Jones,[2] Amnon Koren,[4] Michel C. Nussenzweig[1,3]*

The germinal center (GC) is a microanatomical compartment wherein high-affinity antibody-producing B cells are selectively expanded. B cells proliferate and mutate their antibody genes in the dark zone (DZ) of the GC and are then selected by T cells in the light zone (LZ) on the basis of affinity. Here, we show that T cell help regulates the speed of cell cycle phase transitions and DNA replication of GC B cells. Genome sequencing and single-molecule analyses revealed that T cell help shortens S phase by regulating replication fork progression, while preserving the relative order of replication origin activation. Thus, high-affinity GC B cells are selected by a mechanism that involves prolonged dwell time in the DZ where selected cells undergo accelerated cell cycles.

Antibodies elicited during T cell–dependent immune responses undergo substantial increases in affinity over time (*1*). This phenomenon, known as affinity maturation, takes place in the germinal center (GC), where antigen-specific B cells diversify their antibodies by somatic hypermutation (*2*) and undergo selective clonal expansion (*3*–*7*). Together, these events are essential to the development of effective antibody responses.

GC B cells bearing antibody variants with higher affinity are selectively expanded during iterative rounds of migration between the dark zone (DZ), where they proliferate and hypermutate, and the light zone (LZ), where they capture antigen displayed on the surface of follicular dendritic cells (*8*–*11*). By binding and internalizing more antigen in the LZ, high-affinity clones present more peptide–major histocompatibility complex II (MHCII) and thereby elicit greater help from $CD4^+$ T follicular helper cells (*11*, *12*). The magnitude of T cell help determines how long B cells reside in the DZ, which provides selected cells more time to proliferate and expand in between rounds of competition in the LZ (*13*). Whether this mechanism alone explains how high-affinity B cells are selected remains unknown.

[1]Laboratory of Molecular Immunology, The Rockefeller University, New York, NY 10065, USA. [2]Molecular Biology Program, Memorial Sloan-Kettering Cancer Center, 1275 York Avenue, New York, NY 10065, USA. [3]Howard Hughes Medical Institute (HHMI), The Rockefeller University, New York, NY 10065, USA. [4]Department of Genetics, Harvard Medical School, Boston, MA 02115, USA.
***Corresponding author. E-mail: nussen@rockefeller.edu**

To explore additional mechanisms that could contribute to selection, we used an adoptive transfer model in which antigen presentation by a subset of GC B cells can be acutely and selectively increased (*11*, *14*, *15*). B cells carrying a knock-in antigen receptor specific for the hapten 4-hydroxy-3-nitrophenylacetyl (NP) (B1-8^{hi}) were transferred into ovalbumin (OVA)–primed wild-type mice that were boosted with NP-OVA. Whereas the majority of transferred B1-8^{hi} B cells were $DEC205^{-/-}$ (~85%), a subset (~15%) of the B1-8^{hi} B cells were $DEC205^{+/+}$ (*10*, *16*). DEC205 is an endocytic receptor expressed by GC B cells that delivers antigen to MHCII processing compartments (*14*). Targeting DEC205 with an antibody that is fused at its C terminus to OVA (αDEC–OVA), but not the irrelevant control antigen *Plasmodium falciparum* circumsporozoite protein (αDEC-CS) (*17*), increases the amount of cognate peptide–MHCII displayed on the surface of B1-8^{hi} $DEC205^{+/+}$ GC B cells, which leads to their selective expansion (*11*–*13*).

To determine whether B cells receiving high levels of T cell help show a specific change in gene expression, we compared DZ cells in the G_1 phase of the cell cycle from αDEC-OVA– and control αDEC-CS–treated GCs, using a fluorescent ubiquitination-based cell cycle indicator ($Fucci^{tg}$) (fig. S1) (*18*, *19*). RNA sequencing revealed that T cell–mediated selection produced a statistically significant increase in gene expression programs associated with the cell cycle, metabolism (including the metabolism of nucleotides), and genes downstream of c-Myc and the E2F transcription factors (Fig. 1, A and B, and fig. S2). Finding an

increase in expression of c-Myc target genes is in agreement with the observation that c-Myc is induced by T cell help in the GC (*20*, *21*). E2F transcription factors are principal drivers of the cell cycle and are activated by cyclin-dependent kinase (CDK) phosphorylation of the retinoblastoma (Rb) protein (*22*, *23*). Consistent with this, Rb was highly phosphorylated in GC B cells receiving enhanced T cell help (Fig. 1C). E2F and c-Myc are crucial drivers of cell cycle phase transitions; moreover, their activation regulates nucleotide metabolism and controls DNA replication dynamics (*23*–*26*), which suggests that T cell help might control the cell cycle dynamics of selected GC B cells in vivo.

To examine cell cycle progression, mice were pulsed sequentially with the nucleoside analog 5-ethynyl-2′-deoxyuridine (EdU) followed 1 hour later by 5-bromo-2′-deoxyuridine (BrdU), and GC B cells were then stained for DNA content (Fig. 2A and fig. S3) (*13*). At 0.5 hours after the BrdU pulse, early S-phase cells were labeled as $EdU^{-}BrdU^{+}$ and had replicated only a small amount of their genome, which made their DNA content similar to that of G_1 cells (Fig. 2, A and B). By contrast, mid/late S-phase cells were labeled as $EdU^{+}BrdU^{+}$, and post–S phase cells (labeled as $EdU^{+}BrdU^{-}$) were either in G_2/M phase or in the G_1 phase of the next cell cycle (Fig. 2, A and B). Under control conditions (αDEC-CS), B1-8^{hi} $DEC205^{+/+}$ and B1-8^{hi} $DEC205^{-/-}$ post–S phase GC B cells were similarly distributed between G_2/M and G_1, which indicated equivalent rates of progression through the G_2/M phases of the cell cycle (Fig. 2C). By contrast, inducing selection by αDEC–OVA resulted in rapid progression through G_2/M and return to G_1 (Fig. 2C). Thus, T cell–mediated selection accelerates progression through G_2/M.

To examine S-phase dynamics, we followed GC B cells 2.5 and 5 hours after the EdU/BrdU double-pulse described above. At 2.5 hours, $EdU^{-}BrdU^{+}$ cells, which were in early S phase at 0.5 hours, had progressed into mid/late-S phase as determined by DNA content (Fig. 2, D and E). With only these two additional hours to replicate their genomes, selected GC B cells accumulated more DNA content and had therefore replicated their genomes at a faster rate than control cells obtained from αDEC-CS–treated mice (Fig. 2D and fig. S4). After 5 hours, nearly half of control cells that were labeled in early S phase ($EdU^{-}BrdU^{+}$) had completed S phase and were in G_2/M or G_1 (Fig. 2E). Selection significantly accelerated progression through S phase, as a far greater fraction of B1-8^{hi} $DEC205^{+/+}$ GC cells targeted with αDEC–OVA completed DNA replication in 5 hours than did cotransferred B1-8^{hi} $DEC205^{-/-}$ GC cells (Fig. 2F). We conclude that T cells induce accelerated progression of selected GC B cells through the S and G_2/M phases of the cell cycle.

To determine whether accelerated progression through the cell cycle is also a feature of polyclonal GC responses, we examined the response to NP in C57BL/*6* mice. High-affinity clones in NP-specific GCs carry a tryptophan-to-leucine mutation at position *33* (W33L) or a lysine-to-arginine mutation at position *59* (K59R) in the V_H186.2 antibody gene (*27*, *28*). Two weeks after immunization with NP-OVA, mice were pulsed with EdU, followed 30 min later by a large dose of BrdU to inhibit further EdU uptake (fig. S5). After 3.25 hours, EdU^{+} GC cells were separated into two distinct populations on the basis of DNA content (Fig. 3A): (i) EdU^{+} cells in S/G_2/M that represent a mixed population that initiated S phase at the time of EdU injection and/or progressed slowly through S/G_2/M; and (ii) EdU^{+} cells in G_1 that were close to completing S phase during the EdU injection and/or progressed rapidly through S/G_2/M. If high-affinity GC B cells progress through the cell cycle at an accelerated rate, then they should be enriched in the EdU^{+} G_1 population. Sequencing the V_H186.2 genes of these cells revealed that EdU^{+} G_1 cells were significantly enriched in high-affinity clones compared with EdU^{+} S/G_2/M cells (Fig. 3, B and C). Thus, affinity-enhancing mutations in the polyclonal GC are associated with rapid progression through S/G_2/M.

Once a GC B cell has entered the cell cycle, S phase occupies most of the time it takes for the cell to divide (Fig. 2) (*13*). We therefore sought to understand how T cell help accelerates progression through S phase. Control of S-phase length is a well-documented phenomenon during embryonic development (*29*). In this context, S-phase control operates at the level of initiation of DNA replication; rapid S phases are caused by an increased number of synchronously fired replication origins (*30*–*33*).

To evaluate the dynamics of DNA replication initiation, we sorted and sequenced the genomes of B1-8^{hi} $DEC205^{+/+}$ GC B cells in G_1 and S phase under control conditions or during their selective expansion (fig. S6, A and B). In a population of S-phase cells, genomic sites that replicate early have higher copy number than regions that are replicated later during S phase. Thus, by analyzing the relative copy number of DNA sequences along chromosomes in S-phase cells compared with G_1-phase cells, we obtained genome-wide profiles of DNA replication timing (*34*, *35*). The relative timing of DNA replication among selected and nonselected GC B cells was essentially identical, with the same locations and activation times of origins throughout the genome [correlation coefficient (r) = 0.98] (Fig. 4, A and B, and fig. S6C). Thus, T cell help accelerates S phase by proportionally condensing the replication timing program, while maintaining the overall dynamics of DNA replication albeit on a shorter time scale.

Elevated c-Myc, CDK activity, and nucleotide metabolism can increase the speed of DNA

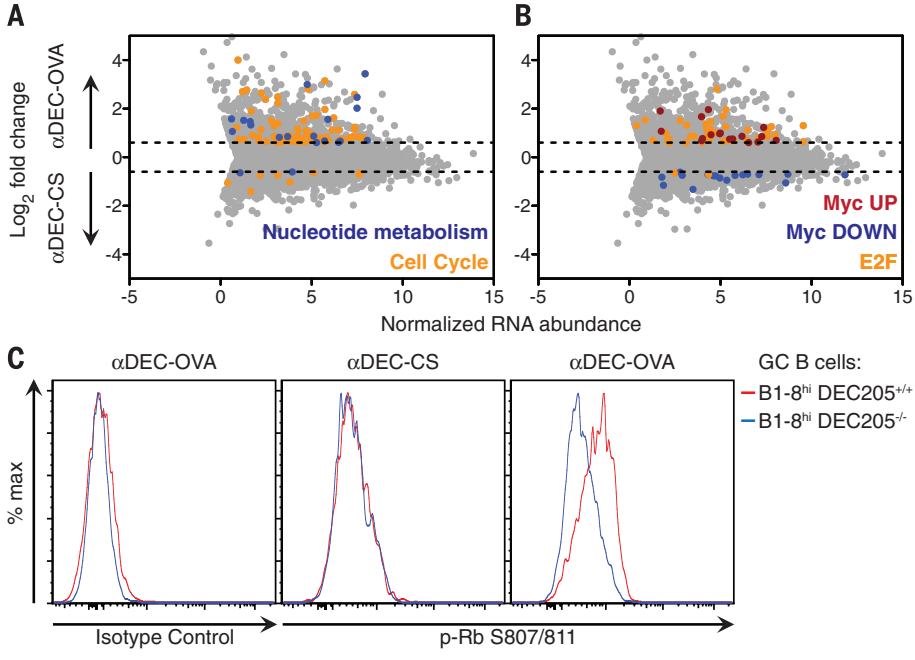

Fig. 1. T cell help regulates cell cycle and metabolic gene expression programs in selected GC B cells. (**A** and **B**) RNA sequencing analysis showing genes up- or down-regulated by a fold-change of at least 0.6 (log_2) upon treatment with αDEC-OVA or αDEC-CS. For clarity, enriched gene sets according to curated reactome gene sets (A) and transcription factor target genes (B) are shown separately. (**C**) Histograms showing intracellular levels of Rb phosphorylation in B1-8^{hi} $DEC205^{+/+}$ and B1-8^{hi} $DEC205^{-/-}$ GC B cells from mice treated 2 days earlier with αDEC-OVA or αDEC-CS. Results represent two (A and B) or three (C) independent experiments with n = 4 to 5 mice per condition for each experiment.

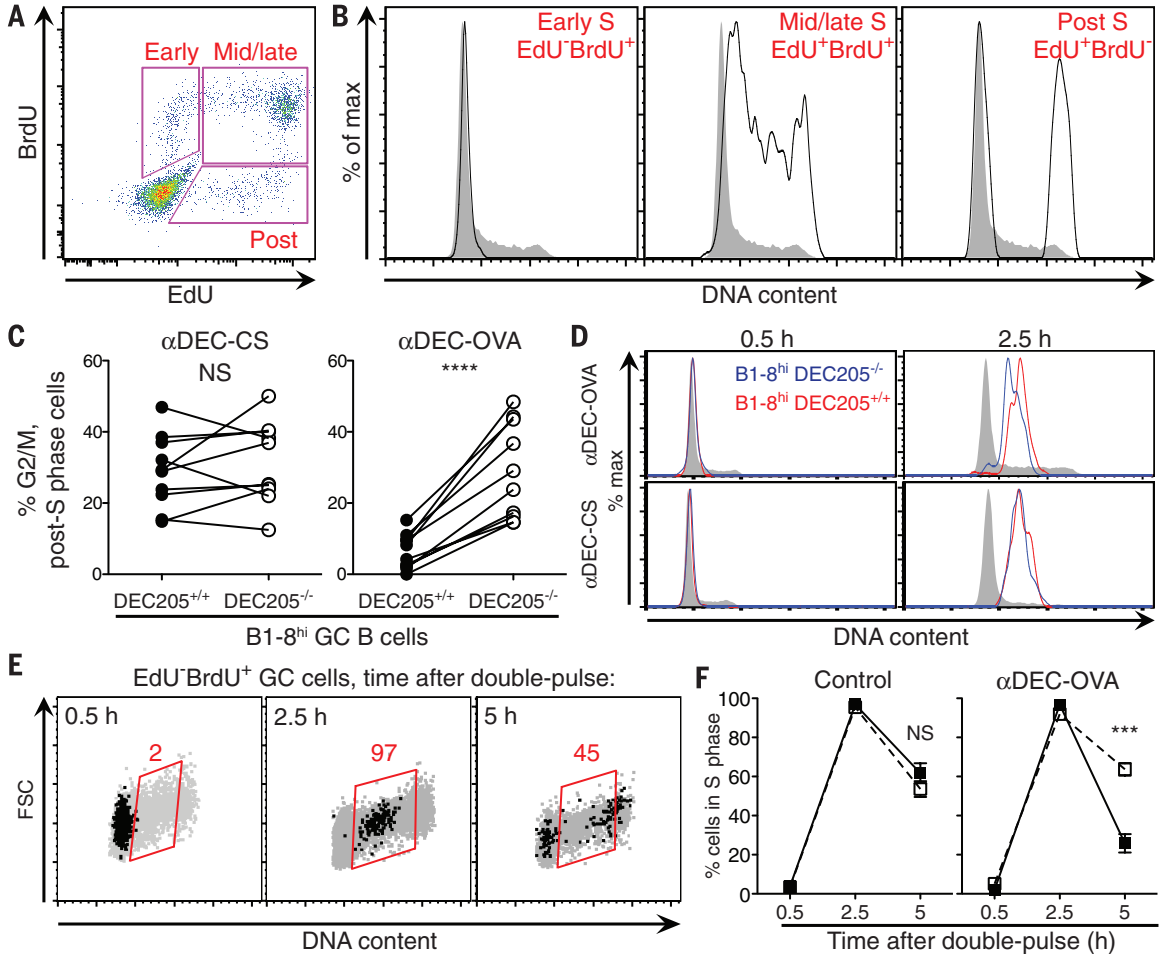

Fig. 2. T cell help regulates progression through S and G_2/M phases during selection. (**A**) Mice were injected with EdU intravenously followed 1 hour later by BrdU and then analyzed by flow cytometry 0.5 hours later. (**B**) Representative histograms displaying DNA content among all GC B cells (gray) and gated populations (black) shown in (A). (**C**) Mean fraction of cells in G_2/M as determined by DNA content among EdU$^+$BrdU$^-$ (post–S phase) B1-8^{hi} DEC205$^{+/+}$ and B1-8^{hi} DEC205$^{-/-}$ GC B cells treated with αDEC-OVA or αDEC-CS (control) 2 days earlier. Lines connect indicated cell populations from the same animal. (**D**) Histograms showing progressive accumulation of DNA content among EdU$^-$BrdU$^+$ GC B cells from 0.5 to 2.5 hours after EdU/BrdU double pulse. (**E**) Flow cytometry plots showing time course of cell cycle progression of EdU$^-$BrdU$^+$ cells (black dots) at 0.5, 2.5, and 5 hours after double-pulse labeling. Gray dots represent all GC B cells in the same mice. Red values represent fraction in S-phase gate. (**F**) Mean fraction of GC B cells in S-phase gate among EdU$^-$BrdU$^+$ B1-8^{hi} DEC205$^{+/+}$ (black squares) and B1-8^{hi} DEC205$^{-/-}$ (white squares) cells as determined by DNA content at 0.5, 2.5, and 5 hours after double-pulse labeling in mice treated 2 days earlier with αDEC-OVA or either PBS or αDEC-CS (control). Error bars represent SEM. Two-tailed paired *t* test was used in (C) and two-tailed Mann-Whitney test in (F). ****$P < 0.0001$. ***$P = 0.0002$. Experiments represent two or three independent experiments with 7 to 10 mice total for each time point and condition.

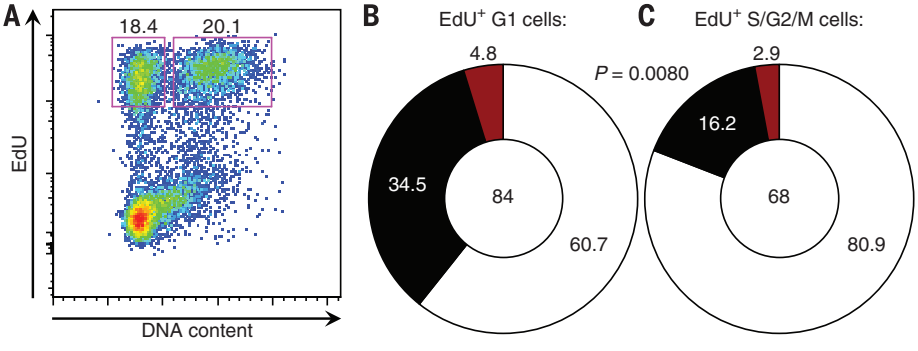

Fig. 3. Affinity-enhancing mutations in polyclonal GCs are associated with accelerated S/G_2/M progression. (**A**) WT mice were immunized with NP-OVA and 14 days later were administered EdU for 0.5 hours before BrdU. At 3.25 hours after BrdU administration, EdU$^+$ G_1 cells and EdU$^+$ S/G_2/M GC B cells were sorted and analyzed for affinity-enhancing mutation in VH186.2 genes. (**B** and **C**) Pie charts show frequency of W33L$^+$ (black) and K59R$^+$ (red) clones among VH186.2 sequences within EdU$^+$ G_1 (B) and EdU$^+$ S/G_2/M (C) GC B cells. One sequence was doubly positive for the W33L and K59R mutations and was counted within the black slice in (C). Total number of clones analyzed is shown in center. *P* value was determined using Fisher's exact test. Results are pooled from two independent experiments with 10 mice each.

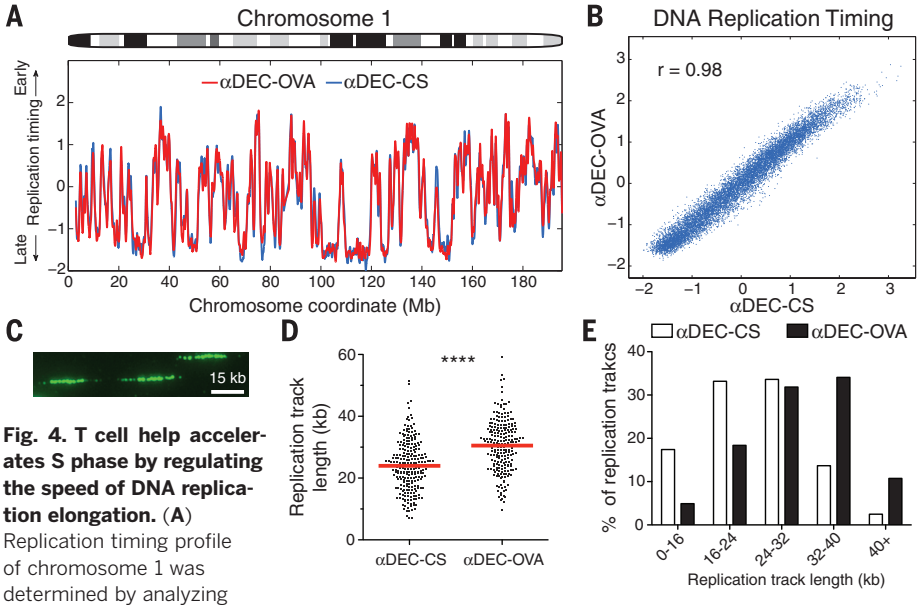

Fig. 4. T cell help accelerates S phase by regulating the speed of DNA replication elongation. (**A**) Replication timing profile of chromosome 1 was determined by analyzing the ratio of DNA copy number between sorted S and G_1 phase B1-8^{hi} DEC205$^{+/+}$ GC B cells treated with αDEC-CS or αDEC-OVA 2 days earlier. (**B**) Genome-wide correlation between replication timing in the two conditions. (**C**) Representative IdU-labeled DNA fibers are shown. (**D**) Replication track lengths from αDEC-CS or αDEC-OVA–treated B1-8^{hi} DEC205$^{+/+}$ GC B cells. Each data point represents an IdU-labeled track, and red lines represent mean values. Results are pooled from two independent experiments and involve >220 measured fibers in total for each condition. (**E**) Distribution of replication track lengths. ****P < 0.0001, two-tailed Mann-Whitney test.

replication fork progression in tissue culture cells, yet a physiological role for this mechanism has not been documented (*26*, *36*, *37*). Because T cell help produces similar molecular changes in selected GC B cells, we examined DNA replication forks by single-molecule analyses (*38*). For this purpose, αDEC-OVA or control αDEC-CS–treated mice were pulsed with the nucleoside analog 5-iodo-2′-deoxyuridine (IdU) (fig. S6D). GC B cells were then isolated by cell sorting and processed to measure the lengths of DNA replication tracks in individual molecules (Fig. 4C). Selection resulted in an increase in the average length of replication tracks and altered the distribution of replication track lengths, which indicated that T cell help regulates DNA replication by increasing the speed of individual DNA replication forks (Fig. 4, D and E) (P < 0.0001).

The GC imparts protective immunity by selectively expanding high-affinity B cells, yet the mechanisms whereby such clones come to dominate the GC population have been obscure (*3*, *4*). T cells discern among GC B cells on the basis of cell surface peptide–MHCII levels and transduce signal(s) that regulate the amount of time selected cells spend proliferating in the DZ (*8*, *11*–*13*). Thus, T cell help influences the choice that a recently divided GC B cell in G_1 must make in the DZ: either to reenter another S phase or, instead, to return to the LZ (*13*). Our results indicate that T cell–mediated selection extends beyond this mode of regulation and accelerates progression through the entire cell cycle in selected GC B cells. Thus, the regulatory effects transduced by T cells work in concert to induce selected GC B cells to spend a longer period of time in the DZ, where they proliferate at a faster rate.

There are few examples of physiological regulation of cell cycle speed in eukaryotes, and, to our knowledge, none known that involve directed signaling by one cell type to another (*29*). High levels of replication factors and CDK activity in the early embryo synchronize initiation from a greater number of origins to increase the rate of cell division (*31*, *39*). By contrast, during B cell selection, T cell help induces higher levels of critical regulators of the cell cycle (c-Myc and CDK) and nucleotide metabolism to accelerate DNA replication elongation, while preserving the temporal order and the number of initiation events throughout the genome. We conclude that selection in the GC involves dynamic regulation of genome replication in S phase, the longest phase of the committed cell cycle.

REFERENCES AND NOTES

1. H. N. Eisen, G. W. Siskind, *Biochemistry* **3**, 996–1008 (1964).
2. M. Muramatsu *et al.*, *Cell* **102**, 553–563 (2000).
3. C. Berek, A. Berger, M. Apel, *Cell* **67**, 1121–1129 (1991).
4. J. Jacob, G. Kelsoe, K. Rajewsky, U. Weiss, *Nature* **354**, 389–392 (1991).
5. C. Kocks, K. Rajewsky, *Proc. Natl. Acad. Sci. U.S.A.* **85**, 8206–8210 (1988).
6. K. Rajewsky, *Nature* **381**, 751–758 (1996).
7. G. D. Victora, M. C. Nussenzweig, *Annu. Rev. Immunol.* **30**, 429–457 (2012).
8. C. D. Allen, T. Okada, H. L. Tang, J. G. Cyster, *Science* **315**, 528–531 (2007).
9. A. E. Hauser *et al.*, *Immunity* **26**, 655–667 (2007).
10. T. A. Schwickert *et al.*, *Nature* **446**, 83–87 (2007).
11. G. D. Victora *et al.*, *Cell* **143**, 592–605 (2010).
12. Z. Shulman *et al.*, *Science* **345**, 1058–1062 (2014).
13. A. D. Gitlin, Z. Shulman, M. C. Nussenzweig, *Nature* **509**, 637–640 (2014).
14. W. Jiang *et al.*, *Nature* **375**, 151–155 (1995).
15. A. O. Kamphorst, P. Guermonprez, D. Dudziak, M. C. Nussenzweig, *J. Immunol.* **185**, 3426–3435 (2010).
16. T. A. Shih, M. Roederer, M. C. Nussenzweig, *Nat. Immunol.* **3**, 399–406 (2002).
17. S. B. Boscardin *et al.*, *J. Exp. Med.* **203**, 599–606 (2006).
18. A. Sakaue-Sawano *et al.*, *Cell* **132**, 487–498 (2008).
19. Y. Aiba *et al.*, *Proc. Natl. Acad. Sci. U.S.A.* **107**, 12192–12197 (2010).
20. D. Dominguez-Sola *et al.*, *Nat. Immunol.* **13**, 1083–1091 (2012).
21. D. P. Calado *et al.*, *Nat. Immunol.* **13**, 1092–1100 (2012).
22. S. P. Chellappan, S. Hiebert, M. Mudryj, J. M. Horowitz, J. R. Nevins, *Cell* **65**, 1053–1061 (1991).
23. H. Z. Chen, S. Y. Tsai, G. Leone, *Nat. Rev. Cancer* **9**, 785–797 (2009).
24. C. V. Dang, *Cell* **149**, 22–35 (2012).
25. D. Dominguez-Sola, J. Gautier, *Cold Spring Harb. Perspect. Med.* **4**, a014423 (2014).
26. A. C. Bester *et al.*, *Cell* **145**, 435–446 (2011).
27. D. Allen, T. Simon, F. Sablitzky, K. Rajewsky, A. Cumano, *EMBO J.* **7**, 1995–2001 (1988).
28. K. Furukawa, A. Akasako-Furukawa, H. Shirai, H. Nakamura, T. Azuma, *Immunity* **11**, 329–338 (1999).
29. J. Nordman, T. L. Orr-Weaver, *Development* **139**, 455–464 (2012).
30. A. B. Blumenthal, H. J. Kriegstein, D. S. Hogness, *Cold Spring Harb. Symp. Quant. Biol.* **38**, 205–223 (1974).
31. C. Collart, G. E. Allen, C. R. Bradshaw, J. C. Smith, P. Zegerman, *Science* **341**, 893–896 (2013).
32. O. Hyrien, C. Maric, M. Méchali, *Science* **270**, 994–997 (1995).
33. S. L. McKnight, O. L. Miller Jr., *Cell* **12**, 795–804 (1977).
34. A. Koren *et al.*, *Cell* **159**, 1015–1026 (2014).
35. A. Koren *et al.*, *Am. J. Hum. Genet.* **91**, 1033–1040 (2012).
36. M. Anglana, F. Apiou, A. Bensimon, M. Debatisse, *Cell* **114**, 385–394 (2003).
37. J. Malínsky *et al.*, *J. Cell Sci.* **114**, 747–750 (2001).
38. D. A. Jackson, A. Pombo, *J. Cell Biol.* **140**, 1285–1295 (1998).
39. J. A. Farrell, A. W. Shermoen, K. Yuan, P. H. O'Farrell, *Genes Dev.* **26**, 714–725 (2012).

ACKNOWLEDGMENTS

We thank A. Miyawaki and T. Kurosaki for mice, T. Eisenreich for help with mouse colony management, K. Yao for technical help, J. Hurwitz and A. Farina for advice, B. Zhang and C. Zhao and the Rockefeller University Genomics Resource Center for assistance with high-throughput sequencing, K. Velinzon for assistance with cell sorting, and all members of the Nussenzweig laboratory for discussion. The data presented in this manuscript are tabulated in the main paper and in the supplementary materials. Supported by NIH Medical Scientist Training Program grant T32GM07739 and National Institute of Allergy and Infectious Diseases, NIH, grant 1F30AI109903-01 (A.D.G.); NIH grants AI037526-19 and AI072529-06 (M.C.N.); and the NIH Center for HIV/AIDS Vaccine Immunology and Immunogen Discovery (CHAVI-ID) 1UM1 AI100663-01 (M.C.N). Z.S. is a Human Frontiers of Science Program Fellow (reference LT000340/2011-L). C.T.M is an EMBO fellow (ALTF 456-2014) and is supported by the European Commission FP7 (Marie Curie Actions, EMBOCOFUND2012, GA-2012-600394). M.C.N. is an HHMI investigator. RNA sequencing data was deposited in the National Center for Biotechnology Information (NCBI), NIH, Gene Expression Omnibus (GEO) and is accessible through accession number GSE71295. Replication timing data was deposited in NCBI's Sequence Read Archive (SRA) and is accessible through accession number SRP061569.

SUPPLEMENTARY MATERIALS

www.sciencemag.org/content/349/6248/643/suppl/DC1
Materials and Methods
Figs. S1 to S6
References (*40*, *41*)

3 May 2015; accepted 8 July 2015
Published online 16 July 2015
10.1126/science.aac4919

NEUROSCIENCE

Natural light-gated anion channels: A family of microbial rhodopsins for advanced optogenetics

Elena G. Govorunova,[1] Oleg A. Sineshchekov,[1] Roger Janz,[2] Xiaoqin Liu,[2] John L. Spudich[1]*

Light-gated rhodopsin cation channels from chlorophyte algae have transformed neuroscience research through their use as membrane-depolarizing optogenetic tools for targeted photoactivation of neuron firing. Photosuppression of neuronal action potentials has been limited by the lack of equally efficient tools for membrane hyperpolarization. We describe anion channel rhodopsins (ACRs), a family of light-gated anion channels from cryptophyte algae that provide highly sensitive and efficient membrane hyperpolarization and neuronal silencing through light-gated chloride conduction. ACRs strictly conducted anions, completely excluding protons and larger cations, and hyperpolarized the membrane of cultured animal cells with much faster kinetics at less than one-thousandth of the light intensity required by the most efficient currently available optogenetic proteins. Natural ACRs provide optogenetic inhibition tools with unprecedented light sensitivity and temporal precision.

Microbial rhodopsins are functionally diverse (*1*, *2*). Several are used as molecular tools for optogenetics to regulate cellular activity with light (*3*–*5*). Membrane-depolarizing phototaxis receptors from green (chlorophyte) flagellate algae (*6*), best known as channelrhodopsins (ChRs) function as millisecond–time scale light-gated cation channels (*7*, *8*) and are widely used to depolarize genetically targeted populations of excitable cells. Hyperpolarizing rhodopsin ion pumps have been used to suppress neuron firing (*9*–*13*), but they transport only a single charge per captured photon and therefore have limited capacity. Recently, ChRs were engineered to conduct Cl^-, but these optogenetic tools still retain some cation conductance and could be made highly light-sensitive only at the expense of slowing the channel kinetics with additional mutations (*14*, *15*). Ideal for optogenetic hyperpolarization would be natural light-gated anion channels optimized by evolution to be strictly anion-selective and highly conductive with rapid kinetics.

Of the ~50 known ChRs from chlorophytes, all that have been tested are exclusively cation channels (*7*, *8*, *16*–*18*). Photoreceptor currents similar to those mediated by ChRs in chlorophytes also occur in the phylogenetically distant cryptophyte algae (*19*). However, several rhodopsin proteins from genes cloned from these organisms did not exhibit channel activity (*19*, *20*). The nuclear genome of the cryptophyte *Guillardia theta* has been completely sequenced (*21*). A BLAST search of model proteins identified 53 with sequence similarity to that of microbial (type I) rhodopsins. None showed high similarity to ChRs, but the models of one particular cluster (Fig. 1A and fig. S1) did contain some key residues characteristic of chlorophyte ChRs (Fig. 1B and fig. S2).

Gene fragments encoding seven transmembrane domains of *G. theta* proteins 111593, 146828, and 161302 were well expressed in transfected human kidney embryonic (HEK293) cells. The first

[1]Center for Membrane Biology, Department of Biochemistry and Molecular Biology, University of Texas Medical School, Houston, TX 77030, USA. [2]Department of Neurobiology and Anatomy, University of Texas Medical School, Houston, TX 77030, USA.
*Corresponding author. E-mail: john.l.spudich@uth.tmc.edu

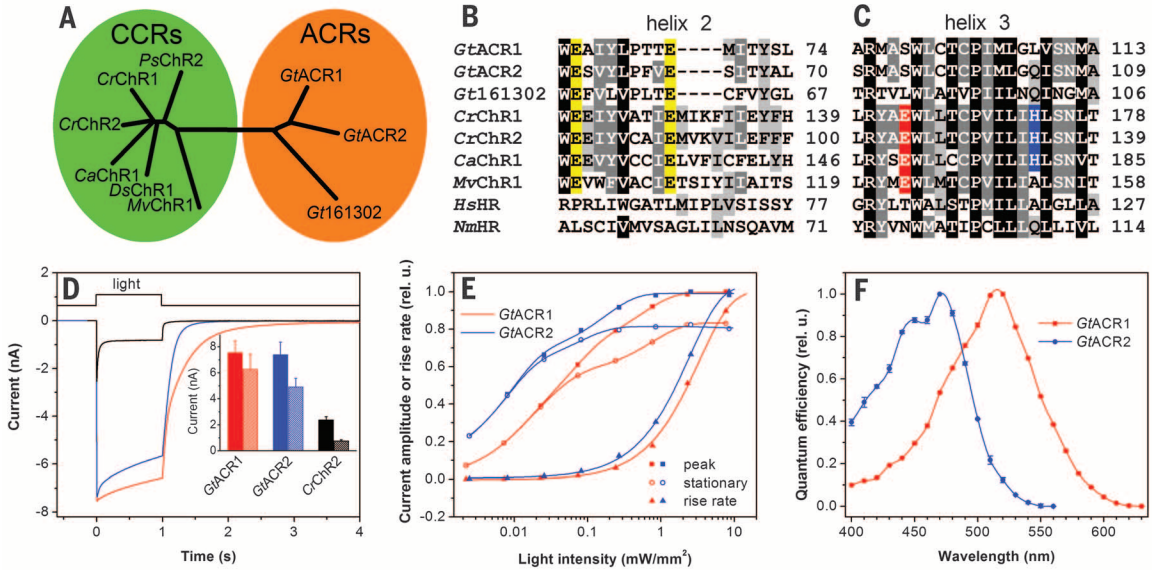

Fig. 1. Phylogeny and photoactivity of *G. theta* ACRs. (**A**) Phylogenetic tree of CCRs and ACRs. (**B** and **C**) ClustalW alignments of transmembrane helices 2 (B) and 3 (C). Abbreviated organism names are: *Gt*, *Guillardia theta*; *Cr*, *Chlamydomonas reinhardtii*; *Ca*, *Chlamydomonas augustae*; *Mv*, *Mesostigma viride*; *Hs*, *Halobacterium salinarum*; *Nm*, *Nonlabens marinus*. The last residue numbers are shown on the right. Conserved Glu residues in helix 2 are highlighted in yellow, Glu residues in the position of bacteriorhodopsin Asp85 in red, and His residues corresponding to His134 of *Cr*ChR2 in blue. (**D**) Photocurrents of *Gt*ACR1, *Gt*ACR2, and *Cr*ChR2 in HEK293 cells in response to a saturating light pulse at −60 mV. (Inset) Mean amplitudes of peak (solid bars) and stationary (hatched bars) currents (n = 18 to 20 cells). (**E**) Dependence of the peak and stationary current amplitudes and rise rates on stimulus intensity. (**F**) Action spectra of photocurrents.

two constructs generated photocurrents, whereas the third did not. The first two functioned as light-gated anion channels; therefore we named them *Gt*ACR1 and *Gt*ACR2 (*Guillardia theta* anion channel rhodopsins 1 and 2).

With our standard solutions for electrophysiological recording (126 mM KCl in the pipette and 150 mM NaCl in the bath, pH 7.4; for other components see table S1), the currents generated by *Gt*ACR1 and *Gt*ACR2 were inward at the holding potential (E_h) of –60 mV (Fig. 1D). The mean plateau currents from *Gt*ACR1 and *Gt*ACR2 were, respectively, eight and six times larger than those from *Cr*ChR2 (*Cr*, *Chlamydomonas reinhardtii*), the most frequently used optogenetic tool, with a

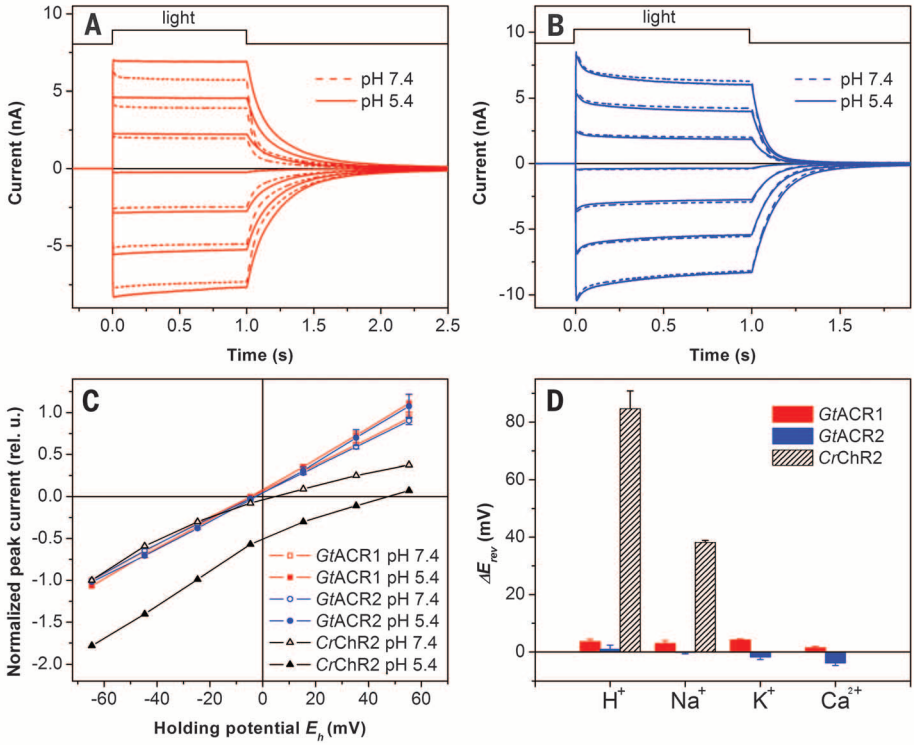

Fig. 2. ACRs do not conduct cations. Photocurrents generated by *Gt*ACR1 (**A**) and *Gt*ACR2 (**B**) in HEK293 cells at the membrane potentials changed in 20-mV steps from –60 mV at the amplifier output (bottom to top). The pipette solution was standard, and the bath solution was as indicated. (**C**) *IE* relationships measured at various pH of the bath. The data (mean values ± SEM, n = 4 to 6 cells) were corrected for liquid junction potentials (table S1) and normalized to the value measured at –60 mV at pH 7.4. Representative data for *Cr*ChR2 are shown for comparison. (**D**) E_{rev} shifts measured upon variation of the cation composition of the bath. The data are mean values ± SEM (n = 3 to 6 cells).

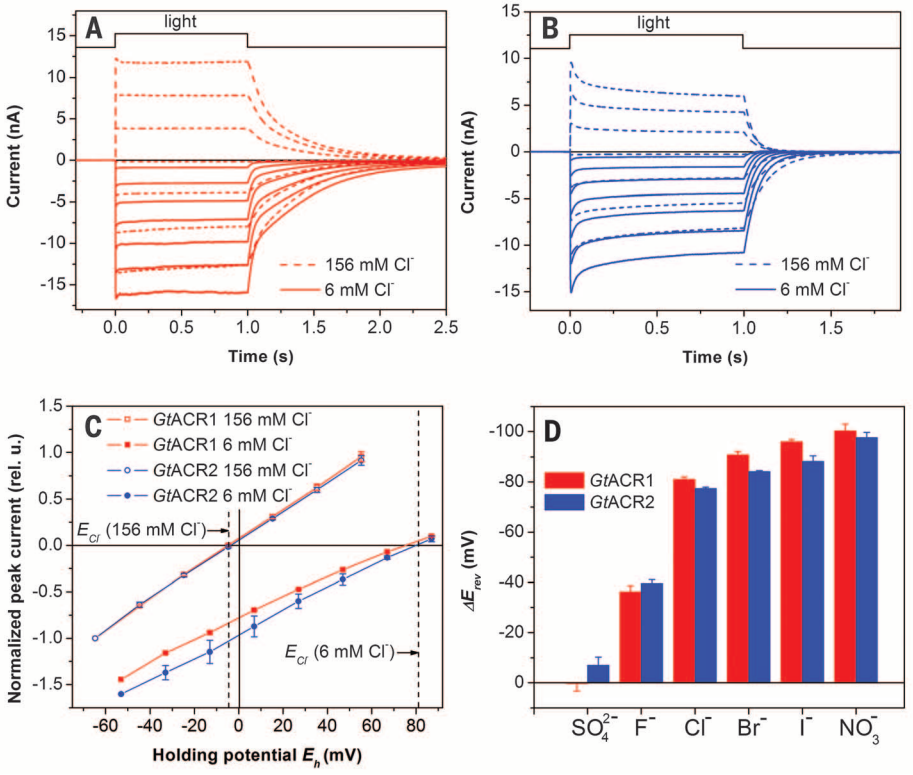

Fig. 3. Anion selectivity of ACRs. Photocurrents generated by *Gt*ACR1 (**A**) and *Gt*ACR2 (**B**) in HEK293 cells at the membrane potentials changed in 20-mV steps from –60 mV at the amplifier output (bottom to top). The pipette solution was standard, and the bath solution was as indicated. (**C**) *IE* relationships measured at various Cl^- concentrations in the bath. The data (mean values ± SEM, n = 4 to 6 cells) were corrected for liquid junction potentials (table S1) and normalized to the value measured at –60 mV at 156 mM Cl^-. The dashed vertical lines show the Nernst equilibrium potential for Cl^- at the bath concentrations used. (**D**) E_{rev} shifts measured upon variation of the anion composition of the bath. The data are mean values ± SEM (n = 3 to 6 cells).

lesser degree of inactivation (Fig. 1, inset). The dependence of the current rise rate on the stimulus intensity exhibited a higher saturation level than the current amplitude (Fig. 1E) and therefore was used for construction of the action spectra. *Gt*ACR1 showed maximal sensitivity to 515-nm light, with a shoulder on the short-wavelength slope of the spectrum (Fig. 1F). The sensitivity of *Gt*ACR2 peaked at 470 nm, with additional bands at 445 and 415 nm (Fig. 1F).

The sign of *Gt*ACR1 and *Gt*ACR2 photocurrents reversed when the membrane potential was shifted to more positive values (Fig. 2, A and B, respectively). In the tested range from –60 to 60 mV, the current-voltage relationships (*IE* curves) were linear (Fig. 2C), unlike those for chlorophyte ChRs (*22*). To characterize the ion permeability of *G. theta* rhodopsins, we measured *IE* curves and determined the reversal potential (E_{rev}) upon variation of the ionic composition of the bath solution. In contrast to chlorophyte ChRs, for which protons are the most highly permeable ions, E_{rev} of the currents generated by *Gt*ACR1 and *Gt*ACR2 were not affected by pH (Fig. 2C). Moreover, no E_{rev} shifts were observed when the large nonpermeable organic cation *N*-methyl-glucamine (NMG^+) was replaced with Na^+, K^+, or Ca^{2+} (Fig. 2D). We conclude that *Gt*ACR1 and *Gt*ACR2 are not permeable by cations conducted by chlorophyte ChRs.

When most of the Cl^- in the bath was replaced with the large anion aspartate, yielding a Nernst equilibrium potential for Cl^- (E_{Cl}) of 81 mV, E_{rev} shifted to 75 ± 2.4 and 80 ± 1.4 mV (mean ± SEM, n = 4 to 5 cells) for *Gt*ACR1 and *Gt*ACR2, respectively (Fig. 3C), as would be expected only if the currents were exclusively due to passive Cl^- transport. We compared the permeability of various anions by substituting them for nonpermeable Asp^- in the bath. For both *G. theta* ACRs, I^-, NO_3^-, or Br^- caused even greater E_{rev} shifts than Cl^-. F^- caused a smaller shift, whereas SO_4^{2-} was nonpermeable. The permeability sequence $NO_3^- > I^- > Br^- > Cl^- > F^- > SO_4^{2-} = Asp^-$ determined for ACRs is in accord with the lyotropic series characteristic of many Cl^- channels from animal cells (*23*).

The cytoplasmic Cl^- concentration in most animal cells, including neurons, is low (*24*). Under such conditions (5 mM Cl^- in the pipette and 156 mM in the bath), *G. theta* ACRs generated hyperpolarizing currents in HEK293 cells at E_h above the Nernst equilibrium potential for Cl^- (E_{Cl}) (fig. S3). The amplitude of *Gt*ACR2 photocurrents was similar, but the kinetics was faster than that of *Gt*ACR1 currents, which is advantageous for control of neuronal activity. Hyperpolarizing photocurrents generated by *Gt*ACR2 at the less-than-1000th lower light intensity were equal to the maximal currents generated by the proton pump archaerhodopsin-3 (Arch), a popular tool for optogenetic spike suppression (*12*), and by the recently reported slow ChloC mutant (*14*) (Fig. 4A, black arrow). The stimulus-response curve for the mutant was less steep than for *Gt*ACR2 because of the slower current kinetics of the latter (Fig. 4E). However, even at nonsaturating light intensities, *Gt*ACR2 remained more than 100 times more photosensitive than slow ChloC (Fig. 4A, red arrow). The larger amplitude of *Gt*ACR2 photocurrents was not due to its higher expression level, as assessed by measuring relative tag fluorescence (fig. S4). Higher unitary conductance of ACRs is shown by stationary noise analysis of macroscopic current fluctuations, which

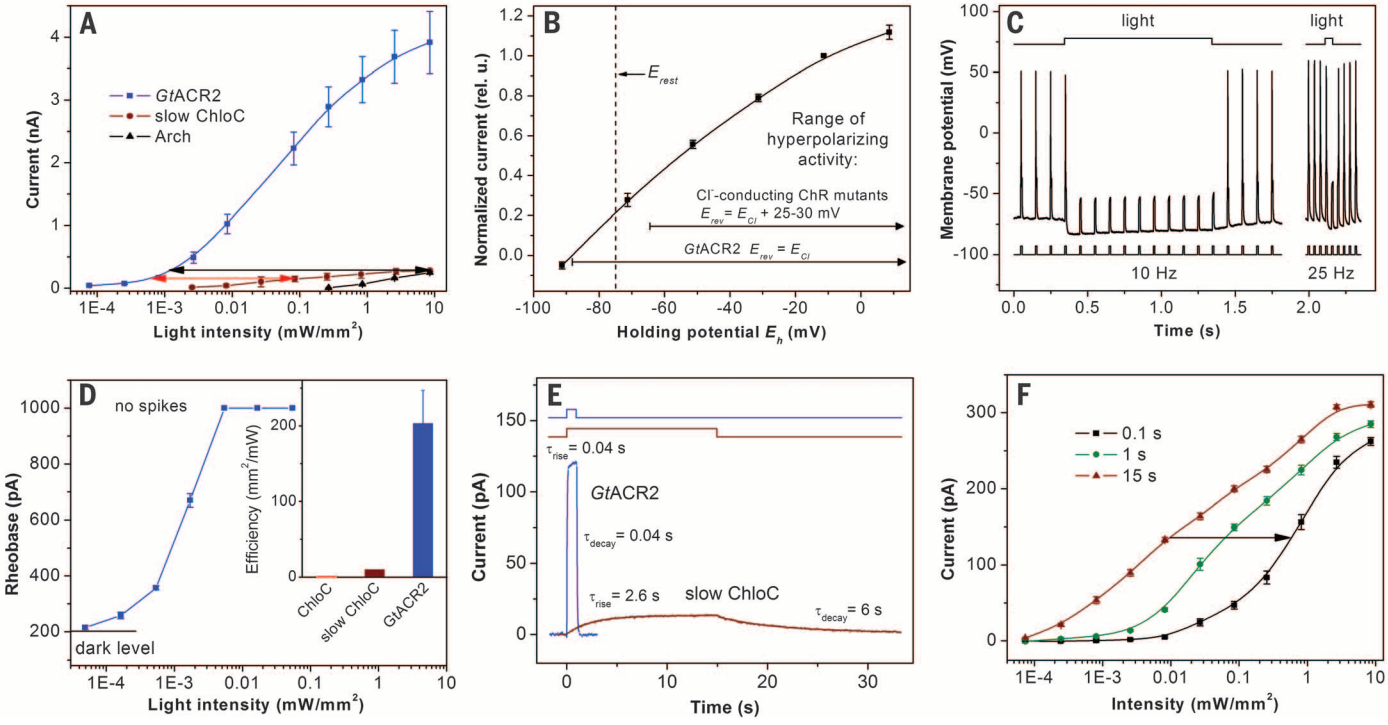

Fig. 4. *Gt*ACR2 as a hyperpolarizing tool. (**A**) Light-intensity dependence of photocurrents generated by *Gt*ACR2, slow ChloC, and Arch in HEK293 cells at 20 mV. The arrows show the difference in light sensitivity. (**B**) *IE* relationship for *Gt*ACR2 in neurons. The data (mean values ± SEM, n = 5 cells) were corrected for LJP (table S2). The dashed vertical line shows the resting potential (E_{rest}). The ranges of activity for Cl^--conducting ChR mutants are from (*14*, *15*). (**C**) Photoinhibition of spiking induced by pulsed current injection in a typical neuron expressing *Gt*ACR2. The light intensity was 0.026 mW/mm^2. (**D**) The dependence of the rheobase of current ramp-evoked spikes on the light intensity in a typical neuron expressing *Gt*ACR2. The data are mean values ± SEM (n = 5 repetitions). Light was applied 0.1 s before the beginning of the current ramp. (Inset) Comparative efficiency of *Gt*ACR2 and the ChloC mutants represented as a reciprocal of the minimal light intensity sufficient to fully suppress spiking. The data for *Gt*ACR2 are the mean value ± SEM (n = 7 neurons). Data for the ChloC mutants under continuous illumination are from (*14*). (**E**) Kinetics of the photocurrents generated by *Gt*ACR2 in response to a 1-s light pulse and by slow ChloC in response to a 15-s light pulse (light intensity for both traces was 0.002 mW/mm^2). The time constants (τ) were determined by single exponential fits of the recorded traces. The fitted curves are shown as thick lines of the same color as the data. (**F**) The light-intensity dependence of slow ChloC current amplitude measured at different times after the start of illumination. Data are mean values ± SEM (n = 5 cells). The arrow shows the increase in the light intensity necessary to reach the same current amplitude at 0.1 as at 15 s illumination.

gave values for *Gt*ACR1 and *Gt*ACR2 more than 10 times higher than those for *Cr*ChR2 (fig. S5) (*25*).

In cultured rat pyramidal neurons, *Gt*ACR2 generated hyperpolarizing currents at E_h above −88 mV (Fig. 4B and fig. S6A). This value corresponds exactly to E_{Cl} under our conditions (table S2). This strict selectivity is a second advantage of ACRs over the previously reported Cl^--conducting ChR mutants, for which E_{rev} is 25 to 30 mV more positive than E_{Cl}, due to residual cation permeability (*14*, *15*). The range of potentials at which *Gt*ACR2 hyperpolarizes the membrane is therefore wider and extends through the values typical for resting potentials of neurons (Fig. 4B). In current clamp experiments, *Gt*ACR2 allowed precisely controlled optical silencing of spikes at frequencies up to at least 25 Hz (Fig. 4C and fig. S6B).

To compare the efficiency of *Gt*ACR2 with that of slow ChloC in neurons, we measured the rheobase of current ramp-evoked spikes at different light intensities using the same solutions and current injection protocol as in (*14*). In *Gt*ACR2-expressing neurons, full suppression of spiking was observed at 0.005 mW/mm^2 (Fig. 4D). The fast ChloC mutant, comparable in its kinetics to *Gt*ACR2, could not fully suppress spiking even at 10 mW/mm^2 of light, whereas a relatively higher efficiency of slow ChloC with full suppression at ~0.1 mW/mm^2 (the reciprocal of this value is plotted in the Fig. 4D, inset) was achieved only at the expense of a dramatically slower kinetics and the necessity to illuminate for at least 12 s (*14*) (Fig. 4E). As *Gt*ACR2-driven current reached its maximum within 0.1 s (Fig. 4E), its intensity dependence at any length of the light pulse above 0.1 s was identical to that shown in Fig. 4A. In contrast, the rise of current generated by slow ChloC was 65 times slower (Fig. 4E). Taking into account the intensity dependence of the current amplitude measured with light stimuli of different duration (Fig. 4F), full suppression of spiking by slow ChloC with 0.1-s stimuli would occur at 7 mW/mm^2, whereas by *Gt*ACR2 it would be reached at an intensity about three orders of magnitude lower.

The membrane potential, membrane resistance, and rheobase in the dark were not affected by *Gt*ACR2 expression in neurons, and the neuronal morphology of *Gt*ACR2-expressing neurons was also normal (fig. S7).

Phylogenetically and functionally, ACRs constitute a distinct family of rhodopsins that are fundamentally different from cation channelrhodopsins (CCRs). As natural anion channels, ACRs provide hyperpolarizing optogenetic tools optimized by evolution for extremely high light sensitivity, absolute anion selectivity, and rapid kinetics.

REFERENCES AND NOTES

1. J. L. Spudich, O. A. Sineshchekov, E. G. Govorunova, *Biochim. Biophys. Acta* **1837**, 546–552 (2014).
2. O. P. Ernst *et al.*, *Chem. Rev.* **114**, 126–163 (2014).
3. K. Deisseroth, *Nat. Methods* **8**, 26–29 (2011).
4. B. Y. Chow, E. S. Boyden, *Sci. Transl. Med.* **5**, 177ps5 (2013).
5. J. Y. Lin, P. M. Knutsen, A. Muller, D. Kleinfeld, R. Y. Tsien, *Nat. Neurosci.* **16**, 1499–1508 (2013).
6. O. A. Sineshchekov, K.-H. Jung, J. L. Spudich, *Proc. Natl. Acad. Sci. U.S.A.* **99**, 8689–8694 (2002).
7. G. Nagel *et al.*, *Science* **296**, 2395–2398 (2002).
8. G. Nagel *et al.*, *Proc. Natl. Acad. Sci. U.S.A.* **100**, 13940–13945 (2003).
9. F. Zhang *et al.*, *Nature* **446**, 633–639 (2007).
10. X. Han, E. S. Boyden, *PLOS ONE* **2**, e299 (2007).
11. V. Gradinaru, K. R. Thompson, K. Deisseroth, *Brain Cell Biol.* **36**, 129–139 (2008).
12. B. Y. Chow *et al.*, *Nature* **463**, 98–102 (2010).
13. A. S. Chuong *et al.*, *Nat. Neurosci.* **17**, 1123–1129 (2014).
14. J. Wietek *et al.*, *Science* **344**, 409–412 (2014).
15. A. Berndt, S. Y. Lee, C. Ramakrishnan, K. Deisseroth, *Science* **344**, 420–424 (2014).
16. F. Zhang *et al.*, *Cell* **147**, 1446–1457 (2011).
17. E. G. Govorunova, O. A. Sineshchekov, H. Li, R. Janz, J. L. Spudich, *J. Biol. Chem.* **288**, 29911–29922 (2013).
18. N. C. Klapoetke *et al.*, *Nat. Methods* **11**, 338–346 (2014).
19. O. A. Sineshchekov *et al.*, *Biophys. J.* **89**, 4310–4319 (2005).
20. V. Gradinaru *et al.*, *Cell* **141**, 154–165 (2010).
21. B. A. Curtis *et al.*, *Nature* **492**, 59–65 (2012).
22. D. Gradmann, A. Berndt, F. Schneider, P. Hegemann, *Biophys. J.* **101**, 1057–1068 (2011).
23. T. J. Jentsch, V. Stein, F. Weinreich, A. A. Zdebik, *Physiol. Rev.* **82**, 503–568 (2002).
24. P. Bregestovski, T. Waseem, M. Mukhtarov, *Front. Mol. Neurosci.* **2**, 15 (2009).
25. K. Feldbauer *et al.*, *Proc. Natl. Acad. Sci. U.S.A.* **106**, 12317–12322 (2009).

ACKNOWLEDGMENTS

E.G.G., O.A.S., J.L.S., and The University of Texas Health Science Center at Houston have filed a provisional patent application that relates to ACRs. We thank E. S. Boyden [Massachusetts Institute of Technology (MIT), Boston] for the archaeorhodopsin-3 expression construct and C. Lois (MIT) for the pCMV-VSVG and pΔ8.9 plasmids. This work was supported by NIH grants R01GM027750, R21MH098288, and S10RR022531, and a UTHealth BRAIN Initiative grant, the Hermann Eye Fund, and Endowed Chair AU-0009 from the Robert A. Welch Foundation.

SUPPLEMENTARY MATERIALS

www.sciencemag.org/content/349/6248/647/suppl/DC1
Materials and Methods
Figs. S1 to S7
Tables S1 and S2
References (*26*–*29*)

23 January 2015; accepted 10 June 2015
Published online 25 June 2015
10.1126/science.aaa7484

NEURODEGENERATION

TDP-43 repression of nonconserved cryptic exons is compromised in ALS-FTD

Jonathan P. Ling,[1] Olga Pletnikova,[1] Juan C. Troncoso,[1,2] Philip C. Wong[1,3]*

Cytoplasmic aggregation of TDP-43, accompanied by its nuclear clearance, is a key common pathological hallmark of amyotrophic lateral sclerosis and frontotemporal dementia (ALS-FTD). However, a limited understanding of this RNA-binding protein (RBP) impedes the clarification of pathogenic mechanisms underlying TDP-43 proteinopathy. In contrast to RBPs that regulate splicing of conserved exons, we found that TDP-43 repressed the splicing of nonconserved cryptic exons, maintaining intron integrity. When TDP-43 was depleted from mouse embryonic stem cells, these cryptic exons were spliced into messenger RNAs, often disrupting their translation and promoting nonsense-mediated decay. Moreover, enforced repression of cryptic exons prevented cell death in TDP-43–deficient cells. Furthermore, repression of cryptic exons was impaired in ALS-FTD cases, suggesting that this splicing defect could potentially underlie TDP-43 proteinopathy.

Amyotrophic lateral sclerosis (ALS), a fatal adult-onset motor neuron disease characterized by progressive loss of upper and lower motor neurons, and frontotemporal dementia (FTD), a common form of dementia characterized by a gradual deterioration in behavior, personality, and/or language, share a common disease spectrum (*1*, *2*). Transactivation response element DNA-binding protein 43 (TDP-43, *TARDBP*), is a heterogeneous nuclear ribonucleoprotein (hnRNP) thought to provide the neuropathological link to establish such a disease spectrum (*1*, *3*). In sporadic ALS (~97% of all cases) and sporadic FTD (~45% of all cases), TDP-43 clears from the nucleus and forms ubiquitinated, cytoplasmic inclusions, termed TDP-43 proteinopathy (*2*). Missense mutations in TDP-43 are also linked to familial ALS, strongly supporting the idea that TDP-43 proteinopathy is central to the pathogenesis of sporadic disease (*4*, *5*). Numerous genetic mutations associated with familial ALS-FTD—*VCP*, *GRN*, *OPTN*, *ATXN2*, *SQSTM1*, *UBQLN2*, *PFN1*, *TBK1*, and especially *C9ORF72*—result in TDP-43 proteinopathy, suggesting a convergent mechanism of neurodegeneration (*6*–*9*). Indeed, Tdp-43 is a tightly autoregulated (*10*),

[1]Department of Pathology, Johns Hopkins University School of Medicine, Baltimore, MD 21205-2196, USA. [2]Department of Neurology, Johns Hopkins University School of Medicine, Baltimore, MD 21205-2196, USA. [3]Department of Neuroscience, Johns Hopkins University School of Medicine, Baltimore, MD 21205-2196, USA.
*Corresponding author. E-mail: wong@jhmi.edu

essential gene (*11*–*13*) that is required for neuronal physiology in mice (*14*), fruit flies (*15*), and zebrafish (*16*).

TDP-43's consensus binding motif has been identified as the "UG" dinucleotide repeat (*17*). Using a high-throughput sequencing approach combined with cross-linking immunoprecipitation (HITS-CLIP), direct targets of Tdp-43 have been identified (*18*, *19*). Tdp-43 regulates alternative splicing of a subset of conserved exons by binding to UG-rich domains within proximal intronic regions (*18*, *19*). However, the majority of Tdp-43 binds to repetitive elements within distal introns, locations where Tdp-43 has no clear function. To explore the RNA splicing role of Tdp-43, we assessed the transcriptome of cells lacking Tdp-43 with RNA-sequencing (RNA-seq) (*12*). These Cre^{ER}-inducible Tdp-43 knockout mouse embryonic stem (mES) cells (iTDPKO) permit genetic deletion of Tdp-43 within 2 to 3 days of 4-hydroxytamoxifen (4HT) treatment. However, previous sequencing technologies were unable to provide robust transcriptome-wide splicing data. RNA-seq analyses performed on data with greater read length and coverage improved the splicing resolution and allowed us to identify cryptic exons in mES cells lacking Tdp-43 (Fig. 1).

These splicing variants have not been previously documented in any public databases and strictly appear in nonconserved regions of the genome. Traces of cryptic exons, however, can be detected from previously published RNA-seq data (fig. S1). Most cryptic exons introduce frameshifts and/or premature stop codons, characteristic of nonsense-mediated decay (NMD) (table S1). Additionally, we identified a subset of nonstandard cryptic exons that could be categorized as alternative transcriptional start sites, premature polyadenylation sites, or expansions of conserved canonical exons (Fig. 1, C to E).

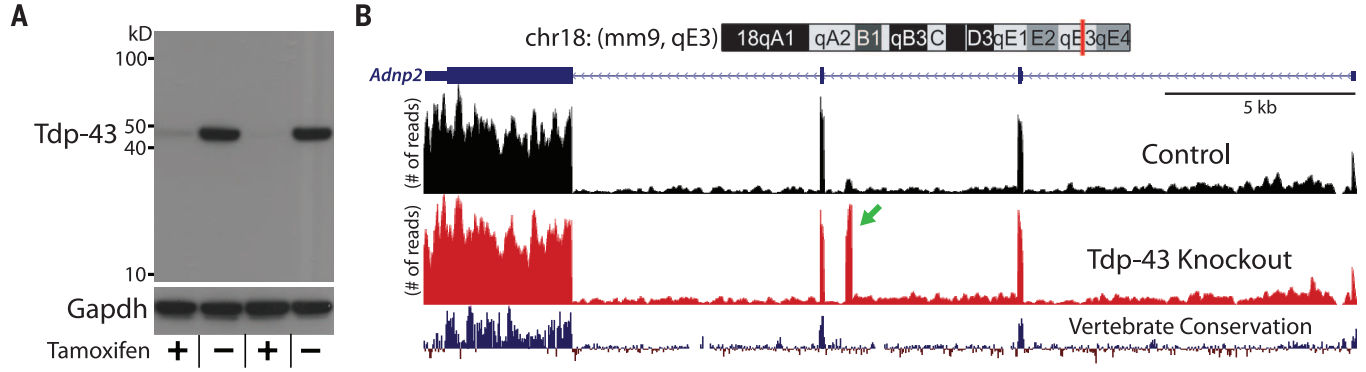

F

Gene	Mouse (mm9) Genomic Sequence
Hgsnat	GUCAGUAAAUACACUCUGCUUAUAUUCGGGCAGUAUAAAAUGGUGAAG...ACAAGAUUGCUUUUAGUAAGAAAUAUGAUUGUGUCUCGUGUGUGUGUGUG
Cluh	CGGCCCUGCCACCUUCUGGUUCUCUUGUCCUAGACGUUCCUGUGCGGC...AGAGCGCAAGUUGGGGUGUGUGUGUGUGUGUGUUAUUGGGGUGGGUUGUC
Sars	AUAAAGGGAAGAGAUUUUACUUUUUUCAAACAGGGUCUCAUGUAGUCC...ACAGCAGGCUUAAAGGUAUGUGUGUGUGUGUGUGUGUGUGUGUGUGUU
Ptcd2	GUGGUCAAAUACCUACUGUUUUUGUCUGUGCAGUGACCUGAUUGCCCA...AGGAGUUUAUGAAGGGUGUGUGUGUGAGUGCAUGUGUGUUUGUGUGUGUG
Adnp2	GCAAAAAGAAAAGAAAAGUGACCUCUGUUUUAGGAGAAAAAGAAAGCA...UUCUCUUGACUGACAGUGAGUUUGUGUGUGUGUGUGUGUGUGUGUGUGUG
Usp15	UGUCUUAAUUUUUUUUCCUUCAUAAAAUAAAAGUAUCCUAGUGUACUC...AAACAGAAUUUAGAGGUGUGUGUGUGUGUGUGUGUGUCUGUGUGUUGU
Synj2bp	UGUGUGUGUGUGUGUGUGUGUAUGUGUGUAGGGUGAAAUGUACACA...UAAGACUUUUAAAACAAAAAAAAAAAAAAAAAAAAAAAAAAAAAAAAAAA
Adipor2	UGUGUGUAUGACAUGUGUGUCUUAUGCUUUCAGAGGCUUGAAGAGGGU...AUUGUGAAUCACCAUGUAGGUGCUGGGACUUGAACCCAGGUUCUCUGUAA
Smg5	GUGUAUCUGUGUACGUGUGUGUCUGUGUUUCAGAAUGGAGAGAUGAAG...CUCCUCUGGCCUCAGGUGUGUGUGUGUGUGCUGUUUCAAAGCAUUUGCCC
A230046K03Rik	UGUCAUCUGAUUGUUGUGUGUGUGUGUUGCUAGAGAGAACCCAAACUG...AAGGGACAGUGACAGGUAAGGACAACAUAGUUGCCAGCAGUGUGGACCTT
Tecpr1	AGCCCCUUGCCAGCUCCUUCUUCCAUUUCCUAGGAGCAUUGUGGGUGU...GUGGAUAGACUGAUGGUGUGUGUCUAGAUGGUGGUGGUGGGUAUAUGAAU
Spata7	UGCUCAUGUUUCUAUUUGUGUUUAAAAUUUUAGGUGUCUAUAUUGGGG...CAAGUGUGUAUUCAGGUGCGUAUGAAUGUGUGUGUAUGCAUAUAGAAGUC
Wbscr22	UGACCAGAAUGAAGCCCGGAAAUACGUUCGCAAGUGAGGAGAGCAUGG...AAUUUGGGAGUGUGUGUGAGUGUGUGUGUGUGUGUGUGUGUGUGUGUG
Sptbn4	UUUUUUUUUUUUUUUUUUUCCUGGAGGGAGGAGGAGGAUCUUGUGACU...AUUACCUUAGCUUGGGUGUGUGUGUGUGUGUGUGUGUGUGUGUGUGCU
	5′ Upstream (Intron) — 5′ Cryptic Exon — 3′ Cryptic Exon — 3′ Downstream (Intron)

Fig. 1. Identification of Tdp-43–associated cryptic exons (*Mus musculus*). (**A**) iTDPKO cells are depleted of Tdp-43 upon treatment with 4HT. (**B**) Visualization of the cryptic exon located in *Adnp2* (red bar) of chromosome 18 (chr18) (top). Gene annotation is shown below, labeling exons (thick) and introns (thin). RNA-seq reads from iTDPKO untreated ("Control") and 4HT treated ("Tdp-43 Knockout") are aligned to the mm9 genome. The cryptic exon (green arrow) is not conserved (vertebrate conservation, bottom). Strand-specific analysis also confirms the incorporation of cryptic exons on the transcribing strand (fig. S11). (**C** to **E**) Most cryptic exons have standard 5′ and 3′ splice sites [*Adipor2*, (C)]. Occasionally, cryptic exons can present as transcriptional start sites [*Sptbn4*, (C)], polyadenylation sites [*Synj2bp*, (D)], or exon extensions [*Wbscr22*, (E)]. (**F**) Cryptic exons are flanked by UG tandem repeats that exist upstream, downstream, or internally.

To determine whether these cryptic exons were direct targets of Tdp-43 binding or missplicing events caused by indirect downstream effects, we looked for evidence of protein-RNA association. Tdp-43 has a very high affinity for UG repeats, with a dissociation constant (K_d) of 14 nM for only six repeats (*20*). As predicted, long UG dinucleotide repeats are adjacent to each cryptic exon (Fig. 1F). Tdp-43 localized to these flanking repeats could potentially act as a general splicing repressor. Further evidence of Tdp-43's role in repressing cryptic exons comes from previous HITS-CLIP data that mapped Tdp-43's direct RNA targets (*19*). As expected, clusters of HITS-CLIP reads were mapped onto cryptic exons, further supporting the hypothesis that Tdp-43 represses cryptic exons via direct interaction (fig. S2).

We next wanted to establish whether these cryptic exons were a main contributor to the cell death observed after genetic deletion of Tdp-43 (*12*). To this end, we designed a fusion protein by coupling TDP-43's N-terminal fragment (N-TDP) to a well-characterized splicing repressor domain, replacing TDP-43's C-terminal fragment (C-TDP) (Fig. 2A). N-TDP contains a dimerization domain, nuclear localization signal, and two UG binding RNA recognition motifs but is insufficient to act as a splicing repressor (*21*–*23*). In contrast, C-TDP is a glycine rich, prion-like domain that harbors the vast majority of mutations associated with ALS and mediates the protein-protein interactions important for splicing (*24*). We replaced the C-TDP in our fusion protein with the minimal splicing repressor domain derived from ribonucleoprotein, PTB-binding 1 (*RAVER1*) (*25*, *26*). This chimeric protein, termed GTR, translocated to the nucleus, bound to UG repeats, and repressed nearby exons (Fig. 2).

The GTR construct and associated controls were then transiently transfected into 4HT-treated iTDPKO cells and screened for survivors by means of flow cytometry (fig. S3). After exposure to 4HT, the majority of Tdp-43–depleted iTDPKO cells underwent apoptosis. Whereas 4HT-treated iTDPKO cells transfected with control constructs also failed to survive, a portion of those transfected with the GTR construct remained viable.

To rule out the possibility that this rescue was only a transient effect of the GTR expression, we generated a stable transfected line of Tdp-43–deficient cells expressing GTR, termed GTR1 (Fig. 2B). The growth rate of GTR1 cells was almost identical to iTDPKO cells (fig. S4), and the majority of up-regulated and down-regulated transcripts in Tdp-43 knockout cells were also restored to normal values in GTR1 cells (Fig. 2G), including several transcripts markedly down-regulated because of nonsense-mediated decay (table S1). To verify that the rescue effect was correlated with repression of cryptic exons, we RNA-sequenced the GTR1 cells. Indeed, the majority of cryptic exons were highly repressed (Fig. 2, C to E, and table S2), with the remaining cryptic exons experiencing varying degrees of partial repression (Fig. 2F). Thus, a deficiency in cryptic exon repression could contribute to cell death.

Because mouse cryptic exons are embedded within nonconserved sequences of the mouse genome, we predicted that human cryptic exons would be located in different regions of the human genome. HeLa cells treated with TDP-43 small interfering RNA (siRNA) (Fig. 3A) expressed numerous cryptic exons (Fig. 3, B to F, and table S3). These human-specific cryptic exons were flanked by UG tandem repeats (Fig. 3G) and were direct targets of TDP-43 (fig. S5). The human cryptic exons shared no overlap with mouse cryptic exons and instead influenced an entirely different set of genes (table S4).

To further validate this model of cryptic exon repression, we engineered a mini-gene reporter construct encompassing a cryptic exon locus identified in *ATG4B* and transfected human HeLa cells lacking TDP-43 (Fig. 4). Under normal conditions, only isoform A was expressed (Fig. 4C, lanes 1, 4, and 7). After TDP-43 was depleted from the cell, cryptic isoforms B and C were no longer repressed (Fig. 4C, lanes 2, 5, and 8). Isoform C was not initially detected through RNA-seq owing to masking by an overlapping cryptic cassette exon; sequencing confirmed its identity as an exon extension (fig. S6). Isoforms B and C were repressed by GTR

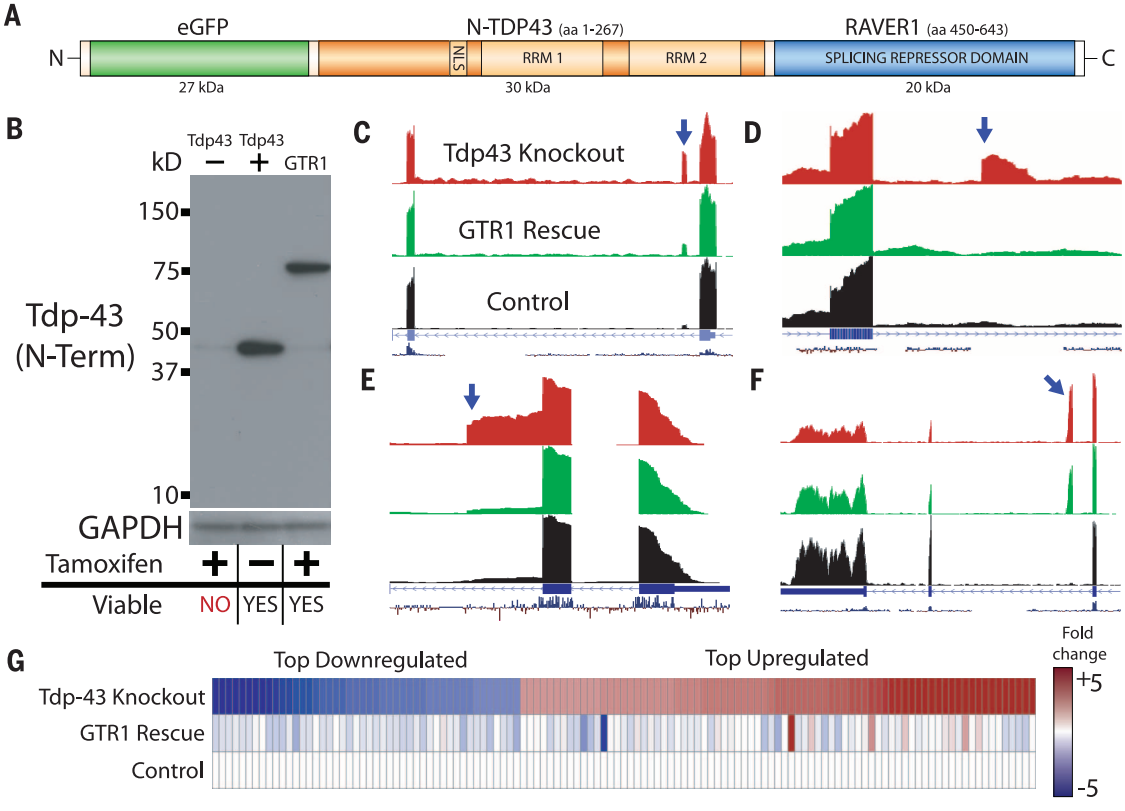

Fig. 2. Repression of cryptic exons is associated with the prevention of cell death induced by loss of Tdp-43. (**A**) Diagram of the green fluorescent protein, N terminus TDP-43, RAVER1 splicing repressor domain chimeric construct (GTR). (**B**) Immunoblot using an antibody that recognizes mouse/human N terminus of Tdp-43. (**C** to **F**) Whereas iTDPKO cells are not viable when depleted of Tdp-43, GTR1 cells are fully viable. GTR represses a variety of cryptic exons; standard cassette [*Adipor2*, (C)], polyadenylation [*Zfp809*, (D)], and exon extensions [*Wbscr22*, (E)]. However, some cryptic exons are only partially rescued [*Synj2bp*, (F)]. (**G**) RNA-seq transcript expression levels for Tdp-43 knockout cells and GTR1 rescue cells were compared with untreated iTDPKO cells. The top 124 down-regulated/up-regulated genes in the Tdp-43 knockout cells were mostly restored to normal levels in the GTR1 rescued cells. Full transcript expression data are provided in the supplementary materials (data table S1).

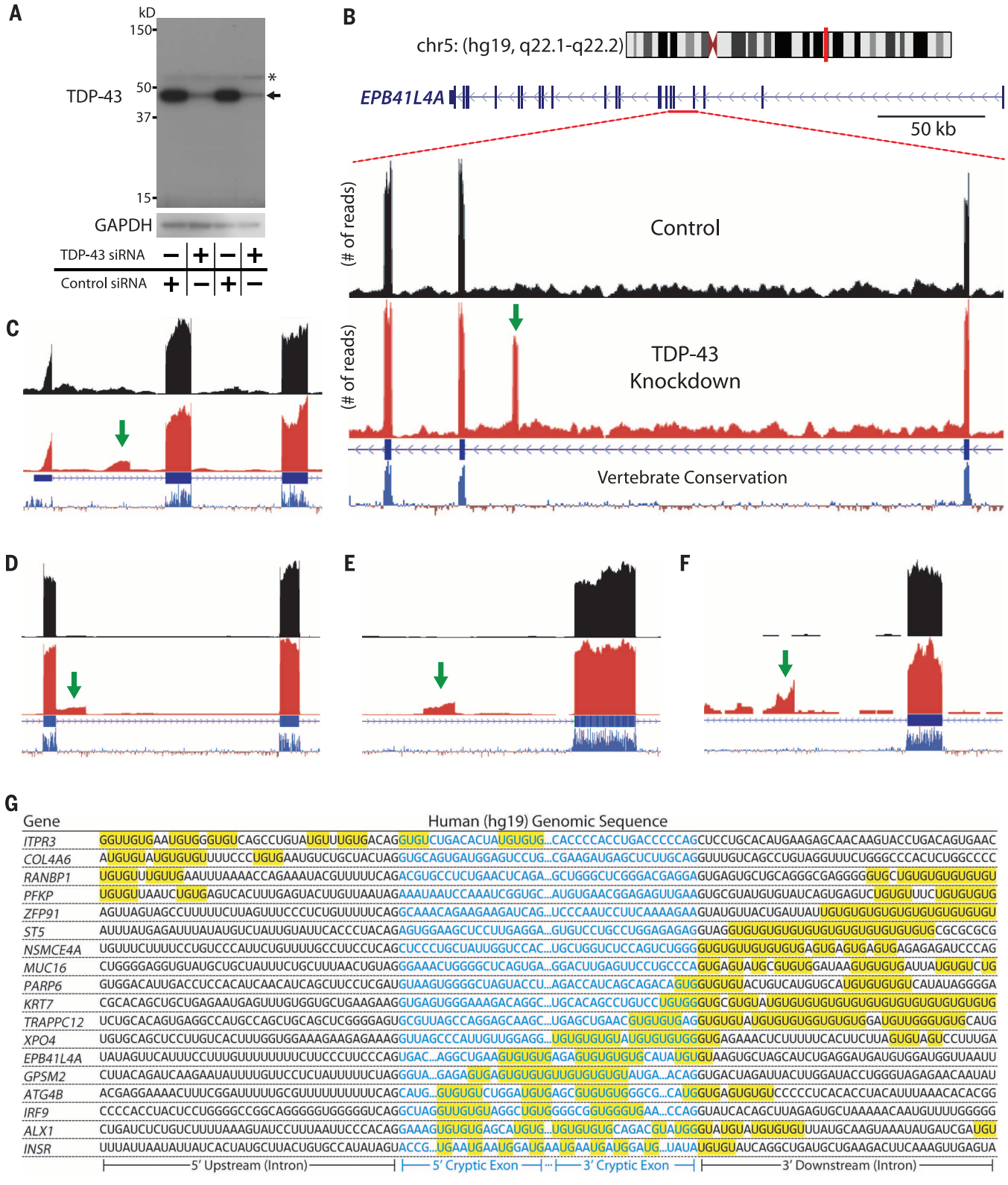

Fig. 3. Identification of TDP-43–associated cryptic exons (*Homo sapiens*). (**A**) TDP-43 protein levels are greatly reduced when HeLa cells are treated with TDP-43 siRNA (asterisk indicates nonspecific band). (**B**) Visualization of the cryptic exon located in *EPB41L4A*. Zoom-in of gene annotation demonstrates that the cryptic exon (green arrow) resides in a nonconserved region. Strand-specific analysis also verifies the incorporation of cryptic exons on the transcribing strand (fig. S12). (**C** to **F**) *IRF9* contains a transcriptional start site (C), *KRT7* contains an exon extension (D), *GPSM2* contains a standard cryptic exon (E), and *INSR* contains a polyadenylation site (F). (**G**) UG repeats are also found adjacent to human cryptic exons.

(Fig. 4C, lanes 3, 6, and 9), supporting the notion that TDP-43 may function as a general repressor whose specificity is determined by its affinity for UG repeats rather than its C-terminal domain.

Having identified a set of cryptic exons that TDP-43 regulates in humans, we then screened postmortem brain tissues from an ALS-FTD cohort (table S5) for the presence of cryptic exons. A reverse transcription polymerase chain reaction (RT-PCR) protocol was designed to amplify across the cryptic exon splice junctions of *GPSM2* and *ATG4B* (Fig. 4D). Corresponding PCR products were readily observed in all ALS-FTD cases tested but not in controls (Fig. 4E) and validated by means of DNA sequencing (fig. S7). Thus, TDP-43 proteinopathy may be correlated with TDP-43 loss of function.

We have found that TDP-43 functions as a splicing repressor of nonconserved cryptic exons (fig. S8). A defect in this regulatory mechanism

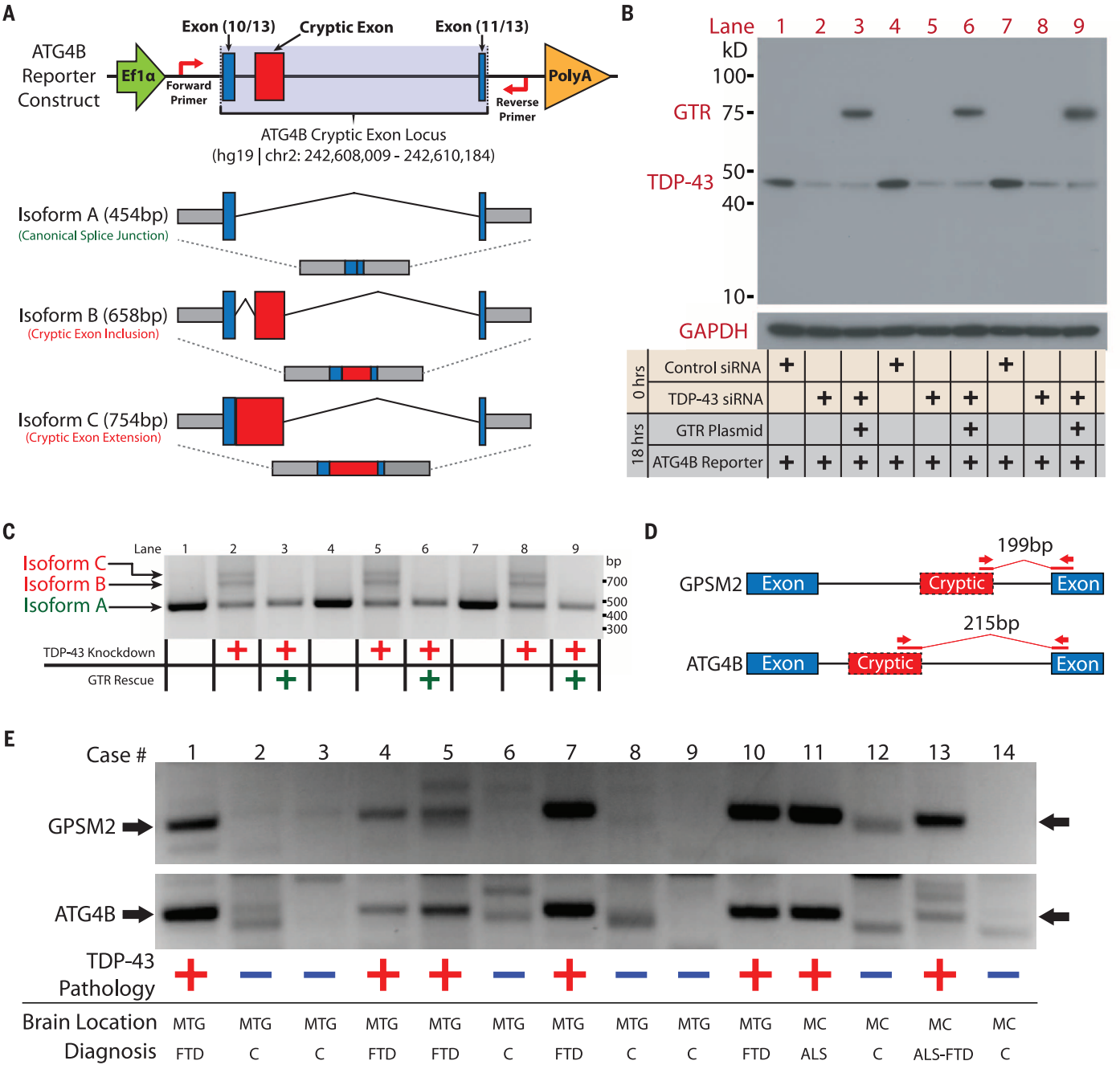

Fig. 4. Validation of human cryptic exons and their detection in ALS-FTD brain tissue. (**A**) Diagram of *ATG4B* reporter construct and potential splicing isoforms. (**B**) Immunoblots of HeLa transfections under normal or TDP-43–depleted conditions and (**C**) the associated electrophoretic gel analysis of splicing isoforms were performed in triplicate. Cryptic isoforms B and C only appeared under conditions of TDP-43 depletion and were rescued by the GTR protein. (**D**) Diagram of RT-PCR detection strategy. Primers were designed to amplify only the cryptic exon splice junction. (**E**) DNA fragments are detected at 199 base pairs (bp) (*GPSM2*) and at 215 bp (*ATG4B*) for all cases that display TDP-43 proteinopathy; control cases do not display these fragments. Full gel images and case demographics are provided in the supplementary materials (fig. S7 and table S5). Cases 1, 7, and 13 are positive for *C9ORF72* expansions; the remaining cases are sporadic. MTG, middle temporal gyrus; MC, motor cortex.

could be linked to TDP-43 proteinopathy in ALS-FTD. Acting as an inhibitory hnRNP, TDP-43 may also regulate conserved exons (*18*, *19*, *27*). Analysis of mouse embryonic stem cell RNA-seq data suggests that some alternatively spliced conserved exons contain UG repeats and may be direct targets of TDP-43 (fig. S9). Further work will be required to determine TDP-43's role regarding splicing of conserved exons.

Although the subset of cryptic exons in mice (table S1) is entirely different from that of humans (table S3), TDP-43's cryptic exon repression function has been maintained across evolution. The protein sequence of TDP-43 is conserved and interchangeable across humans, mice, flies, and nematodes (*17*, *22*), suggesting that TDP-43 cryptic exon repression could extend beyond mammals as well. From the perspective of human disease, however, we believe that studying genes specifically affected by cryptic exons in the human context could help clarify the development of TDP-43 proteinopathy. Two genes in particular—*ATG4B* and *RANBP1*—function in autophagy and nuclear import, respectively. We envision a feed-forward loop in which loss of TDP-43 function could undermine the cell's ability to restore TDP-43 to the nucleus, leading to further loss of function (fig. S10).

The discovery of TDP-43's role in repressing cryptic exons will advance our understanding of human diseases with TDP-43 proteinopathy and form the basis for previously unidentified biomarkers and therapeutic strategies.

REFERENCES AND NOTES

1. E. B. Lee, V. M. Lee, J. Q. Trojanowski, *Nat. Rev. Neurosci.* **13**, 38–50 (2012).
2. S.-C. Ling, M. Polymenidou, D. W. Cleveland, *Neuron* **79**, 416–438 (2013).
3. M. Neumann *et al.*, *Science* **314**, 130–133 (2006).
4. J. Sreedharan *et al.*, *Science* **319**, 1668–1672 (2008).
5. E. Kabashi *et al.*, *Nat. Genet.* **40**, 572–574 (2008).
6. J. Janssens, C. Van Broeckhoven, *Hum. Mol. Genet.* **22** (R1), R77–R87 (2013).
7. A. E. Renton, A. Chiò, B. J. Traynor, *Nat. Neurosci.* **17**, 17–23 (2014).
8. A. Freischmidt *et al.*, *Nat. Neurosci.* **18**, 631–636 (2015).
9. E. T. Cirulli *et al.*, *Science* **347**, 1436–1441 (2015).
10. Y. M. Ayala *et al.*, *EMBO J.* **30**, 277–288 (2011).
11. C. F. Sephton *et al.*, *J. Biol. Chem.* **285**, 6826–6834 (2010).
12. P.-M. Chiang *et al.*, *Proc. Natl. Acad. Sci. U.S.A.* **107**, 16320–16324 (2010).
13. B. C. Kraemer *et al.*, *Acta Neuropathol.* **119**, 409–419 (2010).
14. C. Yang *et al.*, *Proc. Natl. Acad. Sci. U.S.A.* **111**, E1121–E1129 (2014).
15. F. Feiguin *et al.*, *FEBS Lett.* **583**, 1586–1592 (2009).
16. B. Schmid *et al.*, *Proc. Natl. Acad. Sci. U.S.A.* **110**, 4986–4991 (2013).
17. P. J. Lukavsky *et al.*, *Nat. Struct. Mol. Biol.* **20**, 1443–1449 (2013).
18. J. R. Tollervey *et al.*, *Nat. Neurosci.* **14**, 452–458 (2011).
19. M. Polymenidou *et al.*, *Nat. Neurosci.* **14**, 459–468 (2011).
20. P.-H. Kuo, L. G. Doudeva, Y.-T. Wang, C.-K. J. Shen, H. S. Yuan, *Nucleic Acids Res.* **37**, 1799–1808 (2009).
21. Y.-J. Zhang *et al.*, *Hum. Mol. Genet.* **22**, 3112–3122 (2013).
22. Y. M. Ayala *et al.*, *J. Mol. Biol.* **348**, 575–588 (2005).
23. A. D'Ambrogio *et al.*, *Nucleic Acids Res.* **37**, 4116–4126 (2009).
24. T. Nonaka *et al.*, *Cell Reports* **4**, 124–134 (2013).
25. N. Gromak *et al.*, *EMBO J.* **22**, 6356–6364 (2003).
26. A. P. Rideau *et al.*, *Nat. Struct. Mol. Biol.* **13**, 839–848 (2006).
27. X.-D. Fu, M. Ares Jr., *Nat. Rev. Genet.* **15**, 689–701 (2014).

ACKNOWLEDGMENTS

We thank P. Schaughency, S. Wheelan, and the rest of the Next Generation Sequencing Center [Johns Hopkins Medical Institution (JHMI)] staff for their RNA sequencing service. We also thank X. Zhang for flow cytometry assistance (Ross Flow Cytometry Core, JHMI), R. Roth for confocal imaging, and J. Bedont for editorial support. Last, we thank P. Rabin for encouragement and support of FTD studies and C. Onyike for clinical evaluations of cases of frontotemporal lobar degeneration (FTLD). This work was supported in part by The Robert Packard Center for ALS Research, Muscular Dystrophy Association, the Amyotrophic Lateral Sclerosis Association, Target ALS, the Johns Hopkins University Neuropathology Pelda fund, the Johns Hopkins Alzheimer's Disease Research Center (NIH P50AG05146), and the Samuel I. Newhouse Foundation. J.P.L. and P.C.W. have filed a patent application (number 62/180,988) in the United States that pertains to using incorporation of cryptic exons in RNA transcripts identified in human diseases exhibiting TDP-43 proteinopathy as the basis for biomarkers and therapeutic targets/strategies. Raw sequencing files (100 bp, paired-end) have been deposited at the National Center for Biotechnology Information Sequence Read Archive under SRP057819 and SRP057948. The authors declare no conflicts of interest. J.P.L. and P.C.W. designed, analyzed, and interpreted experiments. J.P.L. performed all studies. O.P. and J.C.T. evaluated brain tissues of ALS and FTLD cases and controls. J.P.L. and P.C.W. wrote the manuscript, and all authors discussed results and approved the manuscript.

SUPPLEMENTARY MATERIALS

www.sciencemag.org/content/349/6248/650/suppl/DC1
Materials and Methods
Figs. S1 to S12
Tables S1 to S5
References (*28*–*30*)
Data Table S1

10 March 2015; accepted 13 July 2015
10.1126/science.aab0983

REPRODUCIBILITY:

IS IT AN ISSUE WORTH OUR FOCUS?

61%

of survey respondents believe

irreproducibility is a major barrier to successful translational research

AND only 22% have been able to reproduce other labs' published work.

BUT Recent discussions voice concern about the time and effort involved in validation of key experimental results through independent replication. **Do you agree?**

Learn more and be part of the change.

Educate and advocate for improved reproducibility.

sigma-aldrich.com/reproducibility

Statistics used are from the 2014 State of Translational Research Report.

SIGMA-ALDRICH®

The Ho-Am Prize ignites the passion and innovative spirit for scientific discovery

We welcome your recommendations for the 2016 Ho-Am Prize candidates.

- Award categories are Science, Engineering, and Medicine.
- Researchers of Korean heritage are eligible for the Prize.
- Deadline for submission is Oct. 31, 2015.

*Learn more about candidate recommendation at **www.hoamprize.org**

To continue Samsung Founder "Ho-Am" Byung-Chull Lee's (1910-1987) efforts to maximize both human potential and public interest, Chairman Kun-Hee Lee of Samsung established the Prize in 1990. The Prize is awarded annually to outstanding researchers of Korean heritage around the world who have made important contributions to the advancement of science.

THE HO-AM PRIZE

HOAM
THE HO-AM FOUNDATION

SAMSUNG

Mirus | The Transfection Experts

PASSION

*"Being a geek just means that you're passionate about something."**
Olivia Munn, American actress

Geek out.

Whatever you call it, we're committed. Our work at Mirus began with the desire for great science. Great science that has led to nucleic acid delivery technologies our customers depend on. Two decades after our inception, transfection continues to be our passion, providing scientists the most reliable products and expertise that include:

- ***Trans*IT-X2®:** a novel, polymeric broad spectrum delivery reagent for high efficiency plasmid DNA and/or siRNA delivery.
- ***Trans*IT®-Insect:** our newest passion that offers transfection for high yield baculovirus production in insect cells.
- ***Trans*IT®-LT1:** the first and still most widely used, low toxicity, broad spectrum delivery reagent.

PASSION VISION Celebrating 20 YEARS INSPIRATION

mirusbio.com
Providing gene delivery expertise since 1995

Cell Energy Phenotype Test

The XFp Cell Energy Phenotype Test Kit enables a unique real-time assay on live cells that determines their baseline metabolic phenotype and potential. This 1-hour test measures both the mitochondrial and glycolytic activity of the cells, and compares their baseline values with metabolic activity under stressed conditions, induced by a single injection, to determine the metabolic potential—the cells' ability to respond to an energy demand. This kit has been designed specifically for use with the XFp Extracellular Flux Analyzer. The new XFp Cell Energy Phenotype Test is the only method available that can provide a metabolic phenotype with which scientists can make direct, functional comparisons of both metabolic pathways between groups of live cells. With this information cancer researchers can then quickly realize the functional consequences of somatic mutations in terms of metabolic adaptations and reprogramming events that drive tumor malignancies.

Seahorse Bioscience
For info: 978-671-1600
www.seahorsebio.com

Cell Culture Growth Supplement

A new GroPro Cell Culture Growth Supplement allows for culturing of primary cells and cell lines without the concern for transmission of bovine prions and xenogeneic reactions. The new GroPro line delivers higher standards of purity, more affordable cell culture solutions in biomedical research. This new GroPro supplement is a convenient, ready-to-use human platelet lysate (HPL) formulation that can be used at the same supplementation percentages as fetal bovine serum (FBS) in traditional cultures. HPL has proven to be an excellent cost effective substitute for FBS in cell culture growth medium without the risk of xenogeneic infections or immune reactions. Currently, the use of HPL in culture medium requires the addition of heparin to prevent alloimmune aggregation which can create visible clots in the medium. The GroPro product line does not require the use of heparin thus reducing deleterious downstream effects, yet formulated to be used at normal FBS concentrations.

ZenBio
For info: 866-234-7673
www.zen-bio.com

Live Cell Imager and Counter

The JuLI FL is the next generation, smart fluorescence live cell movie analyzer and counter. The JuLI FL uses novel optics to capture live-cell images from various cell culture dishes. It can perform cell-based assays, including cell counting, cell viability, and GFP/RFP expression level checking. This gives the user quantified cell confluence results with low variation and growth curve data. The JuLI features time-lapse image capturing and movie making for cell counting with GFP or RFP expression level checking. It can be used as a single unit or with a dual system to obtain comparative data. The easy-to-operate system features a user friendly interface with LCD touchscreen. Its compact size means that it fits any bench or can be placed inside a cell culture incubator with ease. Simple steps guide the user at each stage of the system setup, image capture, and the analysis operations.

Eikonix
For info: +44-(0)-1223-515440
www.eikonix.com

Stem Cell Media

A new pluripotent stem cell (PSC) medium is designed to offer researchers unprecedented schedule flexibility, allowing 2-day breaks from culture feeding without having to make changes to current workflows or compromise culture quality. Many stem cell media components, such as fibroblast growth factor 2 (FGF2), lose activity at physiologically relevant temperatures and, therefore, stem cell cultures must be fed daily to preserve pluripotency and tri-lineage differentiation potential. To achieve this, scientists typically must work through the weekend or delegate feeding steps to other scientists, which can introduce unnecessary variability. With this optimized formulation, Essential 8 Flex Medium grows and maintains PSCs over an extended length of time. Unlike other PSC culture solutions that promise, "weekend-free feeding," the new Gibco medium does not require substantial split-ratio adjustments prior to the break in feeding. Moreover, Essential 8 Flex Medium retains nearly 90% FGF2 activity after 72 hours.

Thermo Fisher Scientific
For info: 800-955-6288
www.thermofisher.com

Reprogramming Bundle

The L7 PBMC Reprogramming Bundle is a robust, streamlined and comprehensive platform for the generation of human induced pluripotent stem cells (hiPSCs) and the maintenance of stem cells from a variety of sources. This new bundle slots seamlessly into the existing L7 workflow to enable researchers to reprogram peripheral blood mononuclear cells (PBMCs) for use in downstream experiments. The L7 hPSC System offers a complete workflow that combines primary cells, reprogramming kits, transfection tools, and culturing media, along with a matrix, passaging solution, and cryosolution. As such, it streamlines the reprogramming of somatic cells to generate hiPSCs, as well as supporting the ongoing maintenance and utilization of human embryonic stem cells (hESCs) and hiPSCs. hiPSCs created using the new L7 PBMC Reprogramming Bundle can efficiently differentiate into all three germ layers and are ready for use across a wide range of applications, from basic research and disease modeling, through to drug development and regenerative medicine.

Lonza Bioscience Solutions
For info: 301-898-7025
www.lonza.com

Electronically submit your new product description or product literature information! Go to www.sciencemag.org/products/newproducts.dtl for more information.

Newly offered instrumentation, apparatus, and laboratory materials of interest to researchers in all disciplines in academic, industrial, and governmental organizations are featured in this space. Emphasis is given to purpose, chief characteristics, and availability of products and materials. Endorsement by *Science* or AAAS of any products or materials mentioned is not implied. Additional information may be obtained from the manufacturer or supplier.

want new technologies?

antibodies
apoptosis
biomarkers
cancer
cytometry
data
diseases
DNA
epigenetics
genomics
immunotherapies
medicine
microbiomics
microfluidics
microscopy
neuroscience
proteomics
sequencing
toxicology
transcriptomics

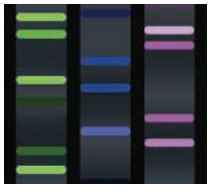

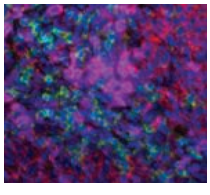

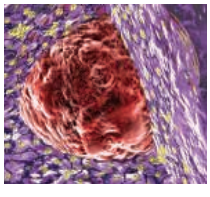

watch our webinars

Learn about the latest breakthroughs, new technologies, and ground-breaking research in a variety of fields. Our expert speakers explain their quality research to you and answer questions submitted by live viewers.

VIEW NOW!
webinar.sciencemag.org

Science
AAAS

Brought to you by the *Science*/AAAS Custom Publishing Office

@SciMagWebinars

JOIN AAAS

Get instant access to *Science*. Support all of the sciences.

The American Association for the Advancement of Science (AAAS) is a non-profit community that is open to everyone, from Nobel laureates to high school students. Ours is a global membership of over 120,000 people who believe in the power of science to make the world a better place.

From the moment you join, you get immediate access to everything that AAAS's award-winning journal *Science* has to offer, including:

- 51 weeks of home delivery of *Science*;
- Instant online retrieval of every *Science* article ever published, from today, dating back to 1880;
- Anytime, anywhere access via the *Science* mobile site and apps for Android, iPad, and iPhone devices;
- Members-only newsletters; and more.

As a member, you are also making a critical contribution to AAAS's efforts to provide a public voice for all of science. With public skepticism about science increasing, and public funding for research more uncertain than ever, this work has never been more important.

AAAS is hard at work promoting science in government offices, in schools, and in the public commons all around the world—with programs like AAAS Senior Scientists and Engineers, which brings volunteer scientists into public school classrooms, or our sweeping petition drives calling for the preservation of federal R&D funding.

Visit **promo.aaas.org/joinaaas** and join today. Together we can make a difference.

Science
AAAS

R&D SYSTEMS™
a bio-techne brand

Do You Suffer from **Panel Envy?**

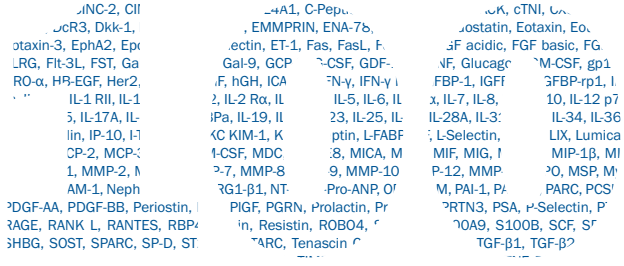

analytes in 1 Luminex® assay.

EXPLORE NOW
rndsystems.com/**100Plex**

#PanelEnvy #100Plex

Science Careers Advertising

For full advertising details, go to ScienceCareers.org and click For Employers, or call one of our representatives.

Tracy Holmes
Worldwide Associate Director
Science Careers
Phone: +44 (0) 1223 326525

THE AMERICAS

E-mail: advertise@sciencecareers.org

Fax: +1 (202) 289 6742

Tina Burks
Phone: +1 (202) 326 6577

Nancy Toema
Phone: +1 (202) 326 6578

Online Job Posting Questions
Phone: +1 (202) 312 6375

EUROPE / INDIA / AUSTRALIA / NEW ZEALAND / REST OF WORLD

E-mail: ads@science-int.co.uk

Fax: +44 (0) 1223 326532

Sarah Lelarge
Phone: +44 (0) 1223 326527

Kelly Grace
Phone: +44 (0) 1223 326528

Online Job Posting Questions
Phone: +44 (0) 1223 326528

JAPAN

Katsuyoshi Fukamizu (Tokyo)
E-mail: kfukamizu@aaas.org
Phone: +81 3 3219 5777

Hiroyuki Mashiki (Kyoto)
E-mail: hmashiki@aaas.org
Phone: +81 75 823 1109

CHINA / KOREA / SINGAPORE / TAIWAN / THAILAND

Ruolei Wu
Phone: +86 186 0082 9345
E-mail: rwu@aaas.org

ScienceCareers
FROM THE JOURNAL SCIENCE AAAS

ScienceCareers.org

UCONN | SCHOOL OF MEDICINE

Tenure Track Faculty Position in Epigenomics

The Department of Genetics and Genome Sciences at the University of Connecticut School of Medicine is seeking a highly qualified individual with an outstanding background in epigenetics and expertise in areas that include but are not limited to genome-wide studies of noncoding RNA, gene regulation and expression, DNA methylation, chromatin structure/function/organization and the analysis/interpretation of epigenomic data sets. The ideal candidate will build on our established strengths that include RNA biology, genomics (e.g. ENCODE) and translational research. The successful applicant will also develop his/her world-class research program in the context of the recently established Institute for Systems Genomics (http://isg.uconn.edu/) that coalesces the interdisciplinary research strengths of UConn's schools and colleges (www.uconn.edu) and the Jackson Laboratory (www.jax.org). The Institute leverages the significant investment from the state, including the $865M Bioscience CT initiative, $172M Tech Park program, the $200M Bioscience Innovation Fund, and $1.5B Next Generation CT.

Applications are invited for a position at the Assistant, Associate or Full Professor level. Faculty will enjoy superb resources including a generous start-up package as well as state-of-the art core facilities for human pluripotent stem cells, mouse transgenics and gene targeting, next-generation sequencing, flow cytometry, confocal microscopy and fluorescence imaging. The successful candidate will be expected to establish an independent and innovative research program that will attract extramural funding and to actively contribute to a rich scientific environment.

Candidates are invited to visit the departmental web page (http://genetics.uchc.edu) and should apply by submitting a curriculum vitae and three letters of reference via the University of Connecticut Health Center Employment Services website, **https://jobs.uchc.edu**, search number 2015-833. Questions regarding this search should be addressed to:

Marc Lalande Ph.D.,
Professor and Chair
Department of Genetics and Genome Sciences
University of Connecticut School of Medicine
Farmington, CT 06030-6403
Email: **ucsci_admin@uchc.edu**

UConn Health is an Equal Opportunity Employer M/F/V/PwD

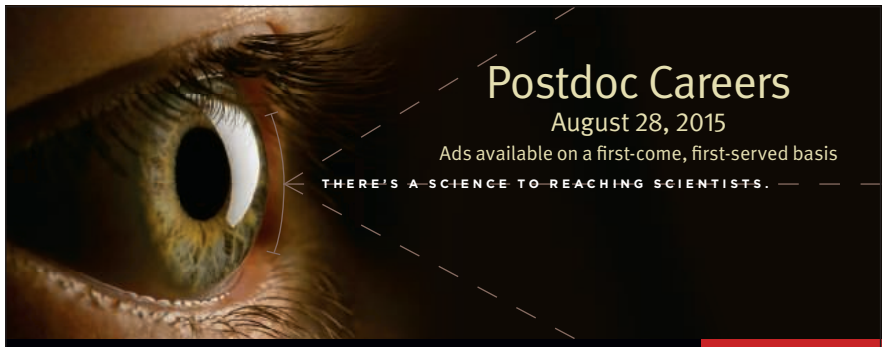

Why choose this postdoc feature for your advertisement?

- Read and respected by 570,400 readers around the globe
- Special bonus distribution to 25,000 scientists beyond our regular circulation
- Relevant ads in the career section with special postdoc banner
- 67% of our weekly readers are Ph.D.s.

SCIENCECAREERS.ORG

Science Careers
AAAS

To book your ad: **advertise@sciencecareers.org**

The Americas
+202-326-6582

Europe/RoW
+44(0)1223-326500

Japan
+81-3-3219-5777

China/Korea/Singapore/Taiwan
+86-186-0082-9345

The NIH Intramural Research Program is Recruiting Tenure-Track "Earl Stadtman Investigators"

The National Institutes of Health, the U.S. government's premier biomedical and behavioral research enterprise and a component of the Department of Health and Human Services, is pleased to announce its seventh annual call for "NIH Earl Stadtman Investigators," a broad recruitment of tenure-track investigators (assistant professor equivalent) for the NIH intramural research program.

Come join the team whose hallmarks are stable funding, intellectual freedom, shared resources, and access to a wide range of scientific expertise. A fantastic array of scientists already has been hired through the "Stadtman" recruitment in the last six years.

A variety of basic and translational/clinical positions are available, with areas of active recruitment including (but not limited to): Behavioral Sciences, Biochemistry, Biomedical Engineering, Biophysics, Biostatistics, Cancer Biology, Cell Biology, Cell Metabolism, Chemical Biology, Chromosome Biology, Circadian Biology, Computational Biology/Bioinformatics (including natural language processing and text mining), Developmental Biology, Epidemiology, Genetics, Genomics, Health Disparities, Hearing & Balance, Immunology, Infectious Diseases, Microbiology, Molecular Pharmacology, Neurodevelopment, Neurosciences, Sensory Biology, Social Sciences, Structural Biology, Systems Biology, Toxicology, Translational and Clinical Research, and Virology.

Who we are: Among our approximately 1,100 principal investigators and 5,000 trainees in the NIH intramural research program are world-renowned experts in basic, translational, population-based, and clinical research. Similar to academia, we offer our scientists the opportunity to mentor outstanding trainees at all levels (e.g., graduate students and postdoctoral fellows) in a research setting.

Whom we seek: We seek a diverse cadre of creative thinkers eager to take on innovative, high-impact research.

Qualifications/eligibility: Applicants must have an M.D., Ph.D., D.D.S./D.M.D., D.V.M., D.O., R.N./Ph.D., or equivalent doctoral degree and have an outstanding record of research accomplishments as evidenced by high quality publications in peer-reviewed journals. Applicants should be non-tenured scientists. Appointees may be U.S. citizens, resident aliens, or non-resident aliens with, or eligible to obtain, a valid employment-authorization visa.

How to apply: Applicants must submit four items: (1) a CV, which should include mentoring and leadership activities; (2) a three-page proposal titled Research Goals, i.e., the research you hope to perform at the NIH; (3) a one-page statement titled Long-term Research Vision and Impact, i.e., what you hope to achieve for yourself, your field, and society; and (4) contact information for three professional references. Submit these through our online application system at http://tenuretrack.nih.gov/apply between August 1 and **September 30, 2015 (11:59 p.m. EDT)**. You will be asked to designate a primary and secondary scientific area of expertise to aid in assigning your application to the appropriate review committee. Requests for letters of recommendation will be sent to your references when you submit your application. Reference letters will be accepted via upload to the website until October 7, 2015 (11:59 p.m. EDT). We cannot accept paper applications.

What to expect: Search committees, composed of experts in various fields, will review and evaluate applicants based on criteria which include publication record, mentoring experience, scientific vision, potential scientific impact of current and proposed research, awards, and references. Select applicants will be invited to the NIH for interviews and will be considered candidates. These candidates will also present seminars open to the public. Some applicants not selected as Earl Stadtman Investigator candidates may be considered for other open NIH research positions. Please find answers to frequently asked questions at http://tenuretrack.nih.gov/apply/faq/stadtman.html.

More information about our program is at http://irp.nih.gov. The inspiring story of Earl and Thressa Stadtman's research at the NIH is at http://history.nih.gov/exhibits/stadtman. Specific questions regarding this recruitment effort may be directed to Dr. Roland Owens, Assistant Director, NIH Office of Intramural Research, at owensrol@mail.nih.gov. DHHS and NIH are Equal Opportunity Employers.

THE NIH IS DEDICATED TO BUILDING AN INCLUSIVE AND DIVERSE COMMUNITY IN ITS TRAINING AND EMPLOYMENT PROGRAMS

POSITIONS OPEN

Princess Margaret Cancer Centre UHN

Chair in Regenerative Radiation Medicine at the Princess Margaret Cancer Centre

The Princess Margaret Cancer Centre Research Institute is seeking an outstanding scientist, whose research program is focused in the area of stem cell biology, tissue injury, and/or tissue regeneration. The Peter and Sheila Godsoe Chair in Regenerative Radiation Medicine has been established to support a research effort aimed at developing strategies to mitigate or repair normal tissue injury, secondary to therapeutic ionizing radiation. The Princess Margaret Cancer Centre Research Institute is the largest cancer research center in Canada, and amongst the largest in North America. This Research Institute is part of the Princess Margaret Cancer Centre, which houses the largest single institution Radiation Medicine Program, consulting on >8000 new cancer patients, and delivering >10,000 courses of radiation treatments each year.

We are seeking candidates who have an outstanding research track record in cellular, molecular or tissue biology, with an understanding or interest in the effects of ionizing radiation on normal tissues; knowledge in neural, lung, intestinal or salivary gland regeneration would be an asset. The successful applicant will be expected to lead a world-class research program on this specific topic, with an emphasis on potential applications into the clinic. The Princess Margaret Cancer Center Research Institute encompasses a broad spectrum of fundamental and translational cancer research programs, with significant strengths in stem cell biology, regenerative medicine, epigenetics, cell signaling, immunology, proteomics, structural biology, nanotechnology, radiation biology, hypoxia, and molecular imaging.

The successful candidate will become the Inaugural Endowed Peter and Sheila Godsoe Chair in Regenerative Radiation Medicine, and be eligible for appointment at the appropriate level in the Departments of Radiation Oncology, Medical Biophysics, or related departments at the University. The position is available immediately, but the search will remain open until the position is filled.

Interested candidates should send their CV, as well as a description of their research interests and program, highlighting leadership experience or potential to:

Dr. Brad Wouters
Interim Director, Princess Margaret Cancer Centre Research Institute
7-504, 610 University Avenue
Toronto, Ontario M5G 2M9
oci.faculty.search@uhnresearch.ca

If emailing, please use the subject line: **Regenerative Medicine Scientist**

POSITIONS OPEN

University of Minnesota
Diabetes and Endocrinology Metabolism
Physician-Scientist / Ph.D.
(Associate Professor - Tenured / Tenure Track)

The Division of Endocrinology and Diabetes Metabolism in the Department of Medicine at the University of Minnesota is seeking an outstanding scientist in the field of diabetes and obesity to participate in building a nationally-recognized research division within a growing department. The ideal candidate will have a proven track record in extramural funding, a history of collaborative research, and experience in teaching and mentoring. Responsibilities include maintaining an active research program, participating in educational activities of the division, and leading activities to build collaborative research in diabetes and obesity. Qualifications include an advanced scientific degree (PhD, MD, DO, or any combination), academic experiences that will allow appointment at the level of associate professor, or higher (dependent on qualifications), tenured or tenure track. Physician scientists are urged to apply, but will have limited responsibilities in the clinical aspects of the division.

The Division of Endocrinology and Diabetes Metabolism in the Department of Medicine at the University of Minnesota consists of 14 University-based faculty, 6 faculty based at the Minneapolis Veterans Administration Medical Center, and 3 faculty at Hennepin County Medical Center. Faculty are involved in all aspects of endocrinology practice and investigation, with particular strengths in diabetes and obesity. Training efforts are supported by a NIH T32 in Diabetes, Endocrinology, and Metabolism, as well as an AFGME-certified endocrinology training program. Opportunities exist for joint appointments in basic science departments for candidates interested in graduate education.

Qualified applicants are invited to apply online at: **https://www.myu.umn.edu/employment** and submit their CVs to Elizabeth Seaquist, M.D., DEM Director, at **seaqu001@umn.edu**.

The University of Minnesota is an Equal Opportunity Employer and Educator.

AWARDS

CALL FOR NOMINATIONS

The Donald Seldin~Holly Smith Award for Pioneering Research

The American Society for Clinical Investigation seeks nominations of outstanding physician-scientists who have demonstrated creativity and accomplishments to lead advances in biomedical research. The recipient of this high-level recognition will be announced at the ASCI's annual meeting in April 2016, will receive an unrestricted award of $30,000 to advance academic efforts, and will deliver the inaugural Seldin~Smith Award Lecture at the ASCI's April 2017 meeting.

The nomination deadline is October 2, 2015.
Details are available at:
www.the-asci.org/seldin-smith-award

ASCI

THE AMERICAN SOCIETY FOR CLINICAL INVESTIGATION

Founded in 1908, the ASCI seeks to support the scientific efforts, educational needs, and clinical aspirations of physician-scientists to improve human health.

By **Elisabeth Pain**

Biology, wet and dry

Sarah Teichmann's work on how cells regulate gene expression and build protein complexes recently won her a European Molecular Biology Organization Gold Medal. At 40, Teichmann holds a joint appointment with the European Bioinformatics Institute and the Wellcome Trust Sanger Institute in Hinxton, U.K. She leads a systems biology group of 17 researchers that uses both computational methods and lab experimentation. *Science* Careers asked Teichmann how she combines the two approaches. This interview has been edited for clarity and brevity.

Q: What came first, informatics or biology?
A: Biology, but informatics has always been at the heart of my research. I felt inspired by computational biology when, as an undergraduate, I read a 1992 commentary by Cyrus Chothia where he made a simple calculation of the likely number of protein families. I felt excited about discovering general principles in biology and became convinced that computational biology would provide the necessary tools.

By the time I started looking for a Ph.D. in the mid-1990s, data sets had become large enough to gain a global view of the protein structure universe and of protein and gene sequences. So I went to work with Chothia at the Medical Research Council Laboratory of Molecular Biology in Cambridge, exploring protein families and the domain organization of proteins in the first completely sequenced genomes.

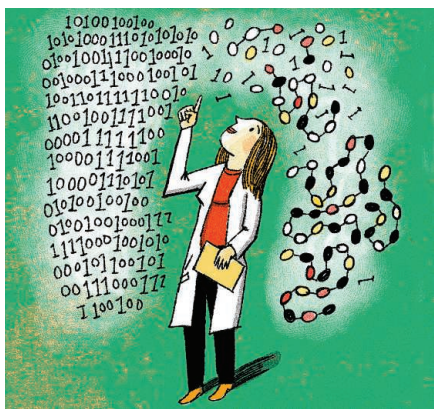

"What unifies both wet and dry work is the conceptual part of the science."

Q: Was computational biology a risky career choice?
A: Yes. But I never looked back, even though at one point I came to feel that computational biology and bioinformatics were viewed as eccentric and unorthodox. My Ph.D. mentor exuded such unwavering optimism and confidence, however, that it made his lab a great place to work. Altogether, during my Ph.D., I published 10 papers.

Q: What are the pros and cons of combining computational and experimental approaches?
A: The beauty of a "wet-dry" group is that you have the ability to interpret your own experimental data computationally and to test computational predictions experimentally. The challenge, however, is maintaining the right balance and harnessing the potential of both sides of the group.

Q: How did you learn these two approaches?
A: During my first degree in the natural sciences at the University of Cambridge, I took math, physics, chemistry, and biology at a high level. I built on this through short courses and learning by doing. Today, I'd recommend more structured courses in algorithms and programming.

Q: How do you feel about experimental work?
A: I discovered early on that my fine motor skills are not up to some of the very tricky handling needed to be a top experimentalist in molecular biology. I have huge respect and gratitude for people who generate data through wet-lab experiments. What unifies both wet and dry work is the conceptual part of the science, which has to be logical and original, and both require exceptional dedication.

Q: Is there anything you wish you had done differently?
A: I made career choices mostly based on the package and colleagues I would have. In retrospect, it is also important to consider questions such as whether the scientific strategy and values of an institute are aligned with your own. I've also learned to shed my introverted nature and appreciate how important it is to talk to people often and openly.

Q: Has it been hard to maintain a good work-life balance?
A: Yes. I have two young daughters, and I believe that our society is a long way from empowering both men and women to balance their professional and family lives. There should be financial and cultural support for both men and women to work shorter hours for several months after the birth of an infant. Ultimately, fair and equal treatment would decrease unconscious bias in all of us. ■

Elisabeth Pain is Science *Careers contributing editor for Europe. Send your story to SciCareerEditor@aaas.org.*

ILLUSTRATION: ROBERT NEUBECKER

Published by AAAS